Electroanalytical Studies

A thesis submitted for the degree of

Doctor of Philosophy

in Physical and Theoretical Chemistry

Yifei Zhang

Somerville College

Trinity Term 2022

Abstract

This thesis focuses on electroanalysis using underpotential deposition (UPD) with anodic stripping voltammetry (ASV). This method is developed for arsenic, which shows visually clear signals for sub 10 ppb concentrations in water. In this method arsenic is deposited as As(0) ad-atoms onto the surface of metal electrode, and the ad-atoms are stripped off with a linear potential scan and the Faradaic stripping signal using for quantitative analysis. The novelty and strength of this method is in its use for sub-monolayer UPD rather than bulk deposits as in previous ASV work both generally and specifically for As.

The fundamentals of electrochemistry and the principles of electrochemical methods are introduced in **Chapter 1**. The need for arsenic detection and quantification arising from environmental contamination by arsenic is discussed in **Chapter 2**. **Chapter 3** summarises the generic chemicals, reagents and instrumentation used in this thesis.

Chapter 4 reports the reliability of drop cast techniques since electrodes modified with small amounts of nanoparticles are subsequently considered for As detection. The investigation is made with reference to Pt nanoparticles and reviews methods to reduce the 'coffee ring effect' generated during the drop cast, where most of the Pt nanoparticles were seen to be accumulated at the edge of the surface of electrode and only small amounts of the nanoparticles were distributed at the centre of the electrode. The key conclusion is that the formation of a ring-like pattern did not affect the overall linear diffusion to the electrode since both types of surface give plausible voltammetric responses unless only tiny amounts of nanoparticles are used.

Chapter 5 reports electroanalysis of arsenite, As(III), in water on Pt macroelectrodes and Pt nanoparticle modified glassy carbon electrodes via the underpotential deposition with anodic stripping voltammetry. No interference was seen from Cu(II) at realistic concentrations but high concentrations of chloride inhibited the deposition of the As ad-atoms. A visually clear detection limit was recorded at 4 ppb, suggesting that this method has practical value noting the WHO limit of 10 ppb for safe drinking water. However, many samples will contain either unknown or high levels of chloride so attention was turned to the use of gold as a substrate for UPD deposition to

overcome this problem whilst retaining the benefits seen for the UPD-ASV method, notably in respect of being free from interference by Cu.

Chapter 6 investigates the electroanalysis of As(III) on Au macroelectrodes and Au nanoparticle modified glassy carbon electrodes via underpotenital deposition with anodic stripping voltammetry. The deposition was optimized for the gold surfaces and visually clear detection limits were found to be 0.8 ppb and 0.4 ppb on the Au macroelectrode or Au nanoparticles, respectively. A particular merit is that detection on Au substrate can avoid the interference from both Cu(II) and Cl(-I) in contrast to what is seen for bulk deposition or on a Pt substrate.

Chapter 7 evolves further the work reported in **Chapter 6** which was exclusively focused on As(III). However, arsenate, As(V) is also common in groundwater with the contamination of arsenic. In this chapter, the total arsenic was measured without the need for an extra chemical reduction step of As(V) to As(III) as in previous work. The As(III)/As(V) speciation was found by tuning the deposition potential during the pre-concentration step. This method was used for total arsenic detection in water with a deposition potential at – 1.3 V, and As(III) can be selectively deposited at – 0.9 V, which means that the As(III)/As(V) speciation is possible. A visually clear signal of 0.8 ppb was obtained for the detection of arsenic with this method.

Overall the UPD-ASV approach using gold macroelectrodes is found to be suitable for the laboratory based analysis of As contaminated water samples, giving a LOD and visually clear signals at concentrations substantially below the WHO limit and free from interference either by chloride or copper ions.

Acknowledgements

There are countless people have given me invaluable support and help during my DPhil studies. First and foremost, I would like to express my deep gratitude to my supervisor, Professor Richard G. Compton, for accepting me in his group and providing extraordinary support and inspiration during my DPhil. Thank you for the constructive feedbacks you have given in electrochemistry, and your patience and positive spirit brought the light in my life during the difficult time amid Pandemic. Benefiting from your advice and support, I was able to start my life in electrochemistry and to be a proper scientist. The idea to become a 'frog' rather than a 'bird' always encourage me to move down to the right path of science.

Second, my sincere appreciation goes to Dr. Danlei (Daisy) Li for your generous help and support during my first two years of DPhil studies. Thank you for helping me out with running experiments and data analysis.

Third, I would like to thank all members of Compton Group members (2019 - 2022). To Archana, Haotian and Yuanyuan, it has been so lucky to study with you and to have you through my DPhil together. Many thanks to Dr. Minjun (Jake) Yang for the help on microscopic images. Thanks to Dr. Christopher Batchelor-McAuley Dr. Xin Chang and Dr. Bertold Rasche for your professional advice. Thanks to Dr. Ruiyang (Ryan) Miao, Dr. Yanjun (Grace) Guo, Dr. Yuanzhe Wang and Dr. Ruochen (Collin) Xie for your significant support and courage. Thanks to Yuqi (Rachel) and Joe for your support.

Finally, I deeply thank my family and my girlfriend, Jia Wei for their endless caring, love and support during these three years. Your support make me strong and brave. I also thank my friends in Oxford, China and Canada for bringing such fun and help to me. I am so lucky to have all of you!

Glossary

Roman Symbols

Symbol	Meaning	Unit
A	Electrode area	m^2
$A_{surface}$	Surface area of nanoparticles	m^2
$A_{geometric}$	Geometric area	m^2
a_j	Activity of species j	mol m^{-3}
c_j	Concentration of species j	mol m^{-3}
D	Diffusion coefficient	m^2 s^{-1}
E	Applied potential at the electrode	V
E^0	Standard electrode potential	V
E_f^0	Formal potential	V
F	Faraday Constant	C mol^{-1}
G	Gibbs energy	J mol^{-1}
$G_{\dagger}^0$	Standard Gibbs energy of activation	J mol^{-1}
$\Delta G_{red}^{\dagger}$	Gibbs energies of activation of reduction	J mol^{-1}
$\Delta G_{ox}^{\dagger}$	Gibbs energies of activation of oxidation	J mol^{-1}

I	Electrical current	A
I_p	Peak current	A
j	Flux of reactant	mol m^{-2} s^{-1}
j_{red}	Flux of reductive reactant	mol m^{-2} s^{-1}
j_{ox}	Flux of oxidative reactant	mol m^{-2} s^{-1}
k^0	Standard electrochemical rate constant	m s^{-1}
k_{red}	Rate constants for the reduction reaction	m s^{-1}
k_{ox}	Rate constants for the oxidation reaction	m s^{-1}
m_T	mass transport coefficient	m s^{-1}
n	Number of electrons transferred	Dimensionless
n’	number of electrons transferred before the rate determining step	Dimensionless
Q	Charge	C
R	Electrical resistance	Ω
R	Gas Constant	J mol^{-1} K^{-1}
T	Absolute temperature	K
t	Time	s
v	Potential scan rate	V s^{-1}

$x; y; z$	Cartesian coordinate	Dimensionless
z_j	Charge of species j	Dimensionless

Greek Symbols

Symbol	Meaning	Unit
α	Cathodic transfer coefficient	Dimensionless
Λ	Dimensionless reorganization energy	Dimensionless
β	Anodic transfer coefficient	Dimensionless
δ	Diffusion layer thickness	m
ϕ	Electrical potential	V
ϕ_s	Potential of solution phase	V
ϕ_m	Potential of metal phase	V
$\overline{\mu}_j$	Electrochemical potential of species j	J mol^{-1}
μ_j	Chemical potential of species j	J mol^{-1}
γ_j	Activity coefficient of species *j*	Dimensionless
χ_{DL}	Debye length	Å

ε_0	permittivity of free space	$C^2\ J^{-1}\ m^{-1}$
ε_r	dielectric constant	$C^2\ J^{-1}\ m^{-1}$
Γ	Surface coverage	mol cm^{-2}

Abbreviations

Abbreviation	Meaning
AA	Acrylic acid
AAS	Atomic absorption spectroscopy
AFS	Atomic fluorescence spectroscopy
AdsSV	Adsorptive stripping voltammetry
AMI	Amiloride
ASV	Anodic stripping voltammetry
BDDE	Boron doped diamond electrode
CE	Counter electrode
CNT	Carbon nanotube
CRE	Coffee ring effect
CV	Cyclic voltammetry
CSV	Cathodic stripping voltammetry

DMA	Dimethyl arsenate
DMG	Dimethylglyoxime
DPV	Differential pulse voltammetry
EDL	Electric double layer
EFSA	European Food Safety Authority
FIP	Fipronil
GCE	Glassy carbon electrode
GO	Graphene oxide
HER	Hydrogen evolution reaction
HG	Hydride generation
HMDE	Hanging mercury drop electrode
HOMO	Highest occupied molecular orbital
HOR	Hydrogen oxidation reaction
HPLC	High performance liquid chromatography
HR-CTEM	High resolution-conventional transmission electron microscopy
ICP-MS	Inductively coupled plasma mass spectroscopy
IHP	Inner Helmholtz Plane

ISV	Insertive stripping voltammetry
ITO	Indium tin oxide
LG	Liquid-gas
LOD	Limit of detection
LMO	Lithium manganese oxide
LUMO	Lowest unoccupied molecular orbital
LSV	Linear sweep voltammetry
MMA	Methyl arsenate
MSCV	Multiple scan cyclic voltammetry
MSE	Mercury/mercurous sulfate electrode
NP	Nanoparticles
OER	Oxygen evolution reaction
OHP	Outer Helmholtz Plane
OTS	Octadecyltrichlorosilane
PBS	Phosphate buffer saline
PCTFE	Polychlorotrifluoroethylene
PME	Particle modified electrode
PS	Polystyrene

PtNP	Platinum nanoparticle
RE	Reference electrode
SAW	Surface acoustic waves
SCE	Saturated calomel electrode
SEM	Scanning electron microscope
SHE	Standard hydrogen electrode
SPCE	Screen-printed carbon electrode
SV	Stripping voltammetry
SWV	Square wave voltammetry
TMA	Trimethyl arsenite
TMAO	Trimethylarsine oxide
USEPA	United States Environmental Protection Agency
UPD	Underpotential deposition
WE	Working electrode
WHO	World Health Organization

Table of Contents

Chapter 1.

Introduction to Electrochemistry

Electrochemical methods are widely used in fundamental studies and in applications including, as in this thesis, the detection of toxic species. This chapter introduces basic concepts and theories about electrochemistry, including electrochemical equilibrium, kinetics and mass transport. Then, the electrochemical methods specifically involved in this thesis are presented, notably cyclic voltammetry, anodic stripping voltammetry and underpotential deposition.

1.1. Electrochemical Equilibrium

Electrochemical reactions study the interactions between chemical changes and the transfer of electric charge between two conducting phases, usually an electrode and the electrolyte [1]. Consider a simple case with one-electron transfer, where an electrode is immersed into a solution containing redox species, A and B:

$$A_{aq} + e^-_{metal} \rightleftharpoons B_{aq} \tag{1.1}$$

The metal behaves as an electron donor and acceptor towards the redox couple. Then a charge separation may be established between the electrode and the solution at the equilibrium point, which can generate an electrode potential at the electrode/solution interface. This can be explained with reference to the energy levels of the redox species that participate in the potential determining equilibrium, as shown in Figure 1.1. The electrons in the metallic electrode form a conduction band, filling up continuous energy levels to the Fermi level, an energy maximum of the conduction band. In the electronic structure of an electrode, electrons are delocalized, which means they can move freely in the conduction bands. However, for

species A and B in solution phase, the electronic energy levels are discrete and an unoccupied molecular orbital of A is involved. As shown for 'before electron transfer' in Figure 1.1, the transfer of electrons is thermodynamically favourable from the Fermi level of electrode to the lowest unoccupied molecular orbital (LUMO) of A forming B, since the Fermi level of the electrode is higher than LUMO of A. After the electron transfer, the energy of Fermi level decreases (Figure 1.1) as a result of developing positive charge while on the other hand, the energy levels of the solution phase increases reflecting developing negative charge. At some points the energy levels equalise and close to this point electron transfers from the highest occupied molecular orbital (HOMO) of B to electrode (metallic phase) take place, and the reverse reaction happens. Once the reaction rates of forward and backward reactions are matched, the system reaches a dynamic equilibrium and no further net charge transfer is observed. This equilibrium situation corresponds to a charge separation between the solution phase and the metallic phase, and an electrode potential is generated on the metal [1, 2].

In the case of the electrochemical equilibrium such as Eqn. (1.1), the matching of the Gibb's energies of A and B involves both chemical energies and electrical energies during the electron transfer between the two phases (solution phase and electrode), which may have two different electrical potentials. To quantify this, the electrochemical potential, $\bar{\mu}_j$, of a species *j* is introduced:

$$\bar{\mu}_j = \mu_j + Z_j F\phi \tag{1.2}$$

where μ_j and Z_j are the chemical potential (J mol^{-1}) and the charge of species *j*, respectively, F is the Faraday Constant of 96485 C mol^{-1} and ϕ is the potential (V) of particular phase, solution phase (ϕ_s) or metal phase (ϕ_m) where species *j* is found. Note that the first term, μ_j, and the second term, $Z_j F\phi$, represent the chemical energy and the electrical energy of species

j, respectively. To analyse the electrochemical equilibrium of Eqn. (1.1), if the temperature and the pressure are constant, the electrochemical potentials can be expressed as:

$$\bar{\mu}_A + \bar{\mu}_{e^-} = \bar{\mu}_B \tag{1.3}$$

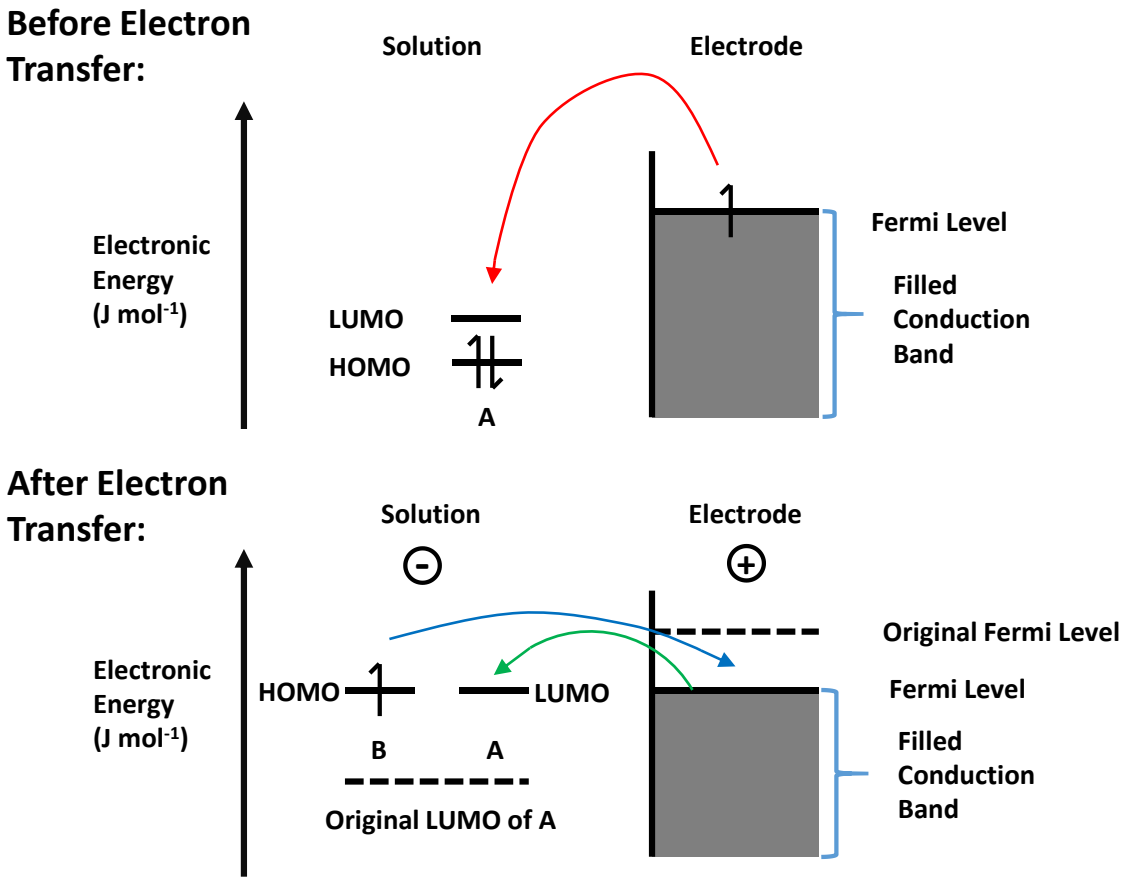

Figure 1.1 An illustration of the change of energy levels of ions in solution and metallic electrode during the chemical equilibrium between A and B.

Substituting Eqn. (1.2) to Eqn. (1.3):

$$(\mu_A + Z_A F\phi_S) + (\mu_{e^-} - F\phi_M) = (\mu_B + (Z_A - 1)F\phi_S) \tag{1.4}$$

Namely:

$$F(\phi_S - \phi_M) = \mu_B - \mu_A - \mu_{e^-} \tag{1.5}$$

Then the chemical potential (μ_j) can be further expressed using:

$$\mu_j = \mu_j^0 + RTln\frac{c_j}{c_0} \quad (1.6)$$

where μ_j^0 is the standard chemical potential, R is the universal gas constant (8.314 J K^{-1} mol^{-1}), T is the absolute temperature (K), c_j is the concentration of species j (mol m^{-3}) in solution and c_0 is the standard concentration of one molar (1 M), the latter assuming ideality.

Substituting Eqn. (1.6) into Eqn. (1.5) obtains:

$$\phi_M - \phi_S = \frac{\Delta\mu^0}{F} + \frac{RT}{F}\ln\left(\frac{c_A}{c_B}\right) \quad (1.7)$$

where:

$$\Delta\mu^0 = \mu_A^0 + \mu_{e^-} + \mu_B^0 \quad (1.8)$$

Eqn. (1.7) is the Nernst equation applied to the interface between a single electrode and solution [3-5]. It quantitatively describes the electrochemical equilibrium of A and B in Eqn. (1.1), and it depends on the concentrations of the species A and B in the equilibrium. Note that the chemical potentials above are associated with the species in solution. As for reaction involving gases, the gaseous pressure of j and the standard gaseous pressure replace c_j and c_0 in Eqn. (1.6) with p_j and p_0, respectively. As for solids, the chemical potentials are approximate to their standard chemical potentials, thus, the concentrations of solid species are not involved.

Eqn. (1.7) only applies to the ideal solutions. Thus, the activity of species j, a_j, is introduced to the non-ideal solution, in which ion-ion and ion-solvent interactions are considered:

$$a_j = \gamma_j c_j \quad (1.9)$$

where γ_j is the activity coefficient of species j. Then the Eqn. (1.7) can be modified as:

$$\phi_M - \phi_S = \frac{\Delta\mu^0}{F} + \frac{RT}{F}\ln\left(\frac{a_A}{a_B}\right) \tag{1.10}$$

It is impossible to measure the ($\phi_M - \phi_S$) value in experiments with a single electrode/solution interface since the potential difference measured by a voltmeter must, for measurement, be connected to a circuit which inevitably creates a second electrode/solution interface. Thus, a second electrode (also known as 'reference electrode') is introduced to the system [2]. Then the ($\phi_M - \phi_S$) measured between the two electrodes can be measured as:

$$E = (\phi_M - \phi_S)_{\,working} - (\phi_M - \phi_S)_{\,reference} \tag{1.11}$$

where E is the potential between the electrode of interest (a 'working electrode' in voltammetric studies) and the reference electrodes. The former is the interface of interest, such as the electrode probing the redox couple A/B in Eqn. (1.1). Hence the Nernst equation for the two-electrode system can be expressed as:

$$E = E^0 + \frac{RT}{F}\ln\left(\frac{a_A}{a_B}\right) \tag{1.12}$$

where E^0 is the standard electrode potential of the redox couple of A/B. The latter and E are, directly or indirectly, measured against standard hydrogen electrode (SHE).

Substituting Eqn. (1.12) with Eqn. (1.9) obtains:

$$E = E^0 + \frac{RT}{F}\ln\left(\frac{\gamma_A c_A}{\gamma_B c_B}\right) = E^0 + \frac{RT}{F}\ln\left(\frac{\gamma_A}{\gamma_B}\right) + \frac{RT}{F}\ln\left(\frac{c_A}{c_B}\right) \tag{1.13}$$

Then the concept of the formal potential is introduced:

$$E_f^0 = E^0 + \frac{RT}{F}\ln\left(\frac{\gamma_A}{\gamma_B}\right) \tag{1.14}$$

So that:

$$E = \mathrm{E}_f^0 + \frac{RT}{F}\ln\left(\frac{c_A}{c_B}\right) \tag{1.15}$$

The formal potentials can sometimes, but not always, be approximated by the corresponding standard electrode potentials. As for aqueous solutions, E^0 are measured under standard conditions, in which the pH is 0 and the temperature is 298 K [2, 6]. At the same temperature, if the pH value changes 1, the formal potential can change 0.059 V for a single electron transfer process [2]. The electrode potential described in Eqn. (1.15) is based on fast electron transfers. The kinetics of the electron transfer process will be elaborated in the next section.

1.2. Electrode Kinetics

In the previous section, the Nernst equation was introduced. It applies to the limit of fast electron transfer between A and B. To quantitatively describe the rate of the chemical reactions and the rate of electron transfers, the kinetics of electrode processes will be discussed in this section.

The single-electron redox reaction between A and B in Eqn. (1.1) can be described as follows:

$$A_{aq} + e^-_{metal} \underset{k_{ox}}{\overset{k_{red}}{\rightleftharpoons}} B_{aq} \tag{1.16}$$

where k_{red} and k_{ox} are the heterogeneous electron transfer rate constants for the reduction (forward) reaction and the oxidation (backward) reaction, respectively. The electrode transfer process between the species A or B and the electrode occurs via quantum mechanical tunnelling between two locations. Hence, the distance between A and the surface of electrode should be

within 10 – 20 Å if the electron transfer is to occur, since the rate of tunnelling drops very sharply with separation. Thus, for reduction, A must first diffuse from bulk solution to the surface of electrode within the critical distance for electron tunnelling before electron transfer takes place.

The electron transfer leads to a net electrical current, I (A), at the electrode. The current is given by the equation:

$$I = FAj \tag{1.17}$$

where A is the geometric area of the electrode (m^2) and j is the flux of reactant (mol m^{-2} s^{-1}) undergoing electrolysis. The flux represents a measure of the rate of the interfacial reaction. The net rate law then can be written as:

$$j = j_{red} - j_{ox} = k_{red}c_{A,0} - k_{ox}c_{B,0} \tag{1.18}$$

where j_{red} and j_{ox} represent the fluxes of the reductive and oxidative reactions, and $c_{A,0}$ and $c_{B,0}$ are the concentrations of the species A and B at the surface of electrode, respectively. Note that the surface concentrations usually differ from those in bulk solution due to the formation of diffusion layers [7].

In most cases, the rate constants k_{red} and k_{ox} are potential dependant [2]. This general expression follows the Arrhenius Equation, which relates the rate constants to the Gibbs energy of activation:

$$k_{red} = A_{red}\exp\left(\frac{-\Delta G_{red}^{\dagger}}{RT}\right) \tag{1.19}$$

$$k_{ox} = A_{ox}\exp\left(\frac{-\Delta G_{ox}^{\dagger}}{RT}\right) \tag{1.20}$$

where A_{red} and A_{ox} are the pre-exponential factors for reduction and oxidation, respectively, which depend on the frequency factor, viz the number of collisions per second of the electroactive species with the electrode surface. $\Delta G^{\dagger}_{red}$ and $\Delta G^{\dagger}_{ox}$ are the Gibbs energies of activation of reduction and oxidation (J mol^{-1}), respectively. R is the universal gas constant (8.314 J mol^{-1} K^{-1}) and T is the absolute temperature (K).

A schematic diagram of the energy profile of Eqn. (1.1) for the reaction process is shown in Figure 1.2. $G^0_{reactants}$, $G^0_{\dagger}$ and G^0_{products} are the standard molar Gibbs energy of reactants, transition states and products, respectively. The $\Delta G^{\dagger}_{red}$ and $\Delta G^{\dagger}_{ox}$ in Figure 1.2 can also be expressed as:

$$\Delta G^{\dagger}_{red} = G^0_{\dagger} - G^0_{reactants} \tag{1.21}$$

$$\Delta G^{\dagger}_{ox} = G^0_{\dagger} - G^0_{products} \tag{1.22}$$

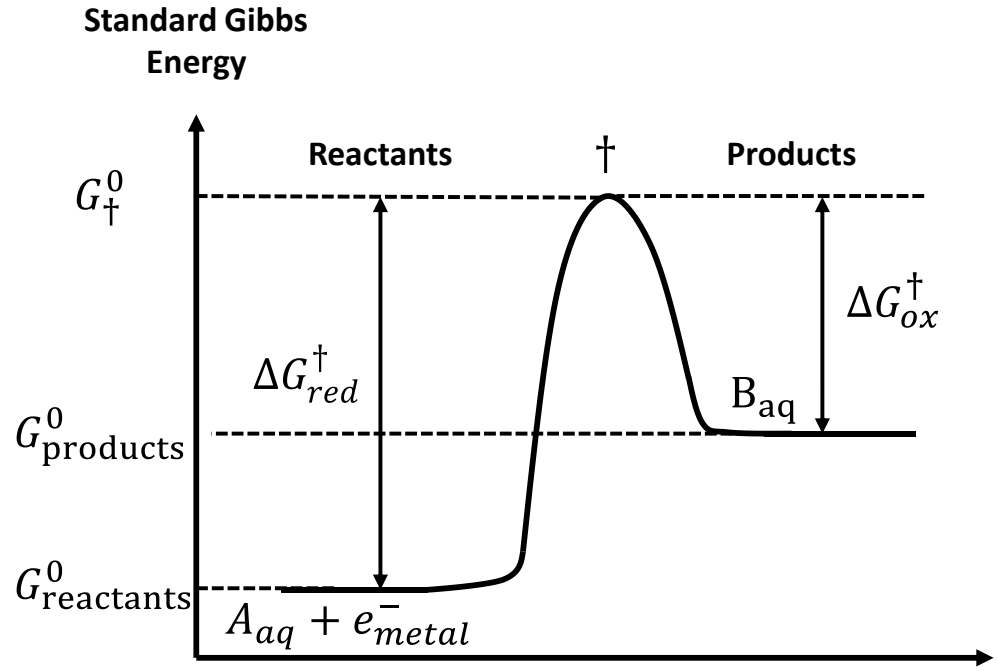

Figure 1.2 An electrochemical reaction profile of a single-electron transfer reaction

Considering the reaction of Eqn. (1.16) and Eqn. (1.2) in Section 1.1:

$$G^0_{reactants} = G^0_A + G^0_{e^-} = C_1 + (Z_A - 1)F\phi_s - F(\phi_M - \phi_S) \quad (1.23)$$

$$G^0_{products} = G^0_B = C_2 + (Z_A - 1)F\phi_s \quad (1.24)$$

where C_1 and C_2 are constants. Then assuming that the transition state is intermediate between the reactants and products in terms of its sensitivity to the electrode potentials, $G^0_\dagger$ then can be described based on Eqn. (1.23) and Eqn. (1.24) as:

$$G^0_\dagger = C_3 + (Z_A - 1)F\phi_s - \beta F(\phi_M - \phi_S) \quad (1.25)$$

where C_3 is a different constant. β is also known as transfer coefficient ($0 < \beta < 1$) [2]. If β is close to zero, the transition state will be product like while if β is close to unity, the transition state is reactant like [2, 8-10]. It is helpful to define a second transfer coefficient α as:

$$\alpha = 1 - \beta \quad (1.26)$$

In practice, the value of α or β is found to be 0.5 suggesting that the transition state locate at the midpoint between reactants and products, and the electrical behaviour is similar between reactants and products.

The Gibbs energy of activation can be expressed as [10]:

$$\Delta G^\dagger_{red} = G^0_\dagger + \alpha F(E - E^0_f) \quad (1.27)$$

$$\Delta G^\dagger_{ox} = G^0_\dagger - \beta F(E - E^0_f) \quad (1.28)$$

where α and β are the cathodic and anodic transfer coefficients, respectively. E is the applied potential and E^0_f is the formal potential as mentioned in Eqn. (1.14).

From Eqns. (1.21) ~ (1.28) as well as Eqn. (1.19) and Eqn. (1.20) gives:

$$k_{red} = k_{red}^0 \exp\left[\frac{-\alpha F\left(E - E_f^0\right)}{RT}\right] \quad (1.29)$$

$$k_{ox} = k_{ox}^0 \exp\left[\frac{\beta F\left(E - E_f^0\right)}{RT}\right] \quad (1.30)$$

where k_{red}^0 and k_{ox}^0 are the standard reduction and oxidation electrochemical rate constants (m s^{-1}), respectively. $(E - E_f^0)$ represents the potential applied to the working electrode relative to the formal potential of A/B redox couple with both potentials measured relative to the same reference electrode, SHE. It is clear from the discussion in the last section and Eqn. (1.11) that

$$E - E_f^0 = (\phi_M - \phi_S)_{working} + C_4 \quad (1.31)$$

where C_4 is a constant. Then substituting Eqn. (1.18) with Eqn. (1.29) and (1.30) for the description of flux at the electrode/solution interface:

$$j = k_{red}^0 \exp\left[\frac{-\alpha F\left(E - E_f^0\right)}{RT}\right] c_{A,0} - k_{ox}^0 \exp\left[\frac{\beta F\left(E - E_f^0\right)}{RT}\right] c_{B,0} \quad (1.32)$$

which is recognized as the Butler-Volmer equation [9, 11, 12]. If the dynamic equilibrium reached at the surface of the working electrode, there is no net current flow,

$$j = 0 \quad (1.33)$$

From Eqn. (1.26), Eqn. (1.31) and Eqn. (1.32), the Butler-Volmer equation becomes:

$$E = E_f^0 + \frac{RT}{F} \ln\left(\frac{c_A}{c_B}\right) + \frac{RT}{F} \ln\left(\frac{k_{red}^0}{k_{ox}^0}\right) \quad (1.34)$$

From the discussion in last section, if there is no net current, the Nernst equation can be written as Eqn. (1.15), so that it follows that:

$$k_{red}^0 = k_{ox}^0 = k^0 \quad (1.35)$$

where k^0 is defined as the standard electrochemical rate constant. The electrochemical rate constant, Eqn. (1.29) and (1.30), can be written as:

$$k_{red} = k^0 \exp\left[\frac{-\alpha F\left(E-E_f^0\right)}{RT}\right] \tag{1.36}$$

$$k_{ox} = k^0 \exp\left[\frac{\beta F\left(E-E_f^0\right)}{RT}\right] \tag{1.37}$$

Considering the reaction shown in Eqn. (1.16), Eqn. (1.32) indicates that the net rate flux of the reaction is balanced by the reduction and oxidation processes of A/B redox reaction. Under extreme potentials, where E_f^0 is substantially more positive than E, the reduction term is predominant, and with the substitution from Eqn. (1.35), Eqn. (1.32) becomes:

$$j = k^0 \exp\left[\frac{-\alpha F\left(E-E_f^0\right)}{RT}\right] c_{A,0} \tag{1.38}$$

On the other hand, if E is substantially more positive than E_f^0, the oxidation term is predominant, and Eqn. (1.32) can be rearranged with Eqn. (1.35):

$$j = k^0 \exp\left[\frac{\beta F\left(E-E_f^0\right)}{RT}\right] c_{B,0} \tag{1.39}$$

If $c_{A,0}$ and $c_{B,0}$ are not substantially changed from their bulk concentrations, then it can be derived that:

$$ln|I_{red}| = -\frac{\alpha FE}{RT} + C_5 \tag{1.40}$$

$$ln|I_{ox}| = \frac{\beta FE}{RT} + C_6 \tag{1.41}$$

where I_{red} and I_{ox} are the reduction and oxidation currents respectively. C_5 and C_6 are constants. Eqn. (1.40) and (1.41) are also known as the Tafel Law [13-16]. The well-known Tafel plots

are shown schematically in Figure 1.3. The plot of $ln|I_{red}|$ vs. E (Figure 1.3a) is for reduction and $ln|I_{ox}|$ vs. E (Figure 1.3b) is for oxidation. The slope of the Tafel plots reveals the transfer coefficients α and β.

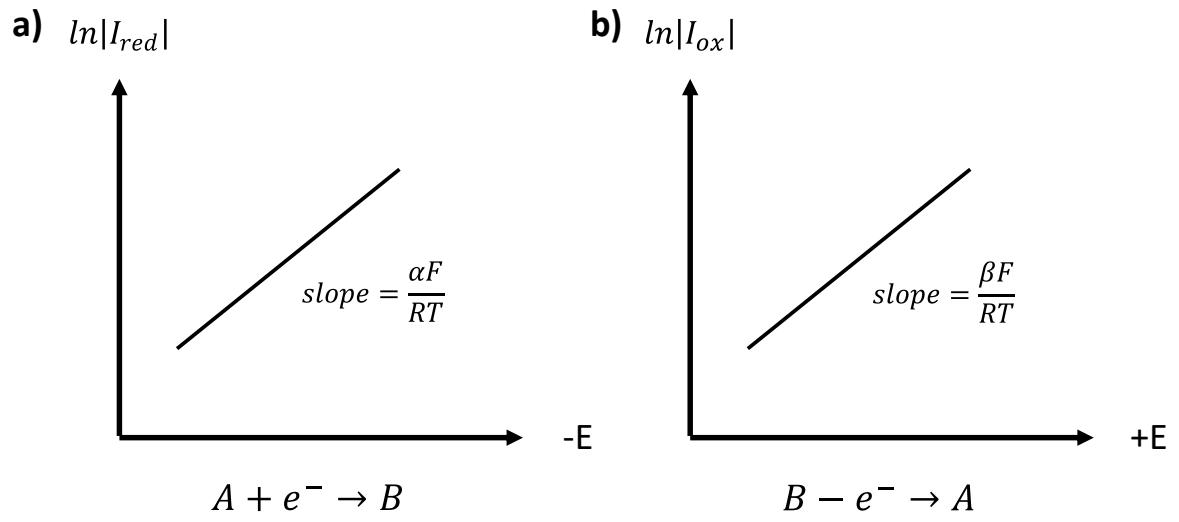

Figure 1.3 Tafel plots of a single-electron transfer process a) the reduction process and b) the oxidation process

Note that this procedure requires the constancy of the concentration terms $c_{A,0}$ and $c_{B,0}$ in Eqn. (1.38) and (1.39). In reality, however, the Tafel plot may suffer from the reactant depletion effects. Thus, it is important to discuss mass transport as is undertaken in the next section.

1.3. Mass Transport

The previous section discussed electron transfer at the electrode/solution interface, under the assumption of constant concentrations of reactants at the surface of the electrode. However, the reactions at the surface electrode/solution interface necessarily consume the reactants, so requiring consideration of the transport of the reactants from bulk solution to the surface of electrode. Mass transport can occur via any or all of diffusion, convection and migration. In this section, these three processes will be introduced and studied.

1.3.1. Diffusion

Diffusion describes the net movement of species from high concentrations to low concentrations. For an electrode/solution interface, if a potential is applied to the electrode, the reactants near to the surface of electrode may be consumed creating a concentration gradient of reactants between the interfaces to the bulk solution. At any point of this concentration gradient, a diffusive flux can be quantified by Fick's 1st law [2, 17]:

$$j = -D\frac{\partial c}{\partial x} \tag{1.42}$$

where j is the flux (mol cm^{-2} s^{-1}) that describes the number of moles of species passing through the unit area in unit time. $\frac{\partial c}{\partial x}$ is the local concentration gradient at point x and D is the diffusion coefficient (cm^2 s^{-1}). Note that the negative sign in Eqn. (1.42) shows the species move down the concentration gradient. A schematic plot of concentration of reactant against the distance from the surface of electrode during electrochemical reaction is shown in Figure 1.4, where the so-called Nernst diffusion layer is indicated. The diffusion layer embraces the zone of the depletion of reactants around the surface of electrode.

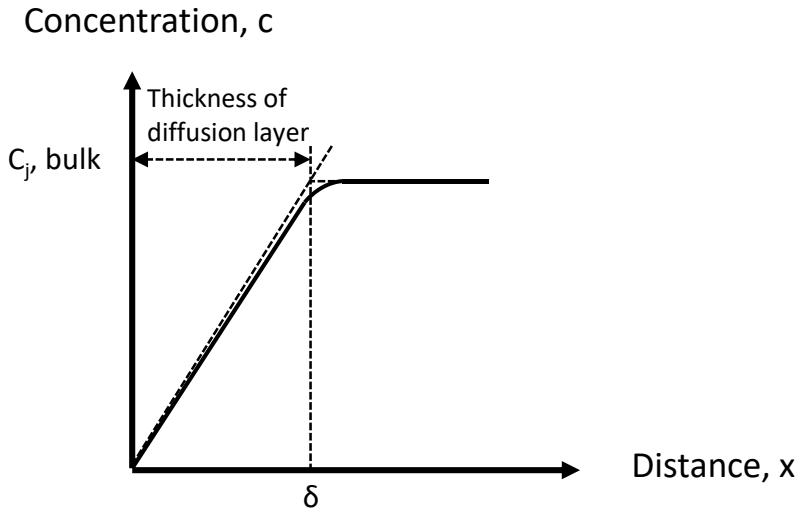

Figure 1.4 A schematic plot of the Nernst diffusion layer.

To further develop Fick's first law, consider the scheme in Figure 1.5. A box with a width of 2δx is divided at point x and each side has a width of δx. The cross-sectional area, A_{cs} is shown in Figure 1.5 at point x and particles with concentrations of c_1 and c_2 occupy the left and right portions of the box. The particles move in the solution randomly in both directions along the x direction and some pass through the cross-sectional area shown. The number of particles moving from left to right and right to left in a given time interval of δt can be written as $\frac{1}{2}c_1A_{cs}\delta_x$ and $\frac{1}{2}c_2A_{cs}\delta_x$, respectively where the factor of ½ arises since only half of the particles travel in the appropriate direction to pass through the interface. Thus, the net rate of particles transported through A_{cs} can be written as:

$$Rate_{net} = \frac{(c_1-c_2)A_{cs}\delta_x}{2\delta t} \tag{1.43}$$

The local gradient $\frac{\partial c}{\partial x}$ can be estimated as $-\frac{(c_1-c_2)}{\delta x}$, then Eqn. (1.43) can be rearranged as:

$$Rate_{net} \sim -\frac{A_{cs}(\delta_x)^2}{2\delta t}\left(\frac{\partial c}{\partial x}\right) \tag{1.44}$$

Thus, the diffusion flux j from Eqn. (1.42) can be rearranged as:

$$j = -\frac{(\delta_x)^2}{2\delta t}\frac{\partial c}{\partial x} \tag{1.45}$$

The diffusion coefficient D ($cm^2\ s^{-1}$) then can be expressed as:

$$D = \frac{(\delta_x)^2}{2\delta t} \tag{1.46}$$

It can be seen from Eqn. (1.46) that the diffusion coefficient shows the mean square distance of a particle traveled in the solution in a certain time. This is the famous Einstein-Smoluchowski equation [18-20]:

$$\sqrt{< x >^2} = \sqrt{2Dt} \tag{1.47}$$

where $\sqrt{< x >^2}$ is the root mean square displacement (m) in time, t. Furthermore, the Eqn. (1.42) can be expanded in three dimensions as:

$$\frac{\partial c}{\partial t} = D(\frac{\partial^2 c}{\partial x^2} + \frac{\partial^2 c}{\partial y} + \frac{\partial^2 c}{\partial z^2}) \tag{1.48}$$

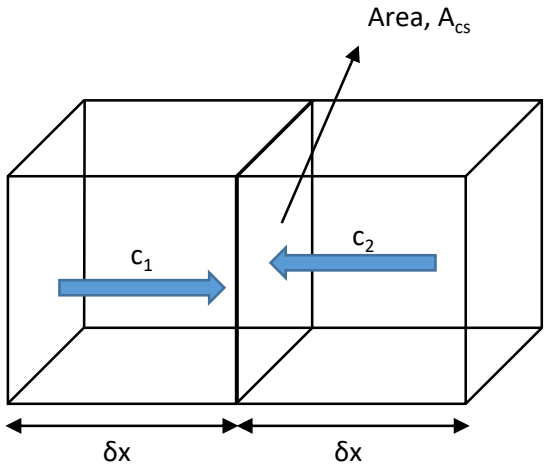

Figure 1.5 A schematic figures used to derive the Einstein-Smoluchowski equation (see text).

Thus, the root mean square displacement becomes:

$$\sqrt{< x >^2 + < y >^2 + < z >^2} = \sqrt{6Dt} \tag{1.49}$$

Next we derive Fick's Second Law of diffusion which describes the change of concentration with respect to time. Consider fluxes of materials entering and leaving a solution slab with a thickness of δx and the area of A_{cs} (Figure 1.6). The difference of the number of particles entering and leaving the slab within a time period of δt is:

$$\delta n = (j(x) - j(x + \delta x))A_{cs}\delta t \tag{1.50}$$

which can be rearranged as:

$$(c(t + \delta t) - c(t))A_{cs}\delta x = (j(x) - j(x + \delta x))A_{cs}\delta t \tag{1.51}$$

$$\frac{\partial c}{\partial t} = -\frac{\partial j}{\partial x} \tag{1.52}$$

Substituting Fick's First Law (Eqn. (1.42)) into Eqn. (1.53) obtains Fick's Second Law:

$$\frac{\partial c}{\partial t} = D\frac{\partial^2 c}{\partial x^2} \tag{1.53}$$

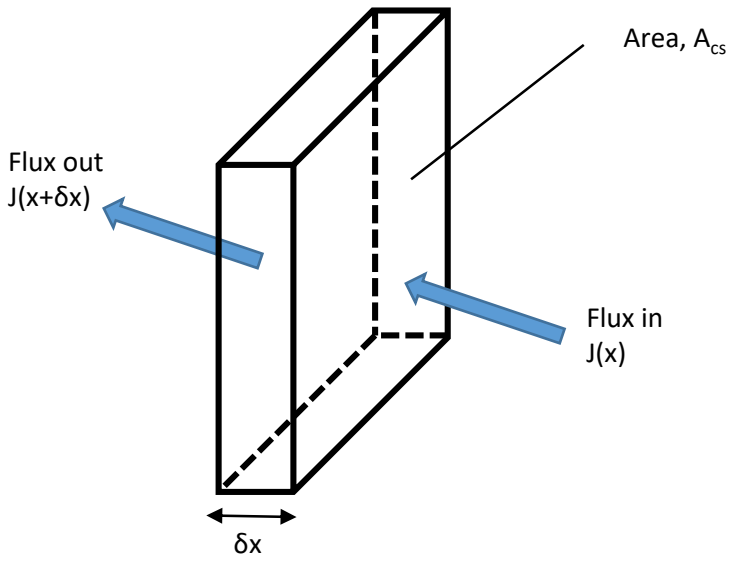

Figure 1.6 A schematic representation of flux in and out of a 'slab'.

1.3.2. Convection

Convection is a form of mass transport, which embraces two types, natural convection and forced convection [21, 22]. Natural convection refers to the movement of species from regions with high densities to those with low densities. It may sometimes occur at the surface of the working electrode due to the consumption of reactants and the formation of products. In addition, thermal variations may contribute to the density gradient at the surface of the electrode, such as arising from the heat produced from the chemical reactions which may cause the difference of the local density from that of the bulk solution, although this is usually negligible but natural convection is encouraged by experiments of longer duration [21]. Thus, a shorter electrochemical experimental time is preferred so that the influence from natural convection can be neglected. The other form of convection is forced convection, where

mechanical forces such as stirring, pumping or electrode rotation are deliberately introduced to promote mass transport [23]. It is a controlled movement and it is usually introduced to dominate the mass transport, which can alter the rate of mass transport to realise, for example, enhanced quantitative analysis [2, 23, 24].

1.3.3. Migration

The third form of mass transport is migration, which refers to the movement of charged species in a solution due to an electric field. In electrochemical experiments the latter is generated from the potential drop at the electrode/solution interface [1, 2]. The migratory flux of a species j, $J_{m,j}$, at point x can be expressed as:

$$J_{m,j}(x) = -\frac{z_j F}{RT} D_j c_j \frac{\partial \Phi(x)}{\partial x} \tag{1.54}$$

where z_j is the charge of species j, D_j is the diffusion coefficient of j, c_j is the concentration and $\frac{\partial \Phi(x)}{\partial x}$ represents potential gradient or electric field (V m^{-1}).

For charged species, both diffusion and migration occur near the surface of electrode. The total flux $J_j(x)$ (mol m^{-2} s^{-1}) of species j can be expressed as:

$$J_j(x) = J_{d,j}(x) + J_{m,j}(x) \tag{1.55}$$

where $J_{d,j}(x)$ is the diffusional flux and $J_{m,j}(x)$ is the migratory flux. Note that the direction of migratory flux depends on the charge of the species and the electric field, which means the direction of migratory flux and diffusive flux can be the same or in opposition. Figure 1.7 illustrates three cases of species j where the particle with positive (Figure 1.7a), negative (Figure 1.7b) and neutral (Figure 1.7c) charge. It is clear that the migratory flux is in the same direction with diffusive flux when the cations are reduced at cathodes or anions are oxidized at

anodes, while in the opposite directions when cations are oxidized at cathodes or anions are reduced at anodes. Thus, the presence of migration may significantly affect the current and hence the experimental results.

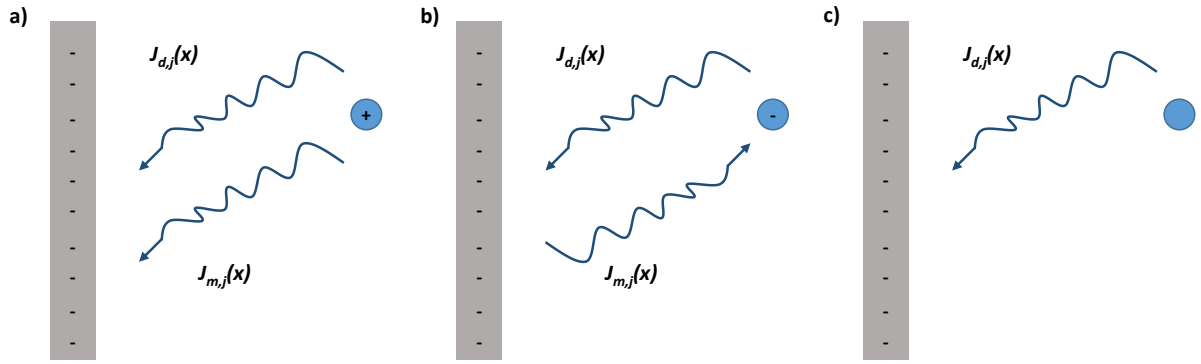

Figure 1.7 Reduction process of different migratory flux of a) positively charged species, b) negatively charged species, and c) uncharged species.

Migration can be minimized in experiments by adding supporting electrolyte consisting of non-electroactive ions with a high concentration usually of 10^{-1} M or above, leading to what is known as 'fully supported' conditions [25]. These inert ions carry the majority of the charge flowing in solution so that the effect from migration on the analyte of interest is suppressed or reduced to a negligible level. There are also several advantages of using high concentrations of supporting electrolyte. First, the addition of supporting electrolyte can enhance the conductivity of solution and reduce the resistance between working electrode and reference electrode, which allows a more precise potential to be applied between the two electrodes. Second, the high concentrations of supporting electrolyte provides a constant ionic composition and a uniform ionic strength, which fixes the activity coefficients of all species along with the formal potential of redox couple in system under study. Third, and very importantly, supporting electrolyte compresses the potential drop at the electrode-solution interfaces so that migration is negligible and analytes are transported by diffusion to the electrochemical interface. In particular conditions of full support compress the electric double layer (EDL) to within 10 to 20 Å, which is within the distance of quantum tunnelling for electron transfer between electrode and

solution so that the full 'driving force' for the electrode reaction is available at locations compatible with electron transfer between the two phases.

Figure 1.8 illustrates the electrical double layer with anions adsorbed at a positively charged surface in solution. When the electrode surface is positively charged, the anions and solvent molecules in solution move towards the surface of electrode and be specifically adsorbed onto the electrode driven by electrostatic forces. It forms a compact layer at the surface of electrode, which is also known as Inner Helmholtz Plane (IHP) in which the adsorbed anions are inferred to be dehydrated. The plane next to the IHP is the Outer Helmholtz Plane (OHP), where the nearest solvated anions locate via long-range electrostatic force, which are also considered as non-specifically adsorption to the electrode. The region next to the OHP is the diffuse layer, in which solvated ions are loosely attracted to the electrode. These layers form the electric double layer at the surface of electrode which create an overall electrically neutral zone at the electrode/solution interface.

The potential profile at the bottom of Figure 1.8 also shows that the most potential drop occurs within the compact layer and with a lesser more gradual drop between the diffuse layer and the bulk solution. The thickness of the diffuse layer is related to the Debye length (Å) [26], defined as:

$$\chi_{DL} = \frac{1}{zF}\sqrt{\frac{\varepsilon_0 \varepsilon_r RT}{2c}} \tag{1.56}$$

where χ_{DL} is the Debye length (Å), z is the charge of the species, F is the Faraday Constant (96485 C mol^{-1}), ε_0 is the permittivity of free space, ε_r is the dielectric constant, R is the gas constant (8.314 J mol^{-1} K^{-1}) and T is the absolute temperature (K). From Eqn. (1.56), it can be seen that the increase of concentrations of supporting electrolyte can decrease the Debye length. Thus, high concentrations of supporting electrolyte reduce the thickness of EDL, and the

distance between electrode and bulk solution can be shorter than the value of 20 Å, which is required for quantum mechanical tunnelling.

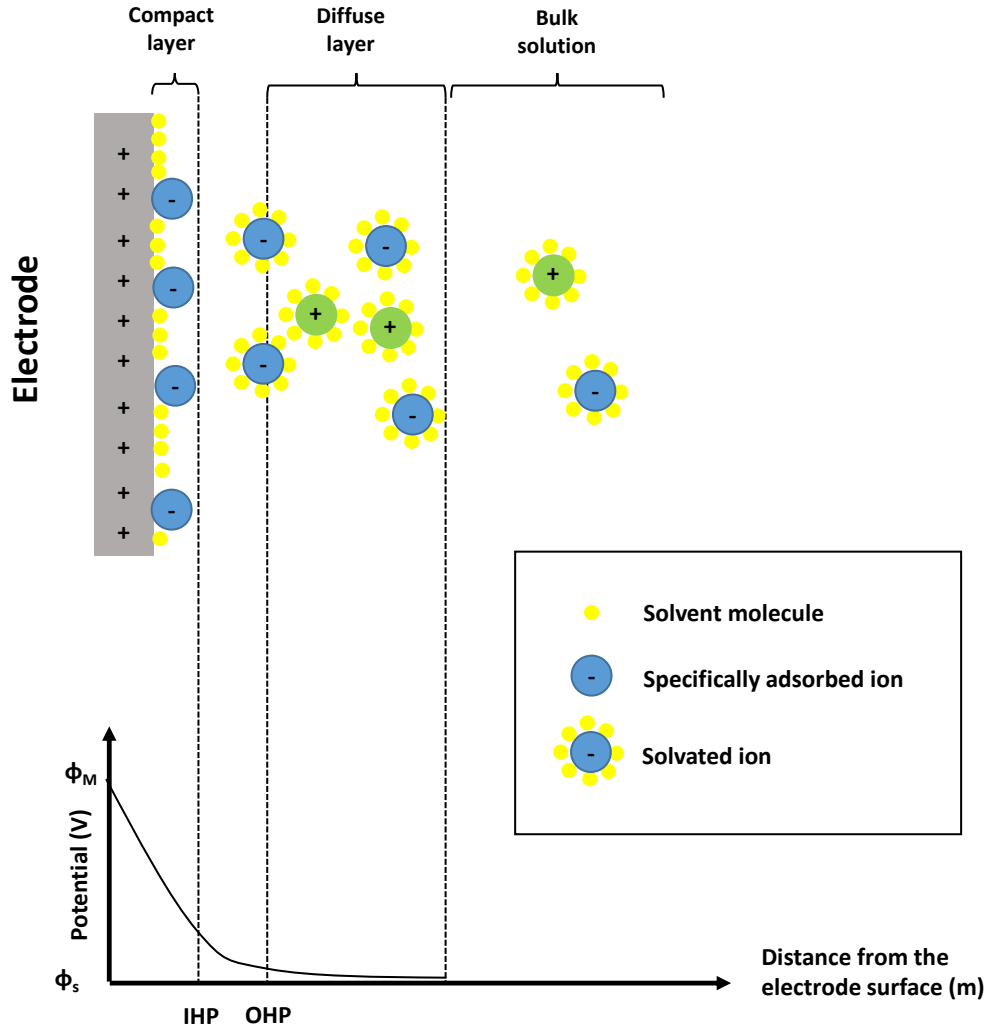

Figure 1.8 A model of electric double layer (top) and a schematic diagram of potential drop across the double layer (bottom). The anions are specifically adsorbed onto the positive surface of electrode. The yellow, blue and green spheres represent solvent molecules, anions and cations, respectively.

1.4. Electrochemical Cells

To perform electrochemical measurements, a three-electrode system is commonly used. This comprises a working electrode (WE), a reference electrode (RE) and a counter electrode (CE). Figure 1.9a shows the scheme of three-electrode system in solution and Figure 1.9b

shows the electrical circuit of the system controlled by a potentiostat. The WE provides an interface for electrochemical reactions to take place and the RE is required for the application of a controlled potential difference at the WE (discussed in Section 1.1). However, if current were to pass through the RE, the chemicals inside will react and change, so altering the reference electrode potential. To avoid this, a counter electrode is introduced to the system and current is made to pass through the CE rather than through the reference electrode by the potentiostat. The CEs are usually made from materials with excellent electrical conductivity and are chemically inert [2, 27]. When the reaction takes place at a WE, the potentiostat will control the CE (by altering the CE voltage) to pass the same amount of current that passes through the working electrode and the current is measured as a function of the potential applied to the WE.

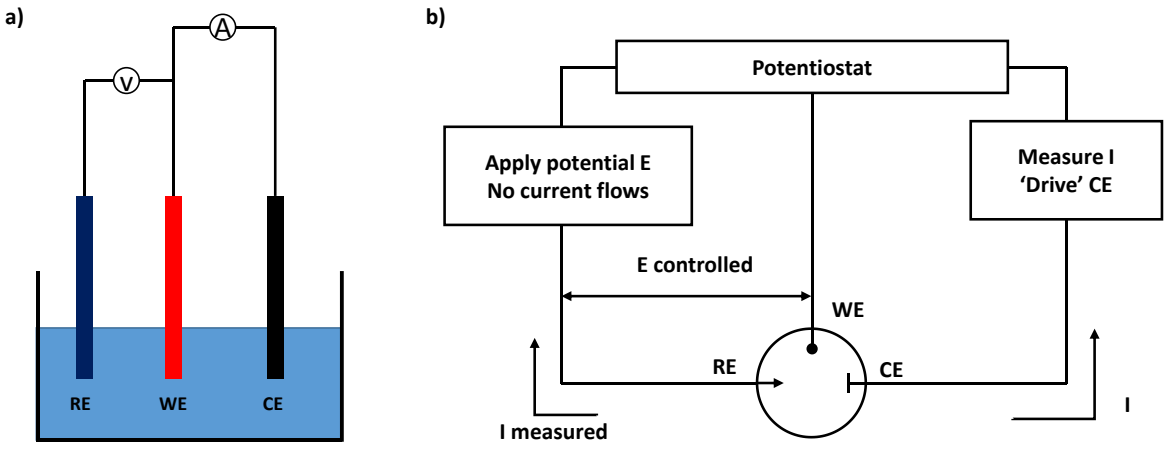

Figure 1.9 a) A schematic diagram of a three-electrode cell during electrochemical measurements in solution and b) the circuit of three-electrode system with a potentiostat. WE: working electrode, RE: reference electrode, CE: counter electrode.

As Figure 1.9b illustrated, the potentiostat can provide a constant potential, E, between the RE and the WE, viz:

$$E = (\phi_M - \phi_s)_{WE} + IR - (\phi_M - \phi_S)_{RE} \quad (1.57)$$

where IR reflects the electrical resistance, R, of bulk solution between the RE and the WE and I is the current flowing. As $(\phi_M - \phi_S)_{RE}$ is constant (discussed in Section 1.1) and the IR term can be neglected if no current passes through the RE [2], defined changes of potential between the RE and WE can be achieved in $(\phi_M - \phi_s)_{WE}$ of the WE.

1.5. Electrochemical Methods

This section introduces some electrochemical techniques used to study the mechanisms of electrochemical reactions and some of the methods used to enhance signals for quantitative analysis. These include cyclic voltammetry (CV), linear sweep voltammetry (LSV), and stripping voltammetry (SV).

1.5.1. Cyclic Voltammetry

Cyclic voltammetry (CV) is the most important and widely employed method for the study of electrode kinetics, mechanism and diffusion [2, 28]. It measures the current response of electrochemical reaction in solution, when subjected to a linear potential sweep at the working electrode with a constant scan rate, ν (V s^{-1}). Figure 1.10 illustrates the plot of potential vs time, where the potential on the working electrode is changing linearly from E_1 to E_2 with the scan rate of ν then sweep back to E_1 with the same scan rate [29]. The scan rate of CV can be determined with equation:

$$\nu = \frac{\partial E(t)}{\partial t} \tag{1.58}$$

and is given by the slope of the potential versus time plot. Experimentally the linear ramp is controlled digitally and comprises many small potential steps each representing a potential

change (Figure 1.10). The results of each measurement are presented as a cyclic voltammogram where the current is plotted against potential.

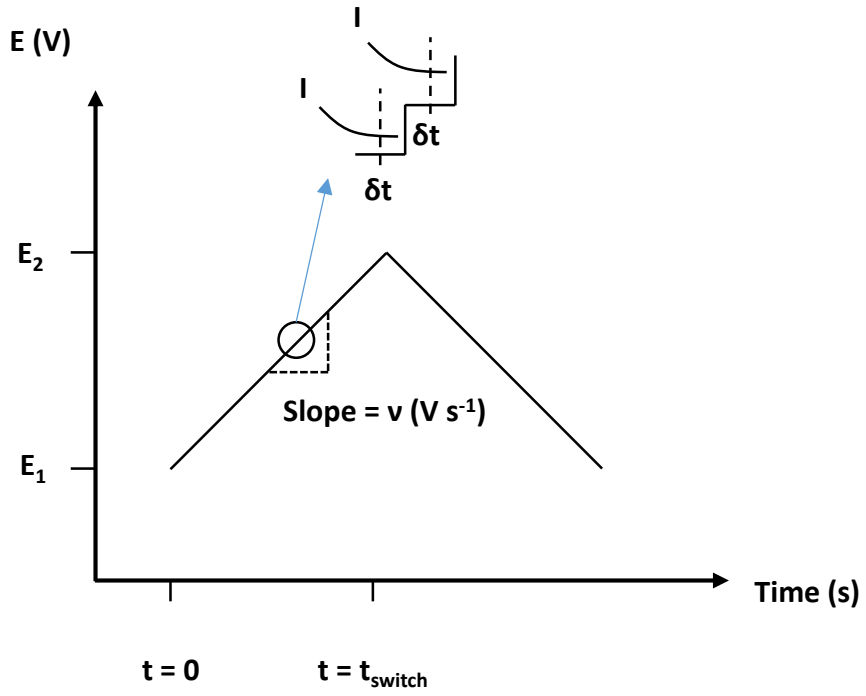

Figure 1.10 Potential sweep of staircase cyclic voltammetry

At a macrodisc electrode, peaks can be observed from the voltammograms due to the effects from electrode kinetics and linear diffusion. The voltammogram is usually started at a potential with zero Faradaic current and electrochemical reaction begins when the potential sweeping to the formal potential as the reaction rate increases with the potential leading to an increase in current. Meanwhile, the depletion of reactants becomes greater resulting in an increase of the current only until almost all of the reactants at the surface of electrode have been consumed where the current reaches the maximum (peak current). At this point, the electron transfer rate is balanced with the rate of diffusion of the reactants to the electrode. When sweeping to higher potentials, the diffusion of reactants is not be able to replenish sufficient reactants at the surface of electrode so that the current starts to drop with the continued increase in potential. As a result, a peak can be observed at the forward scan of the voltammogram and the product accumulates near to the electrode. Likewise, a peak can be

observed at the reverse scan corresponding to the reverse of the electrochemical reaction on the forward scan.

Three generic types of voltammetric profiles with different electrode kinetics can be observed at macroelectrodes, namely reversible, quasi-reversible and irreversible electrode processes. The extent of reversibility illustrates the rate of electrochemical reaction relative to the rate of mass transport. The rate of mass transport is measured with the mass transport coefficient m_T (m s^{-1}) [2], defined as:

$$m_T = \frac{D}{\delta} \tag{1.59}$$

where D is the diffusion coefficient (m^2 s^{-1}) and δ is the diffusion layer thickness (m). The sweep time t (s) for conducting a voltammetric experiment can be roughly expressed as:

$$t \propto \frac{RT}{Fv} \tag{1.60}$$

where R is Universal Gas Constant (8.314 J K^{-1} mol^{-1}), T is the absolute temperature (K), F is the Faraday Constant (96485 C mol^{-1}), and v is the voltage scan rate (V s^{-1}). Thus m_T is dependent on these terms:

$$m_T \propto \sqrt{\frac{FDv}{RT}} \tag{1.61}$$

If the rate constant $k^0 >> m_T$, the reaction is reversible, corresponding to the fast electrode kinetics; if $k^0 << m_T$, the process is irreversible, corresponding to the slow electrode kinetics. The transition between the reversible and irreversible can be followed by means of the parameter, Λ, first introduced by Matsuda and Ayabe [30]:

$$\Lambda = \frac{k^0}{\sqrt{\frac{FDv}{RT}}} \tag{1.62}$$

It suggests three ranges for the classifications of reversible, quasi-reversible and irreversible processes at macroelectrodes:

$$\text{Reversible: } \Lambda \geq 15, k^0 \geq 0.3\sqrt{v}\ cm\ s^{-1} \tag{1.63}$$

$$\text{Quasi-reversible: } 15 > \Lambda > 10^{-3}, 0.3\sqrt{v} > k^0 > 2 \times 10^{-5}\sqrt{v}\ cm\ s^{-1} \tag{1.64}$$

$$\text{Irreversible: } \Lambda < 10^{-3}, k^0 \leq 2 \times 10^{-5}\sqrt{v}\ cm\ s^{-1} \tag{1.65}$$

where the temperature is 298 K and the transfer coefficient α is assumed to be 0.5.

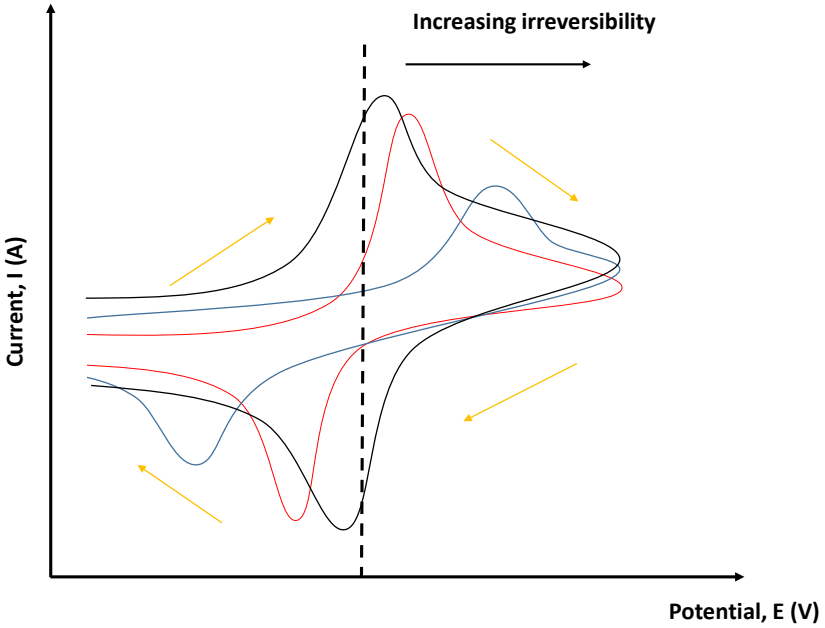

Figure 1.11 Cyclic voltammograms for a one-electron transfer process at a macrodisc electrode corresponding to a reversible (black), quasi-reversible (red) and irreversible system (blue). Orange arrows show the scan direction.

Peak currents and peak potentials recorded as a function of scan rate are important voltammetric features for inferring electrode reaction kinetics. Figure 1.11 shows the cyclic voltammograms for a one-electron transfer process of a reversible, quasi-reversible and irreversible system. The differences of peak-to-peak separation (ΔE_{pp}, defined as the difference between anodic and cathodic peak potentials [2]) can be observed clearly. For a reversible

system, the relationship between the concentration of reactants at the surface of electrode and peak potential can be described by Nernst Equation (Eqn. (1.15)), thus the ΔE_{pp} has been calculated to be ca 57 mV at 298 K for the one-electron transfer redox system (black line in Figure 1.11). The peak to peak separation is independent of the voltage scan rate. On the other hand, for irreversible system, slow electrode kinetics result in larger ΔE_{pp} and higher overpotentials are required for the reactions (blue line in Figure 1.11). The peak to peak separation increases with scan rate. The case of quasi-reversibility shows intermediate behaviour (red line in Figure 1.11).

The peak current I_p of a one electron process at a macroelectrode can be described via the Randles-Ševčik equations at 298 K [2, 31, 32]:

$$Reversible: I_p = 0.446FA[A]\sqrt{\frac{FDv}{RT}} \quad (1.66)$$

$$Irreversible: I_p = 0.496\sqrt{\alpha}FA[A]\sqrt{\frac{FDv}{RT}} \quad (1.67)$$

where F is the Faraday Constant (96485 C mol^{-1}), A is the surface area of electrode (m^2), [A] is the concentration of reactant A (mol m^{-3}), D is the diffusion coefficient (cm^2 s^{-1}), and α is the transfer coefficient. For multi-electron transfer process, the Randles-Ševčik equations can be written as [2, 31, 32]:

$$Reversible: I_p = 0.446nFA[A]\sqrt{\frac{nFDv}{RT}} \quad (1.68)$$

$$Irreversible: I_p = 0.496\sqrt{n' + \alpha_{n'+1}}nFA[A]\sqrt{\frac{FDv}{RT}} \quad (1.69)$$

where n is the number of electrons transferred, n' is the total number of electrons transferred before the rate determining step, and $\alpha_{n'+1}$ is the transfer coefficient of the rate determining step.

Linear sweep voltammetry (LSV) is analogous to CV except only a forward potential sweep is applied. Note that for both CV and LSV, the voltage scan rate is constant, given by Eqn. (1.58).

1.5.2. Stripping Voltammetry

Stripping voltammetry is a widely employed electrochemical method in electroanalytical chemistry for quantitatively measurements of target ions and molecules in solution which takes place via the pre-concentration of analytes onto the surface of electrode [33-38]. The general idea of stripping voltammetry was first suggested by Zbinden in 1931 [39]. It has since been used to detect diverse analytes in water, blood, food and even in gasoline [36-38].

Figure 1.12 illustrates the schematic diagram of stripping voltammetry. Unlike CV or LSV in which the sensitivity is limited by the rate of diffusion to the electrode, stripping voltammetry is usually significantly enhanced via a 'pre-concentration step' which allows the accumulation of analytes at the surface of the electrode. This is followed by a 'stripping step' which generates the current used for the analytical measurement. Stripping voltammetry usually offers a lower limit of detection (LOD) and a higher sensitivity than CV or LSV.

There are three main versions of this method, anodic, cathodic and adsorptive stripping voltammetry, which differ in the nature and anodic or cathodic character of the pre-concentration and stripping steps. For anodic stripping voltammetry (ASV) and cathodic

stripping voltammetry (CSV), the pre-concentrations step involves Faradaic reactions. However, for adsorptive stripping voltammetry (AdsSV), the analytes are accumulated at the surface of electrode via adsorption rather than electrolytic deposition during the pre-concentration step. Illustrative reactions during the different pre-concentration steps are shown below [2]:

$$ASV: M^{n+}(aq) + ne^- \rightarrow M(electrode) \quad (1.70)$$

$$CSV: 2M^{n+} + mH_2O \rightarrow M_2O_m(electrode) + 2mH^+ + 2(m-n)e^- \quad (1.71)$$

$$AdsSV: A(aq) \rightarrow A(ads) \quad (1.72)$$

For inducing the 'stripping' process, a potential sweep that oxidizes or reduces the accumulated material is applied to the working electrode and a voltammogram with a peak corresponding to the analyte can be obtained. According to Faraday's law, integrating the peak area reveals the stripping charge Q (C) passed during the stripping time t_0. The stripping charge corresponds to the amount of analyte accumulated onto the surface of electrode. The surface coverage Γ (mol cm^{-2}) is defined to quantify the amount of analyte that was accumulated [1, 2]:

$$\Gamma = \frac{Q}{nFA} = \frac{\int_0^{t_0} Idt}{nFA} \quad (1.73)$$

where n is the number of electrons transferred in the stripping step and A is the area of the electrode surface. For practical analytical applications, the charge of the stripping peak is usually measured through evaluation of area of the stripping peak and a calibration curve usually generated using analyte of known concentration showing the charge of the stripping peak against the concentration of the analytes. This often generates a linear relationship the slope of which defines the sensitivity. Then a sample solution of unknown concentration can be analyzed using the observed stripping peak area and the calibration plot.

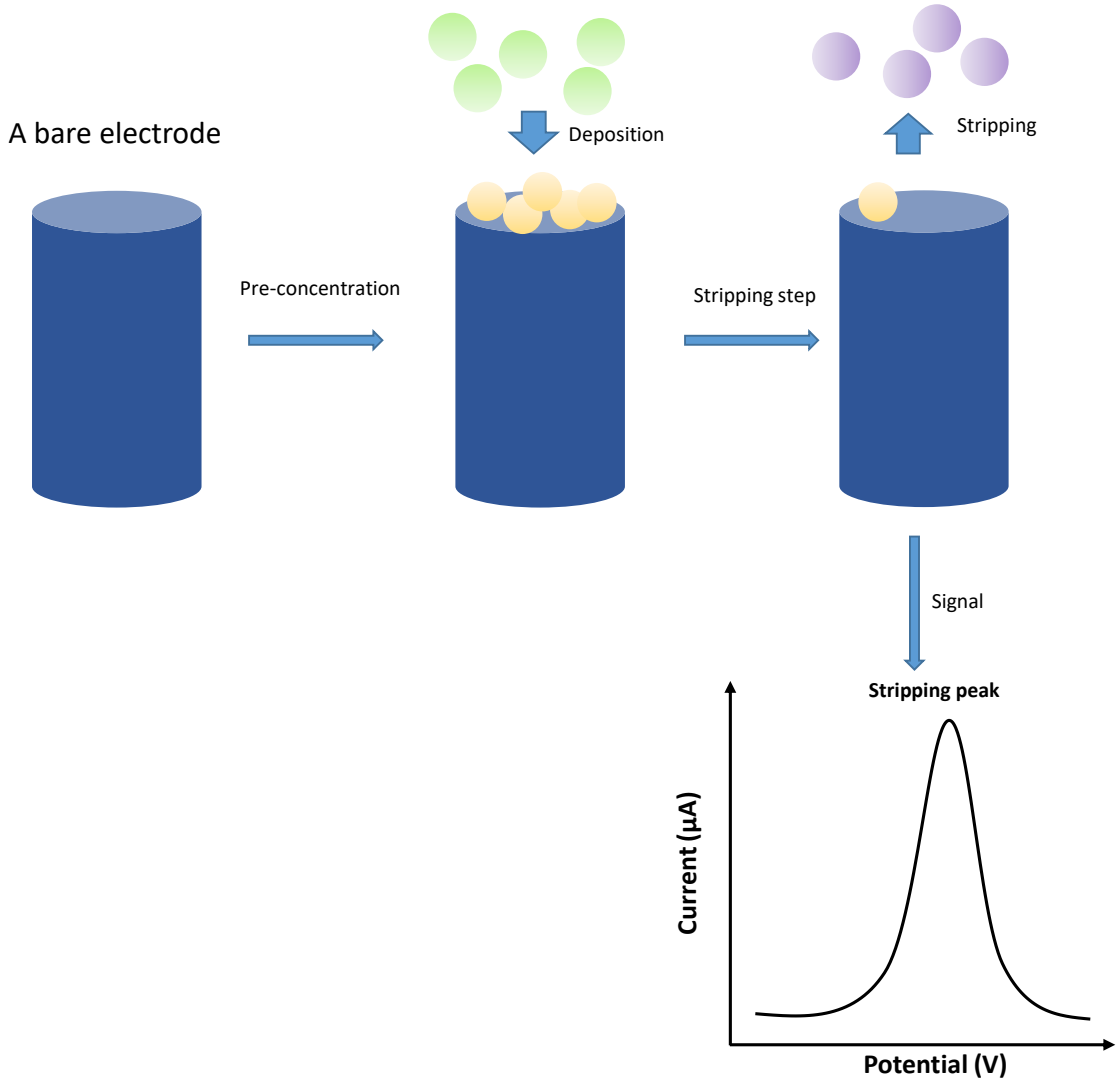

Figure 1.12 A schematic diagram of stripping voltammetry on a macrodisc electrode.

Examples of stripping voltammetry include the following:

(A) Anodic stripping voltammetry: The analysis of As(III) in drinking water on a Au/Fe_3O_4 nanoparticles modified glassy carbon electrode (AuNP/Fe_3O_4-GCE) was carried out with ASV that As was deposited at – 0.3 V (vs SCE) for 13 min in 0.1 M PBS buffer (pH = 5) [40], which gave a LOD of 9.7×10^{-4} ppb and a sensitivity of 1015 A M^{-1}. The electrochemical reactions are:

$$Pre-concentration: As(III)(aq) + 3e^- \rightarrow As(electrode) \quad (1.74)$$

$$Stripping\ step: As(electrode) \rightarrow As(III)(aq) + 3e^- \quad (1.75)$$

Note the formation of bulk As in the pre-concentration step which is anodically oxidised in the stripping step.

(B) Cathodic stripping voltammetry: Lead can be determined with CSV at a hanging mercury drop electrode (HMDE) with a deposition at – 0.15 V (vs Ag/AgCl) for 90 s in 10 mM TES (*N*-tris(hydroxymethyl)methyl-2-aminoethansulfonic acid) buffer (pH = 7) then followed up with a linear scan from – 0.4 V to – 1.1 V, giving a LOD of 0.002 ppb with a sensitivity of 1.05 A M^{-1} [41]. The electrochemical reactions are:

$$Pre-concentration: Pb^{2+}(aq) + 2H_2O \rightarrow PbO_2(electrode) + 4H^+ + 2e^- \quad (1.76)$$

$$Stripping\ step: PbO_2(electrode) + 4H^+ + 2e^- \rightarrow Pb^{2+}(aq) + 2H_2O \quad (1.77)$$

Note the formation of Pb(IV) oxide in the preconcentration step and the cathodic reduction of this for the stripping step.

(C) Adsorptive stripping voltammetry: J. Wang *et al* used AdsSV to detect Ni via complexation of dimethylglyoxime (Ni-DMG) on a bismuth film modified glassy carbon electrode (Bi-GCE), with 180 s of pre-concentration at – 0.7 V (vs Ag/AgCl) in 10 mM ammonia buffer (pH = 9) [42]. The LOD was determined to be 0.8 ppb, and the electrochemical reactions are:

$$Pre-concentration: Ni-DMG(aq) \rightarrow Ni-DMG(ads) \quad (1.78)$$

$$Stripping\ step: Ni-DMG(ads) \rightarrow Reduced-Ni-DMG(aq) + ne^- \quad (1.79)$$

Anodic Stripping Voltammetry

Anodic stripping voltammetry (ASV) is the most widely used stripping method offering low limits of detection (LODs) (10^{-10} – 10^{-11} M) and sensitivities as high as 10^3 A M^{-1}. In ASV,

the stripping step is conducted by scanning the voltammetry towards positive potentials relative to that for pre-concentration, which produces a characteristic peak (stripping peak) allowing the quantitative analysis of the target species [2, 36, 43].

This method has been applied using many different electrodes such as gold, platinum, silver and even particle-modified glassy carbon electrodes. The diversity can be judged from the following range of examples. Simm *et al* used ASV to detect As(III) at Ag macroelectrodes in 1 M HCl with deposition at – 0.3 V (vs SCE) for 60 s, and obtained a LOD of 13.5 ppb [44]. Yoon *et al* detected Cu(II) at a Pt nanoparticle-modified carbon paste electrode in acetate buffer (pH = 5.9) with a pre-concentration at – 0.6 V (vs Ag/AgCl) for 3 min, and obtained a LOD of 1 ppb [45]. ASV was also used to detect various ions in water such as lead, arsenic, copper, cadmium and zinc. Li *et al* detected Pb(II) in 0.1 M acetate buffer (pH = 5.0) at a Fe_3O_4 nanoparticle modified GCE with a deposition of 120 s at – 1.0 V (vs Ag/AgCl) resulting in a LOD of 30 ppb [46]. Dali *et al* combined single walled carbon nanotubes and fungal soil biomass onto a GCE (SWCNTs/biomass-GCE) to detect both Pb(II) and Cu(II). The pre-concentrations was conducted at – 1.2 V (vs Ag/AgCl) for 120 s then followed up with a differential pulse voltammetric scan from – 1.2 V to – 0.2 V, and obtained the LODs of 2 ppb and 11 ppb, respectively [47]. Wei *et al* modified GCE with SnO_2 and reduced graphene oxide (SnO_2/rGO-GCE) in 0.1 M acetate buffer (pH = 5) with the deposition at – 1.0 V (vs Ag/AgCl) for 120 s. It was performed to determine the concentrations of various ions in water, including Cd(II), Pb(II), Cu(II) and Hg(II) with LODs around 10^{-3} ppb [48]. Hwang *et al* used Fe and Chitosan to modify screen-printed carbon electrode (SPCE) and detect As(III) in 0.1 M acetate buffer (pH = 4.5). The deposition was conducted at – 0.6 V (vs Ag/AgCl) for 180s then followed with a square wave voltammetric scan, and a LOD of 1.12 ppb was obtained [49].

ASV on a solid electrode is recognised as a good, reliable method for quantitative analysis in electrochemistry, however, there are still some limitations which may or may not be negligible in real electro-analysis [2, 50]. First, the distribution of the metal deposited onto the surface of electrode may not be uniform. The deposit density can be different over distance scales of hundreds of microns [2]. The effects of variable deposits may lead to broadening of the stripping wave and hence loss of sensitivity. Second, there is the possibility of 'incomplete stripping' during the stripping steps, which means that less than 100% of the deposited species are stripped off. Although it is especially evident at high concentrations, the phenomenon can still be observed under analytical conditions [2, 50]. Third, only in the case of the uniformly accessible electrode or for fully irreversible electrode kinetics can it be assumed that the species at surface of electrode is uniformly stripped off during the quantitative analysis [2]. For non-uniformly accessible electrodes or for reversible electrode kinetics, it can occurs in a spatially non-uniform manner with the parts of the electrode experiencing greater local mass transport undergoing stripping at lower potentials.

In addition, the interference of other ions sometimes also affect the detection with the ASV method. The interferents may interact with the analytes [51], and the ASV can also enhance the signal of the interferents. For example, Cu(II) was considered as an interference when detecting As(III) in water since it forms Cu-As alloys [51]. Cu(II) was also considered as an interference ion for Pb(II) detection due to the competitive deposition onto the electrode during pre-concentration [52]. To solve the interference problem, some methods were also proposed such as introducing EDTA to precipitate the interference ions [53], and to modify the surface of electrodes with particles or organic species [47]. After suppressing the interference from other ions, ASV can be a good method for quantitative analysis, especially suitable for low cost [54, 55] and on-site detections [54].

Cathodic Stripping Voltammetry

Cathodic stripping voltammetry (CSV) developed from the early use of the dropping mercury and the hanging mercury drop electrodes but is now applied using a variety of working electrodes including boron doped diamond electrodes (BDDE) [56]. It is similar to ASV, except pre-concentration of the analytes takes place at an oxidizing potential and the analytical signal is obtained by sweeping cathodically. For example, Holak used a hanging mercury drop electrode (HMDE) to detect arsenic via CSV in 0.36 M H_2SO_4 with a LOD of 2 ppb [57]. Souza *et al* detected amiloride (AMI) at a BDDE with square wave CSV (SWCSV) method in 0.5 M H_2SO_4 and urine, and obtain a detection limit of 34.5 ppb [58].

Apart from metal electrodes, modified electrodes can also be applied with the CSV method. Ensch *et al* coated an indium tin oxide (ITO) electrode with a polymer film polystyrene-*block*-poly(ethylene-*ran*-butylene)-*block*-polystyrene-sulfonate (SSEBS), which was found to be sensitive for Mn(II) detection in water. The deposition was conducted at + 1.2 V for 60 s in 0.2 M acetate buffer (pH = 5) then followed up with a square wave voltammetic scan, resulting in a LOD of 0.3 ppb [59]. Grabarczyk *et al* synthesized Pb film on a glassy carbon electrode (PbFE-GCE) to detect Ga(III) in water with SWCSV. The pre-concentration took place at – 0.7 V (vs Ag/AgCl) for 60 s then the potential was scanned from – 0.7 V to – 1.05 V. It realised a detection limit of 0.209 ppb [60].

As with ASV, detection with CSV can also suffer from interference problems, such as the oxidation of mercury can interfere with the detection of Pb(II), As(III), Ti(I), Cu(II) and Sn(II) [61]. In addition, the toxicity of mercury also limits its application in real world.

Adsorptive Stripping Voltammetry

Unlike ASV or CSV, the pre-concentration of adsorptive stripping voltammetry (AdsSV) does not involve a Faradaic reaction, but rather analyte is pre-concentrated via adsorption rather than via electro-reduction or oxidation.

Examples of AdsSV include the following. Fipronil (FIP) can be detected on glassy carbon electrodes (GCEs) in 0.1 M Britton-Robinson buffer (pH = 8) via AdsSV. Pre-concentration was undertaken for 120 s giving time for FIP to be adsorbed onto the surface of electrode, then the stripping step was made from + 0.6 V to + 1.15 V at a scan rate of 5 mV s^{-1}. The stripping peak can be observed at ca + 0.92 V and the LOD was determined to be 4 μM (1748 ppb) [62]. In a second example Wang *et al* used Bi films onto GCEs for Ni(II) detection in 10 mM ammonia buffer (pH = 9) via the adsorption of Ni-dimethylglyoxime (DMG), and obtained a LOD of 0.8 ppb [42].

A newly developed method, insertive stripping voltammetry (ISV) is similar to AdsSV, in that it does not involve Faradaic reactions during pre-concentration. Instead pre-concentration step includes a potential driven ion insertion into a solid, and it can be used for the detection of non-redox ions notably alkali metals [63, 64]. This method was used for the measurement of low levels of Na^+ in aqueous solution (1 M $NaClO_4$) with a LOD of 0.6 ppb [63], and the quantification of Li^+ in human saliva with a lithium manganese oxide modified glassy carbon electrode (LMO-GCE) [64].

In this thesis, Chapters 5, 6 and 7 all apply ASV as an analytical method to detect arsenic species in aqueous solutions, in which low detection limits and high sensitivities are developed, and are compared with other electroanalytical methods.

Bibliography

[1] A. J. Bard, L.R. Faulkner, Electrochemical Methods: Fundamentals and Applications, 2nd ed., John Wiley & Sons, Inc, New York, 2001.
[2] R.G. Compton, C.E. Banks, Understanding Voltammetry, 3rd Edition, World Scientific2018.
[3] A. Arevalo, G. Pastor, Verification of the Nernst equation and determination of a standard electrode potential, Journal of Chemical Education 62(10) (1985) 882.
[4] F.J. Vidal-Iglesias, J. Solla-Gullón, E. Herrero, A. Rodes, A. Aldaz, Do you really understand the electrochemical Nernst equation?, Electrocatalysis 4(1) (2013) 1-9.
[5] W. Nernst, Theorie der Reaktionsgeschwindigkeit in heterogenen Systemen, Zeitschrift für physikalische Chemie 47(1) (1904) 52-55.
[6] A.J. Bard, R. Parsons, J. Jordan, International Union of Pure and Applied Chemistry, Standard Potentials in Aqueous Solution, Dekker, New York, 1985.
[7] W. Albery, Electrode Kinetics, Clarendon, Oxford, 1975.
[8] A.C. Fisher, Electrode dynamics, 1996.
[9] J.A.V. Butler, Studies in heterogeneous equilibria. Part I. Conditions at the boundary surface of crystalline solids and liquids and the application of statistical mechanics, Transactions of the Faraday Society 19(March) (1924) 659-665.
[10] R. Guidelli, R.G. Compton, J.M. Feliu, E. Gileadi, J. Lipkowski, W. Schmickler, S. Trasatti, Defining the transfer coefficient in electrochemistry: An assessment (IUPAC Technical Report), Pure and Applied Chemistry 86(2) (2014) 245-258.
[11] M. Volmer, The migration of adsorbed molecules on surfaces of solids, Transactions of the Faraday Society 28 (1932) 359-363.
[12] M.C. Henstridge, E. Laborda, Y. Wang, D. Suwatchara, N. Rees, Á. Molina, F. Martinez-Ortiz, R.G. Compton, Giving physical insight into the Butler–Volmer model of electrode kinetics: Application of asymmetric Marcus–Hush theory to the study of the electroreductions of 2-methyl-2-nitropropane, cyclooctatetraene and europium (III) on mercury microelectrodes, J. Electroanal. Chem. 672 (2012) 45-52.
[13] A.J. Appleby, J.H. Zagal, Free energy relationships in electrochemistry: a history that started in 1935, J. Solid State Electrochem. 15(7) (2011) 1811-1832.
[14] G. Burstein, A hundred years of Tafel's Equation: 1905–2005, Corrosion Science 12(47) (2005) 2858-2870.
[15] D. Li, C. Lin, C. Batchelor-McAuley, L. Chen, R.G. Compton, Tafel analysis in practice, J. Electroanal. Chem. 826 (2018) 117-124.
[16] J. Tafel, Über die Polarisation bei kathodischer Wasserstoffentwicklung, Zeitschrift für physikalische Chemie 50(1) (1905) 641-712.
[17] A. Fick, Ueber Diffusion, Ann. Phys. 170(1) (1855) 86.
[18] M. Von Smoluchowski, Zur kinetischen theorie der brownschen molekularbewegung und der suspensionen, Ann. Phys. 326(14) (1906) 756-780.
[19] A. Einstein, On the motion of small particles suspended in liquids at rest required by the molecular-kinetic theory of heat, Ann. Phys. 17(549-560) (1905) 208.
[20] M. Islam, Einstein–Smoluchowski diffusion equation: a discussion, Physica Scripta 70(2-3) (2004) 120.
[21] J.K. Novev, R.G. Compton, Natural convection effects in electrochemical systems, Curr. Opin. Electrochem. 7 (2018) 118-129.
[22] J. Rubio-Garcia, A. Kucernak, A. Charleson, Direct visualization of reactant transport in forced convection electrochemical cells and its application to redox flow batteries, Electrochem. Commun. 93 (2018) 128-132.

[23] I. Montenegro, M.A. Queirós, J.L. Daschbach, Microelectrodes: theory and applications, Springer Science & Business Media2012.
[24] G.H. Sanders, R.G. Compton, Electrode potentials, Oxford University Press1996.
[25] E.J. Dickinson, J.G. Limon-Petersen, N.V. Rees, R.G. Compton, How much supporting electrolyte is required to make a cyclic voltammetry experiment quantitatively "diffusional"? A theoretical and experimental investigation, J. Phys. Chem. C 113(25) (2009) 11157-11171.
[26] E. Huckel, P. Debye, Zur theorie der elektrolyte. i. gefrierpunktserniedrigung und verwandte erscheinungen, Phys. Z 24 (1923) 185-206.
[27] J. Lee, J.H. Bang, Reliable counter electrodes for the hydrogen evolution reaction in acidic media, ACS Energy Letters 5(8) (2020) 2706-2710.
[28] N. Elgrishi, K.J. Rountree, B.D. McCarthy, E.S. Rountree, T.T. Eisenhart, J.L. Dempsey, A practical beginner's guide to cyclic voltammetry, Journal of chemical education 95(2) (2018) 197-206.
[29] R.S. Nicholson, I. Shain, Theory of stationary electrode polarography. Single scan and cyclic methods applied to reversible, irreversible, and kinetic systems, Anal. Chem. 36(4) (1964) 706-723.
[30] H. Matsuda, Y. Ayabe, Zur Theorie der Randles-Sevčikschen Kathodenstrahl-Polarographie, Zeitschrift für Elektrochemie, Berichte der Bunsengesellschaft für physikalische Chemie 59(6) (1955) 494-503.
[31] J.E.B. Randles, Kinetics of rapid electrode reactions, Discussions of the faraday society 1 (1947) 11-19.
[32] A. Ševčík, Oscillographic polarography with periodical triangular voltage, Collection of Czechoslovak Chemical Communications 13 (1948) 349-377.
[33] X. Dai, O. Nekrassova, M.E. Hyde, R.G. Compton, Anodic stripping voltammetry of arsenic (III) using gold nanoparticle-modified electrodes, Anal. Chem. 76(19) (2004) 5924-5929.
[34] M. Iwamoto, R. Osteryoung, Cathodic stripping voltammetry of thioamides on a rotating silver disk electrode, J. Electroanal. Chem. Interf. Electrochem. 169(1-2) (1984) 181-194.
[35] J. Wang, Anodic stripping voltammetry as an analytical tool, Environ. Sci. Technol. 16(2) (1982) 104A-109A.
[36] J. Wang, Stripping analysis: principles, instrumentation, and applications, Vch Pub1985.
[37] K.Z. Brainina, E.A. Vilchinskaya, R.M. Khanina, L.N. Kalnishevskaya, The use of the reference element method for stripping voltammetric analysis of natural waters, Electroanalysis 4(5) (1992) 549-554.
[38] K.Z. Brainina, N. Malakhova, N.Y. Stojko, Stripping voltammetry in environmental and food analysis, Fresenius' journal of analytical chemistry 368(4) (2000) 307-325.
[39] C. Zbinden, Nouvelle méthode de microdétermination de l'ion cuivre, Bull. Soc. Chim. Biol. 13 (1931) 35–38.
[40] H. Cui, W. Yang, X. Li, H. Zhao, Z. Yuan, An electrochemical sensor based on a magnetic Fe 3 O 4 nanoparticles and gold nanoparticles modified electrode for sensitive determination of trace amounts of arsenic (III), Analytical Methods 4(12) (2012) 4176-4181.
[41] E. Fischer, C.M. van den Berg, Determination of lead complexation in lake water by cathodic stripping voltammetry and ligand competition, Anal. Chim. Acta 432(1) (2001) 11-20.
[42] J. Wang, J. Lu, Bismuth film electrodes for adsorptive stripping voltammetry of trace nickel, Electrochem. Commun. 2(6) (2000) 390-393.
[43] K. Brainina, E. Neyman, Electroanalytical stripping methods, John Wiley & Sons1994.
[44] A.O. Simm, C.E. Banks, R.G. Compton, The electrochemical detection of arsenic (III) at a silver electrode, Electroanalysis (N.Y.N.Y.) 17(19) (2005) 1727-1733.

[45] J.H. Yoon, G. Muthuraman, J. Yang, Y.B. Shim, M.S. Won, Pt-nanoparticle incorporated carbon paste electrode for the determination of Cu (II) ion by anodic stripping voltammetry, Electroanalysis (N.Y.N.Y.) 19(11) (2007) 1160-1166.
[46] W.-J. Li, X.-Z. Yao, Z. Guo, J.-H. Liu, X.-J. Huang, Fe3O4 with novel nanoplate-stacked structure: Surfactant-free hydrothermal synthesis and application in detection of heavy metal ions, J. Electroanal. Chem. 749 (2015) 75-82.
[47] M. Dali, K. Zinoubi, A. Chrouda, S. Abderrahmane, S. Cherrad, N. Jaffrezic-Renault, A biosensor based on fungal soil biomass for electrochemical detection of lead (II) and cadmium (II) by differential pulse anodic stripping voltammetry, J. Electroanal. Chem. 813 (2018) 9-19.
[48] Y. Wei, C. Gao, F.-L. Meng, H.-H. Li, L. Wang, J.-H. Liu, X.-J. Huang, SnO2/reduced graphene oxide nanocomposite for the simultaneous electrochemical detection of cadmium (II), lead (II), copper (II), and mercury (II): an interesting favorable mutual interference, J. Phys. Chem. C 116(1) (2012) 1034-1041.
[49] J.H. Hwang, P. Pathak, X.C. Wang, K.L. Rodriguez, J. Park, H.J. Cho, W.H. Lee, A novel Fe-Chitosan-coated carbon electrode sensor for in situ As(III) detection in mining wastewater and soil leachate, Sens. Actuator B-Chem. 294 (2019) 89-97.
[50] J.L. Hardcastle, Novel voltammetric methods in heavily passivating media, University of Oxford, 2002.
[51] A. Idris, J. Mafa, N. Mabuba, O. Arotiba, Dealing with interference challenge in the electrochemical detection of As (III)—a complexometric masking approach, Electrochem. Commun. 64 (2016) 18-20.
[52] E. Bakker, P. Bühlmann, E. Pretsch, Polymer membrane ion-selective electrodes–what are the limits?, Electroanalysis (N.Y.N.Y.) 11(13) (1999) 915-933.
[53] H.-H. Chen, J.-F. Huang, EDTA assisted highly selective detection of As3+ on Au nanoparticle modified glassy carbon electrodes: facile in situ electrochemical characterization of Au nanoparticles, Anal. Chem. 86(24) (2014) 12406-12413.
[54] D.K. Pattadar, J.N. Sharma, B.P. Mainali, F.P. Zamborini, Anodic stripping electrochemical analysis of metal nanoparticles, Curr. Opin. Electrochem. 13 (2019) 147-156.
[55] M.J. Goldcamp, M.N. Underwood, J.L. Cloud, S. Harshman, K. Ashley, An environmentally friendly, cost-effective determination of lead in environmental samples using anodic stripping voltammetry, Journal of chemical education 85(7) (2008) 976.
[56] P. Worsfold, A. Townshend, C.F. Poole, M. Miró, Encyclopedia of analytical science, Elsevier2019.
[57] W. Holak, Determination of arsenic by cathodic stripping voltammetry with a hanging mercury drop electrode, Anal. Chem. 52(13) (1980) 2189-2192.
[58] K.A. Souza, A.M. Nunes, D.M. Pimentel, R.M. Verly, E.S. Gil, A.R. Malagutti, W.T. dos Santos, Altered electrochemistry of amiloride drug on boron-doped diamond electrode: Rapid and selective detection in urine by square-wave cathodic stripping voltammetry for application in doping control, Electrochim. Acta 373 (2021) 137891.
[59] C.A. Rusinek, A. Bange, M. Warren, W. Kang, K. Nahan, I. Papautsky, W.R. Heineman, Bare and polymer-coated indium tin oxide as working electrodes for manganese cathodic stripping voltammetry, Anal. Chem. 88(8) (2016) 4221-4228.
[60] M. Grabarczyk, J. Wasąg, Adsorptive cathodic stripping voltammetric method for determination of gallium using an in situ plated lead film electrode, Electroanalysis 27(11) (2015) 2596-2600.
[61] D.J. Myers, J. Osteryoung, Amperometric titrations employing differential pulse polarography, Anal. Chem. 46(3) (1974) 356-359.
[62] Y. Wang, A.K.S. Kumar, R.G. Compton, Optimising Adsorptive Stripping Voltammetry: Strategies and Limitations, ChemElectroChem 8(12) (2021) 2343-2352.

[63] A.L. Suherman, M. Lin, B. Rasche, R.G. Compton, Introducing “Insertive Stripping Voltammetry”: Electrochemical Determination of Sodium Ions Using an Iron (III) Phosphate-Modified Electrode, ACS sensors 5(2) (2020) 519-526.
[64] A.L. Suherman, B. Rasche, B. Godlewska, P. Nicholas, S. Herlihy, N. Caiger, P.J. Cowen, R.G. Compton, Electrochemical detection and quantification of lithium ions in authentic human saliva using LiMn2O4-modified electrodes, ACS sensors 4(9) (2019) 2497-2506.

Chapter 2. The need for arsenic detection

In the previous chapter, the basic concepts of electrochemistry were introduced from which it is clear it is possible to use electrochemical methods for analysis in aqueous solutions. This chapter addresses the analysis of arsenic, its speciation and the various methods used; the electroanalytical measurement of arsenic is the focus of this thesis.

2.1. Arsenic

2.1.1. Distribution

Arsenic is an element that is more widespread than most of us think; it is the 20th abundant element in natural (0.00005% of the Earth's crust by mass), 14th in seawater and 12th in human body [1-3]. The main source of the arsenic in groundwater is usually from geogenic origins such as volcanic activities or soil erosion [3], but also from human activities including mining and agricultural activities, which accelerate the transport of arsenic from ores or soil to groundwater [1, 2]. The most common arsenic mineral is arsenopyrite (FeAsS), which contains As, Fe and S [4]. Other less common minerals such as orpiment (As_2S_3), realgar (α-As_4S_4) and enargite ($3Cu_2S{\cdot}As_2S_5$) contain As and S [4, 5]. Figure 2.1 shows the pictures of some of the minerals which contain arsenic. Arsenopyrite is an ore with steel grey to silver-white colour (Figure 2.1a), and it is a major source of arsenic [5]. Realgar has a colour of dark red to orange-red with a formula of As_4S_4 (Figure 2.1b) [6, 7]. Orpiment is an transparent orange ore with arsenic sulfide (Figure 2.1c) [8] and enargite is steel grey with copper arsenic sulfide (Figure 2.1b) [9]. Arsenopyrite occurs in gold, copper and tin ores in many countries and areas, including east of US, Canada, UK, North Macedonia, China and Japan [4, 10]. Orpiment can

usually found near to volcanos and was found in China, Egypt and Greece [4]. Realgar can also occur near to volcanos and it was also found in lead, silver and gold ores in Hungary and Bohemia [5]. Enargite is a medium to low temperature hydrothermal mineral usually occurring with quartz, pyrite (FeS_2) in US and copper ores in Canada, Mexico and Peru [4, 5, 10].

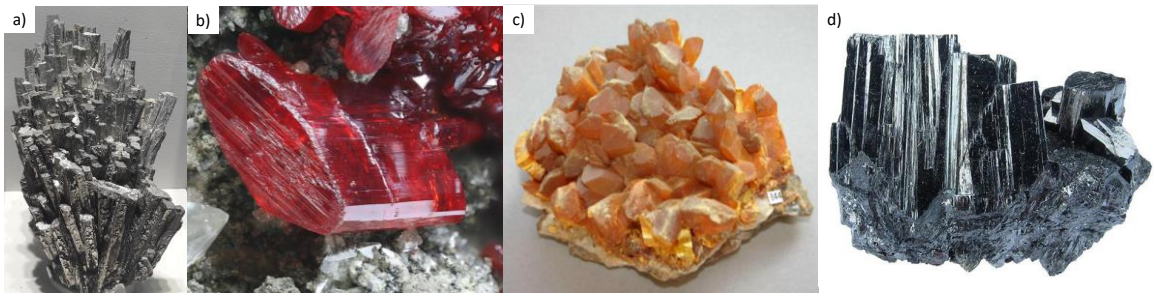

Figure 2.1 Pictures of a) arsenopyrite, b) realgar, c) orpiment and d) enargite. Figure 2.1a is reprinted with permission from Ref. [5]. Copyright 2020 Elsevier. Figures 2.1 b and c are reprinted with permission from Ref. [6, 7] and [8], respectively. Copyright Mindat. Figure 2.1d is reprinted with permission from Ref. [9]. Copyright Minerals.net.

Figure 2.2 Global occurrence of arsenic reported in major countries with arsenic concentrations ≥ 10 μg L^{-1} in groundwater including river and lake water. Reprinted with permission from Elsevier 2021, Ref [1].

Some countries or areas suffer from significant contamination of groundwater by arsenic at levels considered harmful. These include Argentina, Bangladesh, Canada, China, West Bengal (India), UK and USA [1, 3]. The first case of arsenic contamination in groundwater was found and reported in 1993 in Nawabganj of Bangladesh [11-13]. From then

on, high concentrations of arsenic were found in other areas in the Bengal basin [11]. Figure 2.2 shows a world map indicating where the arsenic occurrence reaches above the threshold of 10 ppb in ground water [1]. In UK, arsenic contamination was detected in soil and groundwater samples near to mining operations in west Cornwall with a level as high as 5000 ppm, which was mainly caused by the occurrence of arsenopyrite (FeAsS) and enargite ($3Cu_2S \cdot As_2S_5$) in copper ores [10]. In Asia, there are around 110 million people using water with arsenic exposure [14]. In Europe, the Great Hungarian Plain-Csongrfid Country of Hungary and the eastern part of Croatia are severely affected by the contamination of ground water [15, 16]. In Canada, groundwater in Yellowknife is contaminated by arsenic mainly due to mining industries [17]. In USA, high concentrations of arsenic were mainly found in southwestern US (New Mexico, Arizona and Texas) [18]. In central New Mexico, the arsenic in groundwater level exceeding 50 ppb was reported, which was attributed to the contaminations from As-rich volcanic rocks [19]. Although arsenic affects Canada and USA, the concentrations are mostly of much lower affected places compared to that in Asia [18, 20, 21]. It widely recognised that the arsenic contamination of groundwater is a worldwide problem.

2.1.2. Toxicity

Arsenic has various different oxidation states, including As(-III), As(0), As(+III) and As(+V) [1, 2]. A variety of inorganic and organic forms of arsenic can be found in the world [2]. Figure 2.3 presents the structures of some of the more commonly encountered arsenic species. As(III), As(V), MMA(III), MMA, DMA(III) and DMA have all been found as inorganic or organic arsenic in water samples [1, 22, 23]. In groundwater, the dominant forms of arsenic are arsenite, As(III), and arsenate, As(V), with a minor amount of methylated or demethylated arsenic being detected [22]. The short term consequences of As ingestion by humans include muscular pain, weakness, vomiting and diarrhea, whilst long-term exposure to

arsenic can cause organ failure, cancer, skin disease and behavioral disorder [24]. A picture of skin lesions after arsenic poisoning is shown in Figure 2.4.

Toxicity studies have shown that the various forms of arsenic have different toxicities. The oxidation states determine the toxicity and mobility of arsenic [25], and arsenic metabolism is facilitated by methylation in body to form metabolities which can be excreted in urine [26-28]. The scheme of arsenic biomethylation is shown in Figure 2.5. Most importantly for groundwater and drinking water, arsenite, As(III) is ca 60 times more toxic than arsenate, As(V) [29], and it is recognised that dissolved inorganic arsenic is the main source of arsenic exposure for humans [26, 29]. This thesis is focussed on the detection of inorganic arsenic species, As(III) and As(V).

2.1.3. Regulations

Since arsenic species are toxic and exposure to them may cause cancer, chronic disease or even death [1-3], many countries have formally considered them as toxins and made regulations on them. The United States Environmental Protection Agency (USEPA) has listed arsenic as number one toxin due to its toxicity, and the limit was announced to be 10 ppb in drinking water [30]. The World Health Organization (WHO) also set the recommended level of arsenic in drinking water to be 10 ppb [31]. The same limit (10 ppb) in drinking water was also set by European Food Safety Authority (EFSA) [32]. China also updated their regulations for arsenic in drinking water to 10 ppb in 2017 [33]. Thus, it is important to develop arsenic detection methods to reach the regulations in drinking water. The next section will discuss arsenic detection methods, and their relative merits and limits of detection (LODs).

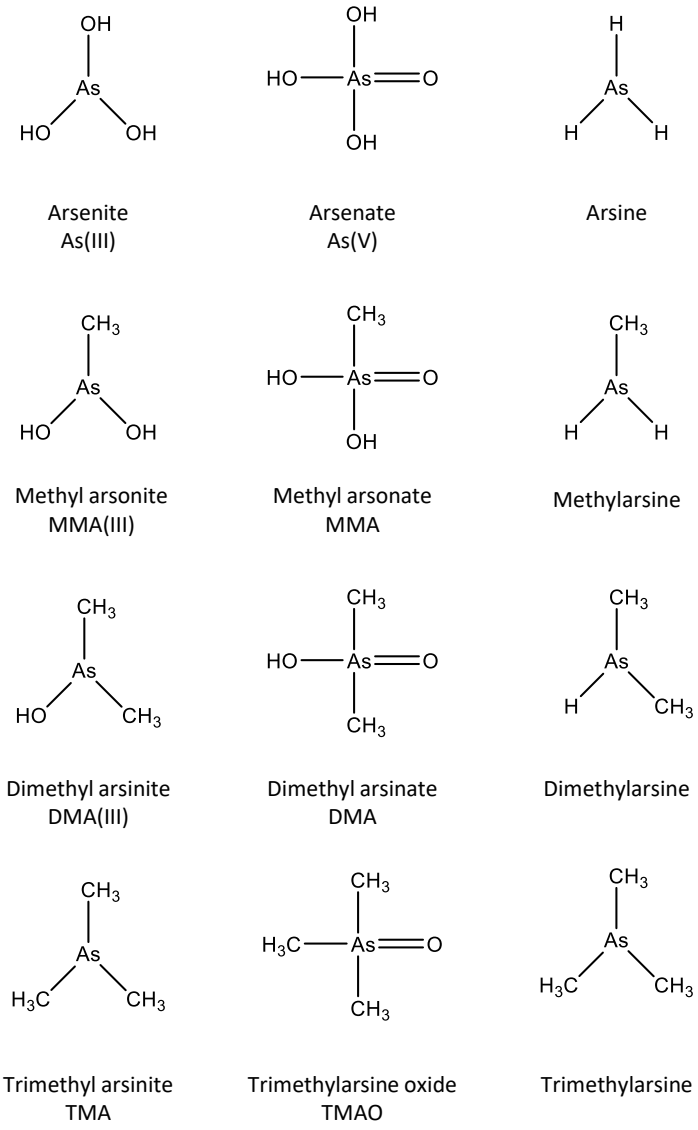

Figure 2.3 The structures and names of some arsenic species.

Figure 2.4 Skin lesions from arsenic poisoning. Reprinted with permission from Ref. [34]. Copyright 2021 Guardian.

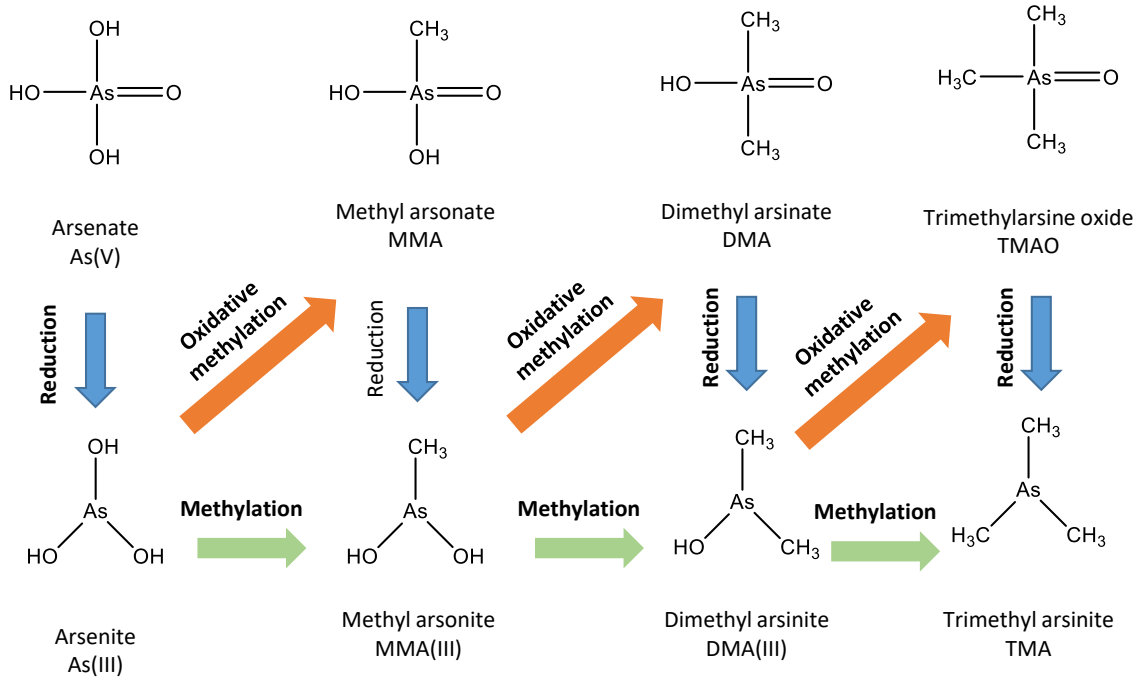

Figure 2.5 A scheme for the biomethylation of inorganic arsenic.

2.2. Arsenic detection methods

During the past few decades, scientists have developed various methods for arsenic detection. This section will discuss various arsenic detection methods including-spectrometric techniques, electrochemical methods and commercialised methods.

2.2.1. Spectrometric techniques

Atomic absorption spectroscopy

Atomic absorption spectroscopy (AAS) can detect and characterize elements either in liquid or in solid form using a specific wavelength from a light source. The individual elements absorb specific wavelengths, which are measured against standards so that the element can be quantified based on the absorption spectrum. The samples containing the analytes of interest are ionized by an atomizer and photons with specific wavelength can be absorbed [35]. Thus, compare to the standard spectrum, the analytes can be qualified and quantified.

Hydride generation (HG) is also popular for arsenic detection in AAS since it was first introduced in 1969 [36]. The hydride generation reaction is shown below:

$$As(OH)_3 + 3BH_4^- + 3H^+ \rightarrow AsH_3 + 3BH_3 + 3H_2O \quad (2\text{-}1)$$

$$BH_3 + 3H_2O \rightarrow H_3BO_3 + 3H_2 \quad (2\text{-}2)$$

Arsenic species react with sodium tetrahydroborate(III) and are reduced to arsine gas. It has been proved that the reducing agents are reliable for the conversion of the sample to volatile forms [37]. The application of HG in AAS can increase the sensitivity for arsenic detection and reduce the possible interferences from the sample [37].

Howard *et al* measured the concentrations of different forms of arsenic species including As(III), As(V) and MMA, and obtained LODs in the range of 0.1 to 0.5 ppb with the 3σ method [38, 39]. Karthikeyan *et al* detected both As(III) and As(V) via hydride generation AAS (HG-AAS) in sea water with LODs of 0.05 and 2 ppb of As(III) and As(V), respectively [40]. The merit of using AAS for As detection is the readily obtained low LODs and the wide range of arsenic species that can be quantified. However, some atoms, ions or molecules can sometimes emit spectra due to excitation by heat, which may limit the precision of the method [35]. For hydride generation, some of the transition metals such as Cu could interfere with the HG step, which is possibly caused by the reaction between the metal ion and the BH_4^- resulting in a precipitate which can capture and catalytically decompose the evolved hydrides [41].

Atomic fluorescence spectroscopy

Atomic fluorescence spectroscopy (AFS) is the method used to quantify elements through the fluorescence emitted from the analytes. Usually, the atomic element absorbs energy from the light source, and electrons are excited from ground states to excited states. Then the electrons relax to the ground state and the photon emitted is detected as fluorescence. Similar to AAS, HG can also be applied to the AFS to generate arsine gas. Gomez-Ariza *et al* used the HG-AFS method to detect total arsenic species including As(III), As(V) and MMA with LODs from 0.1 to 0.3 ppb [42]. Sanchez-Rodas *et al* used AFS to detect As, Se, Sb and Hg selectively with a LODs of 0.2 and 0.1 ppb for As(III) and As(V), respectively [43]. It is clear that AFS can also be used to detect arsenic species selectively with low LODs. However, similar to AAS, some transition metals such as Cu and Fe could interfere with the hydride generation step [42].

Inductively coupled plasma mass spectroscopy

Inductively coupled plasma mass spectroscopy (ICP-MS) is an analytical method used to measure the mass-to-charge ratio of samples are ionized by an inductively coupled plasma

[44]. The ICP is a plasma generated by electric currents which are produced by electromagnetic induction [35]. The high temperature of the plasma can ionize all forms of arsenic regardless of the specific chemical species [45]. Thus this method can be used to detect low concentrations of arsenic without knowledge of the speciation. The LOD is typically in the range of 0.001 to 0.2 ppb [46]. For example, Liu *et al* applied high performance liquid chromatography (HPLC) with ICP-MS and obtained the LODs of 0.04 to 0.5 ppb for As(III), As(V), DMA and MMA [47]. Jackson *et al* combined ion chromatography (IC) with ICP-MS to measure different forms of arsenic in water and obtained LODs below 0.05 ppb for all arsenic species [48].

In UK, the legal minimum wage paid is just € 10 per hour [49]. For AAS and AFS, the time for each measurement is around 1 minute; for ICP-MS, the time is around 3 minutes for each measurement [50]. The costs of the spectrometers are also expensive. In respect of AAS the costs are ca € 9,000 for purchasing a spectrometer and AFS has a similar price [50, 51]. The cost of ICP-MS has a price of ca € 165,000 if to purchase a new spectrometer. Apart from payment to technicians and the cost of spectrometer, the spectrometer also has a cost of € 0.12 and € 1.5 for AAS/AFS and ICP-MS of each analysis, respectively [50]. Assuming that the spectrometer works 1000 hours per year, the cost for each analysis of AAS/AFS comes from the cost of gas (acetylene), € 20000 per year, the cost of hollow cathode lamps, € 6000 per year, and electricity of € 100 per year, where each sample takes ca 1 min with 180,000 samples per year [50]; for ICP-MS, the cost of gas (Ar), € 20000 per year, cost of plasma torch and vacuum pump, € 10000 per year, and the electricity of € 100 per year, where each sample takes ca 3 min with 20,000 samples per year [50]. Thus, the estimated lowest cost for each measurement is around € 0.40 and € 1.8 for AAS/AFS and ICP-MS, respectively. In addition, the shipping of samples to the laboratory also increased cost for measurements.

Although spectrometric methods including AAS, AFS and ICP-MS offer low LODs and good sensitivities, they require highly trained technicians and operate in central facilities, which means they may not available and accessible in rural regions [52]. The shipping of samples from remote areas may also be challenging due to the time and associated cost. Thus, in comparison electrochemical methods may be attractive for arsenic detection because they are rapid and inexpensive. In next section, electrochemical methods of arsenic detection will be discussed.

2.2.2. Electrochemical methods

Electrochemical methods were applied for arsenic detection and quantification over recent decades because they can be rapid, inexpensive and sensitive [53]. The aim of this thesis is the further development of electrochemical methods for real world applications by developing a methodology for fast-read or on-site detection. In this section, the state of the art for electrochemical methods on different electrodes will be discussed in detail.

Unmodified electrodes

Arsenic can be detected on bare metal electrodes, including Pt [54, 55], Hg [56, 57], and Au [55, 58, 59]. The redox reactions can take place on the metal electrodes [53]. Some of the metals such as Pt can be used to catalyze the reaction of As(III) to As(V) [60]:

$$Pt + H_2O = PtOH + H^+ + e^- \quad (2\text{-}3)$$

$$PtOH + As(OH)_3 = PtOHAs(OH)_3 \quad (2\text{-}4)$$

$$PtOHAs(OH)_3 = PtOAs(OH)_3 + H^+ + e^- \quad (2\text{-}5)$$

$$PtOAs(OH)_3 \rightarrow Pt + OAs(OH)_3 \quad (2\text{-}6)$$

The As(III) can be quantified via linear sweep voltammetry (LSV) on Pt and a LOD calculated with 3σ method was determined to be 35 ppb [60].

Bu *et al* reported a method using Pt macroelectrodes to detect As(III) in 0.5 M H_2SO_4 via anodic stripping voltammetry (ASV), and obtained a LOD of 0.075 ppb calculated with 3σ method [39] and a sensitivity of 558 μA μM^{-1} [55]. Lolic *et al* used Pt rotating disc electrode (Pt RDE) for As(III) in 1 M HCl quantification via cyclic voltammetry (CV) [54]. The LOD was determined via 3σ method [39] as 5 ppb.

For Hg, the most common type of electrode used in arsenic detection has been the hanging mercury drop electrode (HMDE) [56, 57]. The merit of the HMDE is that it does not require electrode cleaning and conditioning. He *et al* reported the method of As(III) determination on HMDE via differential pulse cathodic stripping voltammetry (DPCSV) and obtained a LOD of 0.5 ppb (3σ method) [56], and Profumo *et al* detected As(III) via CSV with a LOD of 0.01 ppb on HMDE [57]. It was found that the arsenic oxidation peak appeared as a shoulder of Hg oxidation peak on a HMDE [53, 61], which make it impossible for Hg to detect arsenic via anodic stripping voltammetry (ASV). Although detection on mercury electrode can provide low LODs, Hg is toxic to human body and mercury surfaces are vulnerable to organic interferences [61], so Hg not favoured as a material of arsenic determination in water.

For Au, there are more methods based on Au electrodes than other materials, and most of the methods used were anodic stripping voltammetry (ASV) [53] using the deposition of bulk As. Compared to Pt, Au was preferred as a working electrode due to a higher hydrogen overvoltage which allows Au to be used at a more negative potential to deposit arsenic without the simultaneous evolution of hydrogen. The experiments carried out by Simm *et al* measured As on an Au electrode via ASV with a LOD of 0.75 ppb [58]. Alves *et al* quantified As(III) on a vibrating gold microwire electrode via differential pulse anodic stripping voltammetry

(DPASV) with a LOD of 0.07 ppb [62]. Zakharova *et al* used Au microelectrodes to measure As(III) in water via ASV and the LOD obtained was 0.09 ppb (3σ method) [63]. It is evident that bare metal electrodes can be used for arsenic detection with low detection limits.

However, detection of arsenic may also suffer from the interference of other ions such as Cu^{2+} due to the formation of intermetallic/alloy of Cu-As [64]. Thus, interference from other ions requires more attention when detecting arsenic in water. The work in this thesis, especially in chapters 5 and 6, is partly focussed on overcoming the problem of interference from copper, as well as chloride since these are species commonly encountered in ground and drinking water samples.

Particle - modified electrodes

Particle-modified electrodes are also popular for arsenic detection with electrochemical methods. During the past ten years, modified electrodes were also used for arsenic detection where particles or tubes present high surface areas, along with claimed "robust electrocatalytic ability" [65, 66]. The particles on the electrode modify the diffusive transport from bulk solution and in the case of electrocatalytic particles can promote reaction when electrochemical reaction cannot take place on the surface of electrode. If a sub-monolayer of nanoparticles were deposited on the surface of electrode, it forms a 'spatially heterogeneous electrode' [67] which can shift the voltammetric wave to a lower overpotential when the particles show a greater electrocatalytic activity than the substrate. If the particles are closely spaced, their diffusion layers overlap and the transport to the surface becomes linear semi-infinite diffusion giving a similar peak current to that expected for an electrode of the same geometric area as the substrate. On the other hand, if the particles deposited are closely packed and formed a thick porous layer of conductive particles, the modified electrode would show a semi-infinite diffusion [68] of analyte from bulk solution to the surface of porous layer and a thin layer diffusion [69] due to

electrolytic discharge within the pores of the layer. The time of response in the close packed layers of particles is short and the size of the pores also results in a fast depletion [68]. More discussion about the reliability of particle modified electrodes appears in Chapter 4. The most common metal particles applied for arsenic detections were Pt and Au nanoparticles.

Dai *et al* modified glassy carbon electrodes with Pt nanoparticles (PtNP-GCE) by electrodepostion and detected As(III) via linear sweep voltammetry (LSV) with a LOD of 2.1 ppb (3σ method) [60]. Shin *et al* co-deposited PtNP and FeNP with multiwall carbon nanotubes (MWCNTs) onto a GCE [70]. The modified electrode was used for As(III) detection via anodic stripping voltammetry (ASV) and reported a LOD of 0.75 ppb (3σ method) [70]. Kempegowda *et al* modified a GCE with PtNPs and graphene (Gr/PtNP-GCE) to detect As(III) via square wave anodic stripping voltammetry (SWASV), and obtained a LOD of 0.08 ppb (3σ method) [71].

Measurements were also conducted on AuNP modified electrodes. Chen *et al* used AuNPs modified glassy carbon electrode (GCE) to measure As(III) in 0.1 M PBS buffer containing 0.01 M EDTA for elimination of interference ions [72]. The LOD was determined to be 0.0025 ppb via multiple scan cyclic voltammetry (MSCV) [72]. Xiao *et al* combined AuNPs and CNTs onto GCEs and used ASV with a more negative deposition potential, which resulted in a LOD of 0.1 ppb and a sensitivity of 1985 $\mu A\ \mu M^{-1}$ [73]. Yang *et al* modified GCE with AuNPs and CeO_2/ZrO_2 nanoparticles, which was used to detect As(III) in 0.1 M HAc-NaAc via square wave anodic stripping voltammetry (SWASV) [74]. The LOD was determined to be 0.137 ppb [74].

Although particle modified electrodes can provide sensitive results during arsenic measurements, the methods shown above are laboratory based. More optimizations are

required for on-site or fast-read arsenic detection. Some commercially available sensors are sold for in field arsenic detection and they will be discussed in the next section.

2.2.3. Commercially available sensors

The most common commercially available field test kits for As are based on the Gutzeit test [75]. For example, Hach produces an 'Arsenic Low Range Test Kit' for arsenic detection in water via the Gutzeit reaction [75] and the method of use is shown in Figure 2.6. The water sample is added to the vessel and the zinc powder is used in the sample to reduce the arsenic contents to arsine gas [75] as shown in the equations below:

$$As_2O_3 + 6Zn + 12HCl \rightarrow 2AsH_3 + 6ZnCl_2 + 3H_2O \quad (2\text{-}7)$$

$$H_3AsO_4 + 4Zn + 8HCl \rightarrow AsH_3 + 4ZnCl_2 + 4H_2O \quad (2\text{-}8)$$

A test strip with $HgBr_2$ on the surface is placed on the top of the vessel and the arsine gas generated from arsenic contents can traveled to the top of the vessel. Once the arsine gas reached the test strip, it reacts with the $HgBr_2$ and generate mixed arsenic/mercury halogenides such as AsH_2HgBr, which can discolor the test strip from white to yellow to brown as the concentration increases [76]. The results can be obtained in around 30 minutes [75, 76]. Although the test kits based on Gutzeit reaction can provide results rapidly and the sensor is portable, the arsine gas that generated from the first step of reduction is toxic and dangerous to untrained users. Furthermore, interference from S, Se, Sb and Te were also reported when using this test kit [76].

Electrochemistry is therefore an important area of high potential for commercial in-field arsenic detection since it can provide accurate signals and rapid reactions. The results can

be obtained quickly without interferences in many situations, and the testing is unlikely to be harmful to untrained users.

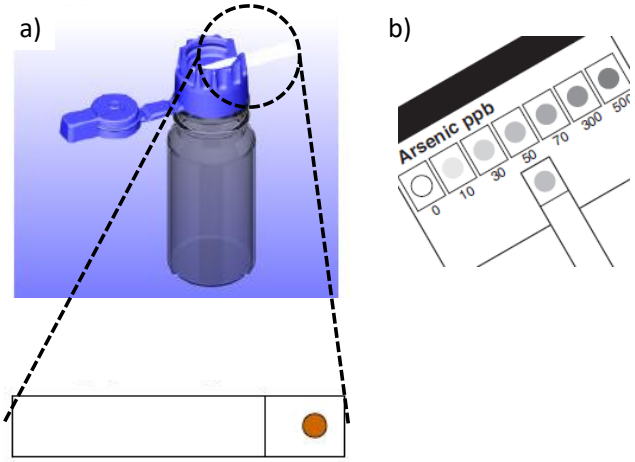

Figure 2.6 Operation of the 'Arsenic Low Range Test Kit' by Hach. a) Detection of arsenic with the test strip after the water sample was added to the vessel and b) reading the colour change on the test strip and comparing with the colour chart. Reprinted with permission from Ref. [76].Hach, Loveland, CO.

2.3. Bibliography

[1]
[10] G.S. Camm, H.J. Glass, D.W. Bryce, A.R. Butcher, Characterisation of a mining-related arsenic-contaminated site, Cornwall, UK, Journal of Geochemical Exploration 82(1-3) (2004) 1-15.
[11] M. Chakraborty, A. Mukherjee, K.M. Ahmed, A review of groundwater arsenic in the Bengal Basin, Bangladesh and India: from source to sink, Current Pollution Reports 1(4) (2015) 220-247.
[12] C.H. Swartz, N.K. Blute, B. Badruzzman, A. Ali, D. Brabander, J. Jay, J. Besancon, S. Islam, H.F. Hemond, C.F. Harvey, Mobility of arsenic in a Bangladesh aquifer: Inferences from geochemical profiles, leaching data, and mineralogical characterization, Geochimica et Cosmochimica Acta 68(22) (2004) 4539-4557.
[13] D. BGS, Arsenic contamination of groundwater in Bangladesh, British Geological Survey (Technical Report, WC/00/19. 4 Volumes). British Geological Survey, Keyworth (2001).
[14] M. Shahid, M. Imran, S. Khalid, B. Murtaza, N.K. Niazi, Y. Zhang, I. Hussain, Arsenic environmental contamination status in South Asia, Arsenic in drinking water and food, Springer2020, pp. 13-39.
[15] I.A. Katsoyiannis, M. Mitrakas, A.I. Zouboulis, Arsenic occurrence in Europe: Emphasis in Greece and description of the applied full-scale treatment plants, Desalin. Water Treat. 54(8) (2015) 2100-2107.
[16] Ž. Romić, M. Habuda-Stanić, B. Kalajdžić, M. Kuleš, Arsenic distribution, concentration and speciation in groundwater of the Osijek area, eastern Croatia, Applied Geochemistry 26(1) (2011) 37-44.

[17] H.E. Jamieson, The legacy of arsenic contamination from mining and processing refractory gold ore at Giant Mine, Yellowknife, Northwest Territories, Canada, Reviews in Mineralogy and Geochemistry 79(1) (2014) 533-551.
[18] L.M. Camacho, M. Gutiérrez, M.T. Alarcón-Herrera, M. de Lourdes Villalba, S. Deng, Occurrence and treatment of arsenic in groundwater and soil in northern Mexico and southwestern USA, Chemosphere 83(3) (2011) 211-225.
[19] K.D. Reid, F. Goff, D.A. Counce, Arsenic concentration and mass flow rate in natural waters of the Valles Caldera and Jemez Mountains region, New Mexico, New Mexico Geology 25(3) (2003) 75-81.
[20] T.J. Sorg, A.S. Chen, L. Wang, Arsenic species in drinking water wells in the USA with high arsenic concentrations, Water Research 48 (2014) 156-169.
[21] M.M. Janković, Arsenic contamination status in North America, Arsenic in drinking water and food, Springer2020, pp. 41-69.
[22] D.Q. Hung, O. Nekrassova, R.G. Compton, Analytical methods for inorganic arsenic in water: a review, Talanta 64(2) (2004) 269-277.
[23] N.R. Council, Chemistry and analysis of arsenic species in water, food, urine, blood, hair, and nails, Arsenic in Drinking Water, National Academies Press (US)1999.
[24] M. Costa, Review of arsenic toxicity, speciation and polyadenylation of canonical histones, Toxicology and applied pharmacology 375 (2019) 1-4.
[25] X. Meng, C. Jing, G.P. Korfiatis, A review of redox transformation of arsenic in aquatic environments, (2003).
[26] X.C. Le, X. Lu, M. Ma, W.R. Cullen, H.V. Aposhian, B. Zheng, Speciation of key arsenic metabolic intermediates in human urine, Anal. Chem. 72(21) (2000) 5172-5177.
[27] A.D. Woolf, Arsenic in tube well water—Bangladesh, 1970s–1990s, History of Modern Clinical Toxicology, Elsevier2022, pp. 45-59.
[28] D.J. Thomas, Arsenic methylation–Lessons from three decades of research, Toxicology 457 (2021) 152800.
[29] M.A. Fazal, T. Kawachi, E. Ichion, Extent and severity of groundwater arsenic contamination in Bangladesh, Water International 26(3) (2001) 370-379.
[30] USEPA, Drinking Water Standard for Arsenic, in: E.P. Agency (Ed.) Environmental Protection Agency, 2001, p. 2.
[31] WHO, Guidelines for drinking-water quality Fourth Edition, WHO chronicle, 2011, pp. 104-8.
[32] E.F.S. Authority, D. Arcella, C. Cascio, J.Á. Gómez Ruiz, Chronic dietary exposure to inorganic arsenic, EFSA Journal 19(1) (2021) e06380.
[33] USDA, China Releases the Standard for Maximum Levels of Contaminants in Foods, United States Department of Agriculture Foring Agricultural Service, 2018.
[34] D. Padmanaban, Water of death: how arsenic is poisoning rural communities in India, 2021. https://www.theguardian.com/global-development/2021/jun/24/water-of-death-how-arsenic-is-poisoning-rural-communities-in-india.
[35] D.A. Skoog, F.J. Holler, S.R. Crouch, Principles of instrumental analysis, Cengage learning2017.
[36] W. Holak, Gas-sampling technique for arsenic determination by atomic absorption spectrophotometry, Anal. Chem. 41(12) (1969) 1712-1713.
[37] T. Näykki, P. Perämäki, J. Kujala, A. Mikkonen, Optimization of a flow injection hydride generation atomic absorption spectrometric method for the determination of arsenic, antimony and selenium in iron chloride/sulfate-based water treatment chemical, Anal. Chim. Acta 439(2) (2001) 229-238.
[38] A. Howard, L. Hunt, Coupled photooxidation-hydride AAS detector for the HPLC of arsenic compounds, Anal. Chem. 65(21) (1993) 2995-2998.

[39] C. Brett, A.M. Oliveira Brett, Electrochemistry: principles, methods, and applications, 1993.
[40] S. Karthikeyan, T.P. Rao, C. Iyer, Determination of arsenic in sea water by sorbent extraction with hydride generation atomic absorption spectrometry, Talanta 49(3) (1999) 523-530.
[41] B. Welz, M. Schubert-Jacobs, Mechanisms of transition metal interferences in hydride generation atomic absorption spectrometry. Part 4. Influence of acid and tetrahydroborate concentrations on interferences in arsenic and selenium determinations, J. Anal. At. Spectrom. 1(1) (1986) 23-27.
[42] J.L. Gómez-Ariza, D. Sánchez-Rodas, I. Giráldez, E. Morales, A comparison between ICP-MS and AFS detection for arsenic speciation in environmental samples, Talanta 51(2) (2000) 257-268.
[43] D. Sanchez-Rodas, W. Corns, B. Chen, P. Stockwell, Atomic fluorescence spectrometry: a suitable detection technique in speciation studies for arsenic, selenium, antimony and mercury, J. Anal. At. Spectrom. 25(7) (2010) 933-946.
[44] G.D. Christian, P.K. Dasgupta, K.A. Schug, Analytical chemistry, John Wiley & Sons2013.
[45] L.V. Rajaković, D.D. Marković, V.N. Rajaković-Ognjanović, D.Z. Antanasijević, The approaches for estimation of limit of detection for ICP-MS trace analysis of arsenic, Talanta 102 (2012) 79-87.
[46] D.C. Harris, Quantitative chemical analysis, 8th ed., Macmillan2010.
[47] X. Liu, W. Zhang, Y. Hu, H. Cheng, Extraction and detection of organoarsenic feed additives and common arsenic species in environmental matrices by HPLC–ICP-MS, Microchem. J. 108 (2013) 38-45.
[48] B.P. Jackson, P.M. Bertsch, Determination of arsenic speciation in poultry wastes by IC-ICP-MS, Environ. Sci. Technol. 35(24) (2001) 4868-4873.
[49] Minimum Wage by Country 2022, 2022. https://worldpopulationreview.com/country-rankings/minimum-wage-by-country.
[50] R. Thomas, Money To Burn: Do you Know What is Costs to Run your Atomic Spectroscopy instrumentation?, 2016. https://www.researchgate.net/publication/330262373_Money_To_Burn_Do_you_Know_What_is_Costs_to_Run_your_Atomic_Spectroscopy_instrumentation.
[51] R. Thomas, Choosing the Right Atomic Spectroscopic Technique for Measuring Elemental Impurities in Pharmaceuticals: A J-Value Perspective, SPECTROSCOPY 33(3) (2018) 10-15.
[52] D. Banik, S.K. Manna, A.K. Mahapatra, Recent development of chromogenic and fluorogenic chemosensors for the detection of arsenic species: Environmental and biological applications, Spectroc. Acta Pt. A-Molec. Biomolec. Spectr. 246 (2021) 19.
[53] Z. Guo, M. Yang, X.-J. Huang, Recent developments in electrochemical determination of arsenic, Curr. Opin. Electrochem. 3(1) (2017) 130-136.
[54] A. Lolic, S. Nikolic, J. Mutic, Optimization of a flow injection system with amperometric detection for arsenic determination, Analytical Sciences 24(7) (2008) 877-880.
[55] L. Bu, T. Gu, Y. Ma, C. Chen, Y. Tan, Q. Xie, S. Yao, Enhanced cathodic preconcentration of As (0) at Au and Pt electrodes for anodic stripping voltammetry analysis of As (III) and As (V), J. Phys. Chem. C 119(21) (2015) 11400-11409.
[56] Y. He, Y. Zheng, M. Ramnaraine, D.C. Locke, Differential pulse cathodic stripping voltammetric speciation of trace level inorganic arsenic compounds in natural water samples, Anal. Chim. Acta 511(1) (2004) 55-61.
[57] A. Profumo, D. Merli, M. Pesavento, Voltammetric determination of inorganic As (III) and total inorganic As in natural waters, Anal. Chim. Acta 539(1-2) (2005) 245-250.

[58] A.O. Simm, C.E. Banks, R.G. Compton, Sonoelectroanalytical detection of ultra-trace arsenic, Electroanalysis (N.Y.N.Y.) 17(4) (2005) 335-342.
[59] P. Salaün, K.B. Gibbon-Walsh, G.M. Alves, H.M. Soares, C.M. van den Berg, Determination of arsenic and antimony in seawater by voltammetric and chronopotentiometric stripping using a vibrated gold microwire electrode, Anal. Chim. Acta 746 (2012) 53-62.
[60] X. Dai, R.G. Compton, Detection of As (III) via oxidation to As (V) using platinum nanoparticle modified glassy carbon electrodes: arsenic detection without interference from copper, Analyst 131(4) (2006) 516-521.
[61] J.H. Luong, E. Lam, K.B. Male, Recent advances in electrochemical detection of arsenic in drinking and ground waters, Analytical Methods 6(16) (2014) 6157-6169.
[62] G.M. Alves, J.M. Magalhães, P. Salaün, C.M. Van den Berg, H.M. Soares, Simultaneous electrochemical determination of arsenic, copper, lead and mercury in unpolluted fresh waters using a vibrating gold microwire electrode, Anal. Chim. Acta 703(1) (2011) 1-7.
[63] E.A. Zakharova, G.N. Noskova, S.G. Antonova, A.S. Kabakaev, Speciation of arsenic (III) and arsenic (V) by manganese-mediated stripping voltammetry at gold microelectrode ensemble in neutral and basic medium, Int. J. Environ. Anal. Chem. 94(14-15) (2014) 1478-1498.
[64] A. Jimana, M.G. Peleyeju, L. Tshwenya, K. Pillay, O.A. Arotiba, Voltammetric Analysis of As(III) at a Cobalt Nanoparticles/Reduced Graphene Oxide Modified Exfoliated Graphite Electrode, Int. J. Electrochem. Sci. 13(11) (2018) 10127-10140.
[65] M. Yang, X. Chen, J.H. Liu, X.J. Huang, Enhanced anti-interference on electrochemical detection of arsenite with nanoporous gold in mild condition, Sens. Actuator B-Chem. 234 (2016) 404-411.
[66] T. Gu, L. Bu, Z. Huang, Y. Liu, Z. Tang, Y. Liu, S. Huang, Q. Xie, S. Yao, X. Tu, Dual-signal anodic stripping voltammetric determination of trace arsenic (III) at a glassy carbon electrode modified with internal-electrolysis deposited gold nanoparticles, Electrochem. Commun. 33 (2013) 43-46.
[67] T.J. Davies, R.R. Moore, C.E. Banks, R.G. Compton, The cyclic voltammetric response of electrochemically heterogeneous surfaces, J. Electroanal. Chem. 574(1) (2004) 123-152.
[68] E. Kätelhön, R.G. Compton, Unscrambling illusionary catalysis in three-dimensional particle-modified electrodes: Reversible reactions at conducting particles, Appl. Mater. Today 18 (2020) 100514.
[69] M.J. Sims, N.V. Rees, E.J. Dickinson, R.G. Compton, Effects of thin-layer diffusion in the electrochemical detection of nicotine on basal plane pyrolytic graphite (BPPG) electrodes modified with layers of multi-walled carbon nanotubes (MWCNT-BPPG), Sens. Actuators, B 144(1) (2010) 153-158.
[70] S.-H. Shin, H.-G. Hong, Anodic stripping voltammetric detection of arsenic (III) at platinum-iron (III) nanoparticle modified carbon nanotube on glassy carbon electrode, Bull. Korean Chem. Soc. 31(11) (2010) 3077-3083.
[71] R. Kempegowda, D. Antony, P. Malingappa, Graphene–platinum nanocomposite as a sensitive and selective voltammetric sensor for trace level arsenic quantification, Int J Smart Nano Mater 5(1) (2014) 17-32.
[72] H.-H. Chen, J.-F. Huang, EDTA assisted highly selective detection of As3+ on Au nanoparticle modified glassy carbon electrodes: facile in situ electrochemical characterization of Au nanoparticles, Anal. Chem. 86(24) (2014) 12406-12413.
[73] L. Xiao, G.G. Wildgoose, R.G. Compton, Sensitive electrochemical detection of arsenic (III) using gold nanoparticle modified carbon nanotubes via anodic stripping voltammetry, Anal. Chim. Acta 620(1-2) (2008) 44-49.
[74] M. Yang, P.H. Li, W.H. Xu, Y. Wei, L.N. Li, Y.Y. Huang, Y.F. Sun, X. Chen, J.H. Liu, X.J. Huang, Reliable electrochemical sensing arsenic(III) in nearly groundwater pH based on

efficient adsorption and excellent electrocatalytic ability of AuNPs/CeO2-ZrO2 nanocomposite, Sens. Actuator B-Chem. 255 (2018) 226-234.
[75] F. Bird, The gutzeit test for arsenic, Analyst 26(July) (1901) 181-188.
[76] Hach, Arsenic Low Range Test Kit. https://ca.hach.com/arsenic-low-range-test-kit/product-details?id=14533981664.

Chapter 3. **Experimental**

In this chapter, the general experimental details are introduced, including chemical reagents, and instrumentation both electrochemical and non-electrochemical. Specific descriptions of each experiment can be found in the Experimental sections of Chapters 4 – 7.

3.1. Chemicals and Reagents

All chemicals and reagents involved in this thesis are used as received without further purification and listed in Table 3.1. All solutions were prepared with deionized water (resistivity: 18.2 MΩ cm, Millipore, 298 K).

Table 3.1 List of chemicals, reagents and materials mentioned in this thesis

Chemical	**Formula**	**Purity**	**Supplier**
Pt nanoparticles (30 nm in diameter) [1]			NanoComposix
Sodium (meta) arsenite [2]	$NaAsO_2$	99%	Fluka
Copper(II) sulphate pentahydrate [3]	$CuSO_4 \cdot 5H_2O$	99%	Sigma-Aldrich
Potassium chloride [4]	KCl	99.5%	Sigma-Aldrich
Sulphuric acid [5]	H_2SO_4	98%	Fisher Scientific
Au nanoparticles (5 nm in diameter) [6]			Sigma-Aldrich

Sodium hydrogen arsenate heptahydrate [7]	$Na_2HAsO_4 \cdot 7H_2O$	98%	Alfa Aesar
Hexaaminеruthenium(III) chloride [8]	$[Ru(NH_3)_6]Cl_3$	98%	Sigma-Aldrich
Nitrogen [9]	N_2	99.99%	BOC Gases plc

Note that the Pt nanoparticles and Au nanoparticles were dispersed in 2 mM sodium citrate as purchased from the supplier and used without any further purification or dilution.

3.2. Electrochemical Instrumentation

All electrochemical experiments were performed in a Faraday cage thermostatted at 298 ± 0.5 K using a μAutolab type III potentiostat (Metrohm, NL). A standard three-electrode system was employed for all measurements which includes a reference electrode, a working electrode and a counter electrode. For the reference electrode, either a saturated calomel electrode (SCE, Radiometer, DK) or a mercury-mercurous sulfate electrode (MSE, BASi, USA) was used. The SCE has a potential of + 0.24 V vs. the standard hydrogen electrode (SHE) [10], and the solution in the electrode was saturated KCl solution (4.0 M). The MSE has a potential of + 0.65 V vs. the standard hydrogen electrode (SHE) [10], and the solution used in the reference electrode was saturated K_2SO_4 solution (1.45 M). For the working electrode, either a glassy carbon electrode (GCE, diameter of 3.00 ± 0.01 mm, geometric area of 0.07 cm^2, BAS technical, UK), a platinum macroelectrode (diameter of 1.66 ± 0.01 mm, geometric area of 0.02 cm^2, BASi, USA) or a gold macroelectrode (diameter of 1.60 ± 0.01 mm, geometric area of 0.02 cm^2, BASi, USA) was employed. For counter electrodes, a platinum wire or a carbon rod was used.

The working electrodes, Pt macroelectrodes, Au macroelectrodes and GCEs were all polished before electrochemical measurements. The electrodes were mechanically polished with alumina slurries of decreasing particle sizes of 1.0, 0.3 and 0.05 μm (Buehler, USA) on soft polishing pads (Buehler, USA), then followed with a water rinse and dried with N_2. The detailed methods for dropcasting onto the polished electrodes are given in Chapters 4, 5 and 6.

3.3. Non-electrochemical instrumentation

The surface of electrodes were characterized with an optical microscope and/or scanning electron microscope (SEM) after drop casting nanoparticles. The optical microscope was used in Chapters 4 and 5, and SEM was used in Chapter 4.

3.3.1. Optical Microscope

All images were obtained using an optical microscope, Zeiss Axio Examiner, A1 Epifluorescence microscope (Carl Zeiss Ltd., UK). The objective lens used was a 10× air objective (NA = 0.5, EC Plan-Neofluar) and the light source employed in this study was a LQ-HXP 120 V lamp. Incident light reaching the surface of the GCE was partly reflected to the camera through the objective lens and the image of the electrode was obtained by a black & white ORCA-Flash 4.0 digital CMOS camera (Hamamatsu, JP). The resolution of the image was 4-megapixel. The images taken from the optical microscope were with the help from Dr. Minjun Yang (Compton Group).

3.3.2. Scanning Electron Microscope

The Scanning Electron Microscopy (SEM) images were obtained using a Zeiss Sigma 300 FEG-SEM with an accelerating voltage of 2.0 kV. Prior to the measurements, the particles

were suspended in water and drop-casted onto a cleaned glassy carbon stub, which was subsequently dried under vacuum. SEM images were made by Dr. Minjun Yang (Compton Group).

3.4. References

[1] NanoComposix, NanoXact Platinum Nanoparticles – Bare (Citrate). https://nanocomposix.com/collections/material-platinum/products/nanoxact-platinum-nanoparticles-bare-citrate?variant=39660083183705.
[2] Merck, Sodium (meta) arsenite. https://www.sigmaaldrich.com/GB/en/product/aldrich/s7400.
[3] Merck, Copper(II) sulfate pentahydrate. https://www.sigmaaldrich.com/GB/en/substance/copperiisulfatepentahydrate249697758998?gclid=Cj0KCQjw0umSBhDrARIsAH7FCockOnIB7bYLCjdElr8hEyvfex7lstJnWEHWhBw1GDWqjDhYFNu5uXcaAuwoEALw_wcB.
[4] Merck, Potassium chloride. https://www.sigmaaldrich.com/GB/en/product/sigald/p3911.
[5] FisherScientific, Sulfuric Acid. https://www.fishersci.co.uk/gb/en/products/I9C8KA5R/sulfuric-acid.html.
[6] Merck, Gold nanoparticles. https://www.sigmaaldrich.com/GB/en/product/aldrich/741949.
[7] Merck, Sodium hydrogen arsenate heptahydrate https://www.sigmaaldrich.com/GB/en/product/sigald/s9663?gclid=Cj0KCQjw0umSBhDrARIsAH7FCodEnH9UWFtlreiIfhmfObbHKGU8i8EkoBsAV9gZb8fjrgq8X5PSoWQaAiwaEALw_wcB.
[8] Merck, Hexaammineruthenium(III) chloride https://www.sigmaaldrich.com/GB/en/product/aldrich/262005?gclid=Cj0KCQjw0umSBhDrARIsAH7FCocK6zJTQsg5IHw6oAT08cxpkIxwafDpYrO5n9ErQOVKk2WqkL01MQkaAt1sEALw_wcB.
[9] B.g. PLC, Nitrogen (Oxygen Free) 230bar Cylinder. https://www.boconline.co.uk/shop/en/uk/nitrogen-(oxygen-free)-size-x-44-x?gclid=Cj0KCQjw0umSBhDrARIsAH7FCoc6AHgcgmXPF9AoZ7fgLtyez-lWajf94zXS31aPhJ4AQLAY2JBHI3AaAvNXEALw_wcB.
[10] A. J. Bard, L.R. Faulkner, Electrochemical Methods: Fundamentals and Applications, 2nd ed., John Wiley & Sons, Inc, New York, 2001.

Chapter 4. **Nanoparticle modified electrodes: the response of drop casted surfaces**

'Drop casting' is widely used to prepare the surface of chemically modified electrodes since it is easy and rapid to implement. The modified layers are often composed of nanoparticles and used for electro-catalysis notably for chemical sensing as well as materials evaluation. However, meaningful voltammetry requires the formation of uniformly modified surfaces for which the coffee ring and its related effects, which are overviewed below, present a significant limitation on the reproducibility of the drop casted surfaces. Approaches for amelioration of the coffee ring effect by various methods are discussed first. Then the morphology of electrodes modified by drop casting layers of platinum nanoparticles (PtNPs) is investigated and shown to exhibit significant heterogeneity of 'coffee rings' formed after evaporation of the carrier solvent. The variation of the heterogeneity with total average coverage is studied and the consequences for quantitative analytical voltammetry assessed, specifically the oxidation of aqueous As(III) using PtNPs modified electrodes. The observed voltammetry is related to the observed structure and the use of such modified electrodes, without concomitant microscopic surface characterisation, is caveated.

The work presented in this chapter has been published in Electrochemistry Communications [1] and ChemElectroChem [2] as a co-first author with Archana Kaliyaraj Selva Kumar (Compton group), and was carried out in collaboration with Dr. Danlei Li (Compton group) who helped with the interpretation of the results, and Dr. Minjun Yang (Compton group) who assisted with the optical microscopic images and obtaining SEM images. This chapter is a fundamental study on drop cast method, and questions the reliability of

electroanalysis especially if ring-like patterns of the drop casted particles are seen on the surface. The results have generic significance for the work reported in Chapters 5 and 6.

4.1. Introduction

To enhance the sensitivity and selectivity, a huge search for improved electrochemical sensors using the amperometric method has been made leading to an astonishing diversity of modified electrodes [3-10]. One approach has become ubiquitous over the last two decades and involves the modification of the surfaces of macro-electrodes with a layer of particles. Although doped diamond [11-13] and single-crystal [14-16] forms are also used, the substrates are also often made of carbon in other forms, such as glassy carbon or graphite [17-22] due to their easy availability and, often, low cost. The modification of electrode surfaces with drop-casted layers of particles such as nanoparticles represents a popular approach to amperometric electrochemical sensing [23-27]. The aim of the modification and the creation of particle modified electrodes (PMEs) is usually to impart greater apparent electrocatalytic behaviour to the surface so that the oxidation or reduction of the target analyte occurs at lower potentials, and ideally with larger currents, than seen at the ‘naked’ (or ‘bare’) electrode so minimising the impact of otherwise interfering species and offering greater analytical sensitivity.

Although the extent of useful enhancement of the sensitivity of electrochemical analytical detection on PMEs has been questioned [28, 29], this chapter raises a different concern from an experimental perspective. In particular we note that the overwhelmingly popular approach for the preparation of PMEs is via the method of drop casting (Figure 4.1). In this method, a drop of liquid containing a suspension of the particles of interest is first deposited (literally ‘drop casted’) on the surface of the electrode to be modified, ideally exclusively confined to the conductive electrode without, for example, over-spillage onto the insulating surround. Then with the aid of an air flow the solvent is evaporated leaving the

particles remaining on the electrode, and the modification of electrode surface via drop cast is then completed. The ease and simplicity of the method explains it very wide use.

If the particles are to act via an electro-catalytic mechanism then a surprisingly small number of particles need to disperse over the electrode surface to ensure a diffusional response that, in terms of which potential the electrode process takes place, is characteristic of the particles and not that of the underlying substrate electrode. In other words, that the catalytic signal is observed at lower potentials than would be seen on the substrate and is such that all the material diffusing to the electrode surface is consumed at the particles before a voltammetric sweep reaches the potential required for reaction on the underlying electrode.

Specifically, theory shows that for measurements of solution phase species on a timescale, t, that for strong overlap the particles need to be within a distance of $\delta = (6Dt)^{1/2}$ of one another where D is the analyte diffusion coefficient [30]. This length corresponds to the root mean square distance diffused (in 3-dimensions) in the time t. Then the PME signal is dominated by the particles, not the substrate. Typically for a species with a diffusion coefficient of 10^{-5} cm^2 s^{-1} for a voltammetric timescale[1] of a few seconds the size of δ can be as large as of the order of ca 100 microns. Hence for a random array of fully dispersed particles a coverage of say just 10^5 particles per cm^2 may thus suffice. In analytical practice, however, much larger amounts are deposited partly because in the case of sparse coverages it cannot be guaranteed that all particles are in electrical contact with the substrate or are not aggregated [31-33]. In the case of PMEs which function via adsorptive pre-concentration then thick layers are essential to provide some enhancements of signal although the conflicting demands of both a large

[1] The “voltammetric timescale” is the time of a voltammetric sweep encompassing the peak resulting from the electrode reaction of interest. The timescale of the sweep is of the order of magnitude of (RT/vF) where v is the voltage scan rate.

strong adsorption and the rapid release of the accumulated analyte for electrochemical detection are not always appreciated [29].

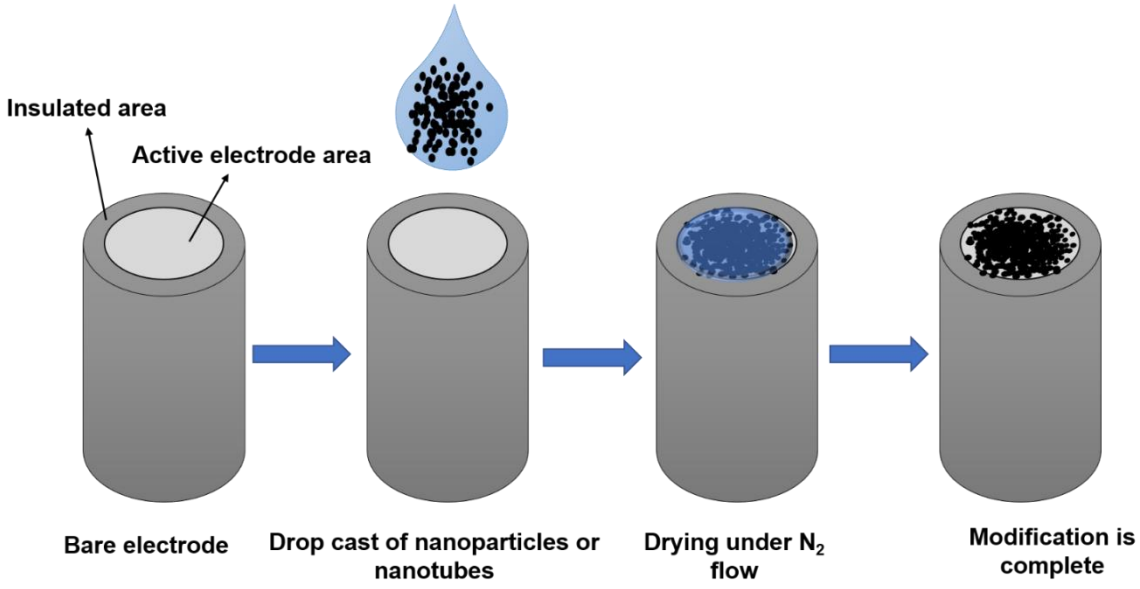

Figure 4.1 A schematic showing the drop casting of nanoparticles or nanotubes onto an electrode.

From an experimental perspective, regardless of whether sub-monolayer or thick layers of particles are desired, it is important to know if the extent to which the electrode has been homogeneously modified (or not) when using the drop casting approach for fabrication. For potentials at which catalysis takes place on the particles, the modified electrode will only exhibit linear diffusion to its geometric area in the absence of macroscopic patches of naked unmodified electrode. Here the size of the patches that must be avoided implies a larger size compared to the diffusion distance δ introduced above via the Einstein equation [30].

In this chapter, first, we describe and then consider the physical basis for the so-called coffee ring effect and related issues as well as approaches for their mitigation; then, we explore the extent to which drop casting can result in reproducible surfaces and the extent to which spatial heterogeneity is induced on the drop casted surface [34].

4.2. Origin of the coffee ring effect

The evaporation of sessile droplets containing suspended particles under ambient conditions often forms a ring-like pattern which is macroscopic in size and visible by eye upon drying. This phenomenon was notably observed, highlighted and interpreted by Deegan *et al*. [35], in respect of coffee stains, where the periphery of the ring was seen to be concentrated with the non-volatile solute particles in contrast to the centre of the stain: this phenomenon has been labelled as the "coffee ring effect" (CRE).

The physical requirements to observe a ring pattern originate in the 'pinning' of the contact line at the edge of the droplet by surface tension forces [36]. Contact line pinning restricts any further spreading of the solvent and a radial outward capillary flow of the solvent from the centre is observed towards the contact line, driven by evaporation since the evaporation is greatest at the edge which is more 'ventilated' than the centre of the drop [36]. This is due to a larger free space at the edge of the droplet which induces the evaporation of more solvent molecules than in the centre. Since the evaporation flux at the periphery is comparatively more than at the centre of the droplet this leads to greater solvent loss at the contact line. The loss is compensated by a flow of solvent from the centre along with the non-volatile solute particles. The rate of local evaporation is, therefore, a major factor controlling the radial outward flow of the solution. The magnitude of the evaporation flux depends on the radius, r, of the droplet, height, h, of the droplet above the centre and the contact angle $\boldsymbol{\Theta_r}$ with the velocity of the particles reflecting the spatial heterogeneity of the evaporative flux (Figure 4.2). The coffee ring effect is noted for its malign consequences related to the disruption of otherwise uniform distribution of particles for example importantly in ink-jet printing [37-39], functional coating with ordered structures functional nanomaterials and in electronics [40-42].

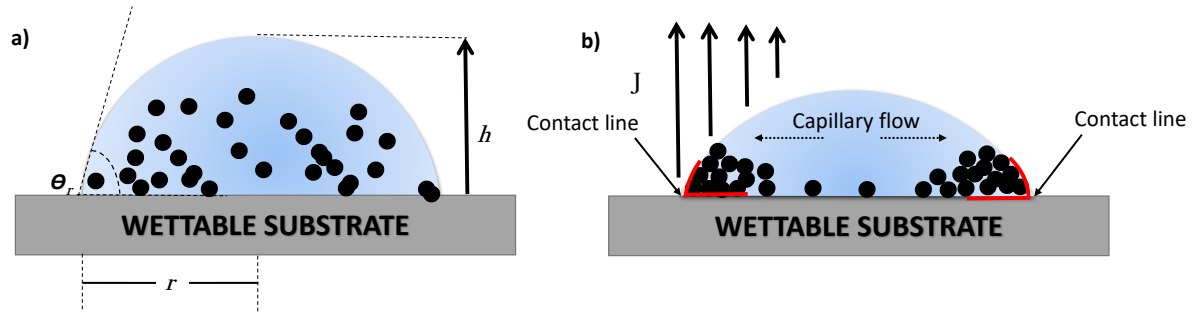

Figure 4.2 A scheme showing a) a droplet containing particles on a solid substrate and b) capillary flow from centre to the edge keeping the contact line fixed during evaporation. Particles in the droplet are moved to the edge due to the capillary flow. h = height of droplet; Θ_r = contact angle; r = radius of the droplet; J = evaporation flux.

As noted above the consequence of the coffee ring effect is that the particles tend to form ring-like patterns on the surface. Typical observations are shown in Figure 4.3, where Anyfantakis *et al.* studied negatively charged polystyrene (PS) particles coated with acrylic acid (AA) [43]. One drop of a PS particle suspension was casted onto the substrate and dried over 300 s (Figures 4.3a, b and c). During the evaporation of a 0.5 µL of droplet with PS-AA particles, weak aggregation at the liquid-gas (LG) interface was observed (Figures 4.3a and d) [43]. The image taken at 245 s showed that the PS-AA particles became packed at the edge of the droplet when most of the solvent had evaporated (Figure 4.3e) and the ring-like pattern could be observed clearly (Figure 4.3b) on complete evaporation. This again shows that along with the solvent evaporation at the droplet edge, there is a flow of solvent with the particles from the centre towards the edge. The dry deposit was thus a classic coffee ring pattern (Figures 4.3c and f).

In another insightful study, Park and Moon [37] used silica microspheres dispersed in water-based ink and a coffee ring was formed after evaporation of the droplet (Figure 4.3g). SEM images of both the edge (Figure 4.3g middle) and the centre (Figure 4.3g bottom) were recorded. Most of the microspheres became agglomerated and stacked at the edge due to the evaporatively driven capillary flow (Figure 4.3g middle). At the same time there were much fewer particles at the centre of the dried droplet (Figure 4.3g bottom).

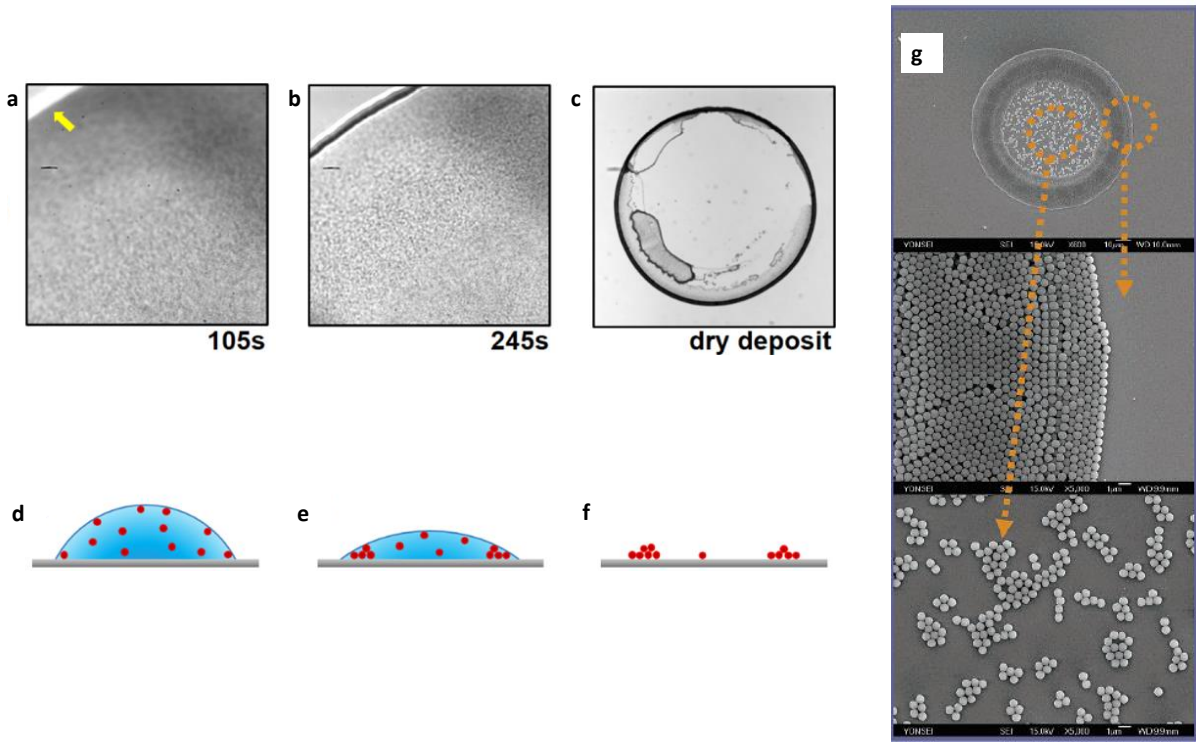

Figure 4.3 a) – c) Snapshots of a droplet containing a suspension of PS-AA (see text) particles during evaporation and imaged at 105s (a), 245s (b), and after full drying deposit (c). The scale bars are 500 μm for the high- (a and b) and low-magnification (c) images. d) – f) cartoons of the PS-AA droplet during evaporation at 105s (d), 245s (e), and dry deposit (f). Reprinted with permission from Anyfantakis et al. Langmuir. 2015;31(14):4113-20. Copyright (2015) American Chemical Society. Ref.[43]. g) SEM images of deposit patterns composed of the silica microspheres produced by ink-jet printing a single ink-jet droplet of water-based ink. The ink concentration was 4 vol% and the substrate was a hydrophilic Si wafer. Reprinted with permission from Park and Moon. Langmuir. 2006;22(8):3506-13. Copyright (2006) American Chemical Society. Ref.[37].

4.3. Approaches to the amelioration of the coffee ring effect

The distribution of non-volatile solute particles on the substrate is governed by various factors as discussed above. Many approaches have been taken with the aim of supressing the coffee ring effect (CRE) to obtain a more uniform distribution of solute particles. These methods are aimed in altering or affecting the capillary flow, and/or unpinning the contact line and preventing the transport of solute particles to the edge of the droplet. The following are some methods which have proven effective in reducing the coffee ring effect in specific cases.

4.3.1. Super hydrophobic surfaces

Super hydrophobic surfaces can help in the suppression of the CRE. One mechanism is by reducing the effectiveness of the contact line pinning by making it slip over the hydrophobized surfaces. The slipping of the contact line pinning induces an inward circulatory flow of the solute particles forming a more homogeneous deposition. Both chemical and physical modifications are involved in making a surface super-hydrophobic but can be prohibitively expensive for routine uses [44-48] as well as changing the chemical nature of the surface, which may be important if the latter is to be an electrode.

In a study by Moon *et al.*, octadecyltrichlorosilane (OTS) was applied onto a silica substrate to create a hydrophobic surface [44]. The OTS-modified self-assembled monolayers (SAMs) produced a Wenzel (Figure 4.4a) or Cassie (Figure 4.4b) state. Thus, when a single ink droplet was evaporated on the substrate, a circulatory fluid flow was generated, which was opposite to the capillary flow, and reduced the coffee ring effect by transporting particles back to the centre. Similarly Jiang *et al.*, deposited oil ink onto a TiO_2 substrate [47], forming a super-hydrophobic surface. When a latex droplet was evaporated on the surface, the inward circulatory flow again counteracted the outward capillary flow, pressed and a homogeneous surface was produced (Figure 4.4c). These two examples very clearly demonstrate that chemically modified hydrophobic surfaces can reduce the coffee ring effect but are probably not suitable for general electrochemical applications.

Meanwhile, some physical (as opposed to chemical) modification methods have also been applied to create a super hydrophobic surface. Snoeijer's and Yang's group used silicon pillar arrays to avoid the coffee ring effect [45, 46]. The array increased the roughness of the surface creating either Wenzel or Cassie states for supported droplets. When a colloid-

containing droplet was evaporating on the microarrays, the contact line was unpinned due to the low surface tension and the particles aggregated in the centre by circulatory flows.

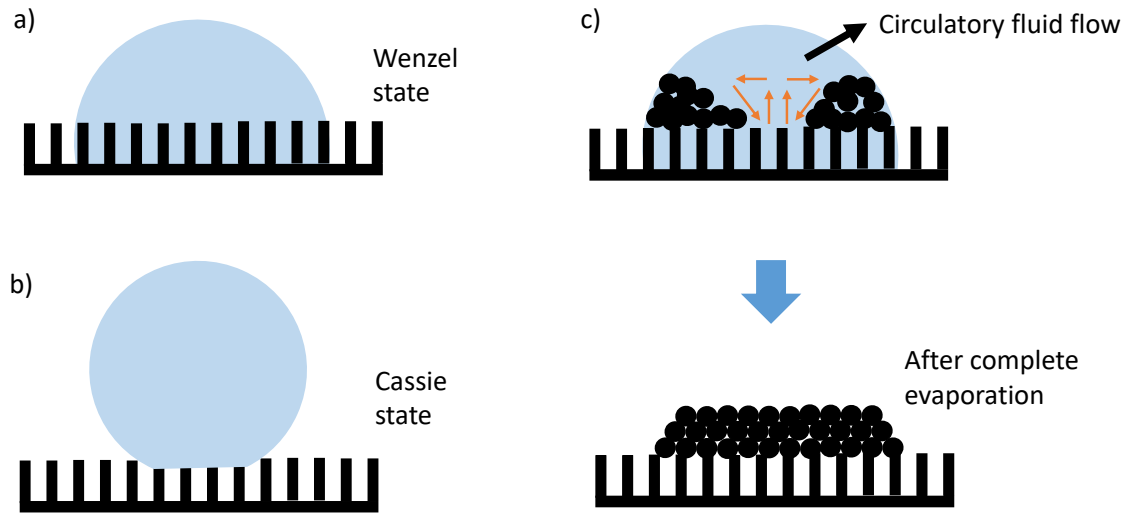

Figure 4.4 A schematic diagram showing a) a Wenzel state, and b) a Cassie state of a hydrophobic surface, and c) the circulatory fluid flow that reduces the coffee ring effect so generating a more uniform distribution of particles after evaporation.

In general, the coffee ring effect is either reduced or suppressed on super hydrophobic surfaces.

4.3.2. Electrowetting

The method of electro-wetting again involves de-pinning of the contact line. Although, super hydrophobic surfaces prevent the pinning of the contact line by slipping, at higher concentrations, the solute particles often stick firmly to hydrophobic substrates [49, 50]. In such cases, electro-wetting may succeed wherein the sessile droplet is deposited on an electrode and a voltage is applied between the droplet and the electrode. This overcomes the pinning forces at the contact line, making it more mobile and not static [50-52].

Eral *et al.*, studied how to tune the contact line and contact angle by changing the voltage used [49]. Drops of an aqueous polystyrene suspension containing 10 mM LiCl were deposited onto glass substrates with conductive indium-tin-oxide (ITO) layers covered with an

insulating 5 µm thick layer of SU8 resist. The latter is an epoxy-based negative photoresist which becomes cross-linked due to exposure to UV. The drops were electrically grounded via immersing a 50 µm diameter Pt wire near the bottom of the drop. AC voltages (200 V_{rms}) with variable frequencies of 6 Hz – 100 kHz were applied to the ITO layer. A scheme of the setup is shown in Figure 4.5a. The ring-like pattern could be observed clearly without electro-wetting (Figure 4.5b) but the resulting deposit shrank in size when the AC current was applied (Figures 4.5c and d). However, if the frequency reached 100 kHz, the pattern after evaporation became as shown in Figure 4.5e, showing that the electro-wetting could usefully reduce and suppress the coffee ring effect.

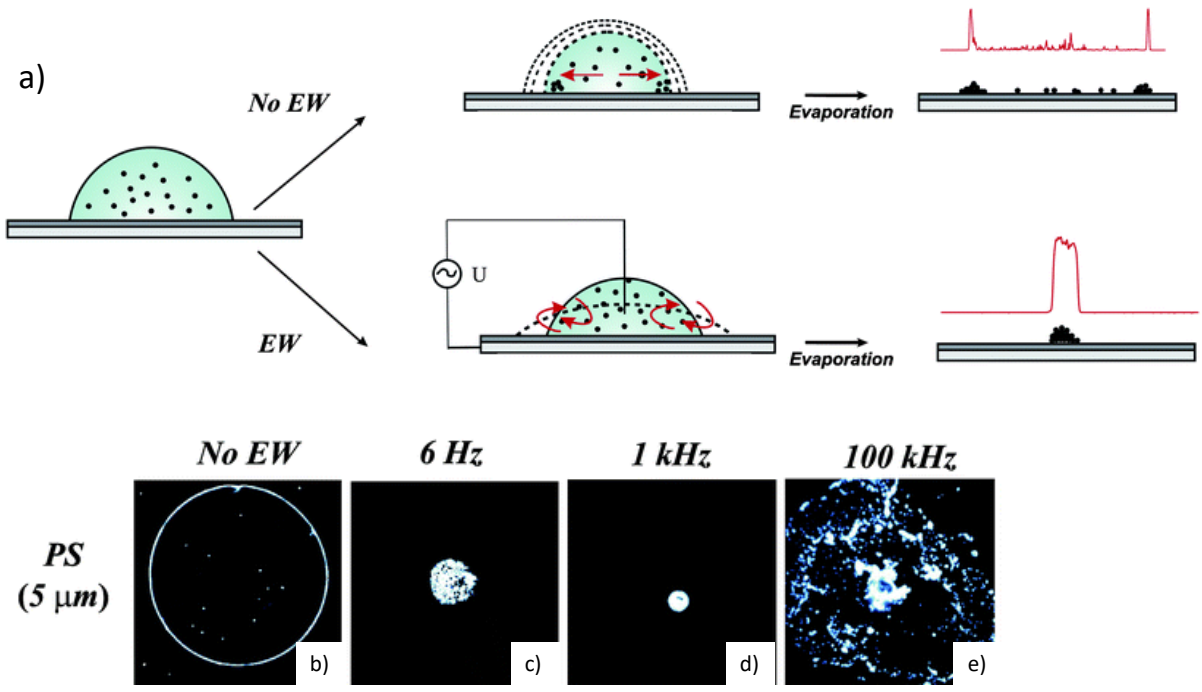

Figure 4.5 a) Schematic representation of the drop evaporation process. Top row represents evaporation without electrowetting and with contact line pinning. Bottom row shows the process with electrowetting and mobile contact lines. b) – e) Suppression of coffee ring effect illustrated for PS particles at three frequency regimes (6 Hz, 1 kHz and 100 kHz). Reprint with permission from Royal Society of Chemistry 2011. Ref. [49].

4.3.3. Acoustics

The introduction of surface acoustic waves (SAWs) into the evaporating droplet can form both standing acoustic waves and standing capillary waves (Figure 4.6). These waves

generate standing wave patterns with nodes such that particles are trapped in the nodal regions of standing acoustic pressure waves with the distance between two adjacent nodal regions corresponding to one-half wavelength of the standing acoustic pressure waves (76 µm) as shown in Figure 4.6. Thus, for example, Cooper *et al* studied the suppression of the coffee ring effect by surface acoustic waves (SAWs) [53]. Polystyrene particles or silica particles of diameter ranging from 0.1 to 10 µm were dispersed in water and a droplet (2 µL) to evaporate when coupled with a SAWs of 9.7 MHz frequency and 1 W of power. After a few seconds, the majority of the particles were trapped in the nodal regions of capillary waves and accumulations of particles appeared at the liquid-gas interface [53]. This pressure gradient at the interface induced the local flow of the solute particles and trapped the particles on the substrate rather than moving toward the edge. The drag force exerted on the particles by the capillary flow was inferred to be less than the acoustic force, therefore no transport of the particles occurred. This physical phenomenon is independent of the properties of the particles and the solvent [54, 55].

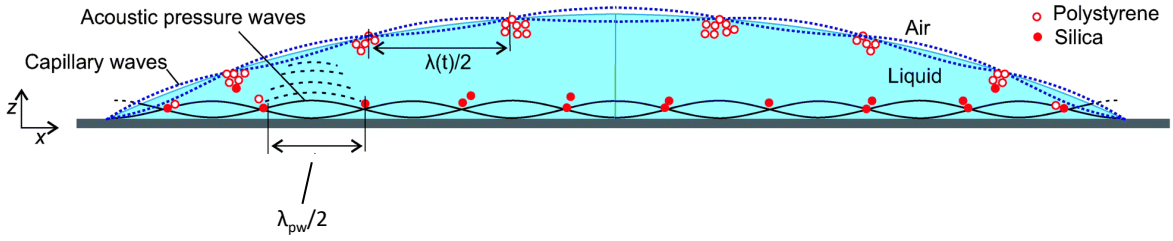

Figure 4.6 Schematic illustration of a droplet excited by SAW. Abbreviation: λ_{PW}: wavelength of acoustic pressure waves, λ(t): wavelength of capillary waves, SAW: surface acoustic waves. Reprinted with permission from Royal Society of Chemistry 2015. Ref.[53].

The coffee ring effect is largely unavoidable if the drop casting from aqueous suspension onto the surface of an electrode is made without electrowetting or the application of acoustic waves. The following experiments investigate if the CRE affects the experimental results seen in electroanalysis. For this purpose the electrochemistry of As(III) solutions with

Pt nanoparticle modified electrodes is investigated as a preliminary to the reports in Chapters 5 and 6.

4.4. Experimental

Reagents and instrumentation: Pt nanoparticles (0.05 mg/mL, 30 nm in diameter) dispersed in 2 mM sodium citrate were supplied by NanoComposix (San Diego, United States). Sodium (meta) arsenite ($NaAsO_2$, 99%) was purchased from Fluka (Buchs, Switzerland). The obtained materials were used without further purification.

Electrochemical measurements were conducted with a standard three electrode system in a Faraday cage at 298 K. Cyclic voltammetric measurements with PtNP modified GC electrode were recorded with an Autolab PGSTAT 30 computer-controlled potentiostat (EcoChemie, Netherlands) and CNT modified GC electrodes experiments were performed using a μAutolab II potentiostat (Metrohm-Autolab BV, Utrecht, Netherlands). The computer software, GPES v.4.9 (Metrohm Autolab B.V., NL) was used to control and measure all electrochemical experiments. A glassy carbon electrode (GCE, diameter of 0.15 cm, geometric area of 0.07 cm^2, BAS technical, UK) served as a working electrode, and a graphite rod was applied as a counter electrode with a saturated calomel electrode (SCE, Radiometer, Copenhagen, Denmark) served as the reference electrode completed the three electrode system.

Preparation of PtNP modified GC electrodes: The GC electrode was successively polished with 1 μm, 0.3 μm and 0.05 μm sized alumina on a polishing pad then rinsed with deionized water prior to experiments. A Pt nanoparticle suspension (see above) was drop casted onto the surface of GC electrode with micropipette and dried with gentle N_2 flow for at least 15 minutes.

The 30 nm Pt nanoparticles have been previously characterised by HR-CTEM [56] and shown to be an aggregate of much smaller nanoparticles of approximate diameter 3 nm (Figure 4.7) [56]. Such morphology is typical of Pt nanoparticles grown in the solution phase [56, 57] and is potentially advantageous in the determination of arsenic because of their high active surface area [56-58].

Optical microscopy and imaging:

Optical measurements were made on a Zeiss Axio Examiner, A1 Epifluorescence microscope (Carl Zeiss Ltd., Cambridge U.K.) using a 10× air objective (NA = 0.5, EC Plan-Neofluar). The light source was a LQ-HXP 120V lamp. In this study, the (epifluorescence) microscope used is that of a surface-reflective equivalent by removing the emission filter from the filter set (MDF-FITC 475 ± 35nm, Thorlabs). This allows a fraction of the incident light, reflected by the electrode surface, to be transmitted to the camera and thus allowing the surface of the opaque glassy carbon electrode to be optically imaged. Image acquisition was provided by a black & white ORCA-Flash 4.0 digital CMOS camera (Hamamatsu, Japan), providing 16-bit images with 4-megapixel resolution. The images taken from the optical microscope were with help from Dr. Minjun Yang (Compton Group).

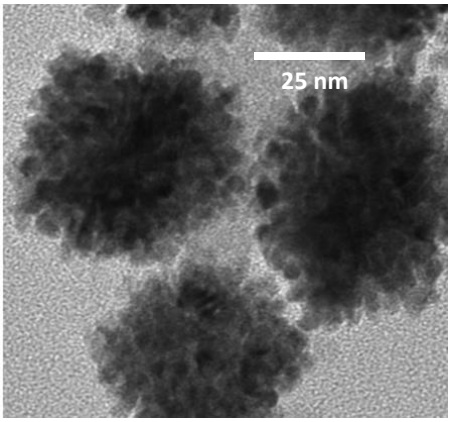

Figure 4.7 HR-CTEM image showing how the overall particle structure comprises of an aggregate of smaller substituent crystallites. Reprinted with permission from Yu et al. Copyright Royal Society of Chemistry 2019.[56]

Scanning Electron Microscopy:

The Scanning Electron Microscopy (SEM) images were obtained using a Zeiss Sigma 300 FEG-SEM with an accelerating voltage of 2.0 kV. Prior to the measurements, the particles were suspended in water and drop-casted onto a cleaned glassy carbon stub, which was subsequently dried under vacuum. SEM images were made by Dr. Minjun Yang (Compton Group).

4.5. Results and discussion

In this section we present and discuss first the responses expected from different types of drop casted surfaces and then second experimental results obtained for the drop casting of an electrode with Pt nanoparticles and the use of the particle modified electrode (PME) for the detection of Arsenic (III) in aqueous solution.

4.5.1. Drop casted surface

For drop casted surface, there are two limiting types of surface which may be formed as a result of drop casting. These are discussed below as Case A and Case B:

Case A This case is that of a thick, porous layer of conductive particles [59] on a substrate electrode (Figure 4.8a). If the layer is sufficiently substantial to obstruct diffusional analyte access to the latter, the modified electrode shows a response due to both the semi-infinite diffusion of the analyte from bulk solution to the surface of the porous layer (at which electrocatalytic effects of the modifier may operate) and due to electrolytic discharge within the pores of the layer. The latter often resembles that of thin layer diffusion [60-62] and the relative contributions of the two types of mass transport depend on the porosity of the

modifying layer and its extent (thickness). The thin layer responses have analytical value in that, in the case of electrochemically irreversible targets, the voltammetric peak potentials are shifted closer to the reversible formal potential of the redox couple of interest [62]. That said in the case of close packed layers of nanoparticles the time response of the electrolysis of the occluded material is too short to be of value because of the tiny physical size of the pores leading to their very rapid depletion [59].

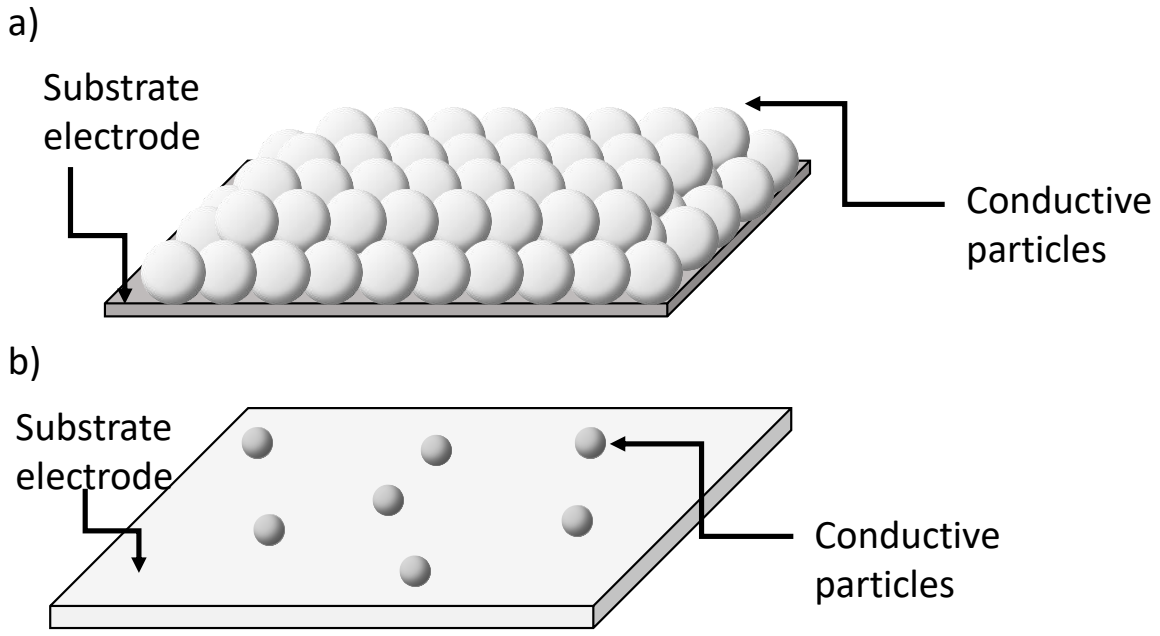

Figure 4.8 Schematic representation of a substrate electrode and drop cast particles illustrating Cases a) A and b) B (see text).

Case B A sub-monolayer coverage of conductive particles on an electrode surface constitutes a 'spatially heterogeneous electrode' [63] and forms Case B (Figure 4.8b). Analytically, it is desirable that the particles show a greater electro-catalytic activity than the substrate. In this case the average inter-particle separation, d, controls the observed voltammetry. Specifically, the response is clear in the light of the Einstein equation [30] for the distance diffused by an analyte in a certain time. It can be readily understood that if $d << (6Dt)^{1/2}$, where D is the analyte diffusion coefficient and t is the voltammetric timescale ($t \sim RT/vF$; v is the voltage scan rate) then all the analyte diffusing to the geometric area of the electrode undergoes

electrolysis at the particles. This, because of the catalytic properties of the particles, occurs at a lower potential than required on the less electro-catalytic substrate. Alternatively, if d >> $(6Dt)^{1/2}$ the exposed areas of the substrate electrode contribute to the voltammetric response.

4.5.2. Pt nanoparticles modified glassy carbon electrodes for As(III) detection

A Pt nanoparticle modified glassy carbon (GC) electrode was applied for Arsenic (III) detection. The nanoparticles were dispersed in an aqueous solution of 2 mM sodium citrate. A selected volume of the Pt nanoparticle suspension droplet (0.05 µg to 15 µg of Pt) was drop casted on the surface of GC electrode and dried with N_2 flow. The Pt particles were aggregates of much smaller nanoparticles, which made them mesoporous and were capped by citrate [56]. According to the optical microscopy images shown in Figures 4.9b and c, a ring-like pattern was formed on the electrode surface after drop casting of Pt nanoparticles rather than a homogeneous structure. The central part of the electrode was mostly, but not entirely, empty of particles so that when immersing into the analyte solution the latter directly contacted the bare electrode (Figure 4.9a) and overall, the drop cast showed a clear so-called coffee ring pattern (Figures 4.9 b1 and c1). The optical images shown in Figures 4.9 b1 and c1 are the surface of the GC electrode, taken directly after drop cast modification. The GC electrode was insulated by the polymer, polychlorotrifluoroethylene *(*PCTFE). Under the optical illumination used, the bright circular region of the image is the GC electrode, and this is surrounded by a black region which is the less reflective PCTFE polymer. In the case of the Pt nanoparticle modified electrode, drop cast directly from supplied suspension in citrate buffer solution, the volume of each drop casts leading to the corresponding mass of Pt residing on the GC electrode were finely controlled and optimised to ensure no overspill beyond the disk and onto the

insulating plastic. Note that the aqueous droplet remains in the shape of a ‘dome’ on GC surface and does not spread out into the insulation plastic during evaporation.

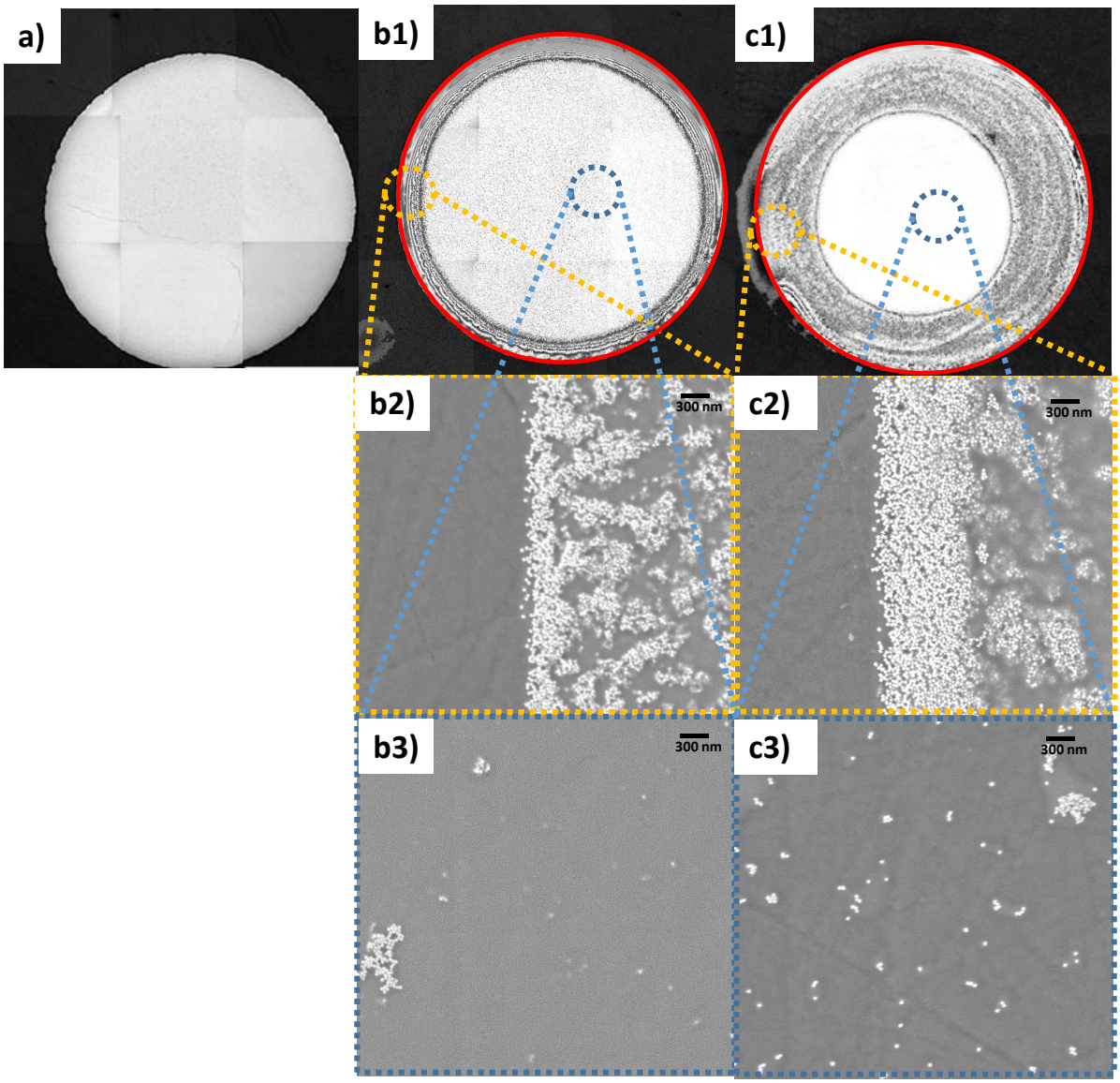

Figure 4.9 Images of a) bare GC electrode under optical microscope. b) 0.05 µg of Pt nanoparticles modified GC electrode under optical microscope (b1), SEM images of Pt nanoparticles at the edge of the drop cast (b2) and SEM images of Pt nanoparticles at the centre of the drop cast (b3). c) 0.35 µg of Pt nanoparticles under optical microscope (c1), SEM images at the edge of the drop cast (c2) and SEM image at the centre (c3). The areas within the red circle are electrode and others are the insulated material (b1 and c1). The geometric area of the GC electrode was 0.07 cm^2 and the average number of particles was 1.6×10^{10} particles cm^{-2}. The diameter of the PtNPs is 30 nm and dispersed in 2 mM sodium citrate solution. The scale bar of SEM images is 300 nm.

SEM images of the periphery of the drop cast showed large amounts of Pt nanoparticles and an ‘edge’ formed by particles was noticed (Figures 4.9 b2 and c2), which was considered to be the location of the contact line [35]. SEM images were recorded to better observe the

particle distributions on the surface of the modified electrodes, especially in the central particle deficient zone. A few particles were found to be randomly distributed in the central area (Figures 4.9 b3 and c3). Note that whilst the (lower resolution) image from optical microscopy indicated an empty area in centre (Figures 4.9 b1 and c1), on the basis of SEM, it contained a few-distributed nanoparticles with separations depending on the mass of particles drop casted rather than none, in the case where 0.35 µg were drop casted the particle-particles distances lay in the range between 300 to 800 nm. This is a key observation in the light of the discussion in the Introduction about the distances required between catalytic centres so that the diffusion fields associated with each overlap to cause diffusion to the full geometric area of the electrode.

Note that a mass of 0.05 µg drop casted would correspond approximately to a coverage of 0.1 monolayers if the particles were to form a uniform close-packed layer. Clearly the particle deficient central zone has a much lower coverage of less than 0.1 monolayers reflecting the large number of particles were 'lost' to form the particle dense rings at the edge of the drop cast. Since these rings are composed of densely packed, electrically conducting, particles they are presumed to be in electrical contact with the substrate.

Having characterized the drop casted surfaces, next the analytical performances of the surfaces were investigated, using a 1 mM aqueous solution of sodium arsenite (As(III)) in 0.1 M H_2SO_4. The Pt PME was then used for As(III) detection using cyclic voltammetry between +0.6 V and +1.05 V. Figure 4.10a shows cyclic voltammograms obtained from arsenic detection with PME of an area of 0.07 cm^2 modified with between 0.05 µg to 15 µg of Pt nanoparticles of diameter 30 nm. The black curve represents the voltammogram measured from an electrode modified with 0.05 µg of Pt nanoparticles, and the red, green, blue, and cyan curve were 0.35, 3.25, 7.5, and 15 µg of nanoparticles, respectively, and the surface coverages were equivalent to 0.1, 0.754, 7.54, 15 and 30 monolayers if the particles were to form a uniform

close-packed layer, which as seen above, they do not. In the voltammogram (Figure 4.10a), a clear oxidative peak at +0.85 V (vs SCE) was observed and this was used to examine the analytical performance of the modified electrode. The peak was assigned to the two-electron oxidation of As(III) to As(V) [64, 65].

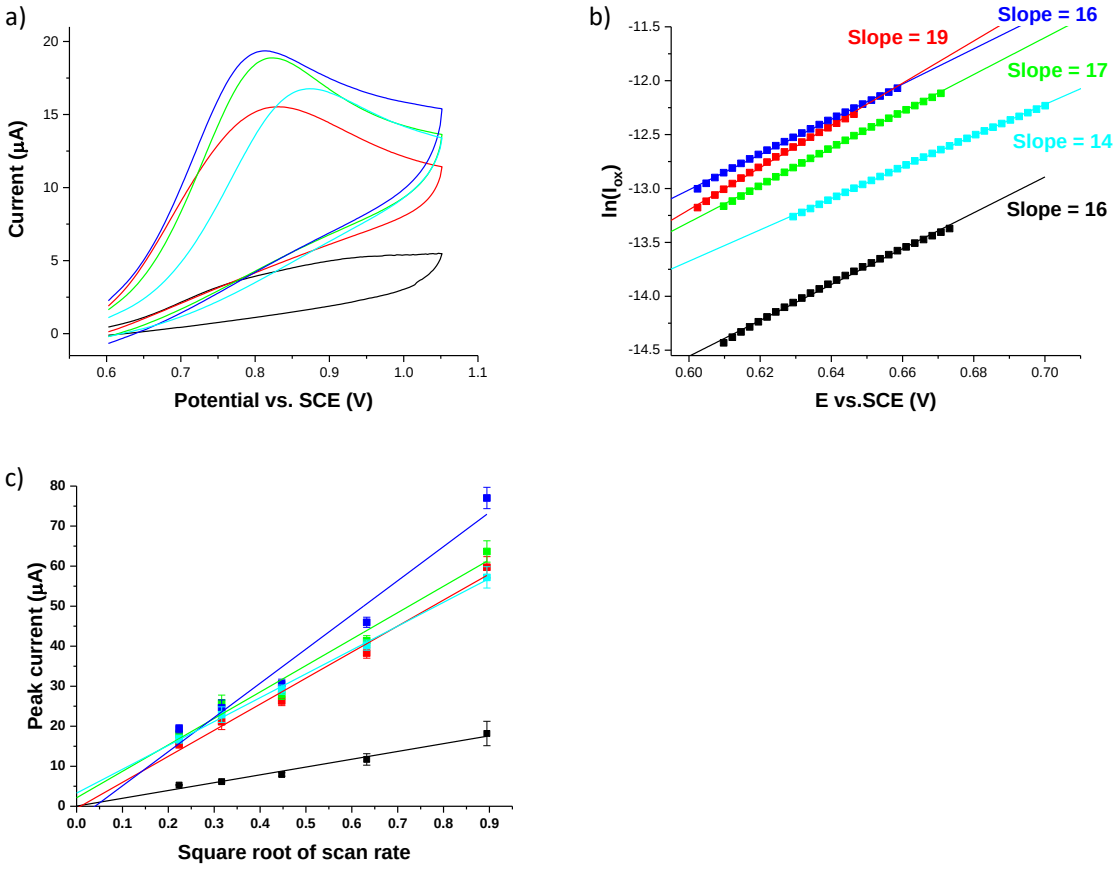

Figure 4.10 Plots of a) cyclic voltammograms, b) Tafel plots, and c) Randles–Ševčík plots of Pt PMEs containing 0.05 to 15 µg of Pt nanoparticles. In all three plots, black, red, green, blue and cyan data points represented 0.05, 0.35, 3.25, 7.5, and 15 µg of Pt nanoparticles. The measurements were conducted in 1 mM $NaAsO_2$ in 0.1 M H_2SO_4 solution. GCE served as a working electrode, and a graphite rod was applied as a counter electrode with a SCE served as the reference electrode completed the three electrode system. The diameter of the PtNPs is 30 nm and dispersed in 2 mM sodium citrate solution.

The voltammograms as shown in Figure 4.10b were analyzed first by means of Tafel analysis. The current analyzed were in the range of 10% to 30% of the peak currents [66]. The black, red, green, blue, and cyan points or line represent the 0.05, 0.35, 3.25, 7.5, and 15 µg of Pt nanoparticles, respectively. The transfer coefficient, β, could be calculated based on Tafel law and the slopes in the Tafel plots in Figure 4.10b, slope = βF/RT, where F is the Faraday

constant, R is the ideal gas constant and T is the temperature. The transfer coefficient under room temperature was ~0.50, which indicates that the intermediate was formed in its electrical behaviour between the reactants and products.

Importantly the black line (0.05 µg) had smaller currents compared to other sets of data (Figure 4.10a), which means the Pt nanoparticles were not sufficiently close together in some areas of the surfaces so as to allow for full diffusional overlap and to give the full diffusional response to arsenic expected for the geometric area of the electrode. This observation is entirely consistent with the data in Figure 4.9b showing the Pt nanoparticles distributed poorly on the surface of the electrode and that the centre of the drop casted zone was deficient in Pt nanoparticles (Figure 4.9 b3). Note that if the drop casted particles were assumed to uniformly distribute on the surface of electrode then an average surface coverage of 0.1 monolayers would lead to a calculated average particle separation of 2 microns which would be ample to achieve diffusional overlap and a voltammetric response reflecting diffusion to the geometric area of the electrode. To read the peak current of the black curve in Figure 4.10a, the voltammogram was zoomed in for reading.

Figure 4.10c shows the peak current vs. the square root of scan rate of Pt PMEs at the modified GCE with different amount of Pt nanoparticles (0.05 µg - 15 µg). The black, red, green, blue, and cyan points or line represented the 0.05, 0.35, 3.25, 7.5, and 15 µg of Pt nanoparticles, respectively. All sets of data points were linearly distributed and intercept approximately through the origin. The linear lines were aligned together except the black line, the 0.05 µg data points, which means the Pt nanoparticles on the GC electrode were under a critical coverage and the response was not that of the geometric area.

The peak current data for the higher coverages (where fully diffusional overlap would lead to linear diffusion to the geometric area of the electrode) were analyzed using the irreversible Randles- Ševčík equation,

$$I_{peak} = 0.496\sqrt{n' + \beta}\, nFA[A]_{bulk}\sqrt{\frac{F\nu D}{RT}} \quad (4\text{-}1)$$

where n′ is electrons transferred before the rate-determining step, n is the overall number of electrons transferred, A is the geometric area of the electrode in cm^2, β is the anodic transfer coefficient, $[A]_{bulk}$ is the bulk concentration of the analyte in mol m^{-3}, ν is the scan rate in V s^{-1} and D is the diffusion coefficient in cm^2 s^{-1}.

The error bars shown in Figure 4.10c were based on 3 experiments per point and confirm good reproducibility. For the As(III)/As(V) redox couple, n is 2; β is 0.46 as calculated from the slopes in Figure 4.10b from which it is inferred that n' is 0. Based on the Randles-Ševčík equation and the average slopes with high surface coverage in Figure 4.10c, the diffusion coefficient was calculated to be $9.7 \pm 0.3 \times 10^{-6}$ cm^2 s^{-1} which was in good agreement with the literature value, 1.0×10^{-5} cm^2 s^{-1} [67].

It is interesting to note that the low coverage (equivalent to ca 0.1 monolayers) electrode produced a linear Randles-Ševčík response whilst obviously giving an erroneously low diffusion coefficient which was lower than half of the literature value. This observation indicates an essential need for drop casting to be supporting by imaging of the electrode surface especially if quantitative information is sought.

Last we note that for the red line (equivalent 0.75 monolayers) in Figure 4.10c, an effectively full diffusional response was seen indicating a sufficient particle density in the central zone so as to ensure diffusional overlap such that all the active part of the electrode experiences linear (planar) diffusion. It is evident in the above that in order to realise

voltammetrically reliable reproducible surfaces, imaging of the drop cast is essential rather than relying on purely voltammetric indications since acceptable Randles- Ševčík plots albeit with erroneous slopes were obtained for partially covered surfaces. In the latter, the scaling of the peak current with the square root of scan rate reflects the existence of macroscopic patches of drop casted particles with the patch dimensions (d) larger than $(6Dt)^{1/2}$. The imaging suggests that these patches are the annular zones forming the coffee ring pattern. The scope for voltammetric misinterpretation is evident.

4.6. Conclusions

Drop-casting is a widely used method for the creation of PMEs, especially for electro-analysis. Often the creation of a random distribution of particles is assumed and this can be encouraged by electrochemical responses which are not inconsistent with the presumed surface morphology. However, it is clear that drop casts which are far from ideal can be formed with Pt nanoparticles forming coffee rings. Since both types of surface give plausible voltammetric responses it is evident that complementary microscopic imaging must be conducted in parallel with the electrochemistry in order to obtain to avoid erroneous conclusions both qualitative and quantitative.

4.7. Bibliography

[1] A.K.S. Kumar, Y. Zhang, D. Li, R.G. Compton, A Mini-review: how reliable is the drop casting technique?, Electrochem. Commun. (2020) 106867.
[2] Y. Zhang, A.K.S. Kumar, D. Li, M. Yang, R.G. Compton, Nanoparticle and nanotube modified electrodes: the response of drop casted surfaces, ChemElectroChem (2020).
[3] K.E. Toghill, R.G. Compton, Electrochemical Non-enzymatic Glucose Sensors: A Perspective and an Evaluation, Int. J. Electrochem. Sci. 5(9) (2010) 1246-1301.
[4] J.H. Zagal, S. Griveau, J.F. Silva, T. Nyokong, F. Bedioui, Metallophthalocyanine-based molecular materials as catalysts for electrochemical reactions, Coord. Chem. Rev. 254(23-24) (2010) 2755-2791.
[5] P. Si, Y.J. Huang, T.H. Wang, J.M. Ma, Nanomaterials for electrochemical non-enzymatic glucose biosensors, RSC Adv. 3(11) (2013) 3487-3502.

[6] Z.L. Wang, Triboelectric Nanogenerators as New Energy Technology for Self-Powered Systems and as Active Mechanical and Chemical Sensors, ACS Nano 7(11) (2013) 9533-9557.
[7] B.J. Sanghavi, O.S. Wolfbeis, T. Hirsch, N.S. Swami, Nanomaterial-based electrochemical sensing of neurological drugs and neurotransmitters, Microchim. Acta 182(1-2) (2015) 1-41.
[8] M. Sajid, M.K. Nazal, M. Mansha, A. Alsharaa, S.M.S. Jillani, C. Basheer, Chemically modified electrodes for electrochemical detection of dopamine in the presence of uric acid and ascorbic acid: A review, Trac-Trends Anal. Chem. 76 (2016) 15-29.
[9] P. Bollella, G. Fusco, C. Tortolini, G. Sanzo, G. Favero, L. Gorton, R. Antiochia, Beyond graphene: Electrochemical sensors and biosensors for biomarkers detection, Biosens. Bioelectron. 89 (2017) 152-166.
[10] N. Baig, M. Sajid, T.A. Saleh, Recent trends in nanomaterial-modified electrodes for electroanalytical applications, Trac-Trends Anal. Chem. 111 (2019) 47-61.
[11] A. Salimi, M.E. Hyde, C.E. Banks, R.G. Compton, Boron doped diamond electrode modified with iridium oxide for amperometic detection of ultra trace amounts of arsenic (III), Analyst 129(1) (2004) 9-14.
[12] E. Majid, S. Hrapovic, Y. Liu, K.B. Male, J.H. Luong, Electrochemical determination of arsenite using a gold nanoparticle modified glassy carbon electrode and flow analysis, Anal. Chem. 78(3) (2006) 762-769.
[13] L. Rassaei, M. Sillanpää, R.W. French, R.G. Compton, F. Marken, Arsenite determination in phosphate media at electroaggregated gold nanoparticle deposits, Electroanalysis (N.Y.N.Y.) 20(12) (2008) 1286-1292.
[14] C. Shen, S. Wang, Y. Jin, W.-Q. Han, In situ AFM imaging of solid electrolyte interfaces on HOPG with ethylene carbonate and fluoroethylene carbonate-based electrolytes, ACS Appl. Mater. Interfaces 7(45) (2015) 25441-25447.
[15] O. Cherstiouk, P. Simonov, E. Savinova, Model approach to evaluate particle size effects in electrocatalysis: preparation and properties of Pt nanoparticles supported on GC and HOPG, Electrochim. Acta 48(25-26) (2003) 3851-3860.
[16] Y. Wang, J.D. Zhang, Z.Y. Zhu, E.K. Wang, A carbon single crystal electrode for an electrochemical quartz crystal microbalance study, J. Electroanal. Chem. 419(1) (1996) 1-6.
[17] A. Kamenev, A. Lyakhov, S. Orlov, Determination of arsenic (III) and copper (II) by stripping voltammetry in a mixed EDTA-phosphoric acid supporting electrolyte, J. Anal. Chem. 60(2) (2005) 156-162.
[18] D. Kato, T. Kamata, D. Kato, H. Yanagisawa, O. Niwa, Au Nanoparticle-Embedded Carbon Films for Electrochemical As3+ Detection with High Sensitivity and Stability, Anal. Chem. 88(5) (2016) 2944-2951.
[19] M. Yang, X. Chen, J.H. Liu, X.J. Huang, Enhanced anti-interference on electrochemical detection of arsenite with nanoporous gold in mild condition, Sens. Actuator B-Chem. 234 (2016) 404-411.
[20] J. Mafa, N. Mabuba, O. Arotiba, An exfoliated graphite based electrochemical sensor for As (III) in water, Electroanalysis 28(7) (2016) 1462-1469.
[21] X. Dai, O. Nekrassova, M.E. Hyde, R.G. Compton, Anodic stripping voltammetry of arsenic (III) using gold nanoparticle-modified electrodes, Anal. Chem. 76(19) (2004) 5924-5929.
[22] A.O. Simm, C.E. Banks, S.J. Wilkins, N.G. Karousos, J. Davis, R.G. Compton, A comparison of different types of gold–carbon composite electrode for detection of arsenic (III), Anal. Bioanal. Chem. 381(4) (2005) 979-985.
[23] C. Xue, Q. Han, Y. Wang, J. Wu, T. Wen, R. Wang, J. Hong, X. Zhou, H. Jiang, Amperometric detection of dopamine in human serumby electrochemical sensor based on gold nanoparticles doped molecularly imprinted polymers, Biosens. Bioelectron. 49 (2013) 199-203.

[24] S. Alim, J. Vejayan, M.M. Yusoff, A. Kafi, Recent uses of carbon nanotubes & gold nanoparticles in electrochemistry with application in biosensing: a review, Biosens. Bioelectron. 121 (2018) 125-136.
[25] E. Asadian, M. Ghalkhani, S. Shahrokhian, Electrochemical sensing based on carbon nanoparticles: A review, Sens. Actuators, B 293 (2019) 183-209.
[26] F.W. Campbell, R.G. Compton, The use of nanoparticles in electroanalysis: an updated review, Anal. Bioanal. Chem. 396(1) (2010) 241-259.
[27] J.M. George, A. Antony, B. Mathew, Metal oxide nanoparticles in electrochemical sensing and biosensing: a review, Microchim. Acta 185(7) (2018) 358.
[28] E.E. Tanner, R.G. Compton, How can electrode surface modification benefit electroanalysis?, Electroanalysis 30(7) (2018) 1336-1341.
[29] S. Eloul, R.G. Compton, Voltammetric sensitivity enhancement by using preconcentration adjacent to the electrode: simulation, critical evaluation, and insights, J. Phys. Chem. C 118(42) (2014) 24520-24532.
[30] A. Einstein, On the motion of small particles suspended in liquids at rest required by the molecular-kinetic theory of heat, Ann. Phys. 17(549-560) (1905) 208.
[31] H.S. Toh, R.G. Compton, 'Nano-impacts': An Electrochemical Technique for Nanoparticle Sizing in Optically Opaque Solutions, ChemistryOpen 4(3) (2015) 261-263.
[32] H. Toh, R. Compton, Electrochemical detection of single micelles through 'nano-impacts', Chem. Sci. 6(8) (2015) 5053-5058.
[33] H.S. Toh, C. Batchelor-McAuley, K. Tschulik, C. Damm, R.G. Compton, A proof-of-concept–Using pre-created nucleation centres to improve the limit of detection in anodic stripping voltammetry, Sens. Actuators, B 193 (2014) 315-319.
[34] H. Li, D. Buesen, R. Williams, J. Henig, S. Stapf, K. Mukherjee, E. Freier, W. Lubitz, M. Winkler, T. Happe, Preventing the coffee-ring effect and aggregate sedimentation by in situ gelation of monodisperse materials, Chem. Sci. 9(39) (2018) 7596-7605.
[35] R.D. Deegan, O. Bakajin, T.F. Dupont, G. Huber, S.R. Nagel, T.A. Witten, Capillary flow as the cause of ring stains from dried liquid drops, Nature 389(6653) (1997) 827-829.
[36] H. Eral, J. Oh, Contact angle hysteresis: a review of fundamentals and applications, Colloid Polym. Sci. 291(2) (2013) 247-260.
[37] J. Park, J. Moon, Control of colloidal particle deposit patterns within picoliter droplets ejected by ink-jet printing, Langmuir 22(8) (2006) 3506-3513.
[38] M. Kuang, L. Wang, Y. Song, Controllable printing droplets for high-resolution patterns, Adv. Mater. 26(40) (2014) 6950-6958.
[39] A. Friederich, J.R. Binder, W. Bauer, Rheological control of the coffee stain effect for inkjet printing of ceramics, J. Am. Ceram. Soc. 96(7) (2013) 2093-2099.
[40] B.-J. de Gans, U.S. Schubert, Inkjet printing of well-defined polymer dots and arrays, Langmuir 20(18) (2004) 7789-7793.
[41] J. Zou, F. Kim, Diffusion driven layer-by-layer assembly of graphene oxide nanosheets into porous three-dimensional macrostructures, Nat. Commun. 5(1) (2014) 1-9.
[42] W. Han, Z. Lin, Learning from "Coffee Rings": Ordered Structures Enabled by Controlled Evaporative Self-Assembly, Angew. Chem., Int. Ed. 51(7) (2012) 1534-1546.
[43] M. Anyfantakis, Z. Geng, M. Morel, S. Rudiuk, D. Baigl, Modulation of the Coffee-Ring Effect in Particle/Surfactant Mixtures: the Importance of Particle-Interface Interactions, Langmuir 31(14) (2015) 4113-4120.
[44] H.-Y. Ko, J. Park, H. Shin, J. Moon, Rapid self-assembly of monodisperse colloidal spheres in an ink-jet printed droplet, Chem. Mater. 16(22) (2004) 4212-4215.
[45] Á.G. Marín, H. Gelderblom, A. Susarrey-Arce, A. van Houselt, L. Lefferts, J.G. Gardeniers, D. Lohse, J.H. Snoeijer, Building microscopic soccer balls with evaporating colloidal fakir drops, Proc. Natl. Acad. Sci. 109(41) (2012) 16455-16458.

[46] L. Cui, J. Zhang, X. Zhang, Y. Li, Z. Wang, H. Gao, T. Wang, S. Zhu, H. Yu, B. Yang, Avoiding coffee ring structure based on hydrophobic silicon pillar arrays during single-drop evaporation, Soft Matter 8(40) (2012) 10448-10456.
[47] D. Tian, Y. Song, L. Jiang, Patterning of controllable surface wettability for printing techniques, Chem. Soc. Rev. 42(12) (2013) 5184-5209.
[48] M. Dicuangco, S. Dash, J.A. Weibel, S.V. Garimella, Effect of superhydrophobic surface morphology on evaporative deposition patterns, Appl. Phys. Lett. 104(20) (2014) 201604.
[49] H.B. Eral, D.M. Augustine, M.H. Duits, F. Mugele, Suppressing the coffee stain effect: how to control colloidal self-assembly in evaporating drops using electrowetting, Soft Matter 7(10) (2011) 4954-4958.
[50] F. Li, F. Mugele, How to make sticky surfaces slippery: Contact angle hysteresis in electrowetting with alternating voltage, Appl. Phys. Lett. 92(24) (2008) 244108.
[51] F. Mugele, J.-C. Baret, Electrowetting: from basics to applications, J. Phys.: Condens. Matter 17(28) (2005) R705.
[52] T.A. Nguyen, M.A. Hampton, A.V. Nguyen, Evaporation of nanoparticle droplets on smooth hydrophobic surfaces: the inner coffee ring deposits, J. Phys. Chem. C 117(9) (2013) 4707-4716.
[53] D. Mampallil, J. Reboud, R. Wilson, D. Wylie, D.R. Klug, J.M. Cooper, Acoustic suppression of the coffee-ring effect, Soft Matter 11(36) (2015) 7207-7213.
[54] S. Mhatre, A. Zigelman, L. Abezgauz, O. Manor, Influence of a propagating megahertz surface acoustic wave on the pattern deposition of solute mass off an evaporating solution, Langmuir 32(37) (2016) 9611-9618.
[55] X. Ding, P. Li, S.-C.S. Lin, Z.S. Stratton, N. Nama, F. Guo, D. Slotcavage, X. Mao, J. Shi, F. Costanzo, Surface acoustic wave microfluidics, Lab Chip 13(18) (2013) 3626-3649.
[56] W. Yu, C. Batchelor-McAuley, X. Chang, N.P. Young, R.G. Compton, Porosity controls the catalytic activity of platinum nanoparticles, Phys. Chem. Chem. Phys. 21(36) (2019) 20415-20421.
[57] X. Jiao, C. Batchelor-McAuley, C. Lin, E. Kätelhön, E.E. Tanner, N.P. Young, R.G. Compton, Role of nanomorphology and interfacial structure of platinum nanoparticles in catalyzing the hydrogen oxidation reaction, ACS Catal. 8(7) (2018) 6192-6202.
[58] X. Jiao, S.V. Sokolov, E.E. Tanner, N.P. Young, R.G. Compton, Exploring nanoparticle porosity using nano-impacts: platinum nanoparticle aggregates, Phys. Chem. Chem. Phys. 19(1) (2017) 64-68.
[59] E. Kätelhön, R.G. Compton, Unscrambling illusionary catalysis in three-dimensional particle-modified electrodes: Reversible reactions at conducting particles, Appl. Mater. Today 18 (2020) 100514.
[60] M.J. Sims, N.V. Rees, E.J. Dickinson, R.G. Compton, Effects of thin-layer diffusion in the electrochemical detection of nicotine on basal plane pyrolytic graphite (BPPG) electrodes modified with layers of multi-walled carbon nanotubes (MWCNT-BPPG), Sens. Actuators, B 144(1) (2010) 153-158.
[61] I. Streeter, G.G. Wildgoose, L. Shao, R.G. Compton, Cyclic voltammetry on electrode surfaces covered with porous layers: an analysis of electron transfer kinetics at single-walled carbon nanotube modified electrodes, Sens. Actuators, B 133(2) (2008) 462-466.
[62] M.C. Henstridge, E.J. Dickinson, M. Aslanoglu, C. Batchelor-McAuley, R.G. Compton, Voltammetric selectivity conferred by the modification of electrodes using conductive porous layers or films: the oxidation of dopamine on glassy carbon electrodes modified with multiwalled carbon nanotubes, Sens. Actuators, B 145(1) (2010) 417-427.
[63] T.J. Davies, R.R. Moore, C.E. Banks, R.G. Compton, The cyclic voltammetric response of electrochemically heterogeneous surfaces, J. Electroanal. Chem. 574(1) (2004) 123-152.

[64] T.D. Cabelka, D.S. Austin, D.C. Johnson, Electrocatalytic Oxidation of As (III): I. Voltammetric Studies at Pt Electrodes in, J. Electrochem. Soc. 131(7) (1984) 1595.
[65] X. Dai, R.G. Compton, Detection of As (III) via oxidation to As (V) using platinum nanoparticle modified glassy carbon electrodes: arsenic detection without interference from copper, Analyst 131(4) (2006) 516-521.
[66] D. Li, C. Lin, C. Batchelor-McAuley, L. Chen, R.G. Compton, Tafel analysis in practice, J. Electroanal. Chem. 826 (2018) 117-124.
[67] D.G. Williams, D.C. Johnson, Pulsed voltammetric detection of arsenic (III) at platinum electrodes in acidic media, Anal. Chem. 64(17) (1992) 1785-1789.

Chapter 5. Arsenic (III) Detection with Underpotential Deposition and Anodic Stripping Voltammetry

This chapter reports a stripping voltammetric method for the detection of aqueous As(III) using a Pt macroelectrode or a Pt nanoparticle-modified glassy carbon electrode (GCE) which, novelly, is based on the underpotential deposition of As atoms. The method consists of a pre-concentration reductive step to accumulate As ad-atoms onto Pt, followed by linear sweep voltammetry (LSV). It is shown that the stripping peak of As ad-atoms improves the response at low concentrations of As(III) as compared to analogous measurements using the deposition of bulk As. Specifically no interference was seen from Cu(II) at realistic concentrations although high concentrations of chloride inhibited the deposition of the ad-atoms. A linear response was found for the concentration range 0.05 to 1 μM As(III) at both types of electrode with a visually clear signal recorded at 0.05 μM (4 ppb), suggesting that this method has practical value noting the WHO limit of 0.13 μM (10 ppb) for safe drinking water.

The work presented in this chapter has been published in ChemElectroChem [1] as a first author paper, and was carried out in collaboration with Dr. Danlei Li (Compton group) who helped with the interpretation of the results.

5.1. Introduction:

As introduced in Chapter 2, arsenic is highly toxic and exists both naturally and in some industrial or mineral effluents [2-6]. Long-term exposure to excess arsenic can cause severe health problems, including cardiovascular diseases, cancer and carcinogenic effects [5, 6]. The dominant inorganic arsenic species are As(-III) (as formally in AsH_3), As(0), As(III), and

As(V). The latter two oxidation states are the major forms found in water [2-4]. As(III) species (notably H_3AsO_3) are much more toxic than As(V) (H_2AsO_4 or $HAsO_4^-$) resulting from their interaction with enzymes in the human body [5-7]. Thus, the convenient detection of As(III) in water is both urgent and necessary. The significant contamination of groundwater by arsenic has been found in over 20 countries [7], in which the arsenic levels are above the World Health Organization's (WHO) arsenic guideline value of 10 μg L^{-1} (10 ppb) in drinking water [8].

There have been many methods developed to determine arsenic levels in water during the past decades [9-11], including important techniques such as atomic absorption spectrometry (AAS) [12], inductively coupled plasma mass spectrometry (ICPMS) [13, 14], and high-performance liquid chromatography with ICPMS (HPLC-ICPMS) [15]. However, these sensitive instrumental methods require dedicated laboratory conditions and have long sample preparation times. Therefore, alternative techniques that can overcome these problems need to be developed. Electrochemical methods can provide highly sensitive and rapid detection [2, 16-18]. In particular stripping voltammetry is a powerful method for quantitative detection of low levels of analytes [19-21]. Many studies have reported using stripping voltammetry methods for detecting As(III) in aqueous solution, including anodic stripping voltammetry (ASV) at gold nanoparticle-modified GCE [22] or at a boron-doped diamond (BDD) electrode [23], and cathodic stripping voltammetry (CSV) at a hanging mercury drop electrode (HMDE) [24].

ASV with bulk As pre-concentration is the most commonly used electrochemical method for As(III) detection in water. Simm *et al* used ASV to detect As(III) at Ag macroelectrode with a sensitivity of 2.6 A M^{-1} and reached a LOD of 13.5 ppb [25] whilst Bu *et al* investigated arsenic in water by linear sweep anodic stripping voltammetry (LSASV) at Au macrodisk electrodes, and obtained a detection limit of 0.14 ppb for As(III) with a

sensitivity of 761 A M^{-1} [26]. Using ASV, Dai *et al* found a LOD of 35 ppb for As(III) at a Pt macroelectrode [27]. To date, using conventional metal electrodes the lowest LOD of 0.003 ppb was reported by Profumo *et al* [28] and the greatest sensitivity of 1985 A M^{-1} was achieved by Xiao *et al* [22]. However, the detection of As(III) via ASV at conventional electrodes is subject to interferences by metal ions, including copper, lead, zinc, iron, silver, bismuth and mercury [2]. The most commonly reported interfering ion is Cu^{2+}, which can alter the stripping peak of As [29]. This interference has been ascribed to the formation of intermetallic compounds or a Cu-As alloy together with the similar reduction potentials of Cu(II) and As(III) noted by Idris *et al* [30].

In recent years, nanomaterials have been incorporated into electrochemical methods for As(III) detection where claimed advantages include their high surface area, increased catalytic sites, and higher adsorption capacities [31-34]. In the context of ASV the high surface areas offer obvious advantages in providing scope for enhanced sensitivity whilst the different surface structures that can prevail at the nanoscale may offer possibilities for changing the metal deposition chemistry to avoid the interference effects noted above. Proof of concept that particle modified glassy carbon electrodes (GCEs) can be employed for the trace detection of As(III) using ASV has been reported in several works based on Pt nanoparticles [35-37]. Xiao *et al* studied Au nanoparticles modified carbon nanotubes (AuCNTs) on glassy carbon electrodes to detect As(III) in water via ASV [22]. The LOD was determined to be 0.1 ppb and the sensitivity was 1985 A M^{-1} via Square Wave ASV. The very high sensitivity was attributed to the high number of tiny Au nanoparticles supported on the large area of CNTs. The dramatically increased area can influence the voltammetric responses [38, 39] in that the overpotential required for slow (‘irreversible’) electron transfer reactions can be lowered [40] whilst the magnitude of the flux of analyte to the electrochemical interface reflects the extent

of the overlap of the diffusional fields of the different centres which is ultimately limited, in the case of full overlap, by diffusion to the full geometrical area of the supporting electrode.

Beyond ASV nanoparticle modified electrodes have been used for diffusional voltammetry. For example, Dai *et al* modified a glassy carbon electrode with Pt nanoparticles via electrodeposition to electrocatalytically oxidize As(III) to As(V), and reported an As(III) detection limit of 2.1 ppb [27] and a similar approach taken using Pt nanoparticles and CNTs [41] presented a LOD of 0.12 ppb. Huang *et al* used Au nanoparticles within a thin Nafion film to modify glassy carbon giving a sensitivity of 23.98 A M^{-1} and a low LOD of 0.047 ppb [42]. Yang *et al* used porous gold nanoparticles to modify glassy carbon electrodes giving a sensitivity 0.617 A M^{-1} cm^{-2} and a low LOD of 1.668 ppb [43] where the number of significant figures is that reported by the authors.

The sensitivity of diffusional signals is ultimately constrained by the rate of transport of redox species to the geometric area of the electrode used whilst stripping voltammetry, as discussed above, is subject to possible interference by species which form alloys and/or intermetallic species with As. Both types of measurements are well explored and optimised. In the present paper we adopt a different strategy based on ASV aiming to overcome the interference problem through avoiding the formation of *bulk* deposits of As or its alloys/compounds. In particular we consider the phenomenon of under potential deposition (UPD) as a possible means of avoiding such interference. This is the deposition (usually) of a metal in the form of a monolayer or sub-monolayer at potentials lower than those required to form the bulk material [24, 44, 45]. The topic has been extensively investigated by surface electrochemists [46-48] but little used analytically [49]. In the present case we note that As undergoes UPD on Platinum surfaces [50-52]. Accordingly, we investigate the possible use of this for the analysis of As at low concentrations via what we term ‘UPD-ASV’. In order to

ensure a sufficiently sensitive stripping signal we use a Pt nanoparticle-modified electrode to give a large area of Pt on which to deposit the As. Comparisons are made with measurements at bulk Pt using a Pt macrodisc electrode and the UPD-ASV approach is shown to be valuable particularly in avoiding interference caused by Cu(II). The measured detection limits using either a Pt macroelectrode or a Pt nanoparticle-modified electrode for As detection were within the requirements for the WHO limits for drinking water with visually distinct and recognisable signals seen at the lowest concentrations reported.

Table 5.1 compares methods developed for arsenic detection in this work with recent literature. Compared to previous work, as will be shown below, our method is only interfered with by chloride at relatively high concentrations and interference by copper is avoided. In addition, the low limits of detection claimed in the literature on the basis of the 3σ method [53-56] contrasts with the values reported from measured voltammetric signals in this work.

Table 5.1 Summary of Different Methods Developed for Arsenic Detection

Authors	Electrode	Method	Interference ion	LOD (ppb)
Bhanjana *et al* [57]	ZrO_2/Nafion-Au electrode	CV	No interfered ions	5
Yang *et al* [53]	np-Au-GCE	SWASV	Humic acid, Pb^{2+}	0.137[1]
Sonkoue *et al* [54]	AgNP-GCE	CV	Cu^{2+}	0.1[1]
Hwang *et al* [55]	Fe/Chitosan-SPCE	SWASV	Cu^{2+}	1.12[1]
Nunez *et al* [56]	Graphene-SPCE	DPAV	Cu^{2+}	0.28[1]

This work	Pt macroelectrode, Pt nanoparticle-modified GCE	ASV	Cl^- (higher than 100 μM)	4*, 4*

AuNP: gold nanoparticle; GCE: glassy carbon electrode; np: nanoporous; SPCE: screen-printed carbon electrode; CV: cyclic voltammetry; SWASV: square wave anodic stripping voltammetry; DPAV: differential pulse anodic voltammetry; ASV: anodic stripping voltammetry; LOD: limit of detection. [1] LOD calculated from the 3σ method. * LOD obtained from measured signals.

5.2. Experimental

5.2.1. Chemical reagents

Commercially available Pt nanoparticles (0.05 mg mL^{-1}, 30 nm in diameter, NanoComposix, USA) were dispersed in 2 mM sodium citrate. Sodium (meta) arsenite ($NaAsO_2$, 99%, Fluka, Switzerland), copper(II) sulfate pentahydrate ($CuSO_4 \cdot 5H_2O$, 99%, Sigma Aldrich, UK), potassium chloride (KCl, 99.5%, Sigma Aldrich, UK), and sulphuric acid (H_2SO_4, 98%, Fisher Scientific, UK) were purchased and used without any further purification. All aqueous solutions were prepared using deionized water (Milipore, UK) with a resistivity of 18.2 MΩ cm at 298 K.

5.2.2. Instrumentation

Electrochemical measurements were conducted with a standard three-electrode system in a Faraday cage at 298 (±0.1) K. A glassy carbon electrode (GCE, diameter of 3.00±0.01 mm, geometric area of 0.07 cm^2, BAS technical, UK) or a platinum macroelectrode (diameter of 1.66±0.01 mm, geometric area of 0.02 cm^2, BASi, USA) served as a working electrode, and a platinum wire was applied as a counter electrode with a mercury-mercurous sulfate reference electrode (MSE, BASi, USA). The solution used in the reference electrode was saturated

K_2SO_4 solution (1.45 M) conferring the reference electrode with a potential of +0.65 V vs. standard hydrogen electrode (SHE). Electrochemical measurements were performed in 0.1 M H_2SO_4 containing various concentrations of As(III) and were recorded with a μAutolab type III potentiostat (EcoChemie, NL) after degassing with nitrogen.

5.2.3. Preparation and characterization of Pt nanoparticle-modified electrodes

The GC electrode was cleaned on polishing pad with alumina of decreasing particle sizes (1, 0.3 and 0.05 μm) then rinsed with deionized water. For drop casting Pt nanoparticles, 5 μL of stock Pt nanoparticle suspension was drop casted onto the GC electrode using micro pipette and dried with a gentle N_2 flow for 15 minutes.

As is shown in Figure 5.1a, the individual particles are formed by aggregation of much smaller nanoparticles of approximate 3 nm in diameter [58], which makes the particles exhibit a distinct porous structure. The particles are capped by citrate, and the real surface area of the mesoporous Pt nanoparticles were calculated to be 0.013 ± 0.003 μm^2 per particle from previous reports based on single entity electrochemistry [58].

According to the optical microscopy images shown in Figure 5.1b, a ring-like pattern was formed on the surface of electrode after the drop casting of Pt nanoparticles, so-called the coffee ring pattern [59]. It was previously characterized by SEM [60] and shown that although most of the particles are deposited as part of the ‘ring’ a few particles remain randomly distributed around the centre of the drop cast (Figure 5.1c) [60] but which is mostly empty of deposit. The average particle-particle distances even in the centre for the mass drop casted were shown to be sufficiently small so as to allow diffusional overlap so that analyte diffusion to the full geometric area of the electrode was observed [60].

5.2.4. Optical Microscopy and imaging

All images were obtained using an optical microscope, Zeiss Axio Examiner, A1 Epifluorescence microscope (Carl Zeiss Ltd., UK). The objective lens used was a 10× air objective (NA = 0.5, EC Plan-Neofluar) and the light source employed in this study was a LQ-HXP 120 V lamp. Incident light reaching the surface of the GCE was partly reflected to the camera through the objective lens and the image of the electrode was obtained by a black & white ORCA-Flash 4.0 digital CMOS camera (Hamamatsu, JP). The resolution of the image was 4-megapixel.

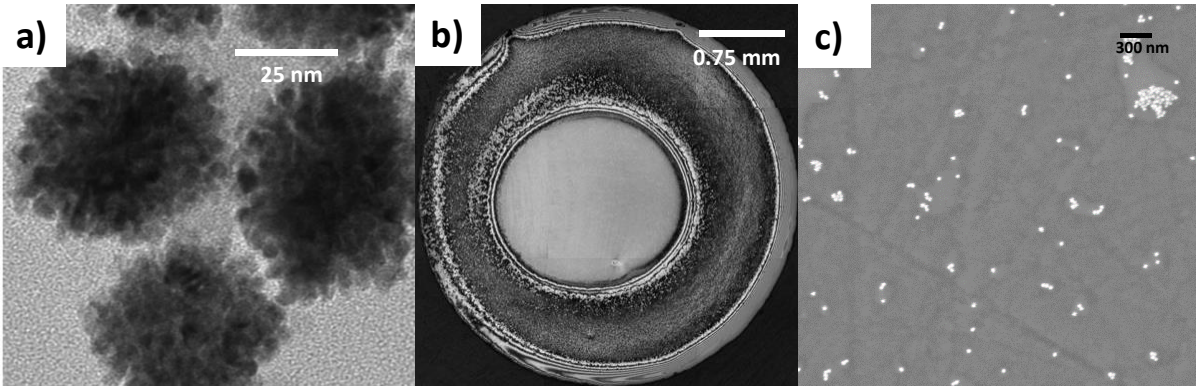

Figure 5.1 a) HR-CTEM image showing how the overall single nanoparticle structure comprises of an aggregate of smaller substituent crystallites. Reprinted with permission from Ref. [58]. Copyright (2019) Royal Society of Chemistry. b) Image of 0.25 µg of Pt nanoparticle drop casted onto a GC electrode. c) SEM images of the centre of the drop cast. Reprinted with permission from Ref. [60]. Copyright (2020) John Wiley & Sons, Inc. The diameter of the GC electrode was 3 mm and the geometric area of the GC electrode was 0.07 cm^2. The average number of particles was 1.6×10^{10} particles cm^{-2}. The diameter of the Pt nanoparticles is 30 nm and dispersed in 2 mM sodium citrate solution. The scale bar is 0.75 mm.

5.3. Results and discussion

In the following sections, first, the electrochemical behaviour of As(III) at both Pt macroelectrodes and Pt nanoparticle-modified electrodes are studied in solution containing 500 µM $NaAsO_2$ with 0.1 M H_2SO_4 using cyclic voltammetry. The voltammetric peaks are assigned and compared with literature. Next, methods for achieving a low limit of detection of As are investigated using anodic stripping voltammetry with the Pt surface pre-concentrated with As(0)

either as bulk As or as ad-atoms formed by under potential deposition (UPD). The applied potential and duration for pre-concentration are optimised on the basis of higher signal-to-background ratio and the benefits of using UPD identified. Finally, attention is given to possible interferences.

5.3.1. Cyclic voltammetry of aqueous As(III) at bulk Pt and at Pt nanoparticles

To examine the electrochemical responses of As(III), a Pt macroelectrode and a Pt nanoparticle-modified GCE were first employed to study the behaviour of As(III) in solution containing 500 μM $NaAsO_2$ with 0.1 M H_2SO_4 using cyclic voltammetry as is shown in Figure 5.2 where the arrow stands for the starting direct of scan. Acidic conditions are used to avoid the formation of insoluble oxides. Figure 5.2a illustrates the cyclic voltammetric response of As(III) in 0.1 M H_2SO_4 with a potential window from - 0.8 V to + 0.9 V (vs. MSE) at 0.1 V s^{-1} at a Pt macroelectrode. Three peaks were observed on the cathodic scan, labelled as peak 1, peak 2 and peak 3 (solid line in Figure 5.2a). Peak 1 at ca - 0.08 V was ascribed to the reduction of Pt-O to Pt [27, 50]. Peak 2 observed at ca - 0.6 V corresponds to the three-electron reduction of As(III) to As(0) [50]. Peak 3 at ca - 0.77 V represents the hydrogen evolution reaction (HER). On the reversal anodic scan, three peaks, peak 4, peak 5 and peak 6 were obtained. Peak 4 with the potential of ca - 0.75 V represents the hydrogen oxidation reaction (HOR). Peak 5 at ca - 0.25 V corresponds to the re-oxidation of As(0) to the parent As(III) species [50]. A larger oxidation peak, peak 6, was observed at ca + 0.4 V at which As(III) was further oxidized to As(V). Comparing with the voltammogram obtained in blank solution (0.1 M H_2SO_4; dashed line in Figure 5.2a), it can be seen that the three absent peaks (peak 2, peak 5 and peak 6) are all As(III)-related peaks, and peaks 3 and 4 correspond to HER and HOR, respectively [50]. Peak 6' observed at ca + 0.5 V in blank solution was assigned to be the oxidation of Pt to Pt-O [50]; this corresponding Pt oxidation peak was merges with the As(III) oxidation peak (peak 6;

solid line in Figure 5.2a) and hardly been distinguished when 500 μM As(III) was added in solution. On the other hand, similar peak current densities of peak 1 were observed in both blank solution and solution containing 500 μM As(III) due to the reduction of Pt-O to Pt in both cases [27, 50].

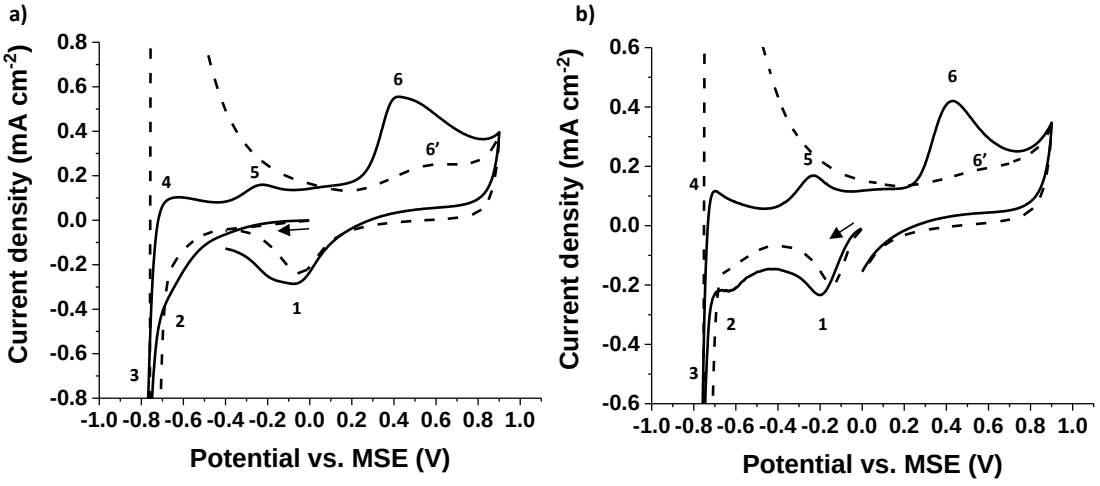

Figure 5.2 CV curves of a) 500 μM $NaAsO_2$ in 0.1 M H_2SO_4 (——) and blank (- - -) at Pt macroelectrode, and b) 500 μM $NaAsO_2$ in 0.1 M H_2SO_4 (——) and blank (- - -) at Pt nanoparticle-modified GC electrodes. The voltammograms were conducted from 0 V and first scanned cathodically to -0.80V at a scan rate of 0.1 V s^{-1} and then scanned anodically to +0.9 V. The current densities were calculated based on the geometric area of Pt macroelectrode, 0.02 cm^2 and estimated Pt nanoparticles surface area, 0.11 cm^2. Calculations of particles surface area are shown in the Appendix section 1. The arrows represent the starting point and the direction of scan.

The cyclic voltammetric response at a Pt nanoparticle-modified GCE with an average surface coverage of 2.2×10^{-14} mol cm^{-2} (ca 0.1 monolayers, calculations are shown in Appendix section 1) is shown in Figure 2b. The potential window of voltammogram was from -0.8 V to +0.9 V and the scan rate was 0.1 V s^{-1}. The voltammetry obtained in the absence of As(III) in 0.1 M H_2SO_4 at the Pt nanoparticle-modified GCE (dashed line in Figure 5.2b) was similar to the one measured at the Pt macroelectrode (dashed line in Figure 5.2a). All peaks were at similar potentials and represent the same electrochemical processes as discussed above. In 500 μM As(III) in 0.1 M H_2SO_4 (solid line in Figure 5.2b), as seen with Pt macroelectrode six voltammetric features were discerned and assigned to the same electrochemical reactions [27, 50] as above. It was noted that peaks 3, 4, 5 and 6 had similar peak potentials (solid line

in Figure 5.2b) to those seen at bulk Pt. However, peak 1 and peak 2 in Figure 5.2b differ from the ones in Figure 5.2a. It is clear that peak 1 only appeared after a full scan of CV at Pt macroelectrode (Figure 5.2a) while at Pt nanoparticle-modified GCE peak 1 was observed during the initial cathodic scan (Figure 5.2b). The absence of peak 1 during the initial cathodic scan on Pt macroelectrode suggests a near oxide-free Pt surface whilst the Pt nanoparticles deposited on GCE may contain Pt oxide on their surfaces which results in the appearance of peak 1 on the cathodic scan in Figure 5.2b. Furthermore, the peak potential of peak 1 at Pt nanoparticles at ca -0.2 V (Figure 5.2b) was more negative compared to the potential at bulk Pt (Figure 5.2a). This potential is similar to that reported by Postek *et al* in 2019 [37] for Pt nanoparticles of size 4 to 7 nm and was assigned to the reduction of Pt oxide to Pt.

Peak 2 (Figure 5.2) was seen at ca -0.6 V for both Pt nanoparticle-modified electrode (solid line in Figure 5.2b)and Pt macroelectrode (solid line in Figure 5.2a), which corresponds to the reduction of As(III) to As(0) [27]. The relatively large current density of peak 2 at Pt nanoparticle-modified electrode is possibly due to the higher surface area and hence more deposition sites for As(0) on the mesoporous Pt nanoparticles, together with reduced interference from the solvent breakdown. Similarly peak 5 on the reverse anodic scan in Figure 5.2b is seen to be enhanced for the nanoparticles over the bulk Pt. However, from an analytical perspective the CV method typically does not provide a suitably low detection limit since this is limited by diffusion. Thus, a different method needs to be applied to approach a low detection limit. The next section focuses on the detection of As using anodic stripping voltammetry where a pre-concentration of As(0) was applied to enhance the signal and to approach a lower detection limit.

5.3.2. Anodic stripping voltammetry of As(III) at bulk Pt and Pt nanoparticles

To examine the possibility of achieving a lower detection limit of As(III) in water, anodic stripping voltammetry was applied for the detection of As(III) in 0.1 M H_2SO_4 on both a Pt macroelectrode and Pt nanoparticle-modified GCEs. The pre-concentration of As(0) was first carried out at -0.7 V for 240 s during which both bulk As(0) and As ad-atoms were deposited at the surface of Pt [50]. Then the deposited As(0) was stripped off from the electrode surface using LSV conducted from -0.7 V to +0.9 V at a scan rate of 0.1 V s^{-1}. The deposition potential and time for ASV were optimized for the signal-to-background ratio and is given in the Appendix sections 2 and 3, respectively.

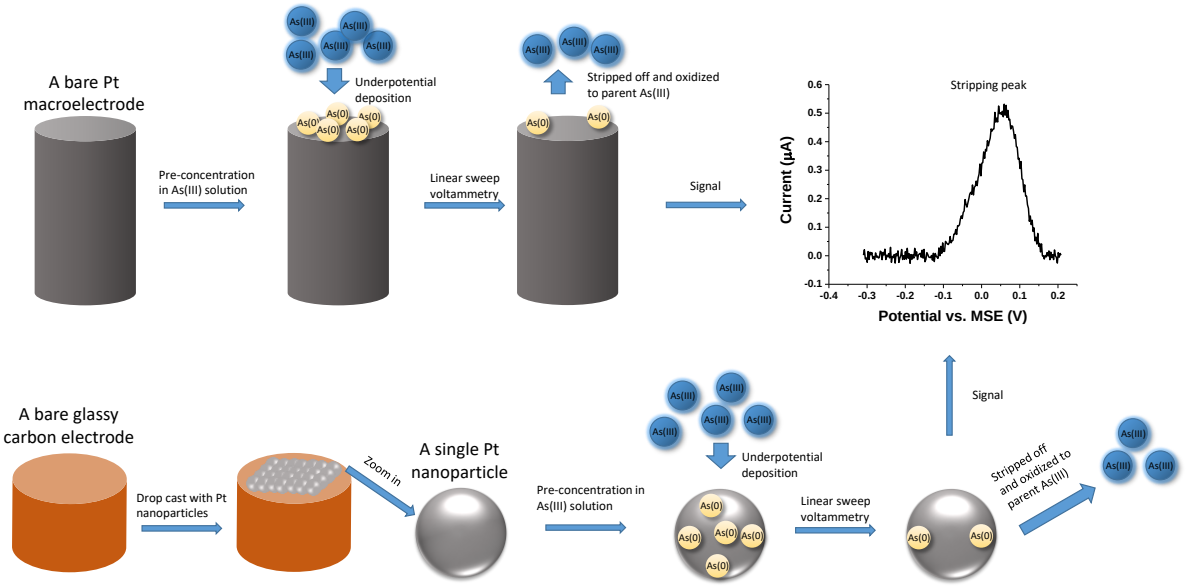

Figure 5.3 A schematic diagram representing the underpotential deposition and anodic stripping voltammetry on a Pt macroelectrode (top) and a Pt nanoparticle (bottom).

The method of using UPD-ASV method to detect arsenic is shown schematically in Figure 5.3. For Pt macroelectrodes, As(III) was reduced to As(0) and As atoms deposited onto the surface of Pt during pre-concentration. When an anodic potential sweep was applied to the electrode, As(0) ad-atoms were stripped off and oxidized to As(III) and a stripping peak was

obtained from the voltammograms. Analogous processes occurring for deposition/stripping from Pt nanoparticle-modified electrodes.

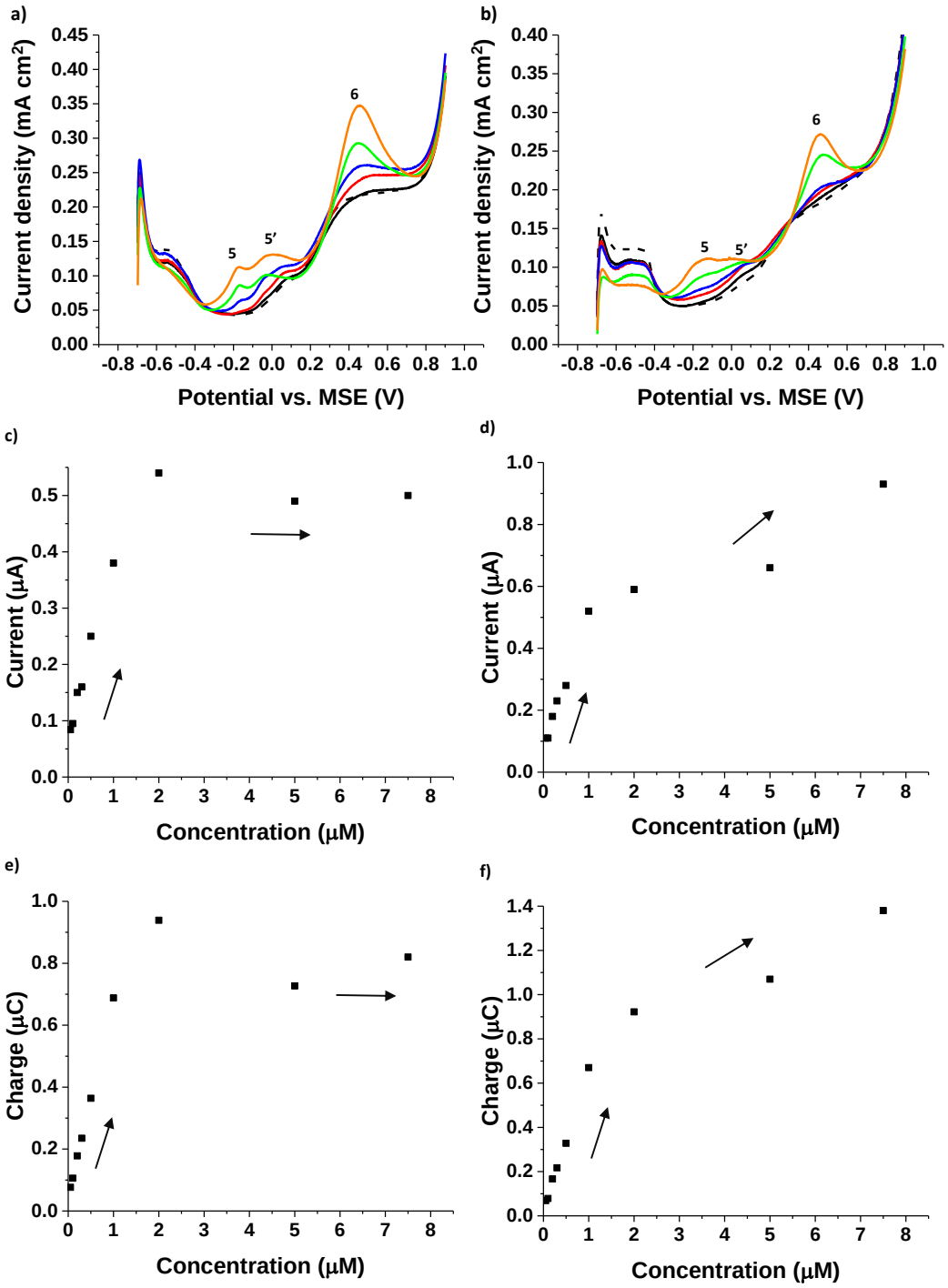

Figure 5.4 LSV curves of various concentrations of As(III) in 0.1 M H_2SO_4 at a) Pt macroelectrode and b) Pt nanoparticle-modified GC electrode. The concentrations of As(III) were 0 µM (black dash line), 0.5 µM (black solid line), 1 µM (red), 2 µM (blue), 5 µM (green) and 7.5 µM (orange). Peak current of peak 5' vs. concentrations of As(III) at c) Pt macroelectrode and d) Pt nanoparticle-modified GCE. Charge of peak 5' vs. concentrations of As(III) at e) Pt macroelectrode and f) Pt nanoparticles GCE. The numbers in c), d), e) and f) were calculated from baseline corrected LSVs. LSV parameters: deposition at -0.7 V vs. MSE for 240s, potential scan rate 0.1 V s^{-1}.

Observations of As-related Peaks in ASV Figure 5.4a illustrates the linear sweep voltammetric response at a Pt macroelectrode in various concentrations of As(III) in 0.1 M H_2SO_4 after pre-concentration of As(0) and three arsenic-related peaks were observed as 5, 5' and 6. Peaks 5 and 6 were observed at ca -0.2 V and ca +0.4 V which corresponded to anodic stripping of bulk As(0) and oxidation of As(III) to As(V), respectively; the peak current of both peaks increased when the concentration of As(III) varies from 0 to 7.5 μM. Peak 5' at +0.05 V was assigned as the stripping peak associated with the oxidation of As(0) ad-atoms [50]. How the peak current of peak 5' varied with concentration of As(III) in solution at a Pt macroelectrode is plotted in Figure 5.4c. It is shown that the peak current of peak 5' increased with the concentration of As(III) and reached a plateau for As(III) concentrations higher than 2 μM. At higher concentrations the peak is obscured by the much larger peak 5. This observation sets the *upper* limit for detection with peak 5' at a Pt macroelectrode as 2 μM. A similar trend was observed by plotting the charge of peak 5' as a function of As(III) concentration as shown in Figure 5.4e. A limiting charge value of ca 9.4×10^{-7} C and a corresponding surface coverage of ca 1.7×10^{-10} mol cm^{-2} (see Appendix section 4 for calculation), are consistent with a sub-monolayer of As(0) ad-atoms deposited onto the surface of Pt.

The same experiment was conducted on a Pt nanoparticle-modified GCE. Figure 5.4b shows the linear sweep voltammetric response at the Pt nanoparticle-modified GCE in which contained approximately 0.1 monolayers of Pt nanoparticles (shown in the section 1 of Appendix). The voltammetric features observed (peaks 5, 5' and 6) are similar in potential and peak shape to that at Pt macroelectrode, which were at -0.2V, +0.05 V and +0.4V, respectively. Calbelka *et al* also reported the As ad-atoms oxidation peak at ca +0.01 V [50], which was similar to our experimental result of peak 5' on both Pt macroelectrode and Pt nanoparticle-modified electrode. Accordingly the peak 5' was assigned as the stripping peak of deposited

As(0) ad-atoms on surface of Pt. The plots illustrating how the peak current and charge of peak 5' varies as a function of As(III) concentration at a Pt nanoparticle-modified electrode are presented in Figures 5.4d and f, respectively. Similar to the bulk Pt, the peak current and charge increased approximately linearly from 0.05 to 2 μM and the slope started to decrease at 2 μM with a charge value of As deposited on the surface as ad-atoms of ca 9×10^{-7} C (ca 0.02 monolayers). The enhancement of signal in Figures 5.4d and f indicate that there were more available deposition sites at the surface of Pt nanoparticles than at bulk Pt for the coverages employed. The coverages were calculated to be less than one monolayer, the exact value reflecting the assumptions made during the estimations in which we assumed only As atoms were closely packed on the surface of the electrode to form a monolayer, however, the oxygen of arsenite may also be adsorbed onto the surface of the electrode, and the estimated coverage of As atoms may be lower than that in reality (See calculations in Appendix Sections 4 and 5).

Table 5.2 Analysis of peak 5' measured in 2 μM As(III) at a Pt macroelectrode and at a Pt nanoparticle-modified GCE. LSV parameters: deposition at -0.7 V vs. MSE for 240s, potential scan rate 0.1 V s^{-1}.

	Concentration (μM)	Charge (C)	Surface area of Pt (cm^2)	Number of moles of As (mol)	Coverage of As ad-atoms (mol cm^{-2})	Monolayers of As ad-atoms
Pt macroelectrode	2	9.4×10^{-7}	0.02	3.3×10^{-12}	1.7×10^{-10}	0.14
Pt nanoparticle-modified electrode	2	9×10^{-7}	0.11	3.2×10^{-12}	2.6×10^{-11}	0.02

Table 5.2 shows the estimated coverage of As ad-atoms from the analysis of peak 5' of ASV at both Pt macroelectrode and Pt nanoparticle-modified GCE with the assumption that As ad-atoms were closely packed on Pt surface. The geometric area was used for Pt macroelectrode while for Pt nanoparticle-modified electrode, the total area of Pt nanoparticles

was used in the analysis. The number of Pt nanoparticles presented on the electrode surface was estimated to be ca 9×10^8 and each nanoparticle to have a surface area of 1.2×10^{-10} cm^2 assuming each particle to be a sphere of radius 15 nm with a roughness factor of 4.4 ± 1.1 [58]. Detailed calculations for Pt macroelectrodes and Pt nanoparticle-modified electrodes are shown in Appendix sections 4 and 5, respectively. The coverage and layers of As ad-atoms at bulk Pt were much higher than that at Pt nanoparticles, which was contributed by the larger surface area of the mesoporous Pt nanoparticles. The continuous increase towards a limiting value of the peak current (Figure 5.4d) and charge (Figure 5.4f) of peak 5' at Pt nanoparticle-modified electrode with concentrations of As(III) higher than 2 μM, is as expected for UPD with the limiting value approaching that of ca one monolayer. Based on the experimental results, under the conditions studied there were less than one monolayer of As ad-atoms deposited onto the surface of Pt even increasing the concentrations of As(III) or lengthening the deposition time. The analytical measurements in this study were thus based on the sub-monolayer of deposited As(0) ad-atoms.

Although linear responses of peaks 5 and 6 as a function of concentration of As(III) in the range 1 to 7.5 μM was observed (Figure A5.7 in Section 7 of Appendix) and these two features are suitable as the basis for the analysis of As(III) as already extensively reported in the literature [27], peak 5 was observed to be difficult to be observed at concentrations lower than 2 μM (150 ppb) and peak 6 had a detection limit of 1 μM (75 ppb) at both bulk Pt and Pt nanoparticles (Figures 5.4a and b). These two detection limits are much higher than the WHO limit for drinking water, 10 ppb. Further attention was thus focussed on the novel use of peak 5'.

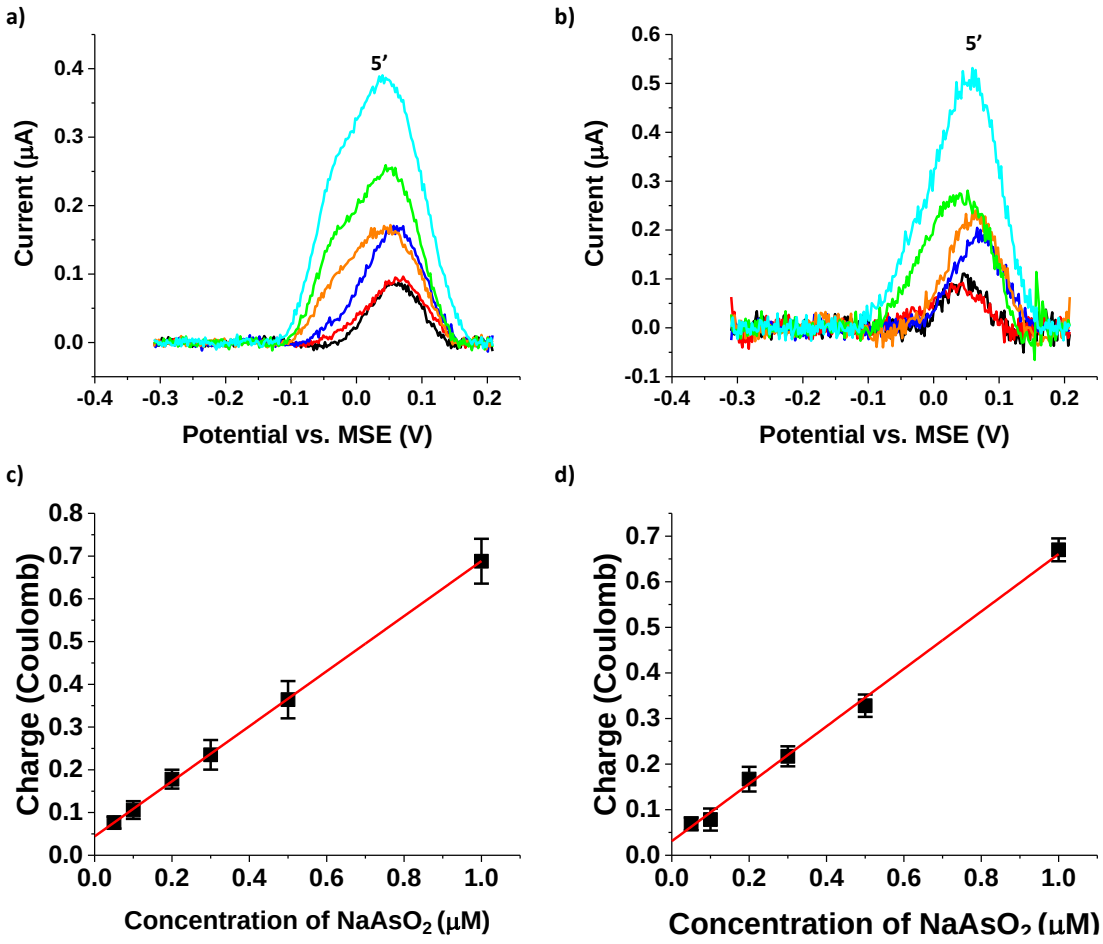

Figure 5.5 Baseline corrected LSV curves of various concentrations of As(III) in 0.1 M H_2SO_4 at a) Pt macroelectrode and b) Pt nanoparticle-modified GC electrode. The concentrations of As(III) were 0.05 μM (black), 0.1 μM (red), 0.2 μM (blue), 0.3 μM (orange), 0.5 μM (green) and 1 μM (cyan). Charge of stripped As(0) ad-atoms vs. the concentration of As(III) at c) Pt macroelectrode and d) Pt nanoparticle-modified GC electrode. The charge was calculated from baseline corrected LSVs and error bars were standard deviations calculated from at least sets of data. LSV parameters: deposition at -0.7 V vs. MSE for 240s, potential scan rate 0.1 V s^{-1}, and baseline was modelled via polynomial method from -0.3 V to +0.2 V for peak 5'.

Calibration Curves and Limits of Detection Figures 5.5a and b show the baseline corrected LSV of peak 5' with various concentrations of As(III) in 0.1 M H_2SO_4 at Pt macroelectrode and Pt nanoparticle-modified electrode, respectively. The full procedure for the baseline corrections is reported in Appendix section 6. The LSVs were obtained with the same procedure as above. Concentrations of As(III) were studied between 0.05 μM and 1 μM, to avoid the interference from peak 5. The peak height and peak width were seen to increase with the concentration of As(III) at both electrodes, corresponding to more As(0) deposited. Note that the estimated covered area of the Pt nanoparticles on GCE was ca 0.008 cm^2

(calculations shown in section 1 of Appendix), which was much smaller than the geometric area of the Pt macroelectrode, 0.02 cm^2. However, the surface area of particles were much larger than geometric area of Pt macroelectrode due to the mesoporous structure and the roughness of surface. The large surface area of mesoporous Pt nanoparticles contributed more deposition sites for As(0), and thus more arsenic ad-atoms can be deposited onto the surface of Pt nanoparticles and generate a similar sized signal as seen at bulk Pt.

The stripping peak of the As(0) ad-atoms (peak 5') was investigated for analytical use. Calibration curves were made at both electrodes (Figures 5.5c and d), and the linear relationship was obtained from 0.05 μM to 1 μM. A LOD of 0.05 μM, 4 ppb, was obtained at both electrodes and the sensitivities of 6.4×10^{-7} C μM^{-1} and 6.3×10^{-7} C μM^{-1} were obtained on bulk Pt and Pt nanoparticle-modified electrodes, respectively. Note that the quoted LOD is estimated on the basis of the visual identification of measureable signals from real samples rather than calculated based on the 3σ method. Examples of the smallest signals deemed 'measureable' are given in the section 8 of the Appendix.

The detection limit obtained using measureable, visually clear signals of 4 ppb meets the detection limits needed to implement the WHO guidelines for arsenic in drinking water (see Introduction). All these experiments were repeated 3 times and the variation was found to be less than 12% and 8% standard deviation at Pt macroelectrode and Pt nanoparticle-modified GCE, respectively.

5.3.3. Interference studies

Having established an analytical procedure based on the stripping of As(0) ad-atoms from Platinum surface, further experiments were conducted to explore if the possible presence of either Cu(II) or chloride ions interfered with the measurements.

Possible interference of Cu(II)

Cu(II) is a very commonly encountered interferent in stripping voltammetry of As since Cu forms alloys and intermetallic compounds with bulk As(0) [30]. Accordingly the interference of Cu(II) with detection of low concentrations of As(III) was studied using ASV by adding different amounts of Cu(II) in the solution. Figure 5.6a illustrates the baseline corrected LSV of 0.5 μM As(III) in 0.1 M H_2SO_4 with additions of Cu(II) (0.5 μM each time) at Pt macroelectrode with a potential range of - 0.3 V to + 0.2 V. The black dashed line was recorded for a solution without Cu(II) where only one peak was observed at ca + 0.05V corresponding to the oxidation of As ad-atoms [50]. With the addition of Cu(II), the signal of peak 5' varied negligibly and the peak potential did not shift. It can be therefore concluded that Cu(II) did not interfere to the oxidation peak of As ad-atoms. Similarly, Figure 5.6b shows the baseline corrected LSV of 0.5 μM As(III) in 0.1 M H_2SO_4 with additions of Cu(II) (0.5 μM each time) at Pt nanoparticle-modified GCE. Again the addition of Cu(II) did not change the signal of peak 5' or shift the potential of it by comparing the voltammograms obtained without (black dashed line in Figure 5.6b) and with Cu(II). We conclude that the formation of Cu-As alloys or intermetallic species was avoided by using As ad-atoms as the indicator.

We further considered the electrodeposition of Cu from high concentrations of Cu(II). The ASVs of 50 μM As(III) in 0.1 M H_2SO_4 with additions of Cu(II) (50 μM each) at bulk Pt and Pt nanoparticles are shown in Figure A5.9 in Section 9 of Appendix. It is shown that only when the concentration of Cu(II) reached 50 μM or higher, the Cu peak at ca - 0.4 V interfered with peak 5 and begins to overlap with peak 5' (Figure A5.9 in Section 9 of Appendix). The method is therefore robust against copper interference except at extremely high concentration where dilution might be used to circumvent the problem.

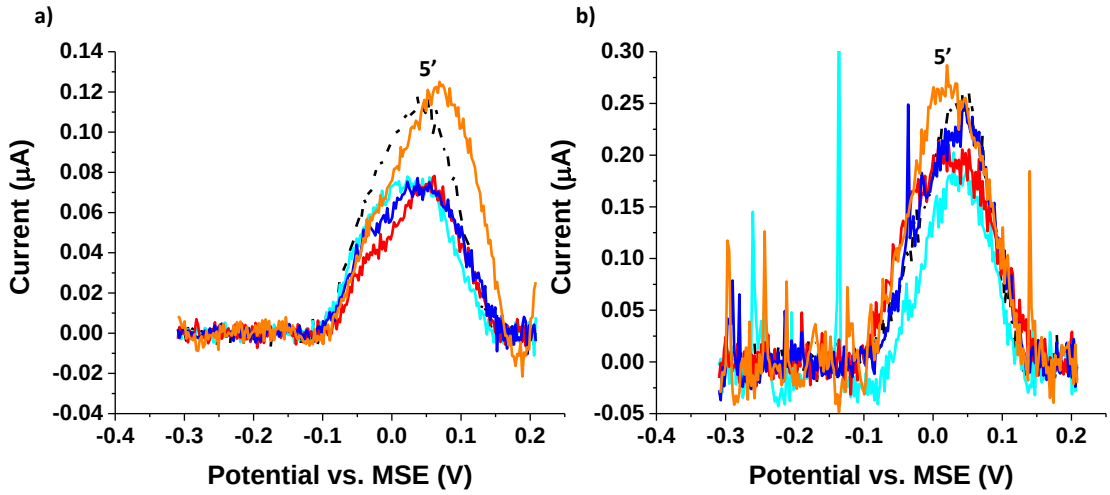

Figure 5.6 Baseline corrected LSV curves of Cu(II) additions (0.5 μM each) to 0.5 μM As(III) in 0.1 M H_2SO_4 in the potential range from -0.3 V to +0.2 V at a) Pt macroelectrode and b) Pt nanoparticle-modified GC electrode. LSV parameters: deposition at -0.7 V for 240s, scan rate was 0.1 V s^{-1}. Cu(II) concentration: 0 μM (black dash line), 0.5 μM (cyan), 1 μM (red), 1.5 μM (blue) and 2 μM (orange).

Possible interference of chloride

Chloride is known to be adsorbed onto Pt surfaces [61]. The peak of Pt to Pt oxide in 0.1 M H_2SO_4 is reported to be shifted to more positive potentials with the addition of 10 μM Cl^- [61]. Meanwhile, the reduction peak of the Pt oxide shifted to less negative potentials. The peak current of oxide formation did not change while the peak current of the oxide removal was reduced with the addition of chloride. Pempegowda et al applied graphene-Pt nanoparticle-modified GCE for As(III) detection with SWASV where chloride was reported as an interferent but only at concentrations above 450 μM [36]. Therefore, the possible interference of chloride under low As(III) concentrations conditions was considered and investigated using ASV in this section.

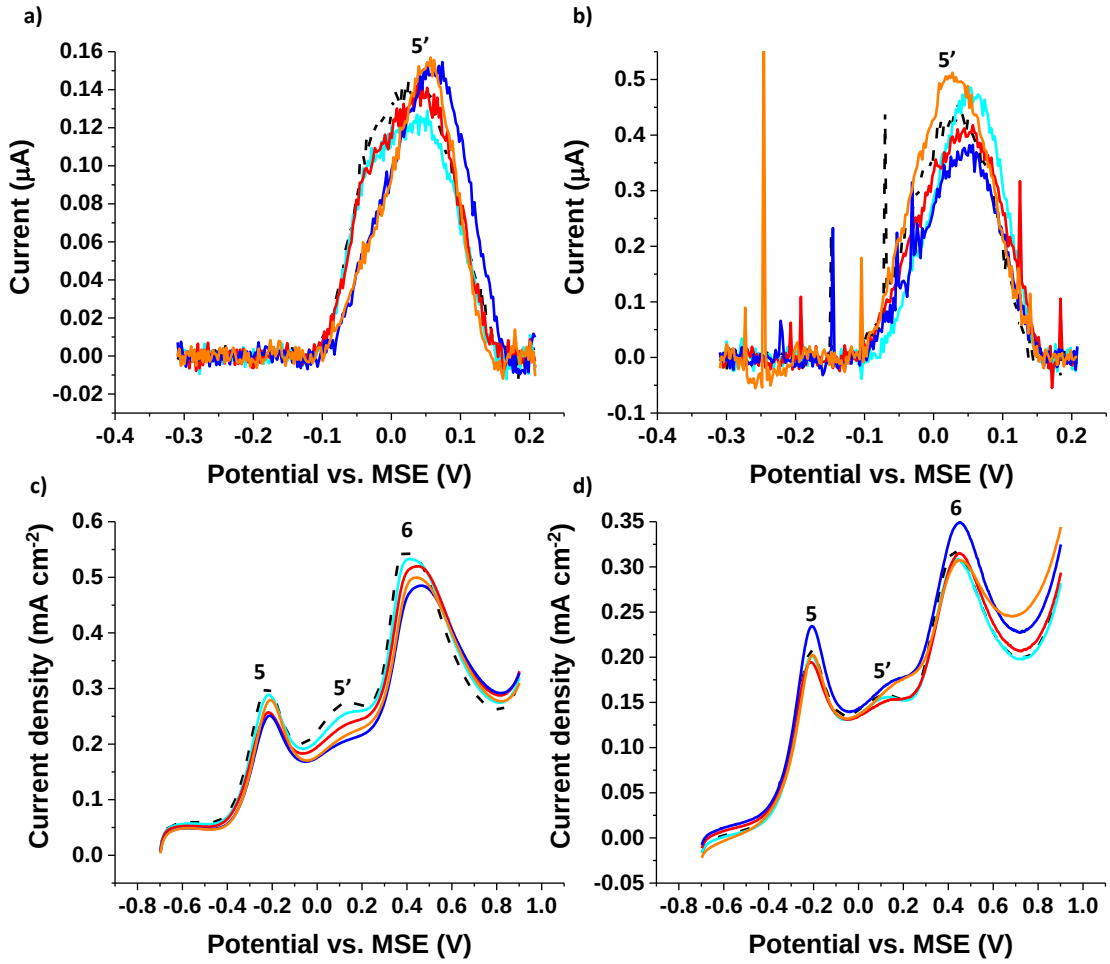

Figure 5.7 Baseline corrected LSV curves of Cl^- additions (0.5 µM each) to 0.5 µM As(III) in 0.1 M H_2SO_4 in the potential range from - 0.3 V to + 0.2 V at a) Pt macroelectrode and b) Pt nanoparticle-modified GCE. Cl^- concentration: 0 µM (black dash line), 0.5 µM (cyan), 1 µM (red), 1.5 µM (blue) and 2 µM (orange). LSV curves of Cl^- additions (50 µM each) to 50 µM As(III) in 0.1 M H_2SO_4 in the potential range from -0.7 V to +0.9 V at c) Pt macroelectrode and d) Pt nanoparticle-modified GC electrode. Cl^- concentrations: 0 µM (black dash line), 50 µM (cyan), 100 µM (red), 150 µM (blue) and 200 µM (orange). LSV parameters: deposition at - 0.7 V for 240s, scan rate was 0.1 V s^{-1}.

Figure 5.7a displays the baseline corrected LSVs of 0.5 µM As(III) in 0.1 M H_2SO_4 in the presence of 0.5 (cyan), 1 (red), 1.5 (blue) and 2 µM (orange) chloride at a Pt macroelectrode with a potential range of - 0.3 V to + 0.2 V. Pre-concentration of As(0) ad-atoms was carried out at - 0.7 V for 240 s and LSV was subsequently conducted from - 0.7 V to + 0.9 V at a scan rate of 0.1 V s^{-1}. With the addition of chloride, the signal of peak 5' at ca + 0.05 V did not change in both peak current and peak potential indicating negligible interference of chloride at these concentrations. The response at higher concentrations is shown in Figure 5.7c for 50 µM As(III) in 0.1 M H_2SO_4 in the presence of 50 (cyan), 100 (red), 150 (blue) and 200 µM (orange)

chloride at a Pt macroelectrode. Three peaks labelled as peaks 5, 5’ and 6 were observed at ca - 0.25 V, ca + 0.05 V and ca + 0.4 V, which were ascribed to the oxidation of bulk As(0), oxidation of As ad-atoms and oxidation of As(III) to As(V), respectively [27, 50]. The black dashed line was recorded for a solution without chloride. It is obvious that the chloride did not interfere with peaks 5 and 6 as literature presented [36]. The signal of peak 5’ was reduced suggesting an upper limit of ca 100 μM above which the analytical use of the peak is not possible probably due to competitive adsorption between As and chloride. Similar limits were observed at Pt nanoparticle-modified electrodes (see Figures 5.7b and d). The sensitivity to chloride imposes limitations for the range of samples amenable to analysis via the proposed method [62].

5.4. Conclusions

The analytical use of under-potential deposition of As on platinum surface combined with anodic stripping of the adsorbed As atoms has been explored using both platinum macro-electrodes and platinum nanoparticle-modified electrodes. A limit of detection within the requirements imposed by the WHO guidelines for safe drinking water was observed with the significant merit that the determinations were free from interference by Cu(II) which often blights the use of ASV when bulk As is deposited. On the other hand, the method was sensitive to the presence of chloride which likely limits the analytical application to largely chloride free media, for example to bottled mineral waters. No particular relative merits of using nanoparticle-modified electrodes over platinum macro-electrodes were observed with similar limits of detection measured. In the next chapter explores under potential deposition on gold electrodes to avoid the chloride interference problem.

5.5. Appendix

Section 1: Calculation of the coverage of Pt nanoparticles on the surface of a glassy carbon electrode (GCE)

To estimate the approximate coverage of nanoparticles in terms of monolayers deposited a cubic close packed arrangement was considered. The Pt nanoparticles as purchased from NanoComposix, have a diameter of ca 30 nm. Hence the area occupied by a single particle on the electrode is 9×10^{-16} m^2 (Figure A5.1). The particle concentration of the Pt nanoparticles used were 1.8×10^{11} particles mL^{-1} [63] and there were 5 μL of Pt nanoparticles suspension dropped onto the electrode. Thus, the number of particles that dropped onto the electrode can be estimated as 9×10^8 particles.

For 5 μL of Pt nanoparticles suspension, the covered/blocked area of particles by the nanoparticles is:

$$9 \times 10^{-16}\, m^2 \times 9 \times 10^8\, particles = 0.008\, cm^2 \quad (5\text{-}1)$$

The particles were drop casted on to a GCE with an area of 0.07 cm^2 hence the approximate monolayer coverage is

$$\frac{0.008\, cm^2}{0.07\, cm^2} = 0.1 \quad (5\text{-}2)$$

The number of moles of Pt nanoparticles on the surface of the GCE is

$$\frac{9 \times 10^8\, particles}{6.02 \times 10^{23}\, mol^{-1}} = 1.5 \times 10^{-15}\, mol \quad (5\text{-}3)$$

Then the estimated surface coverage of Pt nanoparticles on GCE is

$$\frac{1.5 \times 10^{-15}\, mol}{0.07\, cm^2} = 2 \times 10^{-14}\, mol\, cm^{-2} \quad (5\text{-}4)$$

The surface area of each Pt nanoparticle was calculated assuming it is a sphere of radius 15 nm:

$$4 \times \pi \times 15\, nm^2 = 2.8 \times 10^3\, nm^2 = 2.8 \times 10^{-11} cm^2 \quad (5\text{-}5)$$

The surface area of each Pt nanoparticle was estimated assuming each particle to be a sphere with a roughness factor of 4.4 ± 1.1 [58], the approximate surface area of each particle is 1.2×10^{-10} cm^2.

The total surface area of the drop casted Pt nanoparticles was also calculated based on the number of particles times the surface area of each particle, which is:

$$9 \times 10^8 particles \times 4 \times \pi \times 15\, nm^2 = 2.5 \times 10^{12}\, nm^2 = 0.025\, cm^2 \quad (5\text{-}6)$$

Recognising the roughness of the particles is characterised by a roughness factor of 4.4 ± 1.1 [58], the approximate area of Pt available for As deposition is 0.11 cm^2.

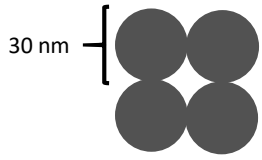

Figure A5.1 A scheme of possible distribution of Pt nanoparticles with a size of 30 nm on surface of GCE.

Section 2: Optimization of the deposition potential

The deposition potential for the underpotential deposition was determined. The CV in Figure 5.9 in the main text shows no discernible feature for the deposition of As ad-atoms since this is likely obscured by the deposition of bulk As, peak 5. However the stripping peak of As ad-atoms was observed at ca +0.05 V in Figure 5.4 of the main text. The purpose of this section is to determine the potential of the ad-atom deposition by considering oxidative voltammograms following deposition at different cathodic limits. Figures 5.9a and b show voltammograms for bulk Pt and Pt nanoparticles respectively with deposition potentials between - 0.6 and - 0.8 V. It can be seen that peak 5' is absent when As is deposited at - 0.6V

but appears in both cases when more negative deposition potentials are used. It is inferred that the deposition potential of the As ad-atoms is ca - 0.7V ± 0.5 V. If the deposition potential was more negative than - 0.7 V, it would suffer the problem from solvent breakdown at both bulk Pt (Figure 5.9a) and Pt nanoparticles (Figure 5.9b). Thus, - 0.7 V was used for the deposition potential.

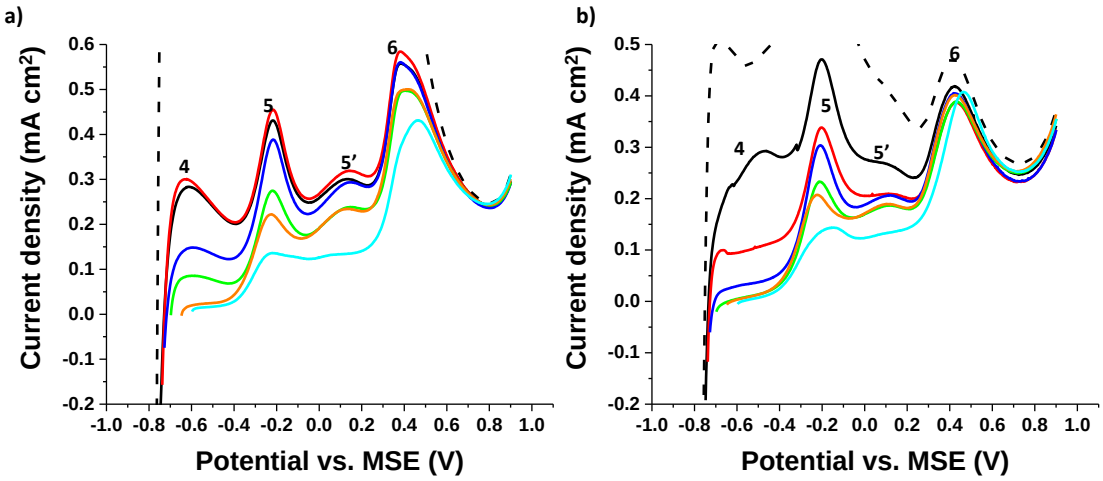

Figure A5.2 LSV curves of 50 µM As(III) in 0.1 M H_2SO_4 at a) Pt macroelectrode and b) Pt nanoparticle-modified GC electrode. LSV parameters: deposition for 210s at different potentials, scan rate was 0.1 V s^{-1}. The deposition potentials are -0.8V (black dash line), -0.75V (black solid line), -0.74V (red), -0.73V (blue), -0.7V (green), -0.65V (orange) and -0.6V (cyan).

Section 3: Optimization of the deposition time

Deposition time during the pre-concentration was also important and need to be determined. The purpose of this section is to determine the time of the ad-atom deposition by considering oxidative voltammograms following peak signal at different deposition time. Figures A5.3 a and b illustrate the LSVs for bulk Pt and Pt nanoparticles respectively with deposition time from 60 s to 300 s. The deposition potential was -0.7 V for all experiments and the scan rate was 0.1 V s^{-1}. Three peaks were observed and labelled as 5, 5' and 6. Peaks 5 and 5' were observed at ca -0.2 V and ca +0.05 V, and represented oxidation peak of bulk As(0) and As ad-atoms, respectively [50]. Peak 6 at ca +0.4 V was ascribed to the oxidation of As(III) to As(V) [27, 50]. It can be seen in both cases that if the deposition time increased, the signal

of peak 5' were enhanced until the deposition time reached to ca 240 s (Figures A5.3 c and d). Thus, the deposition time was chosen to be 240 s for the rest of the study.

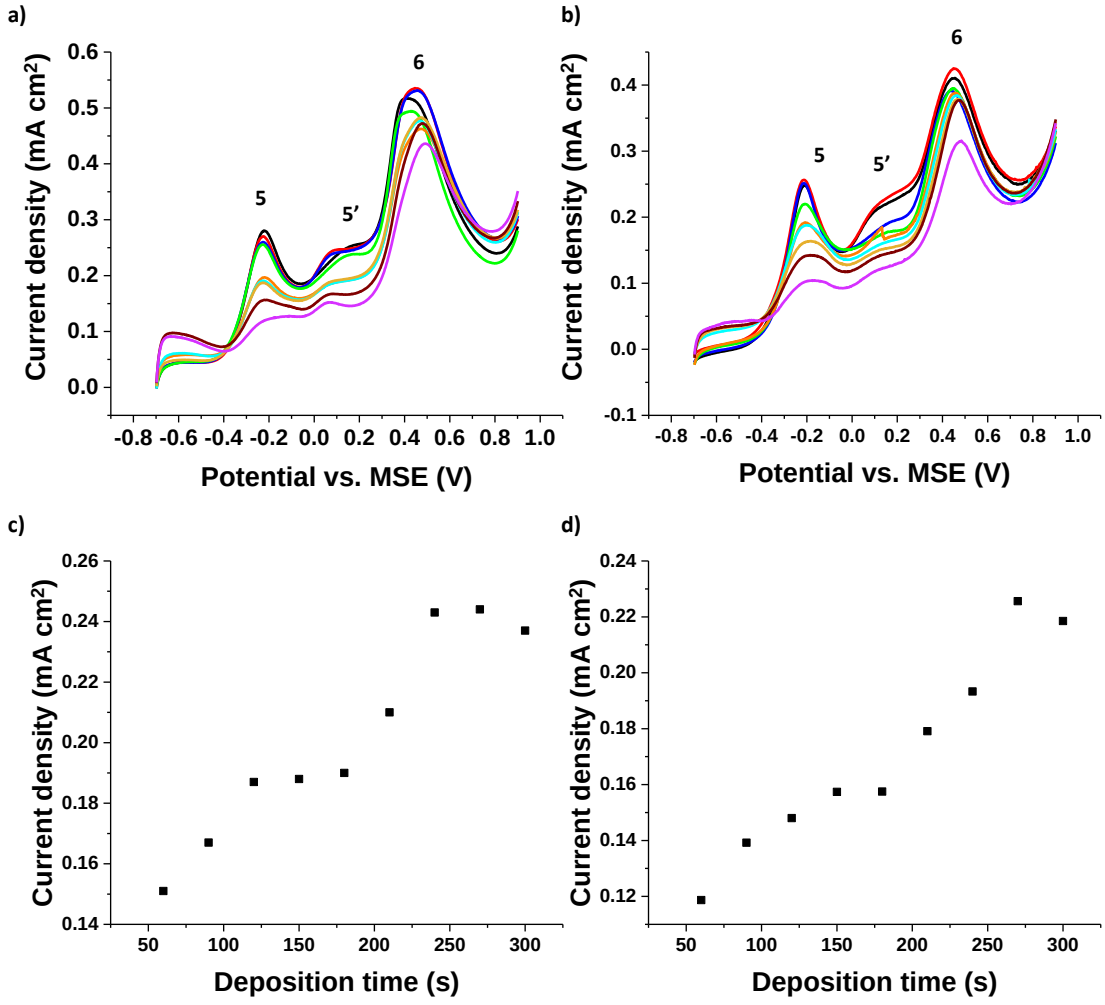

Figure A5.3 LSV curves of 50 µM As(III) in 0.1 M H_2SO_4 at a) Pt macroelectrode and b) Pt nanoparticle-modified GC electrode. LSV parameters: deposition at -0.7V for different time, scan rate was 0.1 V s^{-1}. The deposition times are 300s (black), 270s (red), 240s (blue), 210s (green), 180s (orange), 150s (cyan), 120s (yellow), 90s (purple) and 60s (pink). Plots of current densities of peak 5' vs. deposition time at c) Pt macroelectrode and d) Pt nanoparticle-modified GCE.

Section 4: Calculation of the surface coverage of As during pre-concentration on bulk Pt

The area of peak 5' can be calculated via 'Integrate' in Origin 2017. The area of the peak 5' of 2 µM As(III) in 0.1 M H_2SO_4 at Pt nanoparticle-modified GCE was 9.4×10^{-8} (Figure A5.4b). The charge (Q) of the peak then can be estimated as:

$$Q = \frac{Area\ of\ peak}{Scan\ rate} = 9.4 \times 10^{-7}\ C \qquad (5\text{-}7)$$

The corresponding number of electrons then was estimated as:

$$\frac{Charge\ of\ peak\ 5\prime}{Elementary\ charge} = \frac{9.4 \times 10^{-7}\ C}{1.6 \times 10^{-19}\ C} = 5.9\ \times\ 10^{12} \quad (5\text{-}8)$$

The number of moles of electrons was calculated as:

$$\frac{Number\ of\ electrons}{Avogadro\ constant} = \frac{5.9 \times 10^{12}}{6.02 \times 10^{23}\ mol^{-1}} =\ 9.8\ \times\ 10^{-12}\ mol \quad (5\text{-}9)$$

Each As(III) ion has three electrons transferred during the electrochemical reaction. Thus, the number of moles of As can be estimated as:

$$\frac{Moles\ of\ electrons}{3} = \frac{9.8 \times 10^{-12}\ mol}{3} = 3.3\ \times\ 10^{-12}\ mol \quad (5\text{-}10)$$

The surface area of Pt macroelectrode (with radius of 0.075 cm) is 0.02 cm^2 or 2×10^{12} nm^2. Hence, the estimated surface coverage of As on the surface of Pt could be obtained assuming As atoms were closely packed on the surface of electrode (Figure A5.4a):

$$\frac{Moles\ of\ As}{Surface\ area\ of\ Pt\ macroelectrode} = \frac{3.3 \times 10^{-12}\ mol}{0.02\ cm^2} = 1.7\ \times\ 10^{-10}\ mol\ cm^2 \quad (5\text{-}11)$$

The number of monolayers of As ad-atoms were also estimated. The radius of As atom is 185 pm [64] and diameter is 370 pm. The covered area of single As atom (d^2) is calculated to be 0.14 nm^2.

The number of As deposited can be calculated from the number of moles of As and Avogadro constant, and it is:

$$Moles\ of\ As \times Avogadro\ constant = 3.3\ \times\ 10^{-12}\ mol\ \times\ 6.02\ \times\ 10^{23}\ mol^{-1}\ = 2\ \times\ 10^{12} \quad (5\text{-}12)$$

The number of one monolayer of As atoms on the surface of Pt electrode was estimated assuming As atoms were closely packed on Pt (Figure A5.4a):

$$\frac{Surface\ area\ of\ Pt\ macroelectrode}{Covered\ area\ of\ single\ As\ atom} = \frac{2 \times 10^{12}\ nm^2}{0.14\ nm^2} = 1.4\ \times\ 10^{13} \qquad (5\text{-}13)$$

Therefore, the number of layers of As atoms on Pt is:

$$\frac{Number\ of\ As\ atoms\ deposited}{Number\ of\ one\ monolayer\ of\ closely\ packed\ As\ atoms} = \frac{2 \times 10^{12}}{1.4 \times 10^{13}} = 0.14 \qquad (5\text{-}14)$$

This corresponds to a sub-monolayer (ca 0.14 monolayers) of As atoms on the surface of Pt.

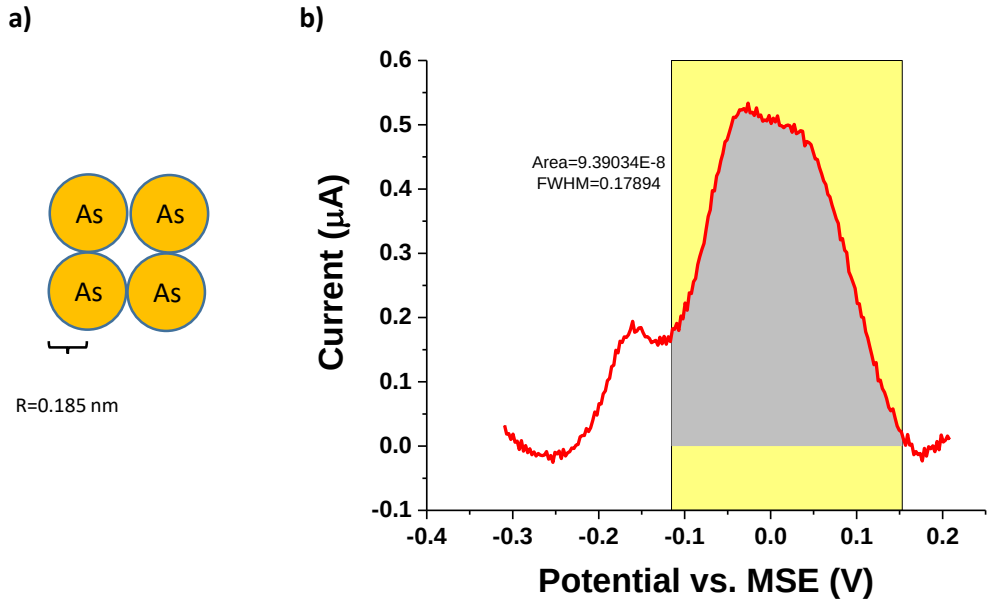

Figure A5.4 a) A scheme of As atoms closely packed at the surface of Pt. b)The baseline corrected LSV curves of peak 5' of 2 µM As(III) in 0.1 M H_2SO_4 at Pt macroelectrode. The grey areas are used for the integration. LSV parameters: deposition at -0.7 V vs. MSE for 240s, potential scan rate 0.1 V s^{-1}, and baseline was modelled via polynomial method from -0.3 V to +0.2 V for peak 5'.

Section 5: Calculation of the surface coverage of As after pre-concentration on Pt nanoparticles

The area of peak 5' was obtained via integration using Origin 2017. The peak was measured using 2 µM As(III) in 0.1 M H_2SO_4 at a Pt nanoparticle-modified GCE (Figure A5.5b) and gave a charge (Q) of 9.2×10^{-7} C.

The corresponding number of electrons was estimated as:

$$\frac{Charge\ of\ peak\ 5\prime}{Elementary\ charge} = \frac{9.2 \times 10^{-7}\ C}{1.6 \times 10^{-19}\ C} = 5.8\ \times\ 10^{12} \quad (5\text{-}15)$$

The number of moles of electrons was calculated as:

$$\frac{Number\ of\ electrons}{Avogadro\ constant} = \frac{5.8 \times 10^{12}}{6.02 \times 10^{23}\ mol^{-1}} = 9.6\ \times\ 10^{-12}\ mol \quad (5\text{-}16)$$

Each As(III) ion has three electrons transferred during the electrochemical reaction. Thus, the number of moles of As can be estimated as:

$$\frac{Moles\ of\ electrons}{3} = \frac{9.6 \times 10^{-12}\ mol}{3} = 3.2\ \times\ 10^{-12}\ mol \quad (5\text{-}17)$$

The estimated surface area of drop casted Pt nanoparticles was also calculated. It was assumed that each nanoparticle was spherical with a radius of 15 nm and a roughness factor of 4.4 ± 1.1 [58]. The estimated surface area of the rough sphere is

$$Roughness\ factor \times Number\ of\ particles \times 4 \times \pi \times r^2 = 4.4 \times 9\ \times\ 10^8\ particles\ \times\ 4\ \times\ \pi\ \times\ 15\ nm^2 = 1.1\ \times\ 10^{13}\ nm^2 = 0.11\ cm^2 \quad (5\text{-}18)$$

Then the estimated surface coverage of As on the surface of Pt nanoparticles can be:

$$\frac{Moles\ of\ As}{Estimated\ surface\ area\ of\ Pt\ nanoparticles} = \frac{3.2 \times 10^{-12}\ mol}{0.11\ cm^2} = 2.9\ \times\ 10^{-11}\ mol\ cm^{-2} \quad (5\text{-}19)$$

The number of As atoms can be calculated from the moles of As and the Avogadro constant, is:

$$Number\ of\ moles\ of\ As \times Avogadro\ constant = 3.2\ \times\ 10^{-12}\ mol\ \times\ 6.02\ \times\ 10^{23}\ mol^{-1}\ = 1.9\ \times\ 10^{12} \quad (5\text{-}20)$$

The As atoms were assumed to be deposited on the surface of every single Pt nanoparticles as Figure A5.5a shows. The number of As atoms per nanoparticle were estimated based on the covered area of single As atom and the number of drop casted Pt nanoparticles:

$$\frac{Number\ of\ As}{Number\ of\ Pt\ nanoparticles} = \frac{1.9 \times 10^{12}}{9 \times 10^{8}} = 2100\ atoms \qquad (5\text{-}21)$$

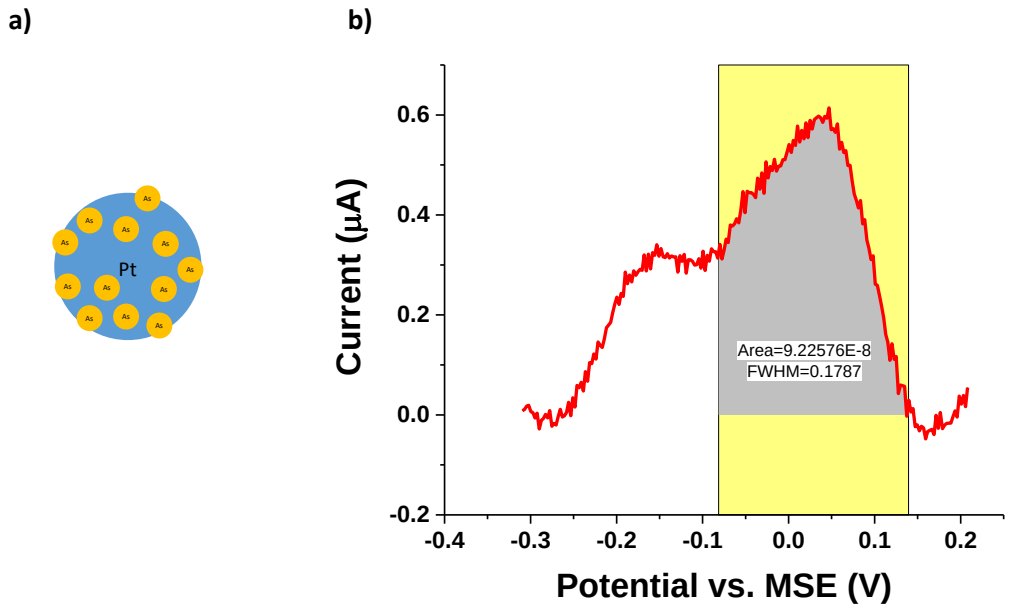

Figure A5.5 a) A scheme of As atoms deposited on the Pt nanoparticles. b) The baseline corrected LSV curves of peak 5' of 2 µM As(III) in 0.1 M H_2SO_4 at Pt nanoparticle-modified GCE. The grey areas in are used for the integration. LSV parameters: deposition at -0.7 V vs. MSE for 240s, potential scan rate 0.1 V s^{-1}, and baseline was modelled via polynomial method from -0.3 V to +0.2 V for peak 5'.

The surface area of each Pt nanoparticle was calculated to be 1.2 × 10^{-10} cm^2 assuming each particle to be a sphere of radius 15 nm with a roughness factor of 4.4 ± 1.1 [58]. Then the area per As atoms on a single Pt nanoparticle can be calculated from the estimated surface area of the rough sphere particles and number of As atoms per Pt nanoparticle:

$$\frac{Estimated\ surface\ area\ of\ each\ Pt\ nanoparticle}{Number\ of\ As\ atoms\ per\ nanoparticle} = \frac{1.2\times10^{-10}\ cm^2}{2100\ atoms} = 6 \times 10^{-14}\ cm^2 = 6\ nm^2 \qquad (5\text{-}22)$$

This corresponds to ca 0.02 monolayers on the surface of a single nanoparticle.

Section 6: Baseline correction for peak 5'

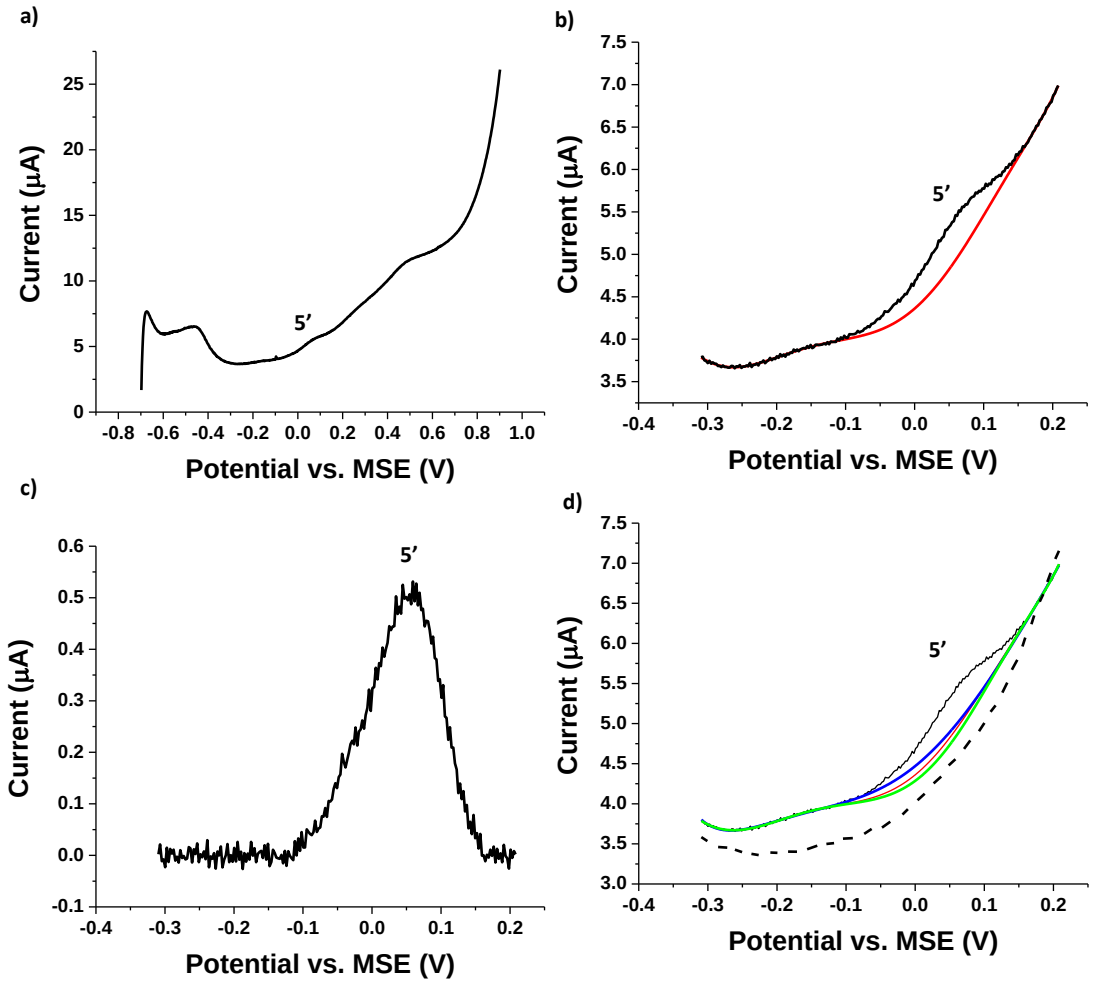

Figure A5.6 a) The original LSV curve of 1 μM As(III) in 0.1 M H_2SO_4 at Pt nanoparticles GCE. b) The LSV curve from -0.3 V to +0.2 V (black line) and simulated baseline (red line). c) The baseline corrected LSV curve from -0.3 V to +0.2 V. d) The LSV curve of 1 μM As(III) from -0.3 V to +0.2 V (black line), LSV curve of 0.1 M H_2SO_4 (black dashed line), 7^{th} order polynomial caseline (red line), 6^{th} order polynomial baseline (blue line) and 8^{th} order polynomial baseline (green line). LSV parameters: deposition at -0.7 V vs. MSE for 240s, potential scan rate 0.1 V s^{-1}.

The baseline was simulated via 'polynomial' method in Origin 2017. An example calculation of baseline correction of 1 μM As(III) in 0.1 M H_2SO_4 at Pt nanoparticles GCE is shown below.

At first, a LSV curve can be obtained from the electrochemical experiments and peak 5' can be seen at ca +0.05 V (Figure A5.6a). Then the LSV curve was zoomed in for the potential window from - 0.3 V to + 0.2 V because the peak 5' was in this range (black line in

Figure A5.6b). The baseline of peak 5' was then simulated from ca -0.15 V to ca +0.1 V with a polynomial order of 7 (red line in Figure A5.6b). The reason to use the 7^{th} order polynomial is because it can fit the background best compared to other orders, such as 6^{th} and 8^{th} (Figure A5.6d). Finally, a baseline subtraction was accessed (black line subtract red line in Figure A5.6b) and a baseline corrected LSV was obtained (Figure A5.6c).

Similar baseline corrections were conducted to obtain baseline corrected LSVs at both bulk Pt and Pt nanoparticles in this study.

Section 7: Linear response of peaks 5 and 6 of As(III) at low concentration

The LSVs of 1 to 7.5 μM at a Pt macroelectrode and Pt nanoparticle-modified GCE for various concentrations of As(III) in 0.1 M H_2SO_4 after pre-concentration of As(0) are shown in Figures A5.7a and b, respectively. The plot of current densities of peak 5 observed at ca -0.2 V vs concentrations of As(III) on bulk Pt and Pt nanoparticles are shown in Figures A5.7c and d, respectively. The plot of peak 6 observed at ca +0.4 V are shown in Figures A5.7e and f. The peak current densities were calculated based on the geometric area of Pt macroelectrode, 0.02 cm^2 and Pt nanoparticles surface area, 0.11 cm^2 (calculations shown in Appendix section 1). Although a linear response can be observed from 1 (75 ppb) to 7.5 μM, the detection limit is above the WHO limit for drinking water (10 ppb). Thus, peaks 5 or 6 were not chosen to be used analytically for As(III) detection.

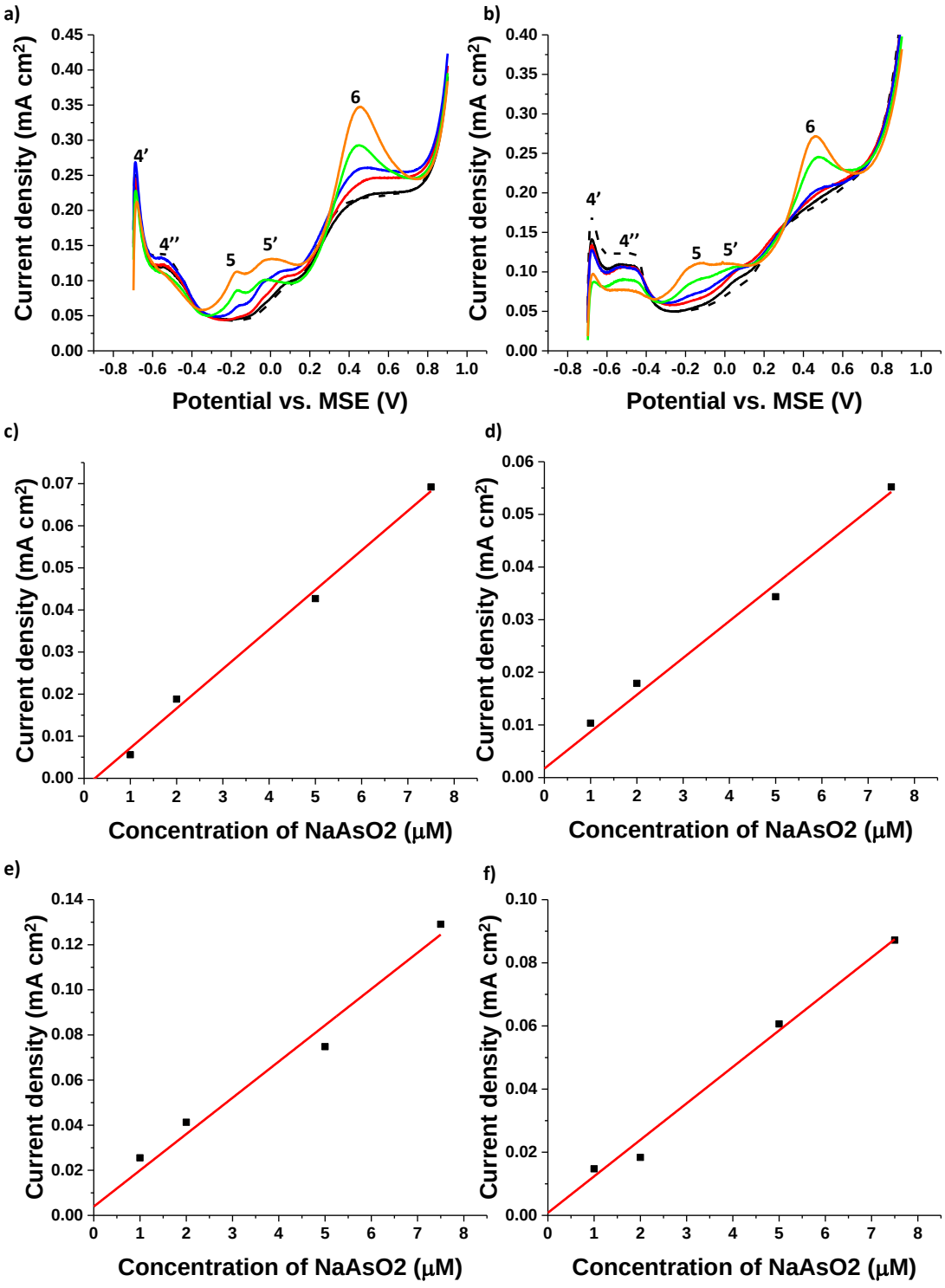

Figure A5.7 LSV curves of 1 to 7.5 µM As(III) in 0.1 M H_2SO_4 at a) Pt macroelectrode and b) Pt nanoparticle-modified GC electrode. LSV parameters: deposition at -0.7V for different time, scan rate was 0.1 V s^{-1}. The concentrations of As(III) were 0 µM (black dash line), 0.5 µM (black solid line), 1 µM (red), 2 µM (blue), 5 µM (green) and 7.5 µM (orange). Plots of current densities of peak 5 vs. As(III) concentrations at c) Pt macroelectrode and d) Pt nanoparticle-modified GCE, and of peak 6 vs. As(III) concentrations at e) Pt macroelectrode and f) Pt nanoparticle-modified GCE.

Section 8: Detection of lowest measurable signal

An example detection of lowest signal was shown in this section. The LSV curve of 0.05 µM As(III) in 0.1 M H_2SO_4 was obtained but the peak 5' at ca +0.05 V was not clear (Figure A5.8a). The LSV curve was zoomed in from -0.3 V to + 0.2 V for the baseline subtraction (black line in Figure A5.8b). A baseline was then simulated with the method shown in section 5 (red line in Figure A5.8b). After the baseline subtraction, a corrected peak 5' was observed (Figure A5.8c).

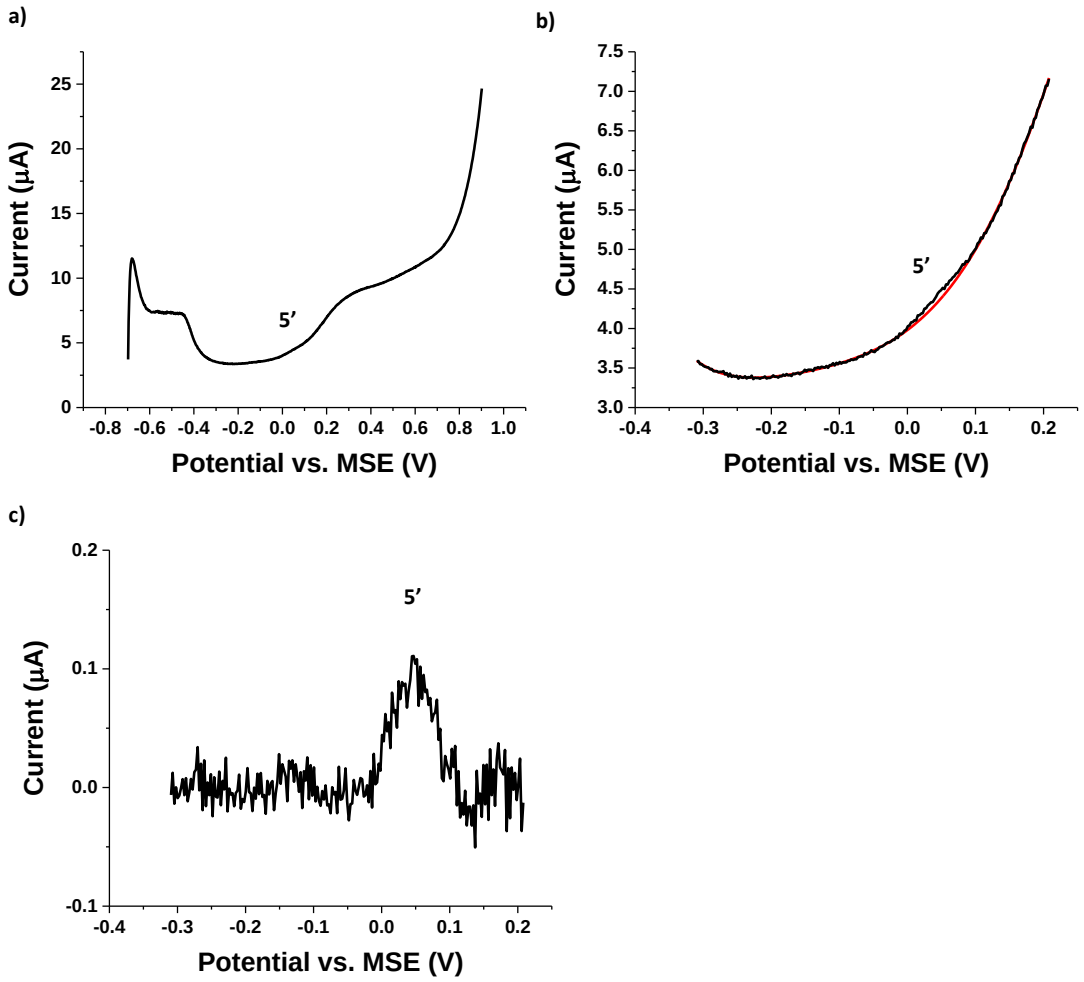

Figure A5.8 a) The original LSV curve of 0.05 µM As(III) in 0.1 M H_2SO_4 at Pt nanoparticles GCE. b) The LSV curve from -0.3 V to +0.2 V (black line) and simulated baseline (red line). c) The baseline corrected LSV curve from -0.3 V to +0.2 V. LSV parameters: deposition at -0.7 V vs. MSE for 240s, potential scan rate 0.1 V s^{-1}

Note that a negative dip can be seen at ca + 0.13 V, which was caused by the subtraction of the baseline simulated by a 7th order polynomial resulting from imperfect fitting leading to a tiny variation.

Section 9: Interference from Cu(II) in 50 µM As(III)

The interference of high concentrations of Cu(II) was studied. Figure A5.9a illustrates the LSV curves of 50 µM As(III) in 0.1 M H_2SO_4 with additions of Cu(II) (50 µM each) at Pt macroelectrode. Deposition was carried out at - 0.7 V for 240 s and LSV was conducted from - 0.7 V to + 0.9 V at a scan rate of 0.1 V s^{-1}. Four peaks labelled as Cu, 5, 5' and 6 were observed at ca - 0.35 V, ca - 0.25 V, ca + 0.05 V and ca + 0.4 V, which represented the oxidation peak of Cu(0) to Cu(II), oxidation of bulk As(0), oxidation of As adatoms and oxidation of As(III) to As(V), respectively [27, 50]. It can be seen clearly that the Cu peak interfered with peak 5 and peak 5' due to the small difference of peak potential and the overlap of those peaks (Figure A5.9a). The Cu peak did not interfered with peak 6 because the peak did not overlap with each other.

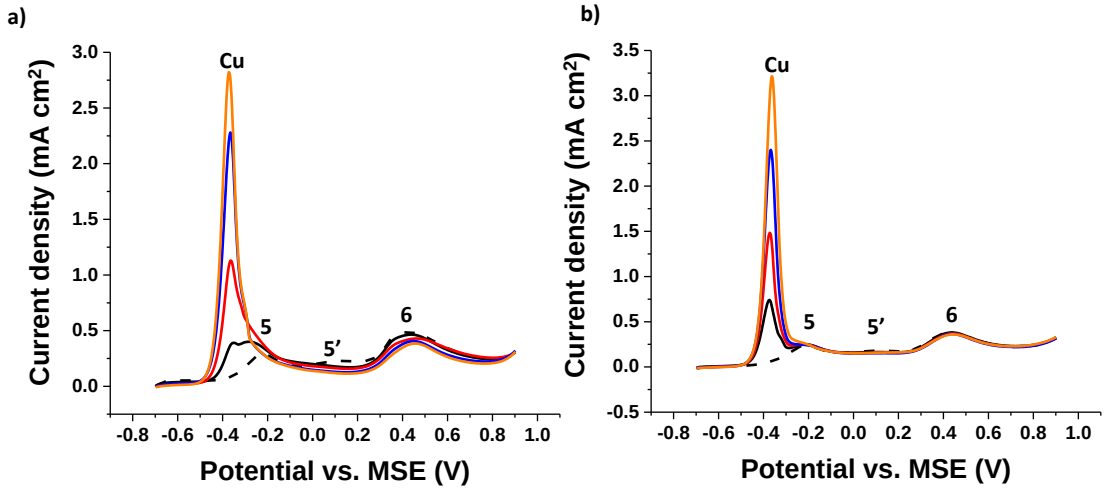

Figure A5.9 LSV curves of Cu(II) (50 µM each) to 50 µM As(III) in 0.1 M H_2SO_4 in the potential range from -0.7 V to +0.9 V (vs. MSE) at a) Pt macroelectrode and b) Pt nanoparticle-modified GC electrode. LSV parameters: deposition at -0.7 V for 240s, scan rate was 0.1 V s^{-1}. Cu(II) concentration: 0 µM (black dash line), 50 µM (black solid line), 100 µM (red), 150 µM (blue) and 200 µM (orange).

Similarly, the electrochemical features at Pt nanoparticles were discerned (Figure A5.9b) and assigned to the same electrochemical reactions [27, 50]. Still, the Cu peak interfered with peaks 5 and 5' but not peak 6. One of the possible methods to reduce the interference from the Cu(II) is to dilute the solution and the Cu(II) will not interfere with peak 5', which is shown in Figure 5.6.

5.6. Bibliography

[1] Y. Zhang, D. Li, R.G. Compton, Arsenic (III) Detection with Underpotential Deposition and Anodic Stripping Voltammetry, ChemElectroChem (2021).
[2] X.C. Xu, X.H. Niu, X. Li, Z.H. Li, D. Du, Y.H. Lin, Nanomaterial-based sensors and biosensors for enhanced inorganic arsenic detection: A functional perspective, Sens. Actuator B-Chem. 315 (2020) 13.
[3] S. Sikdar, M. Kundu, A Review on Detection and Abatement of Heavy Metals, ChemBioEng Rev. 5(1) (2018) 18-29.
[4] A.S. Maghsoudi, S. Hassani, K. Mirnia, M. Abdollahi, Recent Advances in Nanotechnology-Based Biosensors Development for Detection of Arsenic, Lead, Mercury, and Cadmium, Int. J. Nanomed. 16 (2021) 803-832.
[5] X.P. Yu, C.L. Liu, Y.F. Guo, T.L. Deng, Speciation Analysis of Trace Arsenic, Mercury, Selenium and Antimony in Environmental and Biological Samples Based on Hyphenated Techniques, Molecules 24(5) (2019) 23.
[6] S. Li, C. Zhang, S. Wang, Q. Liu, H. Feng, X. Ma, J. Guo, Electrochemical microfluidics techniques for heavy metal ion detection, Analyst 143(18) (2018) 4230-4246.
[7] P. Boffetta, C. Borron, Low-level exposure to arsenic in drinking water and risk of lung and bladder cancer: a systematic review and dose–response meta-analysis, Dose-Response 17(3) (2019) 1559325819863634.
[8] WHO, Guidelines for drinking-water quality Fourth Edition, WHO chronicle, 2011, pp. 104-8.
[9] J.M. Hao, M.J. Han, S.M. Han, X.G. Meng, T.L. Su, Q.W.K. Wang, SERS detection of arsenic in water: A review, J. Environ. Sci. 36 (2015) 152-162.
[10] M. Welna, A. Szymczycha-Madeja, P. Pohl, Comparison of strategies for sample preparation prior to spectrometric measurements for determination and speciation of arsenic in rice, Trac-Trends Anal. Chem. 65 (2015) 122-136.
[11] M.-L. Chen, L.-Y. Ma, X.-W. Chen, New procedures for arsenic speciation: A review, Talanta 125 (2014) 78-86.
[12] G.M. dos Santos, D. Pozebon, C. Cerveira, D.P. de Moraes, Inorganic arsenic speciation in rice products using selective hydride generation and atomic absorption spectrometry (AAS), Microchem. J. 133 (2017) 265-271.
[13] I. Komorowicz, A. Hanć, W. Lorenc, D. Barałkiewicz, J. Falandysz, Y. Wang, Arsenic speciation in mushrooms using dimensional chromatography coupled to ICP-MS detector, Chemosphere 233 (2019) 223-233.
[14] Y.-L. Feng, H.-Y. Chen, L.-C. Tian, H. Narasaki, Off-line separation and determination of inorganic arsenic species in natural water by high resolution inductively coupled plasma

mass spectrometry with hydride generation combined with reaction of arsenic (V) and L-cysteine, Anal. Chim. Acta 375(1-2) (1998) 167-175.
[15] H. Cheng, W. Zhang, Y. Wang, J. Liu, Graphene oxide as a stationary phase for speciation of inorganic and organic species of mercury, arsenic and selenium using HPLC with ICP-MS detection, Microchim. Acta 185(9) (2018) 1-8.
[16] F.W. Campbell, R.G. Compton, The use of nanoparticles in electroanalysis: an updated review, Anal. Bioanal. Chem. 396(1) (2010) 241-259.
[17] M.B. Gumpu, S. Sethuraman, U.M. Krishnan, J.B.B. Rayappan, A review on detection of heavy metal ions in water - An electrochemical approach, Sens. Actuator B-Chem. 213 (2015) 515-533.
[18] B. Bansod, T. Kumar, R. Thakur, S. Rana, I. Singh, A review on various electrochemical techniques for heavy metal ions detection with different sensing platforms, Biosens. Bioelectron. 94 (2017) 443-455.
[19] J. Wang, Stripping analysis: principles, instrumentation, and applications, Vch Pub1985.
[20] K. Brainina, E. Neyman, Electroanalytical stripping methods, John Wiley & Sons1994.
[21] J. Wang, Anodic stripping voltammetry as an analytical tool, Environ. Sci. Technol. 16(2) (1982) 104A-109A.
[22] L. Xiao, G.G. Wildgoose, R.G. Compton, Sensitive electrochemical detection of arsenic (III) using gold nanoparticle modified carbon nanotubes via anodic stripping voltammetry, Anal. Chim. Acta 620(1-2) (2008) 44-49.
[23] K. Pungjunun, S. Chaiyo, I. Jantrahong, S. Nantaphol, W. Siangproh, O. Chailapakul, Anodic stripping voltammetric determination of total arsenic using a gold nanoparticle-modified boron-doped diamond electrode on a paper-based device, Microchim. Acta 185(7) (2018) 1-8.
[24] E. Fischer, C.M. van den Berg, Anodic stripping voltammetry of lead and cadmium using a mercury film electrode and thiocyanate, Anal. Chim. Acta 385(1-3) (1999) 273-280.
[25] A.O. Simm, C.E. Banks, R.G. Compton, The electrochemical detection of arsenic (III) at a silver electrode, Electroanalysis (N.Y.N.Y.) 17(19) (2005) 1727-1733.
[26] L. Bu, T. Gu, Y. Ma, C. Chen, Y. Tan, Q. Xie, S. Yao, Enhanced cathodic preconcentration of As (0) at Au and Pt electrodes for anodic stripping voltammetry analysis of As (III) and As (V), J. Phys. Chem. C 119(21) (2015) 11400-11409.
[27] X. Dai, R.G. Compton, Detection of As (III) via oxidation to As (V) using platinum nanoparticle modified glassy carbon electrodes: arsenic detection without interference from copper, Analyst 131(4) (2006) 516-521.
[28] A. Profumo, D. Merli, M. Pesavento, Voltammetric determination of inorganic As (III) and total inorganic As in natural waters, Anal. Chim. Acta 539(1-2) (2005) 245-250.
[29] D. Jedryczko, P. Pohl, M. Welna, Inorganic arsenic speciation in natural mineral drinking waters by flow-through anodic stripping chronopotentiometry, Talanta 150 (2016) 265-271.
[30] A. Idris, J. Mafa, N. Mabuba, O. Arotiba, Dealing with interference challenge in the electrochemical detection of As (III)—a complexometric masking approach, Electrochem. Commun. 64 (2016) 18-20.
[31] W. Chen, H. Yu, S.-Y. Lee, T. Wei, J. Li, Z. Fan, Nanocellulose: A promising nanomaterial for advanced electrochemical energy storage, Chem. Soc. Rev. 47(8) (2018) 2837-2872.
[32] R. Miao, L. Chen, L. Shao, B. Zhang, R.G. Compton, Electron transfer to decorated graphene oxide particles, Angew. Chem., Int. Ed. 58(36) (2019) 12549-12552.
[33] M. Pumera, Graphene-based nanomaterials and their electrochemistry, Chem. Soc. Rev. 39(11) (2010) 4146-4157.

[34] X. Li, C. Batchelor-McAuley, S.A. Whitby, K. Tschulik, L. Shao, R.G. Compton, Single nanoparticle voltammetry: contact modulation of the mediated current, Angew. Chem., Int. Ed. 55(13) (2016) 4296-4299.
[35] D.D. Han, Z.G. Liu, J.H. Liu, X.J. Huang, The size effect of Pt nanoparticles: a new route to improve sensitivity in electrochemical detection of As(III), RSC Adv. 5(48) (2015) 38290-38297.
[36] R. Kempegowda, D. Antony, P. Malingappa, Graphene–platinum nanocomposite as a sensitive and selective voltammetric sensor for trace level arsenic quantification, Int J Smart Nano Mater 5(1) (2014) 17-32.
[37] W.B. Postek, I.A. Rutkowska, J.A. Cox, P.J. Kulesza, Electrocatalytic effects during redox reactions of arsenic at platinum nanoparticles in acid medium: Possibility of preconcentration, electroactive film formation, and detection of As(III) and As(V), Electrochim. Acta 319 (2019) 499-510.
[38] Y. Zhang, A.K. Selva Kumar, D. Li, M. Yang, R.G. Compton, Nanoparticle-and Nanotube-Modified Electrodes: Response of Drop-Cast Surfaces, ChemElectroChem 7(22) (2020) 4614-4624.
[39] T.J. Davies, R.R. Moore, C.E. Banks, R.G. Compton, The cyclic voltammetric response of electrochemically heterogeneous surfaces, J. Electroanal. Chem. 574(1) (2004) 123-152.
[40] K.R. Ward, M. Gara, N.S. Lawrence, R.S. Hartshorne, R.G. Compton, Nanoparticle modified electrodes can show an apparent increase in electrode kinetics due solely to altered surface geometry: The effective electrochemical rate constant for non-flat and non-uniform electrode surfaces, J. Electroanal. Chem. 695 (2013) 1-9.
[41] H. Xu, L. Zeng, S. Xing, Y. Xian, L. Jin, Microwave-irradiated synthesized platinum nanoparticles/carbon nanotubes for oxidative determination of trace arsenic (III), Electrochem. Commun. 10(4) (2008) 551-554.
[42] J.-F. Huang, H.-H. Chen, Gold-nanoparticle-embedded nafion composite modified on glassy carbon electrode for highly selective detection of arsenic (III), Talanta 116 (2013) 852-859.
[43] M. Yang, X. Chen, J.H. Liu, X.J. Huang, Enhanced anti-interference on electrochemical detection of arsenite with nanoporous gold in mild condition, Sens. Actuator B-Chem. 234 (2016) 404-411.
[44] J.A. Rodrigues, C.M. Rodrigues, P.J. Almeida, I.M. Valente, L.M. Gonçalves, R.G. Compton, A.A. Barros, Increased sensitivity of anodic stripping voltammetry at the hanging mercury drop electrode by ultracathodic deposition, Anal. Chim. Acta 701(2) (2011) 152-156.
[45] J. Orozco, C. Fernandez-Sanchez, C. Jimenez-Jorquera, Underpotential deposition-anodic stripping voltammetric detection of copper at gold nanoparticle-modified ultramicroelectrode arrays, Environ. Sci. Technol. 42(13) (2008) 4877-4882.
[46] C.A. Paddon, R.G. Compton, Underpotential deposition of lithium on platinum single crystal electrodes in tetrahydrofuran, J. Phys. Chem. C 111(26) (2007) 9016-9018.
[47] O.A. Oviedo, L. Reinaudi, S.G. García, E.P.M. Leiva, Underpotential deposition, Monographs in Electrochemistry (2016).
[48] E. Herrero, L.J. Buller, H.D. Abruña, Underpotential deposition at single crystal surfaces of Au, Pt, Ag and other materials, Chem. Rev. 101(7) (2001) 1897-1930.
[49] B.Y. Ren, L.A. Jones, M. Chen, D.K. Oppedisano, D. Qiu, S.J. Ippolito, S.K. Bhargava, The Effect of Electrodeposition Parameters and Morphology on the Performance of Au Nanostructures for the Detection of As (III), J. Electrochem. Soc. 164(14) (2017) H1121-H1128.
[50] T.D. Cabelka, D.S. Austin, D.C. Johnson, Electrocatalytic Oxidation of As (III): I. Voltammetric Studies at Pt Electrodes in, J. Electrochem. Soc. 131(7) (1984) 1595.

[51] W. Zhou, L. Kibler, D. Kolb, XPS study of irreversibly adsorbed arsenic on a Pt (1 1 1) electrode, Electrochim. Acta 49(27) (2004) 5007-5012.
[52] J. Feliu, A. Fernandez-Vega, A. Aldaz, J. Clavilier, New observations of a structure sensitive electrochemical behaviour of irreversibly adsorbed arsenic and antimony from acidic solutions on Pt (111) and Pt (100) orientations, J. Electroanal. Chem. Interf. Electrochem. 256(1) (1988) 149-163.
[53] M. Yang, P.H. Li, W.H. Xu, Y. Wei, L.N. Li, Y.Y. Huang, Y.F. Sun, X. Chen, J.H. Liu, X.J. Huang, Reliable electrochemical sensing arsenic(III) in nearly groundwater pH based on efficient adsorption and excellent electrocatalytic ability of AuNPs/CeO2-ZrO2 nanocomposite, Sens. Actuator B-Chem. 255 (2018) 226-234.
[54] B.M. Sonkoue, P.M.S. Tchekwagep, C.P. Nanseu-Njiki, E. Ngameni, Electrochemical Determination of Arsenic Using Silver Nanoparticles, Electroanalysis 30(11) (2018) 2738-2743.
[55] J.H. Hwang, P. Pathak, X.C. Wang, K.L. Rodriguez, J. Park, H.J. Cho, W.H. Lee, A novel Fe-Chitosan-coated carbon electrode sensor for in situ As(III) detection in mining wastewater and soil leachate, Sens. Actuator B-Chem. 294 (2019) 89-97.
[56] C. Nunez, J.J. Trivino, R. Segura, V. Arancibia, Monographs in Electrochemistry trace levels in urine by differential pulse anodic voltammetry using a simple graphene screen-printed electrode, Microchem. J. 159 (2020) 6.
[57] G. Bhanjana, N. Dilbaghi, S. Chaudhary, K.H. Kim, S. Kumar, Robust and direct electrochemical sensing of arsenic using zirconia nanocubes, Analyst 141(13) (2016) 4211-4218.
[58] W. Yu, C. Batchelor-McAuley, X. Chang, N.P. Young, R.G. Compton, Porosity controls the catalytic activity of platinum nanoparticles, Phys Chem Chem Phys 21(36) (2019) 20415-20421.
[59] A.K.S. Kumar, Y. Zhang, D. Li, R.G. Compton, A Mini-review: how reliable is the drop casting technique?, Electrochem. Commun. (2020) 106867.
[60] Y. Zhang, A.K.S. Kumar, D. Li, M. Yang, R.G. Compton, Nanoparticle and nanotube modified electrodes: the response of drop casted surfaces, ChemElectroChem (2020).
[61] D.M. Novak, B.E. Conway, Competitive adsorption and state of charge of halide-ions in monolayer oxide film growth-processes at Pt anaodes, J. Chem. Soc. Faraday Trans. 77 (1981) 2341-2359.
[62] W.H. Organization, Chloride in Drinking-water, in: W.H. Organization (Ed.) Geneva, 2003.
[63] NanoXact Platinum Nanoparticles – Bare (Citrate). https://nanocomposix.com/collections/material-platinum/products/nanoxact-platinum-nanoparticles-bare-citrate?variant=32333902250073. (Accessed June 24, 2021.
[64] M. Carron, M.E. Mrose, K. Murata, Relation of ionic radius to structures of rare-earth phosphates, arsenates, and vanadates, Mineralogical Society of America, 1958.

Chapter 6. **Arsenic (III) Detection with Underpotential Deposition on Gold**

This chapter reports a new, sensitive stripping voltammetric method for the detection of As(III) in aqueous solution using either a gold macroelectrode or a gold nanoparticle-modified glassy carbon electrode (GCE) based on the underpotential deposition (UPD) of As ad-atoms. The pre-concentration step deposits and accumulates As ad-atoms onto gold and is followed by a potential sweep to strip the ad-atoms with no interference from Cu(II) or Cl^- at either electrode. Linear responses were found for the range 0.01 μM to 0.1 μM or 0.005 μM to 0.1 μM at gold macroelectrodes and gold nanoparticle-modified electrodes, respectively. The visually clearly discernable signals recorded at 0.005 μM (0.4 ppb) on gold nanoparticle-modified electrodes suggests that this method has practical value given the WHO limit of 0.13 μM (10 ppb) for drinking water.

The work presented in this chapter has been published in the Journal of Electroanalytical Chemistry [1] as a first author paper, and was carried out in collaboration with Dr. Danlei Li (Compton group) who helped with the interpretation of the results. This chapter shows significant benefits in using gold electrodes as compared to the platinum electrodes studied in the previous chapter especially in respect of overcoming interference from Cu^{2+} and/or Cl^- .

6.1. Introduction

Anodic stripping voltammetry (ASV) is a commonly used electrochemical method for electro-analysis to enhance sensitivity and to reach lower detection limits during measurements

as compared to direct forms of voltammetry such as linear, cyclic, pulse or sinusoidal voltammetry where the peak currents can be limited by the rate of diffusion [2-5]. Microelectrodes, nanoelectrodes and arrays of these can moderate some of the limitations but ultimately the rate of diffusion to the electrode controls both limits of detection and sensitivity [6-8]. The merit of ASV as applied to the detection of metal ions is that the analyte is pre-concentrated via electro-reduction to deposit and accumulate the corresponding metal on the electrode; then a sweep voltammetry (linear or pulsed) is applied to re-oxidize the metal to metal ions and the resulting 'stripping' peak is used as a signal for the analytical detection. If the period of pre-concentration is prolonged, limits of detection (LOD) are correspondingly lowered. In this way, for example, ASV allows electro-analysis to meet the requirements of the WHO guidelines for drinking water in respect of arsenic [9-11], cadmium [5, 12] and lead [12-14] amongst other targets.

Underpotential deposition (UPD) is the deposition of a metal in the form of a monolayer or sub-monolayer at the potentials lower than that required for the deposition of the bulk metal [15-18]. We have recently suggested the possible use of UPD in ASV as a possible means of overcoming some of the limitations of ASV seen when using the deposition of bulk metals [9]. In particular, a problem can arise when species additional to the target are present which can co-deposit with the target metal to form alloys or solid solutions. It was suggested that UPD may overcome these limitations in some cases and proof of concept was presented for the detection of Arsenic via UPD on platinum surfaces, where both platinum macroelectrodes and platinum nanoparticle modified carbon electrodes were seen to be suitable substrates. Meanwhile, the detection is free from interference by copper ions which is a notorious problem in the ASV analysis of Arsenic. In addition, the approach had good sensitivity and showed limits of detection with visibly discernible and recognisable signals within the WHO requirements. The proof-of-concept suggests UPD-ASV as an analytical method with distinct

advantages in niche applications in addition to the lost cost and rapidity generically associated with electrochemical methods of analysis.

Arsenic species are highly toxic and exist both naturally and in industrial effluents [19-23]. Exposure to arsenic can cause severe health problems including cardiovascular disease and cancer [23-25]. The dominant forms of inorganic arsenic species in water are As(III) (AsO_3^{3-}) and As(V) (AsO_4^{3-}) [19-23]. As(III) species are more toxic than As(V) due to their interaction with enzymes in the human body [23-25]. Thus, it is important to detect As(III) in drinking water. There are many reported methods including atomic absorption spectrometry (AAS) [26] and inductively coupled plasma mass spectrometry (ICPMS) [27, 28]. However, these instrumental methods require specialist laboratory conditions and lengthy sample preparation. Electrochemical methods including ASV methods, on the other hand, can provide sensitive and rapid detection with relative simple and cheap instrumentation [29, 30]. To date, the lowest LOD for As detection in water of 0.003 ppb has been claimed by Profumo *et al* by using cathodic stripping voltammetry (CSV) [31] and the greatest sensitivity was achieved by Xiao *et al* via Square Wave ASV (SWASV) with detection via the stripping of bulk As [32]. Particle modified electrodes (PMEs) have also been applied for arsenic detection. Notably, Hwang *et al* used Fe and Chitosan to modify screen-printed carbon electrode (SPCE) and obtained a LOD of 1.12 ppb via SWASV [33], and Nunez *et al* use graphene-modified SPCE to reach a LOD of 0.28 ppb via differential pulse ASV (DPASV) [34]. The proof of concept study in respect of ASV using UPD signals mentioned above and using Pt macroelectrodes and Pt nanoparticle-modified glassy carbon electrodes (GCEs), gave a visually observed detection limit of 4 ppb [9]. However, most of the ASV methods suffer from the interference of Cu(II) or Cl^- due to the formation of Cu-As alloys and solid solutions, [35] or, in the case of the use of UPD signals at platinum, competitive adsorption of As and Cl^- so precluding measurements in the presence of high levels of chloride [36]. Gold electrodes with the deposition of bulk As

have been used for As(III) detection to reach low detection limits in the work of Xiao *et al* who used Au nanoparticles modified carbon nanotubes (AuCNTs) on [32] and of Yang *et al* who modified a GCE with Au nanoparticles and CeO_2-ZrO_2 for As(III) detection [37]. However the use of bulk As is prone to interference via alloy and/or the formation of intermetallic species. Thus, in this paper, we investigate the possible use of UPD-ASV for the analysis of As at low concentrations on gold surfaces with the aim of avoiding interference from both Cu(II) and Cl^-. The LOD in this paper is determined from visually clear signals rather than those calculated on the basis of 3σ method [33, 34, 38] , while the observed low detection limits acquired at both Au macroelectrodes and Au nanoparticle-modified electrodes were within the requirements for the WHO limits for drinking water with visually recognisable distinct signals seen at the lowest concentrations reported.

6.2. Experimental

6.2.1. Chemical reagents

Commercially available Au nanoparticles (5 nm in diameter, Sigma Aldrich, UK) were supplied suspended in sodium citrate solution. Copper(II) sulfate pentahydrate ($CuSO_4 \cdot 5H_2O$, 99%, Sigma Aldrich, UK), potassium chloride (KCl, 99.5%, Sigma Aldrich, UK), sodium (meta) arsenite ($NaAsO_2$, 99%, Fluka, Switzerland), and sulphuric acid (H_2SO_4, 98%, Fisher Scientific, UK) were purchased and used without any further purification. All aqueous solutions were prepared using deionized water (Milipore, UK) with a resistivity of 18.2 MΩ cm at 298 K.

6.2.2. Instrumentation

All electrochemical measurements were thermostatted at 298 (± 0.1) K and were conducted with a standard three-electrode system in a Faraday cage. A gold macroelectrode

(diameter of 1.60 ± 0.01 mm, geometric area of 0.02 cm^2, BASi, USA) or glassy carbon electrode (GCE, diameter of 3.00 ± 0.01 mm, geometric area of 0.07 cm^2, BAS technical, UK) operated as a working electrode, either a platinum wire or a carbon rod as a counter electrode and a mercury-mercurous sulfate electrode (MSE, BASi, USA) served as the reference electrode with a potential of +0.65 V vs. standard hydrogen electrode (SHE) [3], and the solution used in the reference electrode was saturated K_2SO_4 solution (1.45 M). All electrochemical measurements were performed in 0.1 M H_2SO_4 with various concentrations of As(III), and were recorded with a μAutolab type III potentiostat (EcoChemie, NL) after degassing with nitrogen.

6.2.3. Preparation and characterization of Au nanoparticle-modified electrodes

Glassy carbon electrodes (GCEs) were cleaned with alumina of decreasing particle sizes (1, 0.3 and 0.05 μm) on polishing pads then rinsed with deionized water. For drop casting of Au nanoparticles, 5 μL of stock Au nanoparticle suspension was drop casted onto the GCE using a micro pipette then dried with N_2 flow for around 15 minutes. The GCE was polished after each measurement then the Au nanoparticles were drop casted onto the cleaned GCE.

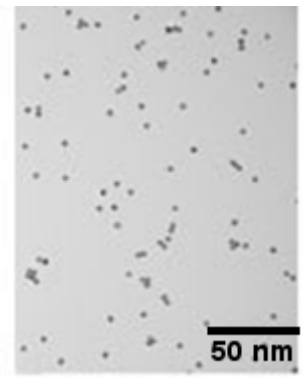

Figure 6.1 TEM image of 5 nm gold nanoparticles. Reproduced with permission from Merck KGaA, Darmstadt, Germany and/or its affiliates. Ref. [39].

Figure 6.1 shows a TEM image of 5 nm gold nanoparticles. Each particle has a size of approximately 4 - 7 nm. The particles are capped by citrate and are dispersed in trisodium citrate solution [39], which prevents the particles from aggregation in aqueous solutions.

6.3. Results and Discussion

In the following sections, first, the electrochemical behaviour of As(III) at Au macroelectrodes and electrodes modified with gold nanoparticles was studied in solutions containing 500 μM $NaAsO_2$ with 0.1 M H_2SO_4 using cyclic voltammetry (CV) and 10 μM $NaAsO_2$ with 0.1 M H_2SO_4. The voltammetric peaks were assigned and compared with literature and the presence of an As UPD peak noted. Next, a novel method based on anodic stripping voltammetry that reached a low detection limit of As was investigated using ASV with Au electrodes using pre-concentration by under potential deposition (UPD) of sub-monolayer quantities of As(0) atoms on the electrode surface. Finally, interference studies addressing Cu^{2+} and Cl^- recognised as common interferents with either As detection via ASV or with UPD on some substrates [36, 40, 41] were conducted.

6.3.1. Electrochemical responses of As(III) on Au electrodes

Cyclic voltammetry of As(III)

To examine the electrochemical behaviour of As(III), a gold macroelectrode was first employed using cyclic voltammetry and anodic stripping voltammetry. Figure 6.2a illustrates the CV response of 500 μM $NaAsO_2$ in 0.1 M H_2SO_4 with a potential window from - 1.0 V to + 1.3 V (vs. MSE) at a gold macroelectrode. The voltammograms shown are all first scans recorded after electrode polishing. The start potential was + 0.6 V and the voltammogram was first scanned cathodically to – 1.0 V at a scan rate of 0.1 V s^{-1} and then scanned anodically to

+ 1.3 V. Three peaks were observed on the cathodic scan, labelled as peak 1, peak 2 and peak 3 (red line in Figure 6.2a). Peak 1 observed at ca + 0.37 V was ascribed to the reduction of Au oxide to Au [42, 43]. Peak 2 observed at ca - 0.66 V corresponds to the three-electron reduction of As(III) to As(0) [43]. Peak 3 at ca - 1.0 V represents the onset of the hydrogen evolution reaction (HER) [42]. On the reverse anodic scan, four peaks, peak 4, peak 5, peak 5' and peak 6, were obtained. Peak 4 with the potential of ca – 0.28 V represents the re-oxidation of As(0) to the parent As(III) species [43]. Peak 5 observed at ca + 0.45 V was ascribed to the oxidation of As(III) to As(V) [42]. Another oxidation peak, peak 5', observed at ca + 0.80 V was considered to be the oxidation of Au to Au oxide [42]. Peak 6 at ca + 1.3 V represents the start of the oxygen evolution reaction (OER) [43]. Comparing the voltammetry in Figure 6.2a with that obtained in blank solution (0.1 M H_2SO_4; black dashed line in Figure 6.2a), it can be seen that the three peaks (peak 2, peak 4 and peak 5) which are absent on the latter are all As(III)-related peaks, whilst peaks 1, 3, 5' and 6 correspond to reduction of Au oxide, HER, oxidation of Au to Au oxide and OER, respectively [43]. There were three reasons to choose + 0.6 V as a starting potential. First, when choosing the starting potentials, it was necessary to scan CV cathodically initially to reduce As(III) to As(0) so that the oxidation peaks can be observed in the reverse scan. Second, the potential at + 0.6 V was far from other reactions, notably the oxidation of Au (ca + 0.8 V), the reduction of Au oxide (ca + 0.35 V) and the oxidation of As(III) to As(V) (+ 0.45 V) (Figures 6.2a and b). Third, it was also important to see if the surface of Au nanoparticles was Au or Au oxide, which is reveal by the existence or not of peak 1 during the first cathodic scan. The start potential of + 0.6 V meets all these requirements.

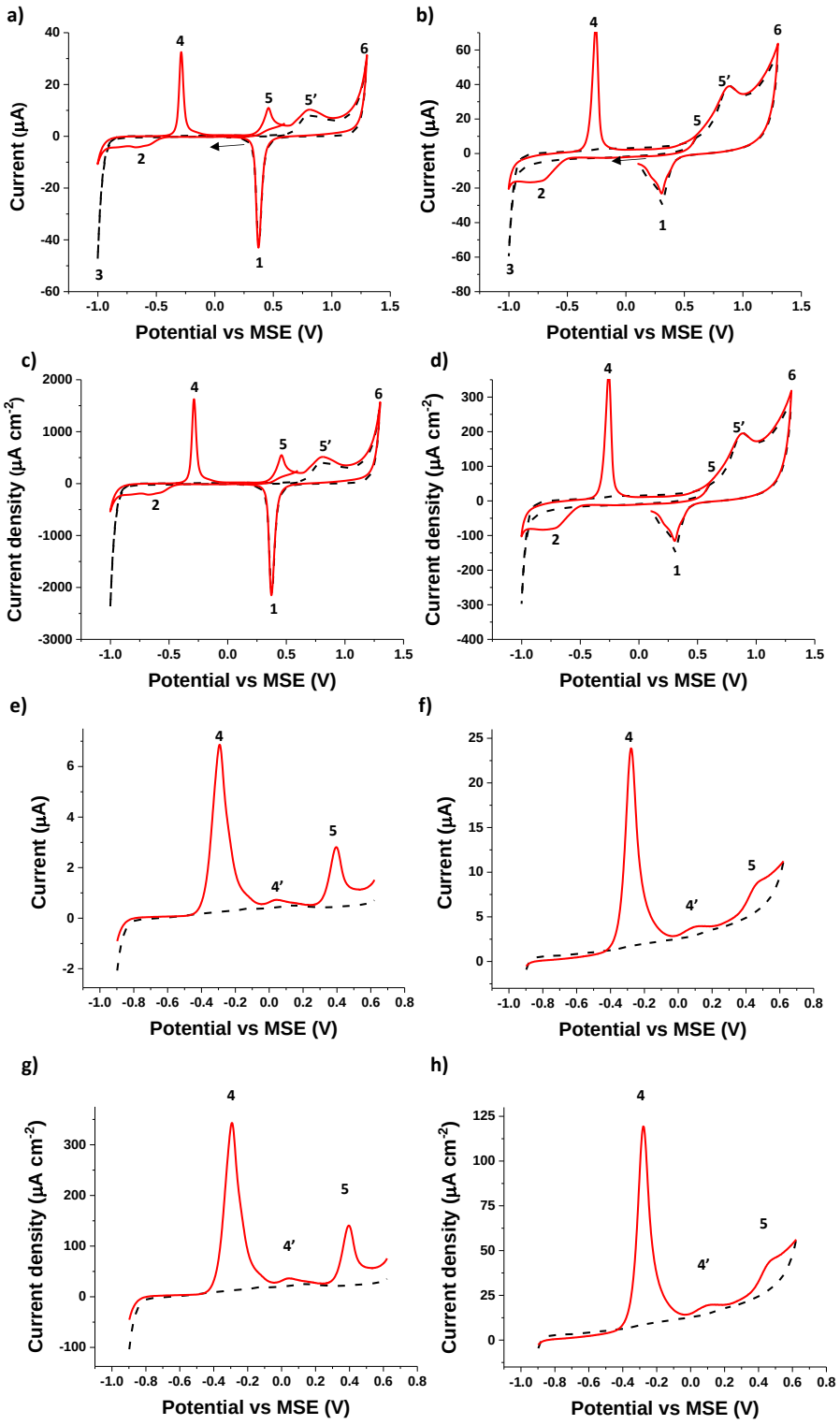

Figure 6.2 CVs of 500 µM As(III) in 0.1 M H_2SO_4 (red) and blank (black dashed line) at a) and c) Au macroelectrodes, and b) and d) Au nanoparticle-modified GCEs. The voltammograms were conducted from + 0.6 V vs MSE and first scanned cathodically to - 1.0 V at a scan rate of 0.1 V s^{-1} followed by an anodic scan to + 1.3 V. The arrows represent the starting point and the direction of scan. Linear sweep voltammograms of 10 µM As(III) in 0.1 M H_2SO_4 (red) and blank (black dashed line) after pre-concentration at - 0.9 V for 300 s at e) and g) Au macroelectrodes, and f) and h) Au nanoparticle-modified GCEs. The current densities were calculated based on the currents and the estimated surface area of the gold surface (see text). The surface area of Au macroelectrode was 0.02 cm^2 and the surface area of Au nanoparticles was 0.2 cm^2 (calculation is shown on Supporting Information Section 1). LSV parameters: deposition at - 0.9 V for 300 s, scan rate was 0.1 V s^{-1}.

Next cyclic voltammetry was conducted at Au nanoparticle-modified GCEs with an average coverage of 6.5 $\times 10^{-12}$ moles cm^{-2} corresponding to ca 1 monolayer of nanoparticles (calculations are shown in Appendix Section 1) in a solution of 0.1 M H_2SO_4 first without the addition of arsenite. The voltammetry was conducted from + 0.6 V and first scanned cathodically to – 1.0 V then scanned anodically to + 1.3 V at a scan rate of 0.1 V s^{-1}. The resulting voltammetry of 0.1 M H_2SO_4 is shown in Figure 6.2b (black dashed line). The peaks 1, 3, 5' and 6 were seen at similar potentials as for Au macroelectrodes (Table 6.1) and assigned to the same reactions [43] as above. This was similar to that measured at the Au macroelectrodes (black dashed line in Figure 6.2a).

Then the cyclic voltammetry was conducted on 500 μM As(III) in 0.1 M H_2SO_4 at Au nanoparticle-modified electrodes using a similar starting potential, potential window and sweep rate as for Figure 6.2a. The resulting voltammogram is shown in Figure 6.2b (red line). Seven voltammetric features were discerned at similar potentials as seen for the Au macroelectrode and assigned to the same electrochemical reactions [42, 43] as above. It was noted that peak 5 is slightly different from the one in Figure 6.2a. In particular whilst peak 5 can be observed clearly at Au macroelectrodes (Figure 6.2) it is less well resolved at Au nanoparticle-modified GCEs (Figure 6.2b) as a result of the broad width of peak 5', which overlaps with peak 5.

Deposition and stripping of As

To further understand the electrochemistry of As at gold, a 10 μM solution of $NaAsO_2$ in 0.1M H_2SO_4 was reduced at – 0.9 V for 300 s resulting in the deposition of As(0). After deposition, a linear sweep voltammetry was conducted from – 0.9 V to + 0.62 V with a scan rate of 0.1 V s^{-1}. Figure 2e illustrates the response at a gold macroelectrode after the pre-concentration of As(0). Three arsenic-related peaks were observed as peaks 4, 4' and 5 (red

line in Figures 6.2e and g). Peaks 4 and 5 observed at ca – 0.28 V and ca + 0.45 V correspond to the chemistry inferred above. The peak 4' at ca + 0.05 V was assigned as the stripping peak associated with the oxidation of As(0) ad-atoms based on literature reports [44, 45]. All three of the peaks assigned to As were absent in the blank solution (black dashed line in Figures 6.2e and g).

The presence of peak 4' in Figure 6.2e presents the possibility of using anodic stripping voltammetry for analytical use based on the stripping of UPD As rather than bulk As as has hitherto been exclusively used for As. To further explore this possibility, analogous measurements were made using gold nanoparticle-modified electrodes.

Reduction of 10 μM $NaAsO_2$ in 0.1 M H_2SO_4 was carried out at – 0.9 V for 300 s to deposit As(0), then a linear sweep voltammetry was recorded from – 0.9 V to + 0.62 V with a scan rate of 0.1 V s^{-1} at Au nanoparticle-modified GCEs. The voltammetric response at Au nanoparticle-modified GCEs is shown in Figure 6.2f. Peaks 4, 4' and 5 were again seen (red line in Figure 6.2f) and assigned as above and elsewhere [43-45] whilst in the absence of As(III) these features disappeared (black dashed line in Figure 6.2f). The voltammetric peaks showed similar peak potentials to those seen on Au macroelectrodes (Table 6.1). It was noted that peak 5 in ASV (Figure 6.2f) is more clearly resolved than seen in CV at the Au nanoparticle-modified GCEs (Figure 6.2b).

The active surface area for arsenic deposition was estimated based on either (a) the surface area of nanoparticles and assuming that the nanoparticles on the glassy carbon electrode are fully accessible or, (b) the surface area of the Au macroelectrode, which were 0.2 cm^2 and 0.02 cm^2 respectively (see calculations in Appendix Section 1). The experimental results in Figure 6.2 showed that the current on Au nanoparticles was ca 4 times higher than that at Au macroelectrodes. The reason was inferred to be partly due to the agglomeration of the drop

casted Au nanoparticles, and partly due to the overlapping diffusion layers of adjacent nanoparticles. The agglomeration can reduce the active surface area of the nanoparticles whilst the diffusional overlap means that the current is not expected to scale with the particle area.

Having fingerprinted the electrochemistry using CV and ASV we next turn to investigating ASV using the UPD peak which offers likely superior analytical response as compared to cyclic voltammetry [9, 41] or ASV using bulk As signals as discussed in the Introduction. The next section focuses on the detection of As using anodic stripping voltammetry with underpotential deposition on gold to approach a lower detection limit.

Table 6.1 The peak potentials vs. MSE of all assigned peaks in CV and ASV at both Au macroelectrodes and Au nanoparticle-modified GCEs.

Peak number	Peak potentials at Au macroelectrodes	Peak potentials at Au nanoparticle-modified GCEs
1	+ 0.37 V	+ 0.35 V
2	- 0.66 V	- 0.70 V
3	- 1.0 V	- 1.0 V
4	- 0.28 V	- 0.28 V
4’ (in ASV)	+ 0.05 V	+ 0.10 V
5	+ 0.45 V	+ 0.45 V
5’	+ 0.8 V	+ 0.85 V
6	+ 1.3 V	+ 1.3 V

6.3.2. The Analytical Use of As UPD Stripping Signals

Proof of concept of using the UPD-ASV method for the detection of low concentrations of As(III) was introduced in Chapter 5 in the specific and exclusive context of platinum

electrodes. In this chapter, Anodic Stripping Voltammetry is applied for the detection of As(III) in 0.1 M H_2SO_4 on both gold macroelectrodes and Au nanoparticle-modified GCEs seeking to overcome the limitations of platinum electrodes as explained in the Introduction. The pre-concentration of As(0) was first carried out at – 0.9 V for 300 s, which results in first As ad-atoms being deposited at the surface of gold [43-45] and then, in higher concentrations of As(III), bulk As on top of the ad-atoms. Then the deposited As(0) was stripped off from the electrode surface using LSV with a potential sweep conducted from – 0.9 V to + 0.62 V at a scan rate of 0.1 V s^{-1} and the signals were used to quantify As(III). The signal used for the UPD-ASV analysis is the charge of peak 4', which was calculated from the area of baseline corrected voltammogram. The procedure to obtain a baseline corrected peak 4' is shown in Appendix Section 2.

Observations of As UPD stripping signals

To understand and apply the As UPD signal for analytical use, experiments were first conducted in various concentrations of As(III) in 0.1 M H_2SO_4 using Au macroelectrodes. The pre-concentration of As(0) was carried out in various concentrations of As(III) at – 0.9 V for 300 s followed with a linear potential sweep from – 0.9 V to + 0.62 V at a scan rate of 0.1 V s^{-1}. Figure 6.3a illustrates the baseline corrected linear sweep voltammetric responses of peak 4' at gold macroelectrodes measured in As(III) solutions of concentrations from 0.01 μM to 2 μM in 0.1 M H_2SO_4. The peak 4', assigned as the stripping peak of As ad-atoms, was observed at ca + 0.05 V and the charge of the peak increased with the concentration of As(III) as shown in Table A6.1 in Appendix Section 5. The charges of peak 4' are plotted against concentration of As(III) in Figure 6.3c. The charge increases linearly to begin with before reaching a plateau consist with the formation of an estimated 0.03 layers of As ad-atoms (see Appendix Section 3 for calculations). The initial linear range is approximately from 0.01 μM to 0.1 μM, at which

corresponds to a coverage of ca 1.0×10^{13} molecules cm^{-2} and 0.014 monolayers of ad-atoms (again Appendix Section 3 for the calculations). The plateau is reached for As(III) concentrations higher than 1 μM with a corresponding surface coverage of ca 2.0×10^{13} molecules cm^{-2}, consistent with a sub-monolayer of As ad-atoms deposited onto the surface of Au (Table 6.1). This observation sets the upper limit (ca 1 μM) for detection with UPD ASV using peak 4' at Au macroelectrodes but giving visually clear signals for concentrations as low as 0.01 μM (see Appendix Section 4 for both raw and corrected voltammograms). To further discover the possible application of peak 4', analogous experiments were made at Au nanoparticle-modified electrodes.

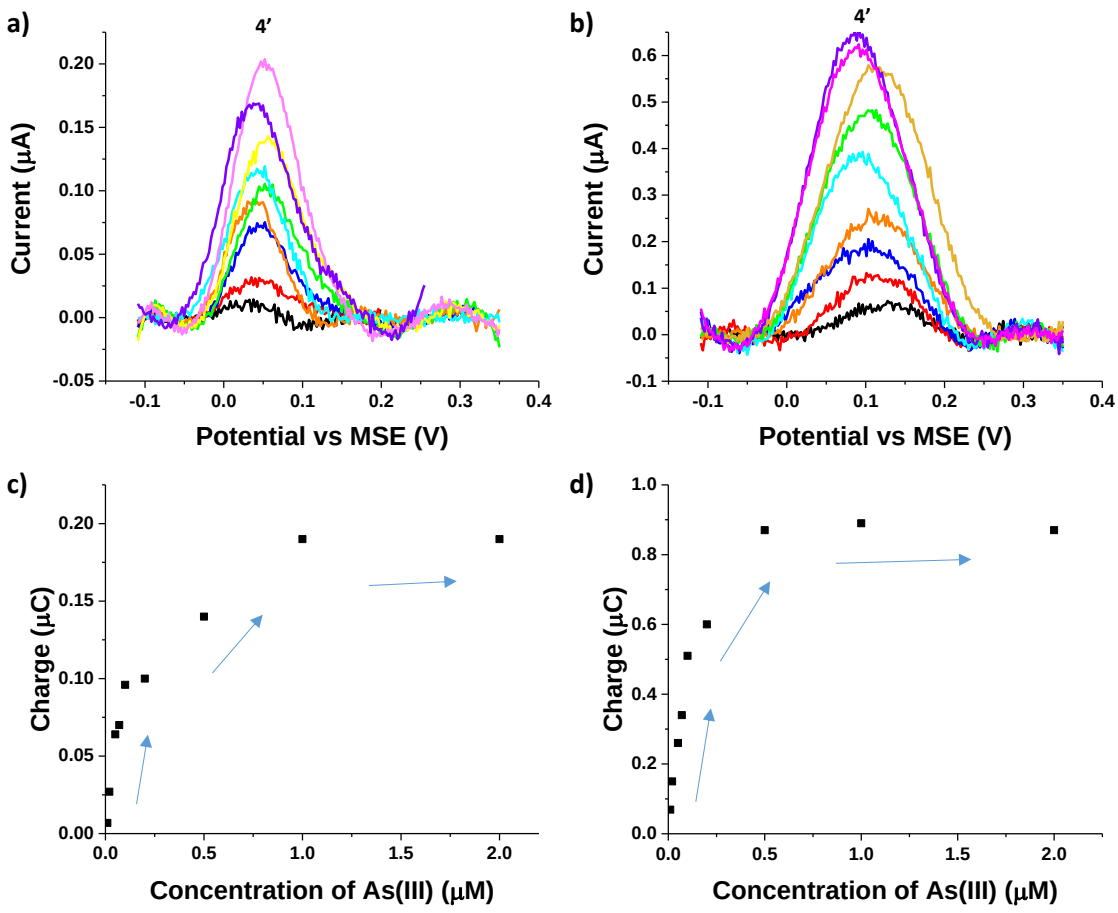

Figure 6.3 Baseline corrected stripping voltammograms of various concentrations of As(III) in 0.1 M H_2SO_4 at a) Au macroelectrodes and b) Au nanoparticle-modified GCEs. Also shown are plots of the charge of peak 4' vs concentrations of As(III) in 0.1 M H_2SO_4 at c) Au macroelectrodes and d) Au nanoparticle-modified GCEs. The concentrations of As(III) were 0.01 μM (black), 0.02 μM (red), 0.05 μM (blue), 0.07 μM (orange), 0.1 μM (cyan), 0.2 μM (green), 0.5 μM (yellow), 1 μM (purple), and 2 μM (pink). ASV parameters: deposition at - 0.9 V vs. MSE for

300 s, potential scan rate 0.1 V s^{-1}, and baseline was modelled via polynomial method from - 0.1 V to + 0.35 V for peak 4'.

The pre-concentration of As(0) was carried out at – 0.9 V for 300 s in various concentrations of As(III) solution then followed up with a LSV from – 0.9 V to + 0.62 V at a scan rate of 0.1 V s^{-1} at Au nanoparticle-modified GCEs. The baseline correction for peak 4' is also followed the procedure as above. Figure 3b shows the baseline corrected LSVs of peak 4' at Au nanoparticle-modified GCEs which was obtained from 0.01 μM to 2 μM of As(III) in 0.1 M H_2SO_4. Similar to Au macroelectrodes, peak 4' was observed at ca + 0.1 V (Figure 6.3b) and the peak charge was increased with the concentration of As(III) (Table A6.1 in Appendix Section 5). The charges of peak 4' vs concentrations of As(III) are plotted in Figure 6.3d. A similar trend is seen as observed for Au macroelectrodes reaching a limiting value of 0.87 μC (Table A6.1 in Appendix Section 5) at 0.5 μM (Figure 6.3d), which corresponds to an estimated coverage of ca 9.0 $\times 10^{13}$ molecules cm^{-2} and a deposition of 0.12 monolayers of As ad-atoms (See Appendix Section 5 for illustrative calculations).

Based on the experimental results, there were less than one monolayer of As ad-atoms deposited onto the surface of Au even increasing the concentrations of As(III). The analytical measurements in this study were thus based on the measurement of sub-monolayer of deposited As(0) ad-atoms.

Although peak 4' increased with the concentration of As(III) in the range of 0.01 μM to 1 μM or 0.01 μM to 0.5 μM for Au macroelectrodes and Au nanoparticle-modified electrodes, respectively, it is still necessary to find a linear range at low concentrations to approach a lower detection limit and a higher sensitivity. Further attention was thus focussed on the novel use of peak 4' at lower concentrations of As(III).

Calibration curves and limits of detections

To further probe the linear range to assess the sensitivity and to identify a linear range and the detection limit, concentrations of As(III) below 0.1 μM were studied for both electrodes from an analytical perspective. The deposition time for ASV was optimized to be 300 s at Au macroelectrode in 0.1 μM As(III) as summarized in Appendix Section 6 whilst the deposition potential for ASV was optimized to be – 0.9 V in 10 μM As(III) as summarized in Appendix Section 7. Hence in the following, the pre-concentration was carried out at Au macroelectrodes with various concentrations of As(III) in 0.1 M H_2SO_4 at – 0.9 V for 300 s. Note that the previous literature focuses on the oxidation of bulk As(0) rather than As ad-atoms [32, 43], and so did not require long deposition times but were unlikely to reach real detection limits compatible with the WHO limit, and in any case are prone to interference by Cu(II) ions. In this paper, we focus only on the As ad-atoms to reach the low detection limit and avoid interference from Cu ions but the deposition time is longer than those previous methods. Baseline corrections to peak 4' were applied as above. Figure 6.4a shows the baseline corrected stripping voltammograms of peak 4' with the concentrations of As(III) from 0.01 μM to 0.1 μM at Au macroelectrodes. The peak 4' was observed at ca + 0.05 V and the charge of the peak was increased with the concentrations of As(III) as shown in Table A6.1 in Appendix Section 5. To obtain the relationship between the charge of peak 4' and the concentration of As(III) at Au macroelectrodes, the charges were plotted against the concentrations in Figure 6.4c. A linear relationship, $Charge = 9.5 \times 10^{-7} C\ \mu M^{-1} \times [As(III)] + 4 \times 10^{-9}\ C$, was obtained between 0.01 μM and 0.1 μM, and the error bars were standard deviation calculated from at least three sets of data.

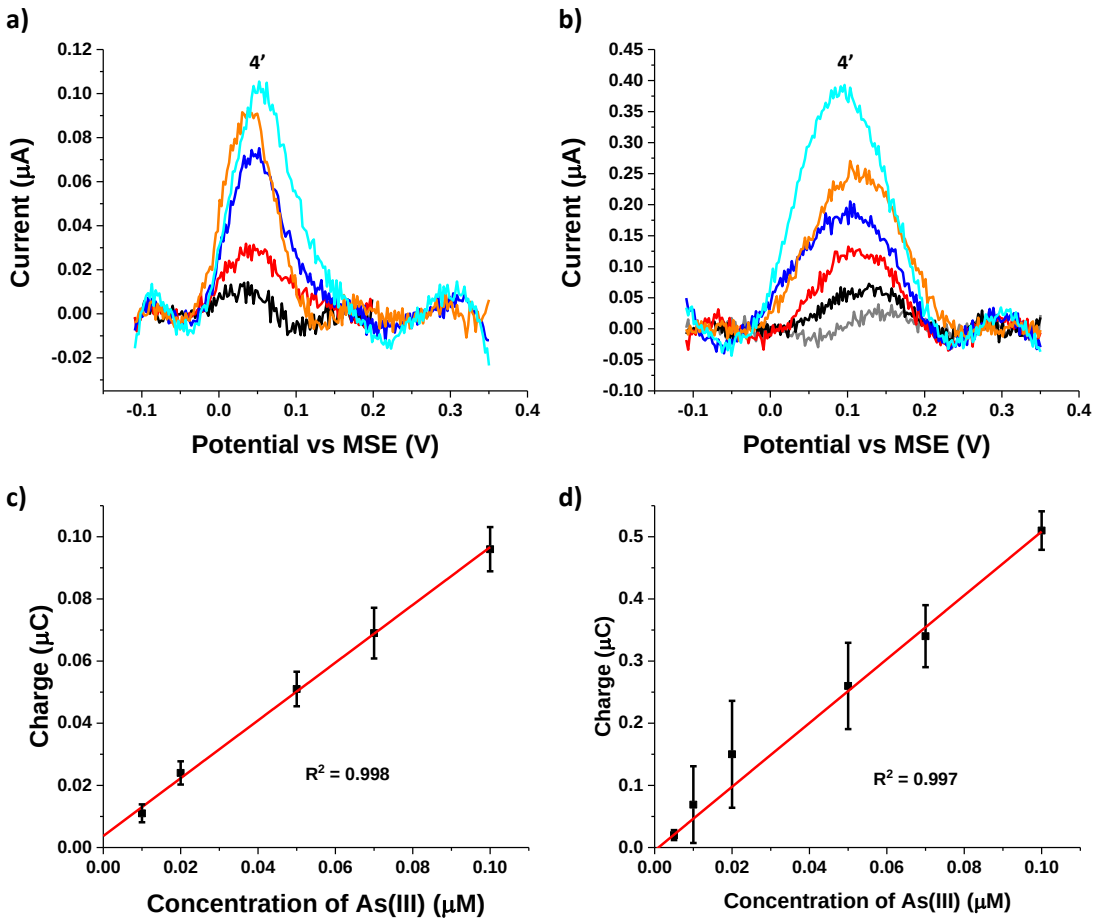

Figure 6.4 Baseline corrected stripping voltammograms of various concentrations of As(III) in 0.1 M H_2SO_4 at a) Au macroelectrode and b) 5 nm Au nanoparticle-modified GC electrode. The concentrations of As(III) were 0.005 µM (grey), 0.01 µM (black), 0.02 µM (red), 0.05 µM (blue), 0.07 µM (orange) and 0.1 µM (cyan). Charge of stripped As(0) ad-atoms vs. the concentration of As(III) at c) Au macroelectrode and d) 5 nm Au nanoparticle-modified GC electrode. The charge was calculated from baseline corrected LSVs and the error bars shown are standard deviations calculated from at least three sets of data. ASV parameters: deposition at - 0.9 V vs. MSE for 300 s, potential scan rate 0.1 V s^{-1}, and baseline was modelled via polynomial method from - 0.1 V to + 0.35 V for peak 4'.

Rather than estimating the LOD using the popular method based on 3σ [46], which is known to give unrealistically low estimates for calibration curves of high linearity since σ will be very small leading to a calculated extremely low detection limit. As Brett and Brett emphasise 'such a limit may not be attainable owing to limitations of the experimental procedure or the instrumentation (noise and drift at low signal levels), apart from any chemical interferences' [46]. For this reason, they recommend the use of 'practical detection limits' based on whether or not it is possible to distinguish the signal from the background. We adopt the latter approach in this paper and the visually identified LOD of 0.01 µM (0.8 ppb) with the

sensitivity of 9.5×10^{-7} C μM^{-1} were acquired on Au macroelectrodes. Note that the quoted LOD is estimated on the basis of the visual identification of measureable signals (shown in Appendix Section 3) from real samples (black line in Figure 6.4c) rather than calculated based on the 3σ method. To further explore the analytical use of peak 4', analogous experiments were made at Au nanoparticle-modified electrodes as follows.

The pre-concentration of As(0) was carried out at – 0.9 V for 300 s in various concentrations of As(III) solution. Stripping used a linear sweep from – 0.9 V to + 0.62 V at a scan rate of 0.1 V s^{-1} at Au nanoparticle-modified GCEs. The baseline correction for peak 4' is also followed the procedure as above. Figure 6.4b presents the baseline corrected stripping voltammograms of peak 4' at Au nanoparticle-modified GCEs which was obtained from 0.005 μM to 0.1 μM. Similar to that at Au macroelectrodes, the peak 4' was observed at ca + 0.1 V and the charge was increased with the concentrations of As(III) (Table A6.1 in Appendix Section 5). The charges of peak 4' vs concentrations of As(III) at Au nanoparticle-modified GCEs was plotted in Figure 6.4d. The linear relationship, $Charge = 5.1 \times 10^{-6} C\ \mu M^{-1} \times [As(III)] - 5 \times 10^{-9}\ C$, was obtained from 0.005 μM to 0.1 μM, and the error bars were standard deviations calculated from at least three sets of data. As above, the LOD was judged based on the need to have a visually clear signal over background and found to be 0.005 μM (0.4 ppb). The grey line in Figure 4b shows the voltammogram corresponding to this limit. The sensitivity was estimated to be 5×10^{-6} C μM^{-1}. In comparison with the results on Au macroelectrodes, a lower LOD and higher sensitivity was obtained at Au nanoparticle-modified GCEs, which suggest a merit of using Au nanoparticle-modified electrodes over Au macroelectrodes during application of As(III) detection in water. The enhancement is attributed to the greater surface area of Au available, which was estimated to be 0.2 cm^2 at Au nanoparticles (see Appendix Section 1 for calculations) while 0.02 cm^2 at Au macroelectrodes (calculations shown in Appendix Section 2).

The detection limits obtained using visually clear signals of 0.8 ppb and 0.4 ppb on Au macroelectrodes and Au nanoparticle-modified GCEs, respectively, meet the WHO guidelines for arsenic in drinking water (10 ppb). To apply this method in real world, interference study is also required. The next section will focus on the interference from Cu(II) and chloride.

6.3.3. Interference studies

Having established an analytical procedure based on the UPD stripping peak of As ad-atoms from gold surface, further experiments were conducted to explore if the detection on gold suffers interference from either copper or chloride as is discussed in this section.

Possible interference by Cu(II)

Cu(II) is a very common interferent in the stripping voltammetry of As using bulk As since it can form Cu-As alloys or intermetallic compounds in the deposition step [47]. Accordingly the interference of Cu(II) with detection of 0.1 μM of As(III) was studied using ASV by adding different amounts of Cu(II). The pre-concentration was conducted at – 0.9 V for 300 s with detection using a linear sweep, as above, from – 0.9 V to + 0.62 V at a scan rate of 0.1 V s^{-1}. Figure 6.5a illustrates the raw ASV of 0.1 μM of As(III) with different amounts of Cu^{2+} from 0.1 μM to 1 mM at Au macroelectrodes. A peak observed at ca – 0.3 V and peak current was increased with the concentrations of Cu(II). This was assigned to the oxidation peak of Cu(0) to Cu(II) [48]. The peak 4' at ca + 0.05 V was difficult to be seen thus a baseline corrections were made for peak 4' with the procedure as above. Figure 6.5c shows the baseline corrected stripping voltammograms of 0.1 μM of As(III) with different amounts of Cu^{2+} from 0.1 μM to 1 mM at Au macroelectrodes. The black dashed line was recorded for a solution without Cu(II) where only one peak was observed at ca + 0.05 V corresponding to the oxidation of As ad-atoms [43-45]. With the addition of Cu(II), the signal of peak 4' varied negligibly and

the peak potential did not shift. Even for concentrations of Cu(II) was as high as 1 mM, the signal of peak 4' was not changed. Thus, it can be concluded that Cu(II) does not interfere to the oxidation peak of As ad-atoms on Au macroelectrodes.

Analogous experiments were made on Au nanoparticle-modified GCEs. The pre-concentration was carried out at – 0.9 V for 300 s then followed up with a linear sweep from – 0.9 V to + 0.62 V at a scan rate of 0.1 V s^{-1}. Figure 6.5b illustrates the raw ASV of 0.1 μM of As(III) with different amounts of Cu^{2+} from 0.1 μM to 1 mM at Au nanoparticle-modified GCEs. Similar to what was seen at Au macroelelctrodes, a Cu^{2+} reduction peak can be observed at ca – 0.3 V and the associated peak current increased with the addition of Cu^{2+}. Baseline correction was applied for peak 4' with the procedure as above and the baseline corrected ASV is shown in Figure 6.5d. The peak 4' can be observed at ca + 0.1 V and again the addition of Cu(II) did not change the signal of peak 4' or shift the potential by comparing the voltammograms obtained without (black dashed line in Figure 6.5d) and with Cu(II). In Figures 6.5c and d, the peak at ca + 0.25 V or ca + 0.30 V was an artefact arising from the baseline correction. It does not relate to any Faradaic reaction. The baseline simulated in that range was based on the polynomial method optimised for the peak of interest and so does not perfectly capture the background outside of potential range of the ad-atom stripping peak. That causes a small peak shown in Figures 6.5c and d at + 0.25 V or + 0.30 V, respectively. We conclude that the formation of Cu-As alloys or intermetallic species was likely avoided by using UPD to form As ad-atoms rather than bulk As at gold surfaces. The standard deviations of peak potential were calculated to be 0.010 and 0.015 for Au macroelectrodes and Au nanoparticle-modified electrodes, respectively, which means the difference of peak potentials in Figures 6.5c and d were negligible.

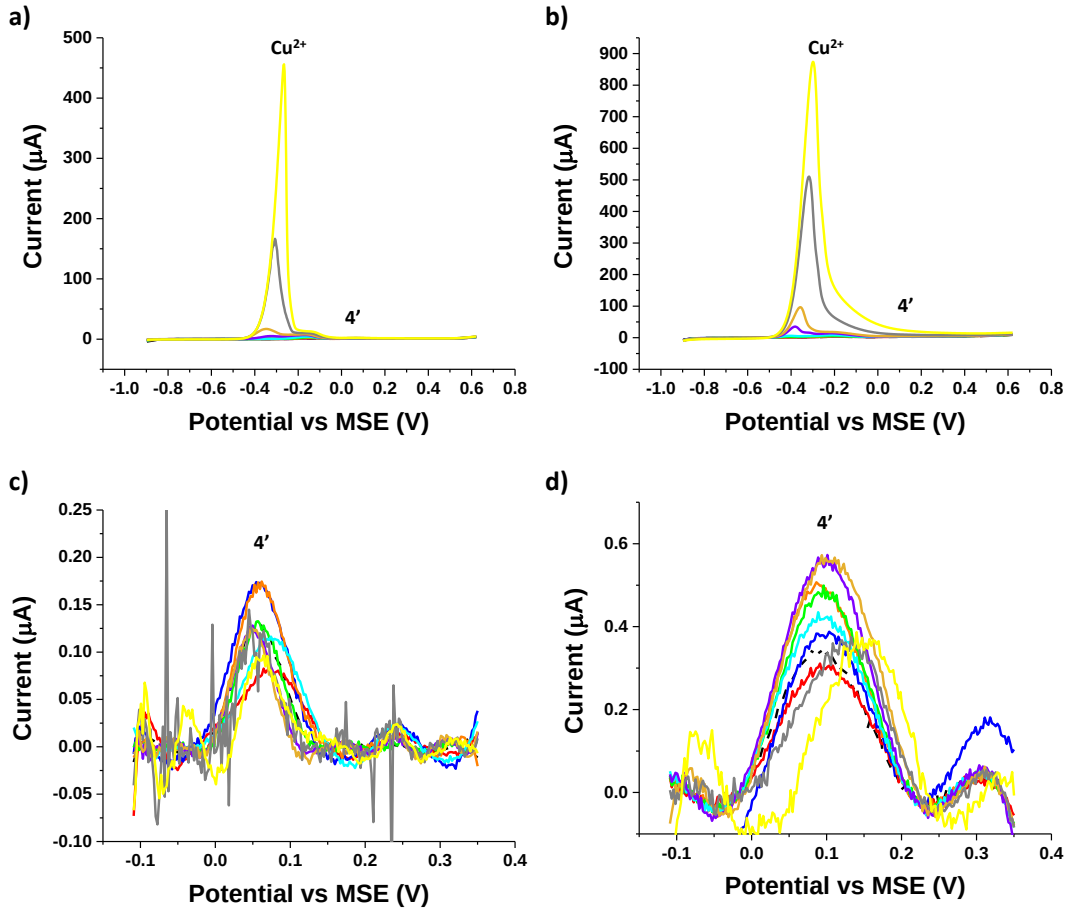

Figure 6.5 Raw ASV curves of 0.1 µM As(III) in 0.1 M H_2SO_4 with various concentrations of Cu^{2+} at a) Au macroelectrodes and b) 5nm Au nanoparticle-modified GC electrodes. Baseline corrected ASV curves of 0.1 µM As(III) in 0.1 M H_2SO_4 with various concentrations of Cu^{2+} in the potential range from - 0.1 V to + 0.35 V at c) Au macroelectrodes and d) Au nanoparticle-modified GC electrodes. ASV parameters: deposition at - 0.9 V for 300 s, scan rate was 0.1 V s^{-1}. Cu(II) concentration: 0 µM (black dashed line), 0.1 µM (red), 0.5 µM (blue), 1 µM (orange), 5 µM (green), 10 µM (cyan), 50 µM (purple), 100 µM (yellow), 500 µM (grey) and 1 mM (light yellow).

Possible interference by Chloride

Chloride ions are recognised as an interferent in As(III) detection on some metal surfaces such as Pt when using the ASV of bulk As and when using UPD-ASV with Platinum electrodes. [9, 36] Thus, Chloride ions were also investigated in an interference study with different concentrations of Cl^-. The pre-concentrations were conducted at – 0.9 V for 300 s with detection via a linear potential sweep from – 0.9 V to + 0.62 V at a scan rate of 0.1 V s^{-1}. Then the baseline correction was applied to peak 4' with the procedure as above. Figure 6.6a presents the baseline corrected stripping voltammograms obtained from 0.1 µM of As(III) in 0.1 M H_2SO_4 with the addition of Cl^- from 1 µM to 0.54 M at Au macroelectrodes. The black

dashed line was recorded for a solution without Cl^- where only one peak was observed at ca + 0.05 V corresponding to the peak 4'. With the addition of Cl^-, the signal of peak 4' varied negligibly. Even for concentrations of Cl^- was as high as 0.54 M, the signal of peak 4' was not changed. Thus, it can be concluded that Cl^- does not interfere to the oxidation peak of As ad-atoms on Au macroelectrodes.

Analogous experiments were made on Au nanoparticle-modified GCEs. The pre-concentration was conducted at – 0.9 V for 300 s with detection using a linear sweep from – 0.9 V to + 0.62 V at a scan rate of 0.1 V s^{-1}. Baseline corrections were also made for peak 4' with the procedure as above. Figure 6.6b displays the baseline corrected ASVs obtained from 0.1 µM of As(III) with various concentrations of Cl^- from 1 µM to 0.54 M at Au nanoparticle-modified GCEs. Similar to what was seen at Au macroelectrodes, again the charge of peak 4' at ca + 0.1 V did not change excessively with the addition of Cl^- as judged by comparison of the voltammograms obtained without (black dashed line in Figure 6.6b) and with Cl^-. The results suggest that the method is free from interference by chloride.

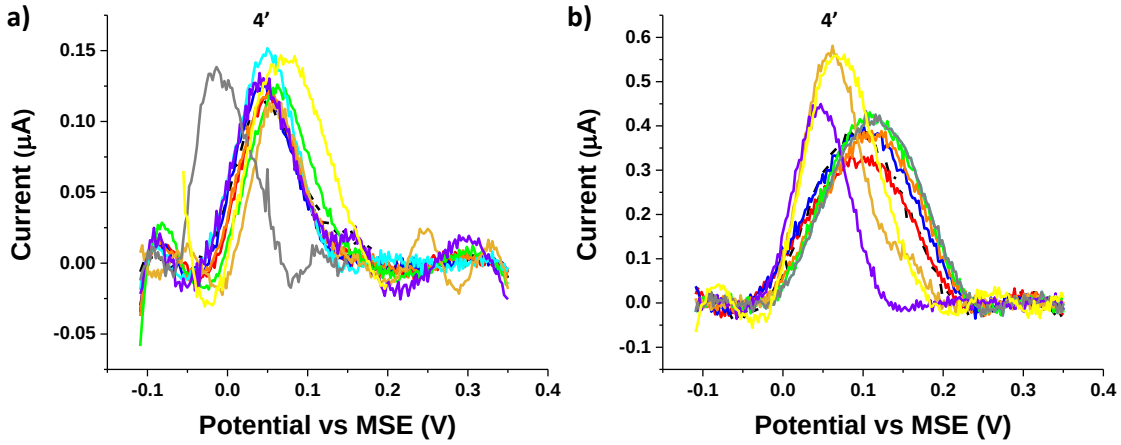

Figure 6.6 Baseline corrected ASV curves of 0.1 µM As(III) in 0.1 M H_2SO_4 with various concentrations of Cl^- in the potential range from - 0.1 V to + 0.35 V at a) Au macroelectrodes and b) Au nanoparticle-modified GC electrodes. ASV parameters: deposition at - 0.9 V for 300 s, scan rate was 0.1 V s^{-1}. Cl^- concentrations: 0 µM (black dashed line), 1 µM (red), 5 µM (blue), 10 µM (orange), 50 µM (green), 100 µM (cyan), 7000 µM (yellow), 20 mM (purple), 100 mM (grey) and 0.54 M (light yellow).

Possible Synergistic Interference by Cu(II) and chloride

The above shows that Cu(II) and chloride do not separately influence the detection of As using the UPD ASV method so offering major advantages over either the use if bulk As for ASV or Pt electrodes for UPD ASV. However, it was deemed prudent to check if the simultaneous presence of both species had any influence at on As(III) detection at both types of electrodes. Pre-concentration was carried out at – 0.9 V for 300 s and detection with a linear sweep from – 0.9 V to + 0.62 V at a scan rate of 0.1 V s^{-1} in various concentrations of As(III) from 0.05 μM to 0.1 μM with the addition of 1 mM Cu^{2+} or 0.54 M Cl^- at Au macroelectrodes. Baseline corrections were then made and the charge was calculated with the procedures as above. Figure 6.7a shows the charge of peak 4' vs concentrations of As(III) obtained from 0.01 μM to 0.1 μM without interferents (black), with 1 mM Cu^{2+} (red), with 0.54 M Cl^- (blue), and with both 1 mM Cu^{2+} and 0.54 M Cl^- (green). The error bars were standard deviation calculated from at least three sets of data. All points with possible interferents are seen to lie within the error bars of the arsenic signal (black points in Figure 6.7a). A linear line was simulated with all points in the plot (yellow line in Figure 6.7a) with an equation of $Charge = 1.0 \times 10^{-6} C\ \mu M^{-1} \times [As(III)] + 1.6 \times 10^{-9}\ C$. Compare to the equation obtained in Figure 6.4c, the sensitivity varied by no more than ca 5% from 9.5×10^{-7} C μM^{-1} to 1.0×10^{-6} C μM^{-1}. Thus, we conclude that there is no synergistic interference of either Cu^{2+} or Cl^- on the oxidation peak of As ad-atoms on Au macroelectrodes.

Similar experiments were also made on Au nanoparticle-modified GCEs. Pre-concentration was again carried out at – 0.9 V for 300 s and detection with a linear sweep from – 0.9 V to + 0.62 V at a scan rate of 0.1 V s^{-1} in various concentrations of As(III) from 0.05 μM to 0.1 μM with the addition of 1 mM Cu^{2+} or 0.54 M Cl^- at Au nanoparticle-modified GCEs. Baseline corrections were made and the charge was calculated with the procedures as above.

Figure 6.7b displays the charge of peak 4' vs concentrations of As(III) obtained from 0.005 μM to 0.1 μM without interferents (black), with 1 mM Cu^{2+} (red), with 0.54 M Cl^- (blue), and with both 1 mM Cu^{2+} and 0.54 M Cl^- (green). The error bars were standard deviation calculated from at least three sets of data. All points lie within the error bars of the arsenic signal (black points in Figure 6.7b). A linear line was simulated with all points in the plot (yellow line in Figure 6.7b) with an equation of $Charge = 5.0 \times 10^{-6} C\ \mu M^{-1} \times [As(III)] - 4.3 \times 10^{-9}\ C$. Compare to the equation obtained in Figure 6.4d, the sensitivity remained the same as 5.0 × 10^{-6} C μM^{-1}. Thus, it can be concluded that neither Cu^{2+} nor Cl^- interfere with the oxidation peak of As ad-atoms on Au surfaces. The sensitivity of the UPD ASV method is not affected by Cu^{2+} and Cl^- or combinations of them.

In comparison with previous methods for detecting As(III) under normal ASV conditions [43], bulk As(0) was deposited at gold surface at ca -0.7 V for 180 s, but did not show measurable stripping peaks for concentrations lower than 50 μM. Cu(II) was reported as the only likely interference in such measurements. As for UPD methods for detecting bulk As(III), Xiao *et al* used square wave voltammetry after deposited bulk As(0) at – 0.8 V for 120 s and calculated a LOD based on 3σ method of 0.1 ppb [32]. Neither method reported a visually clear detection limit as low as 10 ppb.

The significant issues of interference by copper and by chloride have been solved by using UPD ASV. To optimise the electrode used it is interesting to compare the time of measurement and cost of the different approaches and these data are shown in Appendix Section 8. The Au screen printed electrode has the lowest cost and the shortest time for each measurement (Table A6.2 in Appendix Section 8), which encourages the future use of disposable electrodes for real world applications.

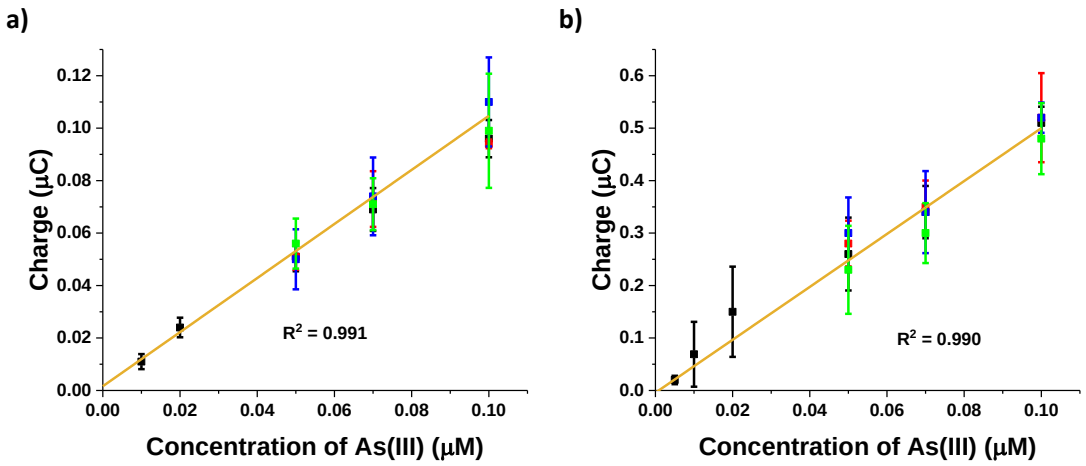

Figure 6.7 Charge of stripped As(0) ad-atoms vs. the concentration of As(III) at a) Au macroelectrode and b) 5 nm Au nanoparticle-modified GC electrode. The points included were various concentrations of As(III) (black), As(III) solutions contained 1 mM Cu^{2+} (red), As(III) solutions contained 0.54 M Cl^{-} (blue), and As(III) solutions contained both 1 mM Cu^{2+} and 0.54 M Cl^{-} (green). The charge was calculated from baseline corrected LSVs and error bars were standard deviations calculated from at least sets of data. The calibration lines (yellow) were calculated based on the charges of all points in the graphs. LSV parameters: deposition at - 0.9 V vs. MSE for 300 s, potential scan rate 0.1 V s^{-1}.

6.4. Conclusions

The analytical use of underpotential deposition of As from As(III), the most toxic form as As on gold surfaces with anodic stripping of adsorbed As ad-atoms has been validated on both gold macroelectrodes and gold nanoparticle-modified electrodes. Limits of detection within the requirements of the WHO guidelines for safe drinking water were observed at both electrodes with clearly visible signals in each case even at the lowest concentrations studied. A particular merit of using UPD-ASV method to detect As(III) using Au substrates is that it can avoid interference from Cu^{2+} and Cl^{-} or combinations of them. The detection limit for gold nanoparticle-modified electrodes was lower and the sensitivity higher than for gold macroelectrodes, suggesting benefits in using nanoparticle-modified electrodes over macroelectrodes. In the next chapter the use of gold electrodes is developed further for the analysis of As(V) and a procedure for the measurement of total As and the As(III) to As(V) speciation is developed.

6.5. Appendix

Section 1: Calculation of the coverage of Au nanoparticles on the surface of a glassy carbon electrode (GCE)

To estimate the approximate coverage of nanoparticles in terms of monolayers deposited, a cubic close packed arrangement was considered. The Au nanoparticles as purchased from Sigma Aldrich, have a diameter of ca 5 nm. Hence the area occupied by a single particle on the electrode is 2.5×10^{-17} m^2 (Figure A6.1). The particle concentration of the Au nanoparticles used were 5.5×10^{13} particles mL^{-1} and there were 5 μL of Au nanoparticles suspension dropped onto the electrode. Thus, the number of particles that dropped onto the electrode can be estimated as 2.75×10^{11} particles.

For 5 μL of Au nanoparticles suspension, the covered/blocked area of particles by the nanoparticles is:

$$2.5 \times 10^{-17}\, m^2 \times 2.75 \times 10^{11}\, particles = 0.07\, cm^2 \quad (6\text{-}1)$$

The particles were drop casted on to a GCE with an area of 0.07 cm^2 hence the approximate monolayer coverage is

$$\frac{0.07\, cm^2}{0.07\, cm^2} = 1 \quad (6\text{-}2)$$

The number of moles of Au nanoparticles on the surface of the GCE is

$$\frac{2.75 \times 10^{11}\, particles}{6.02 \times 10^{23}\, mol^{-1}} = 4.6 \times 10^{-13}\, mol \quad (6\text{-}3)$$

Then the estimated surface coverage of Au nanoparticles on GCE is

$$\frac{4.6 \times 10^{-13}\, mol}{0.07\, cm^2} = 6.5 \times 10^{-12}\, mol\, cm^{-2} \quad (6\text{-}4)$$

The surface area of each Au nanoparticle was calculated assuming it is a sphere of radius 2.5 nm:

$$4 \times \pi \times (2.5\,nm)^2 = 79\,nm^2 = 7.9 \times 10^{-13} cm^2 \quad (6\text{-}5)$$

The total surface area of the drop casted Au nanoparticles was also calculated based on the number of particles times the surface area of each particle, which is:

$$2.75 \times 10^{11} particles \times 4 \times \pi \times 5\,nm^2 = 0.2\,cm^2 \quad (6\text{-}6)$$

Thus, the approximate area of Au available for As deposition is 0.2 cm^2.

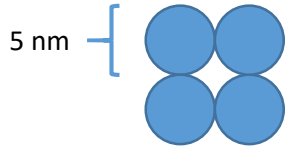

Figure A6.1 A scheme of possible distribution of Au nanoparticles with a size of 5 nm on surface of GCE.

Section 2: Baseline correction and peak area integration for peak 4'

The signal used for the UPD-ASV analysis is the charge of peak 4', which was calculated from the area of baseline corrected voltammogram. A sample correction is shown in this section. To obtain the baseline corrected peak 4', first, the voltammogram between – 0.10 V to + 0.35 V (black line in Figure A6.2b) was zoomed in from the raw LSV curve (Figure A6.2a), and a baseline was simulated via the 'polynomial' method in Origin 2017 with an order of 6 in the range of – 0.10 V to + 0.35 V (red line in Figure A6.2b). Then a baseline subtraction was applied that the part of the raw voltammogram between – 0.10 V to + 0.35 V, and a baseline corrected LSV obtained (Figure A6.2c). Next the area of peak 4' was estimated from the baseline corrected voltammograms using the 'integrate' function in Origin 2017 (grey area in Figure A6.2c), with the charge was calculated from the peak area divided by the scan rate. The apparent 'reduction peaks' at – 0.05 V and + 0.25 V in Figure A6.2c are artefacts from the

baseline correction. They do not relate to Faradaic reactions. The LSVs in this project were all baseline corrected voltammograms estimated using this method.

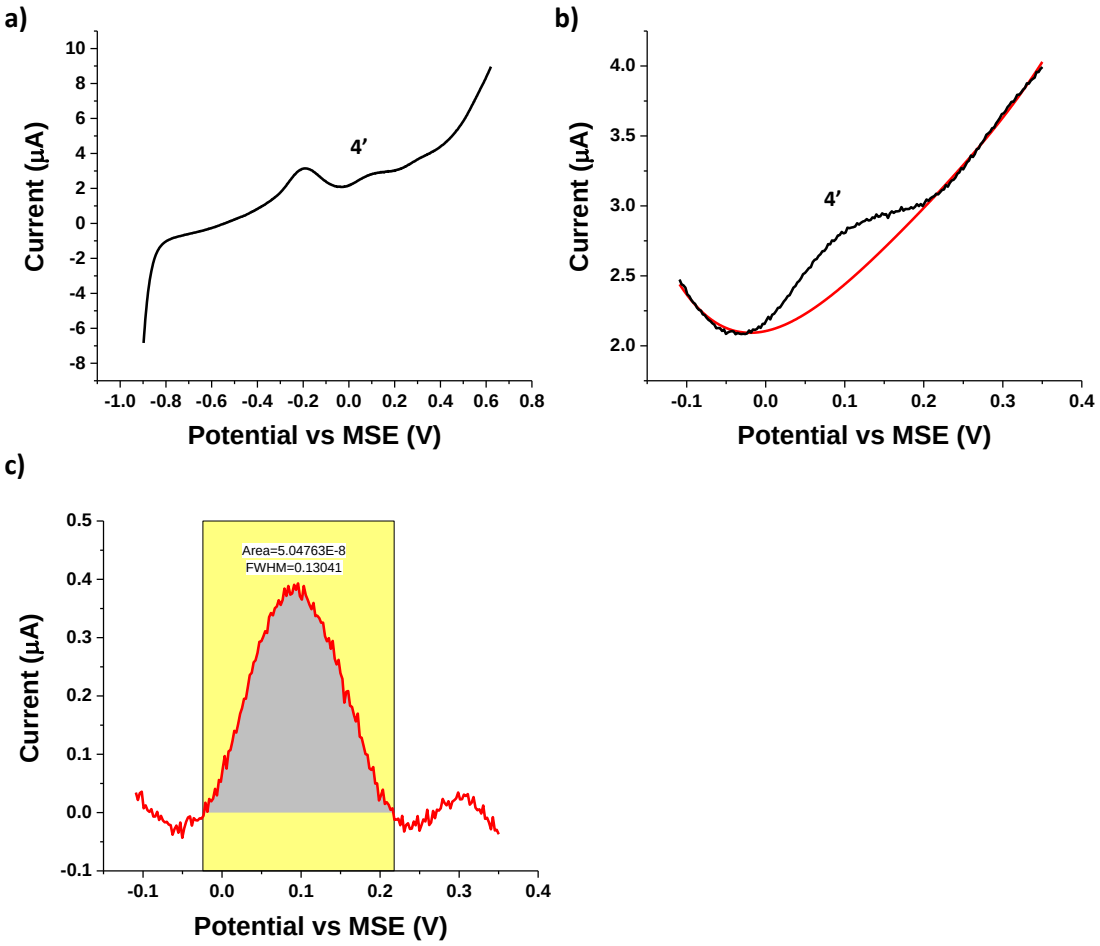

Figure A6.2 a) The original LSV curve of 0.1 µM As(III) in 0.1 M H_2SO_4 at Au nanoparticles GCE. b) The LSV curve from -0.10 V to +0.35 V (black line) and simulated baseline (red line). c) The baseline corrected LSV curve from -0.10 V to +0.35 V (red line) and the peak area (grey area). LSV parameters: deposition at -0.9 V vs. MSE for 300s, potential scan rate 0.1 V s^{-1}.

Section 3: Calculation of the surface coverage of As during pre-concentration on bulk Au

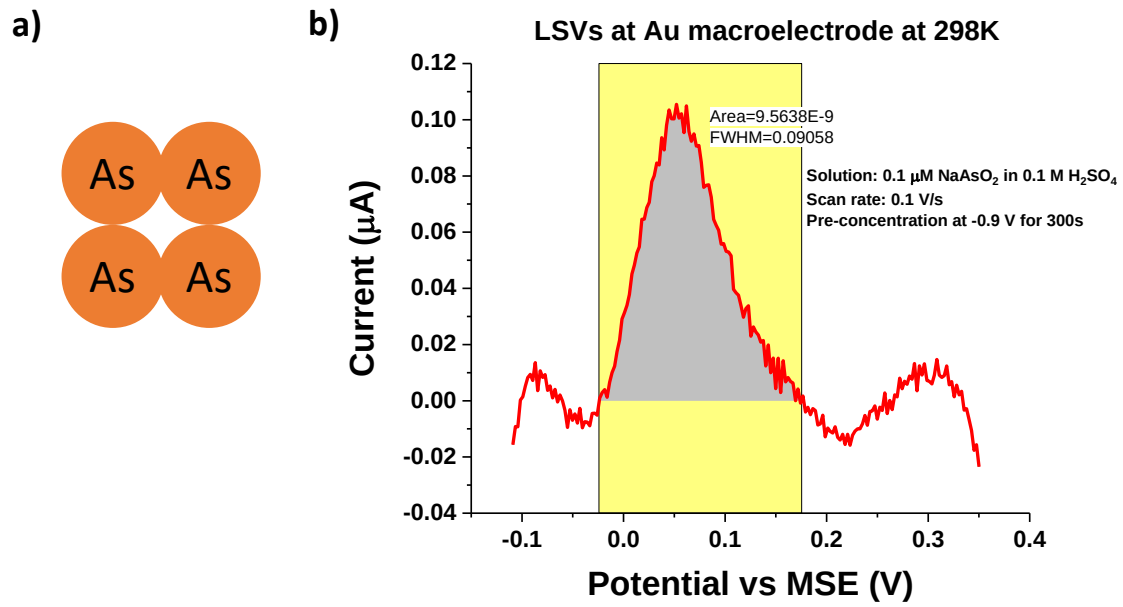

Figure A6.3 a) A scheme of As atoms closely packed at the surface of Au. b) The baseline corrected LSV curves of peak 4' of 0.1 μM As(III) in 0.1 M H_2SO_4 at Au macroelectrode. The grey areas are used for the integration. LSV parameters: deposition at -0.9 V vs. MSE for 300s, potential scan rate 0.1 V s^{-1}, and baseline was modelled via polynomial method from -0.10 V to +0.35 V for peak 4'.

The area of peak 4' can be calculated via 'Integrate' in Origin 2017. The area of the peak 4' of 0.1 μM As(III) in 0.1 M H_2SO_4 at Au macroelectrodes was 9.6×10^{-9} C s V^{-1} (Figure A6.3).The charge (Q) of the peak then can be estimated as:

$$Q = \frac{Area\ of\ peak}{Scan\ rate} = 9.6\ \times\ 10^{-8}\ C \tag{6-7}$$

The corresponding number of electrons then was estimated as:

$$\frac{Charge\ of\ peak\ 4\prime}{Elementary\ charge} = \frac{9.6 \times 10^{-8}\ C}{1.6 \times 10^{-19}\ C} = 6.0\ \times\ 10^{11} \tag{6-8}$$

The number of moles of electrons was calculated as:

$$\frac{Number\ of\ electrons}{Avogadro\ constant} = \frac{6.0 \times 10^{11}}{6.02 \times 10^{23}\ mol^{-1}} = \ 1.0\ \times\ 10^{-12}\ mol \tag{6-9}$$

Each As(III) ion has three electrons transferred during the electrochemical reaction. Thus, the number of moles of As can be estimated as:

$$\frac{Moles\ of\ electrons}{3} = \frac{9.9 \times 10^{-13}\ mol}{3} = 3.3\ \times\ 10^{-13}\ mol \quad (6\text{-}10)$$

The surface area of Au macroelectrode (with radius of 0.08 cm) is 0.02 cm^2 or 2×10^{12} nm^2. Hence, the estimated surface coverage of As on the surface of Au could be obtained assuming As atoms were closely packed on the surface of electrode (Figure A6.3a):

$$\frac{Moles\ of\ As}{Surface\ area\ of\ Au\ macroelectrode} = \frac{3.3 \times 10^{-13}\ mol}{0.02\ cm^2} = 1.7\ \times\ 10^{-11}\ mol\ cm^2 \quad (6\text{-}11)$$

Each As(III) ion has three electrons transferred during the reaction. Thus, the number of As ad-atoms can be estimated as $2.0\ \times\ 10^{11}$. The surface coverage of As on the surface of Au can also be obtained with the number of As atoms deposited and the surface area of the electrode:

$$\frac{Number\ of\ As\ atoms}{Surface\ area\ of\ Au\ macroelectrode} = \frac{2.0 \times 10^{11}\ molecules}{0.02\ cm^2} = 1.0\ \times\ 10^{13}\ molecules\ cm^{-2} \quad (6\text{-}12)$$

The number of monolayers of As ad-atoms were also estimated. The radius of As atom is 185 pm [49] and diameter is 370 pm. The covered area of single As atom (d^2) is calculated to be 0.14 nm^2.

The number of As deposited can be calculated from the number of moles of As and Avogadro constant, and it is:

$$Moles\ of\ As \times Avogadro\ constant = 3.3\ \times\ 10^{-13}\ mol\ \times\ 6.02\ \times\ 10^{23}\ mol^{-1}\ = 2\ \times\ 10^{11} \quad (6\text{-}13)$$

The number of one monolayer of As atoms on the surface of Au electrode was estimated assuming As atoms were closely packed on Au (Figure A6.3a):

$$\frac{Surface\ area\ of\ Au\ macroelectrode}{Covered\ area\ of\ single\ As\ atom} = \frac{2 \times 10^{12}\ nm^2}{0.14\ nm^2} = 1.5 \times 10^{13} \qquad (6\text{-}14)$$

Therefore, the number of layers of As atoms on Au is:

$$\frac{Number\ of\ As\ atoms\ deposited}{Number\ of\ one\ monolayer\ of\ closely\ packed\ As\ atoms} = \frac{2 \times 10^{11}}{1.5 \times 10^{13}} = 0.014 \qquad (6\text{-}15)$$

This corresponds to a sub-monolayer (ca 0.014 monolayers) of As atoms on the surface of Au.

Section 4: Detection of the lowest signal on a Au macroelectrode

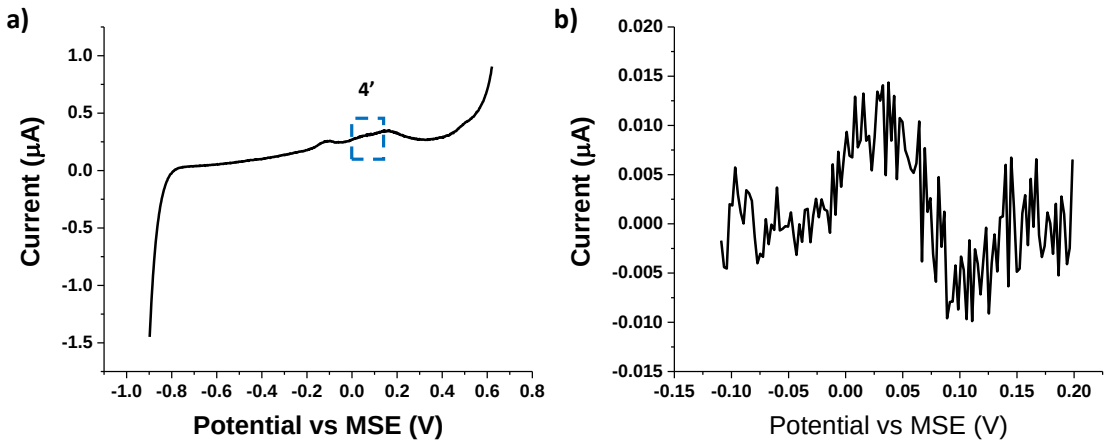

Figure A6.4 a) The raw LSV curve of 0.01 μM As(III) in 0.1 M H_2SO_4 at a gold macroelectrode. b) The baseline corrected stripping voltammogram from – 0.10 V to + 0.2 V. ASV parameters: pre-concentration at – 0.9 V for 300 s, potential scan rate 0.1 V s^{-1}.

An example of detection of lowest signal is shown in this section. The pre-concentration was carried out at – 0.9 V for 300 s in 0.1 M H_2SO_4 then followed up with a LSV from – 0.9 V to + 0.62 V at a scan rate of 0.1 V s^{-1}. Figure A6.4a shows the raw LSV from – 0.9 V to + 0.62 V in 0.01 μM As(III). The peak 4', assigned as the stripping peak of As ad-atoms, was not so clear to be observed. Then a baseline correction was applied to the voltammogram from – 0.10 V to + 0.20 V with the procedure shown in main text. Figure A6.4b illustrates the baseline corrected stripping voltammogram of 0.01 μM As(III). It is clear that the peak 4' after baseline

correction can be observed visually, which suggests a visually detectable LOD of 0.01 μM (8 ppb) of As(III) in water.

Note that there is a dip at ca + 0.10 V shown in Figure A6.4b, which was caused by the subtraction of the baseline in Origin rather than a Faradaic reaction. The tiny variations from the background used for the baseline corrections may also cause small differences in minimum measurable signals in Figure A6.4b.

Section 5: Calculation of the surface coverage of As after pre-concentration on Au nanoparticles

The area of peak 4' was obtained via integration using Origin 2017.The peak was measured using 0.1 μM As(III) in 0.1 M H_2SO_4 at an Au nanoparticle-modified GCE (Figure A6.5) and gave a charge (Q) of 5.0×10^{-6} C.

The corresponding number of electrons was estimated as:

$$\frac{Charge\ of\ peak\ 4\prime}{Elementary\ charge} = \frac{5.0 \times 10^{-6}\ C}{1.6 \times 10^{-19}\ C} = 3.2 \times 10^{13} \quad (6\text{-}16)$$

The number of moles of electrons was calculated as:

$$\frac{Number\ of\ electrons}{Avogadro\ constant} = \frac{3.2 \times 10^{12}}{6.02 \times 10^{23}\ mol^{-1}} = 5.3 \times 10^{-11}\ mol \quad (6\text{-}17)$$

Each As(III) ion has three electrons transferred during the electrochemical reaction. Thus, the number of moles of As can be estimated as:

$$\frac{Moles\ of\ electrons}{3} = \frac{5.3 \times 10^{-11}\ mol}{3} = 1.8 \times 10^{-11}\ mol \quad (6\text{-}18)$$

The available area for As on Au surface is 0.2 cm^2, which was calculated in Appendix Section 1.

Then the estimated surface coverage of As on the surface of Au nanoparticles can be:

$$\frac{Moles\ of\ As}{Estimated\ surface\ area\ of\ Au\ nanoparticles} = \frac{1.8 \times 10^{-11}\ mol}{0.2\ cm^2} = 9\ \times\ 10^{-11}\ mol\ cm^{-2} \quad (6\text{-}19)$$

The number of As atoms can be calculated from the moles of As and the Avogadro constant, is:

$$Number\ of\ moles\ of\ As \times Avogadro\ constant = 1.8\ \times\ 10^{-11}\ mol\ \times\ 6.02\ \times\ 10^{23}\ mol^{-1}\ = 1.1\ \times\ 10^{13} \quad (6\text{-}20)$$

The surface coverage of As on the surface of Au can also be obtained with the number of As atoms deposited and the surface area of the electrode:

$$\frac{Number\ of\ As\ atoms}{Estimated\ surface\ area\ of\ Au\ nanoparticles} = \frac{1.1 \times 10^{13}\ molecules}{0.2\ cm^2} = 5.3\ \times\ 10^{13}\ molecules\ cm^{-2} \quad (6\text{-}21)$$

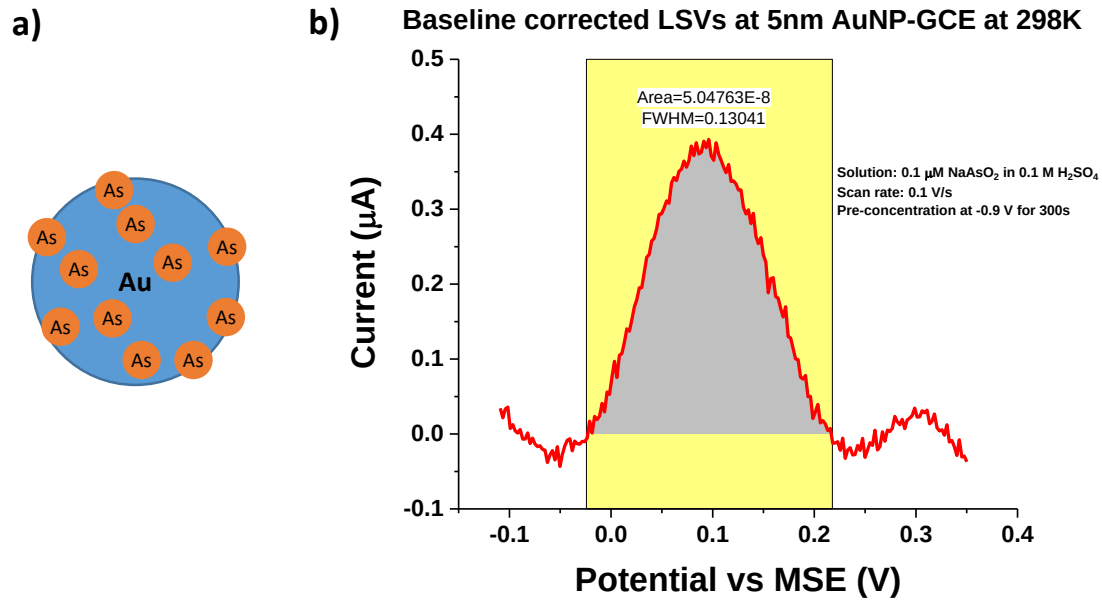

Figure A6.5 a) A scheme of As atoms deposited on the Au nanoparticles. b) The baseline corrected LSV curves of peak 4' of 0.1 µM As(III) in 0.1 M H_2SO_4 at Au nanoparticle-modified GCE. The grey areas in are used for the integration. LSV parameters: deposition at -0.9 V vs. MSE for 300s, potential scan rate 0.1 V s^{-1}, and baseline was modelled via polynomial method from -0.10 V to +0.35 V for peak 4'.

The As atoms were assumed to be deposited on the surface of every single Au nanoparticles as Figure A6.5a shows. The number of As atoms per nanoparticle were estimated based on the covered area of single As atom and the number of drop casted Au nanoparticles:

$$\frac{Number\ of\ As}{Number\ of\ Au\ nanoparticles} = \frac{1.1 \times 10^{13}}{2.75 \times 10^{11}} = 40\ atoms \qquad (6\text{-}22)$$

The surface area of each Au nanoparticle was calculated to be 7.9×10^{-13} cm^2 assuming each particle to be a sphere of radius 2.5 nm. Then the area per As atoms on a single As nanoparticle can be calculated from the estimated surface area of the rough sphere particles and number of As atoms per Au nanoparticle:

$$\frac{Estimated\ surface\ area\ of\ each\ Au\ nanoparticle}{Number\ of\ As\ atoms\ per\ nanoparticle} = \frac{7.9\times10^{-13}\ cm^2}{40\ atoms} = 2\ \times\ 10^{-14}\ cm^2 = 2\ nm^2 \qquad (6\text{-}23)$$

This corresponds to ca 0.073 monolayers on the surface of a single nanoparticle.

Table A6.1 Charge and number of monolayers of As ad-atoms stripped off in peak 4' measured following reductive accumulation in various concentrations of As(III) in 0.1 M H_2SO_4 at both Au macroelectrodes and Au nanoparticle-modified GCEs. LSV parameters: deposition at – 0.9 V for 300 s, potential scan rate 0.1 V s^{-1}.

	Peak charge (μC)		Number of monolayers of As ad-atoms	
Concentrations (μM)	Au macroelectrodes	Au nanoparticle-modified electrodes	Au macroelectrodes	Au nanoparticle-modified electrodes
0.005		0.020		0.003
0.01	0.011	0.069	0.002	0.01
0.02	0.018	0.15	0.003	0.02
0.05	0.051	0.27	0.007	0.04

0.07	0.070	0.35	0.010	0.05
0.1	0.096	0.50	0.014	0.07
0.5	0.14	0.87	0.020	0.12
1	0.19	0.89	0.027	0.13
2	0.19	0.87	0.027	0.12

Section 6: Optimization of deposition time

Deposition time during the pre-concentration was important and need to be determined. The purpose of this section is to determine the time of the ad-atom deposition by considering oxidative voltammograms following peak signal at different deposition time. Figure A6.6a illustrates the baseline corrected LSVs for Au macroelectrodes with deposition time from 60 s to 360 s. The deposition potential was – 0.9 V for all experiments and the scan rate was 0.1 V s^{-1}. Peak 4' observed at ca + 0.05 V represented oxidation peak of As ad-atoms. Figure A6.6b shows the charge of peak 4' vs the deposition time at Au macroelectrodes. It can be seen the charge of peak 4' increased slowly with the deposition time from 60 to 180 s. However, the peak charge enhanced extremely fast from 180 to 300 s, and the charge kept relatively steady when the deposition time reached to ca 300 s. Thus, the deposition time was chosen to be 300 s for expediency for the rest of the study.

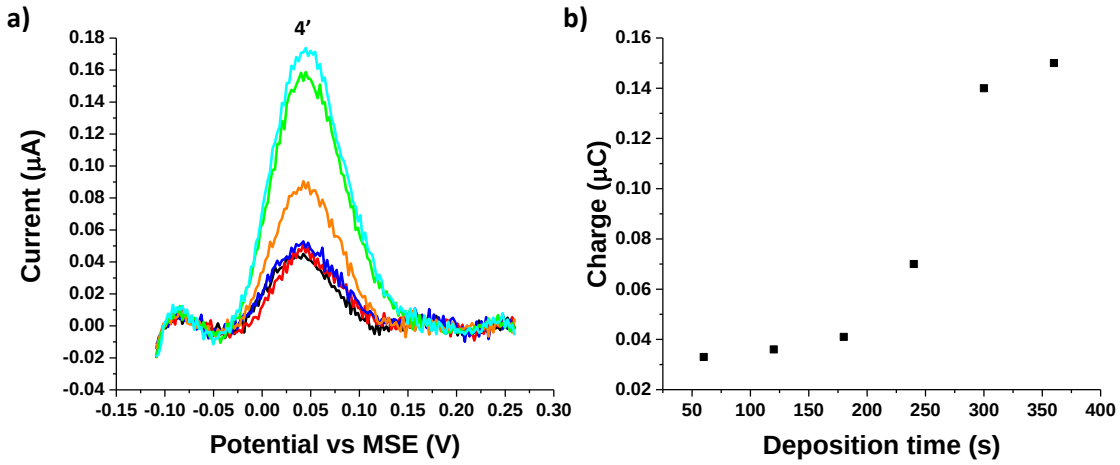

Figure A6.6 a) baseline corrected ASV curves of 0.1 µM As(III) in 0.1 M H_2SO_4 at Au macroelectrode with pre-concentration at -0.9 V for 60s (black), 120s (red), 180 s (blue), 240s (orange), 300s (green) and 360s (cyan). b) Charge of peak 4' vs deposition time.

Section 7: Optimization of deposition potential

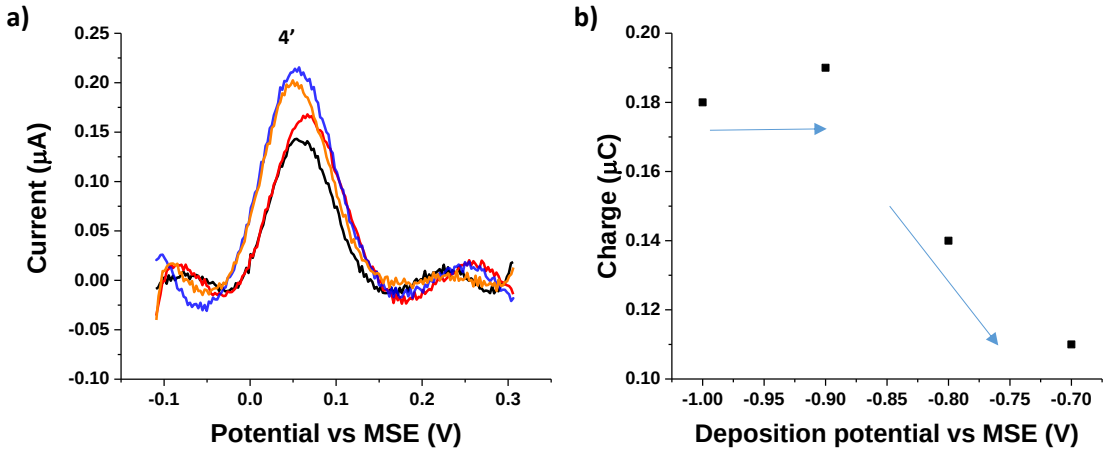

Figure A6.7 a) baseline corrected ASV curves of 10 µM As(III) in 0.1 M H_2SO_4 at Au macroelectrode with pre-concentration at -1.0 V (orange), - 0.9 V (blue), - 0.8 V (red), and – 0.7 V (black) for 300s. b) Charge of peak 4' vs deposition potential.

The deposition potential during pre-concentration was important and need to be determined in addition to deposition duration. The pre-concentration was carried out at potentials from – 1.0 V to – 0.7 V for 300 s in 10 µM As(III) in 0.1 M H_2SO_4 then followed up with a LSV to + 0.62 V. The baseline correction for peak 4' was also followed the procedure as in main text. Figure A6.7a presents the baseline corrected LSVs of peak 4' at Au macroelectrodes which was obtained from 10 µM As(III) with different deposition time. It is

clear to see that the peak charge was increased with more negative deposition potential. The charge of peak 4' vs deposition potential is also plotted in Figure A6.7b. It is clear to see that the charge of peak 4' remains unchanged when the deposition potential was more negative than – 0.9 V. However, when the potential was more positive than – 0.9 V, the charge of peak 4' decreased. This suggests the underpotential deposition at potentials more negative than – 0.9 V. However, the more negative deposition potential could generate high background and noise for lower concentrations of As(III) in ASV due to the reduction of H^+, which makes the signal unreliable. Thus, - 0.9 V was chosen as the deposition potential for the pre-concentration of As ad-atoms in this study.

Section 8: Estimation of time and cost of each measurement

The national minimum wage paid in UK is estimated to be € 10 per hour [1] and the total time for each measurement was estimated as 8 min, 23 min, and 5.5 min on Au macroelectrodes, Au nanoparticle-modified GCEs, and Au screen printed electrodes, respectively. Thus, the time and cost of each measurement has been tabulated and list below:

Table A6.2 Estimation of time and cost of each measurement with the UPD-ASV method on Au macroelectrodes, Au nanoparticle-modified GCEs and Au screen printed electrode.

	Au macroelectrode	Au nanoparticle-modified GCE	Au screen printed electrode
Polishing	2.5 min	2.5 min	
Drop cast		15 min	
Deposition	5 min	5 min	5 min
ASV scan	0.5 min	0.5 min	0.5 min
Total time for one measurement	8 min	23 min	5.5 min

Cost of time	€ 80	€ 230	€ 55
Cost of electrode	€ 357 (permanent electrode)	€ 142 (permanent electrode)	€ 2.20
Cost of each drop cast of Au nanoparticles		€ 0.025	
Total cost of each measurement	€ 80	€ 230	€ 57.2

6.6. Bibliography

[1] Y. Zhang, D. Li, R.G. Compton, Arsenic (III) Detection with Underpotential Deposition on Gold, J. Electroanal. Chem. (2022) 116154.
[2] J. Wang, Analytical Electrochemistry, Wiley-VCH2006.
[3] A. J. Bard, L.R. Faulkner, Electrochemical Methods: Fundamentals and Applications, 2nd ed., John Wiley & Sons, Inc, New York, 2001.
[4] C. Brett, A.M. Oliveira Brett, Electrochemistry: principles, methods, and applications, 1993.
[5] A.J. Borrill, N.E. Reily, J.V. Macpherson, Addressing the practicalities of anodic stripping voltammetry for heavy metal detection: a tutorial review, Analyst 144(23) (2019) 6834-6849.
[6] M. Fleischmann, S. Pons, The behavior of microelectrodes, Anal. Chem. 59(24) (1987) 1391A-1399A.
[7] C. He, M. Tao, C. Zhang, Y. He, W. Xu, Y. Liu, W. Zhu, Microelectrode-Based Electrochemical Sensing Technology for in Vivo Detection of Dopamine: Recent Developments and Future Prospects, Crit. Rev. Anal. Chem. (2020) 1-11.
[8] R.G. Compton, G.G. Wildgoose, N.V. Rees, I. Streeter, R. Baron, Design, fabrication, characterisation and application of nanoelectrode arrays, Chem. Phys. Lett. 459(1-6) (2008) 1-17.
[9] Y. Zhang, D. Li, R.G. Compton, Arsenic (III) Detection with Underpotential Deposition and Anodic Stripping Voltammetry, ChemElectroChem (2021).
[10] L.J. Bu, J. Liu, Q.J. Xie, S.Z. Yao, Anodic stripping voltammetric analysis of trace arsenic(III) enhanced by mild hydrogen-evolution at a bimetallic Au-Pt nanoparticle modified glassy carbon electrode, Electrochem. Commun. 59 (2015) 28-31.
[11] Z. Guo, M. Yang, X.-J. Huang, Recent developments in electrochemical determination of arsenic, Curr. Opin. Electrochem. 3(1) (2017) 130-136.
[12] M. Dali, K. Zinoubi, A. Chrouda, S. Abderrahmane, S. Cherrad, N. Jaffrezic-Renault, A biosensor based on fungal soil biomass for electrochemical detection of lead (II) and cadmium (II) by differential pulse anodic stripping voltammetry, J. Electroanal. Chem. 813 (2018) 9-19.
[13] A. Nsabimana, S.A. Kitte, T.H. Fereja, M.I. Halawa, W. Zhang, G. Xu, Recent developments in stripping analysis of trace metals, Curr. Opin. Electrochem. 17 (2019) 65-71.
[14] E. Desimoni, F. Palmisano, L. Sabbatini, Simultaneous determination of tin and lead at the parts-per-billion level by coupling differential pulse anodic stripping voltammetry with a matrix exchange method, Anal. Chem. 52(12) (1980) 1889-1892.

[15] J. Orozco, C. Fernandez-Sanchez, C. Jimenez-Jorquera, Underpotential deposition-anodic stripping voltammetric detection of copper at gold nanoparticle-modified ultramicroelectrode arrays, Environ. Sci. Technol. 42(13) (2008) 4877-4882.
[16] C.A. Paddon, R.G. Compton, Underpotential deposition of lithium on platinum single crystal electrodes in tetrahydrofuran, J. Phys. Chem. C 111(26) (2007) 9016-9018.
[17] O.A. Oviedo, L. Reinaudi, S.G. García, E.P.M. Leiva, Underpotential deposition, Monographs in Electrochemistry (2016).
[18] F.J. Sarabia, V. Climent, J.M. Feliu, Underpotential deposition of Nickel on platinum single crystal electrodes, J. Electroanal. Chem. 819 (2018) 391-400.
[19] L.Y. Wang, X.L. Peng, H.J. Fu, C. Huang, Y.P. Li, Z.M. Liu, Recent advances in the development of electrochemical aptasensors for detection of heavy metals in food, Biosens. Bioelectron. 147 (2020) 10.
[20] D. Banik, S.K. Manna, A.K. Mahapatra, Recent development of chromogenic and fluorogenic chemosensors for the detection of arsenic species: Environmental and biological applications, Spectroc. Acta Pt. A-Molec. Biomolec. Spectr. 246 (2021) 19.
[21] K. Mao, H. Zhang, Z.L. Wang, H.R. Cao, K.K. Zhang, X.Q. Li, Z.G. Yang, Nanomaterial-based aptamer sensors for arsenic detection, Biosens. Bioelectron. 148 (2020) 15.
[22] X.C. Xu, X.H. Niu, X. Li, Z.H. Li, D. Du, Y.H. Lin, Nanomaterial-based sensors and biosensors for enhanced inorganic arsenic detection: A functional perspective, Sens. Actuator B-Chem. 315 (2020) 13.
[23] S. Sikdar, M. Kundu, A Review on Detection and Abatement of Heavy Metals, ChemBioEng Rev. 5(1) (2018) 18-29.
[24] X.P. Yu, C.L. Liu, Y.F. Guo, T.L. Deng, Speciation Analysis of Trace Arsenic, Mercury, Selenium and Antimony in Environmental and Biological Samples Based on Hyphenated Techniques, Molecules 24(5) (2019) 23.
[25] S. Li, C.C. Zhang, S.N. Wang, Q. Liu, H.H. Feng, X. Ma, J.H. Guo, Electrochemical microfluidics techniques for heavy metal ion detection, Analyst 143(18) (2018) 4230-4246.
[26] G.M. dos Santos, D. Pozebon, C. Cerveira, D.P. de Moraes, Inorganic arsenic speciation in rice products using selective hydride generation and atomic absorption spectrometry (AAS), Microchem. J. 133 (2017) 265-271.
[27] I. Komorowicz, A. Hanć, W. Lorenc, D. Barałkiewicz, J. Falandysz, Y. Wang, Arsenic speciation in mushrooms using dimensional chromatography coupled to ICP-MS detector, Chemosphere 233 (2019) 223-233.
[28] H. Cheng, W. Zhang, Y. Wang, J. Liu, Graphene oxide as a stationary phase for speciation of inorganic and organic species of mercury, arsenic and selenium using HPLC with ICP-MS detection, Microchim. Acta 185(9) (2018) 1-8.
[29] B. Bansod, T. Kumar, R. Thakur, S. Rana, I. Singh, A review on various electrochemical techniques for heavy metal ions detection with different sensing platforms, Biosens. Bioelectron. 94 (2017) 443-455.
[30] K. Pungjunun, S. Chaiyo, I. Jantrahong, S. Nantaphol, W. Siangproh, O. Chailapakul, Anodic stripping voltammetric determination of total arsenic using a gold nanoparticle-modified boron-doped diamond electrode on a paper-based device, Microchim. Acta 185(7) (2018) 1-8.
[31] A. Profumo, D. Merli, M. Pesavento, Voltammetric determination of inorganic As (III) and total inorganic As in natural waters, Anal. Chim. Acta 539(1-2) (2005) 245-250.
[32] L. Xiao, G.G. Wildgoose, R.G. Compton, Sensitive electrochemical detection of arsenic (III) using gold nanoparticle modified carbon nanotubes via anodic stripping voltammetry, Anal. Chim. Acta 620(1-2) (2008) 44-49.

[33] J.H. Hwang, P. Pathak, X.C. Wang, K.L. Rodriguez, J. Park, H.J. Cho, W.H. Lee, A novel Fe-Chitosan-coated carbon electrode sensor for in situ As(III) detection in mining wastewater and soil leachate, Sens. Actuator B-Chem. 294 (2019) 89-97.
[34] C. Nunez, J.J. Trivino, R. Segura, V. Arancibia, Monographs in Electrochemistry trace levels in urine by differential pulse anodic voltammetry using a simple graphene screen-printed electrode, Microchem. J. 159 (2020) 6.
[35] A. Idris, J. Mafa, N. Mabuba, O. Arotiba, Dealing with interference challenge in the electrochemical detection of As (III)—a complexometric masking approach, Electrochem. Commun. 64 (2016) 18-20.
[36] D.M. Novak, B.E. Conway, Competitive adsorption and state of charge of halide-ions in monolayer oxide film growth-processes at Pt anaodes, J. Chem. Soc. Faraday Trans. 77 (1981) 2341-2359.
[37] M. Yang, P.H. Li, W.H. Xu, Y. Wei, L.N. Li, Y.Y. Huang, Y.F. Sun, X. Chen, J.H. Liu, X.J. Huang, Reliable electrochemical sensing arsenic(III) in nearly groundwater pH based on efficient adsorption and excellent electrocatalytic ability of AuNPs/CeO2-ZrO2 nanocomposite, Sens. Actuator B-Chem. 255 (2018) 226-234.
[38] M. Yang, P.-H. Li, W.-H. Xu, Y. Wei, L.-N. Li, Y.-Y. Huang, Y.-F. Sun, X. Chen, J.-H. Liu, X.-J. Huang, Reliable electrochemical sensing arsenic (III) in nearly groundwater pH based on efficient adsorption and excellent electrocatalytic ability of AuNPs/CeO2-ZrO2 nanocomposite, Sens. Actuators, B 255 (2018) 226-234.
[39] Gold Nanoparticles: Properties and Applications. https://www.sigmaaldrich.com/GB/en/technical-documents/technical-article/materials-science-and-engineering/biosensors-and-imaging/gold-nanoparticles.
[40] J. Wei, S.-S. Li, Z. Guo, X. Chen, J.-H. Liu, X.-J. Huang, Adsorbent assisted in situ electrocatalysis: An ultra-sensitive detection of As (III) in water at Fe3O4 nanosphere densely decorated with Au nanoparticles, Anal. Chem. 88(2) (2016) 1154-1161.
[41] A. Buffa, D. Mandler, Arsenic(III) detection in water by flow-through carbon nanotube membrane decorated by gold nanoparticles, Electrochim. Acta 318 (2019) 496-503.
[42] L. Bu, T. Gu, Y. Ma, C. Chen, Y. Tan, Q. Xie, S. Yao, Enhanced cathodic preconcentration of As (0) at Au and Pt electrodes for anodic stripping voltammetry analysis of As (III) and As (V), J. Phys. Chem. C 119(21) (2015) 11400-11409.
[43] X. Dai, O. Nekrassova, M.E. Hyde, R.G. Compton, Anodic stripping voltammetry of arsenic (III) using gold nanoparticle-modified electrodes, Anal. Chem. 76(19) (2004) 5924-5929.
[44] A. Buffa, D. Mandler, Arsenic (III) detection in water by flow-through carbon nanotube membrane decorated by gold nanoparticles, Electrochim. Acta 318 (2019) 496-503.
[45] D. Wang, Y. Zhao, H. Jin, J. Zhuang, W. Zhang, S. Wang, J. Wang, Synthesis of Au-decorated tripod-shaped Te hybrids for applications in the ultrasensitive detection of arsenic, ACS Appl. Mater. Interfaces 5(12) (2013) 5733-5740.
[46] C.M.A. Brett, A.M.O. Brett, Electroanalysis, Oxford Science Publications1998.
[47] A. Jimana, M.G. Peleyeju, L. Tshwenya, K. Pillay, O.A. Arotiba, Voltammetric Analysis of As(III) at a Cobalt Nanoparticles/Reduced Graphene Oxide Modified Exfoliated Graphite Electrode, Int. J. Electrochem. Sci. 13(11) (2018) 10127-10140.
[48] C. Gao, X.-Y. Yu, S.-Q. Xiong, J.-H. Liu, X.-J. Huang, Electrochemical detection of arsenic (III) completely free from noble metal: Fe3O4 microspheres-room temperature ionic liquid composite showing better performance than gold, Anal. Chem. 85(5) (2013) 2673-2680.
[49] M. Carron, M.E. Mrose, K. Murata, Relation of ionic radius to structures of rare-earth phosphates, arsenates, and vanadates, Mineralogical Society of America, 1958.

Chapter 7. Total As and As(III)/As(V) Measurement via Underpotential Deposition on Gold

We report a sensitive stripping voltammetry method for the detection of total arsenic in aqueous solution using gold macroelectrodes based on the underpotential deposition (UPD) of As ad-atoms. The detection of As(III) or total arsenic can be selectively made by changing deposition potential, with detection of the total As content by deposition at high potential (- 1.3 V) and of As(III) by deposition at lower potential (- 0.9 V). The amount of As(V) can be inferred from the difference of the total As and As(III) values. Linear responses were found for both arsenic species in the range 0.01 μM to 0.1 μM at gold macroelectrodes. In each case analytical useful signals were recorded at concentrations as low as 0.01 μM (0.8 ppb) suggesting that this method can be used to detect total arsenic concentrations in drinking water within the threshold value of the WHO of 0.13 μM (10 ppb).

The work presented in this chapter has been submitted for publication as a first author paper.

7.1. Introduction

Anodic stripping voltammetry (ASV) is a widely employed method in electroanalytical chemistry for quantitative measurements of target species in solution, which involves a pre-concentration and a stripping step [1-3]. The pre-concentration step allows the accumulation by electro-reduction of analytes onto the surface of electrode, whilst the stripping step is conducted by scanning the voltammetry anodically, which produces a stripping peak allowing the characterization and quantification of the target [1-3]. In comparison with other direct forms of voltammetry such as cyclic and linear sweep voltammetry, ASV offers lower limits of

detection (LODs) (10^{-10} – 10^{-11} M) and higher sensitivities (10^{3} A M^{-1}) because the pre-concentration step, which can be applied for as long as is needed, circumvents the limitation imposed by the rate of diffusion of analytes from bulk solution to the surface of electrode [4-6]. The method has been widely used for detection of heavy metal ions in drinking water via the detection of bulk metals for example in respect of arsenic [7-10], copper [11-13], lead [13-15] and mercury [16-18] with low detection limits.

Underpotential deposition (UPD) of a metal onto the surface of electrode in the form of a monolayer or a sub-monolayer takes place at potentials lower than those required for the deposition of the bulk metal [10, 19-21]. The proof of concept studies reported in chapters 5 and 6 established the merits of using UPD rather than bulk metal deposition in ASV for As(III) detection, including overcoming the limitations of Cu(II) interference on both platinum and gold surfaces [7, 10], where in particular pre-concentration using UPD prevents a co-deposition of Cu and arsenic and hence interference with the analysis from the widely occurring Cu(II). In the case of Au electrodes it was further shown that chloride ions do not interfere. ASV with UPD was seen to have good sensitivity and, most importantly for application in drinking water, LODs with clear and visually distinct signals within WHO limits [7, 10].

Arsenic appears in groundwater from both natural sources such as volcanic activity and from human activities including mining industries [22-24]. There are four recognised oxidation states of arsenic: As(-III), As(0), As(+III) and As(+V). Although many forms of arsenic species have been detected in water samples, the dominant forms of arsenic are arsenite, As(III), and arsenate, As(V) [22, 25, 26]. The arsenic species are highly toxic and exposure to arsenic can cause severe health problems including cardiovascular disease and cancer [27-29] and whilst As(III) is thought to be more toxic than As(V) [30], the guidelines for water safety [31] are written in terms of the *total* arsenic content. However most analytical methods for As have

focussed on As(III) detection. Rather less attention has been given to As(V) or total arsenic detection [32, 33]. In this chapter we develop the UPD ASV approach to allow analysis of As(V) and total As in addition to As(III).

Instrumental laboratory based methods have been used for measuring total As including atomic absorption spectrometry (AAS) [34] and inductively coupled plasma mass spectrometry (ICPMS) [35, 36], which provide low detection limits and high sensitivities but require strict sample preparation conditions and special laboratory conditions. Accordingly, we see clear benefits for an electrochemical approach but note that previous electrochemical methods for As(V) show rather high LODs as benchmarked against the WHO safety thresholds. As(V) is typically quantified either by indirectly measuring As(III) formed by chemical reduction of As(V), or directly measured using selective deposition. Svancara *et al* detected concentrations of As(III) and As(V) using ASV with bulk deposition coupled with homogeneous chemical reduction of the As(V) [37]. The direct electrochemical measurement of As(V) was realised by Postek who used adsorptive stripping voltammetry but could only realise a LOD of 350 ppb [38] which is greatly in excess of the WHO threshold of 10 ppb. Lower LODs were achieved by electrode modification primarily to enhance the active interfacial areas. Thus Zakharova *et al* [39] used ASV with bulk deposition to detect As(V) at an Au microwire electrode modified with Mn particles in aqueous 0.1 M Na_2SO_3 with a theoretical LOD of 0.35 ppb estimated using the 3σ method [39, 40]; Huang *et al* modified a Pt wire electrode with a Au film and reported a LOD of 0.5 ppb for As(V) using ASV with bulk deposition with the LOD again calculated with the 3σ method [40, 41]; Yamada *et al* utilised Au nanoparticles deposited onto boron doped diamond electrode (BDDE) giving a LOD of 100 ppb for As(V) [42] based on a visually discernible signal. In these methods the use of bulk As deposition in the pre-concentration step makes them inevitably susceptible to interference from Cu [39, 41].

In this chapter we suggest that the combination of UPD and ASV can solve the problems both of attaining low LODs whilst avoiding the interference from Cu seen when bulk deposition is used. In particular the use of highly negative deposition potentials with longer deposition time for bulk deposition may enhance the sensitivity of the detection method [43] but not the selectivity. UPD, on the other hand, can avoid the formation of alloy or/and the intermetallic species of Cu and As in the pre-concentration step [7, 10] since typically sub-monolayer layers are deposited in the preconcentration step. In the following we apply UPD-ASV with deposition on a gold electrode at a potential where both As(V) and As(III) are deposited in sub monolayer amounts to give the total arsenic concentrations in water. This is then followed by measurements of UPD-ASV at a potential where As(III) is selectively deposited, but not A(V) [10]. The concentrations of As(V) then can be determined by subtraction from the total arsenic concentration of the As(III) concentration. The LOD is determined from analytically useful signals in the sub 10 ppb range at Au macroelectrodes. In this way the As(III), As(V) and total As content of aqueous solutions are found for levels of As at and below the WHO recommended level of 10 ppb for drinking water.

7.2. Experimental

7.2.1. Chemical reagents

Commercially available sodium hydrogen arsenate heptahydrate (Na_2HAsO_4, 98%, Alfa Aesar, UK), sodium (meta) arsenite ($NaAsO_2$, 99%, Fluka, Switzerland), and sulphuric acid (H_2SO_4, 98%, Fisher Scientific, UK) were purchased and used without any further purification. All aqueous solutions were prepared using deionized water (Milipore, UK) with a resistivity of 18.2 MΩ cm at 298 K.

7.2.2. Instrumentation

All electrochemical measurements were conducted with a standard three-electrode system in a Faraday cage and were thermostatted at 298 (± 0.1) K. A carbon rod served as a counter electrode and a mercury-mercurous sulfate electrode (MSE, BASi, USA) served as the reference electrode with a potential of +0.65 V vs. standard hydrogen electrode (SHE) [44], and the solution used in the reference electrode was aqueous saturated K_2SO_4 (1.45 M). A gold macroelectrode (diameter of 1.60 ± 0.01 mm, geometric area of 0.02 cm^2, BASi, USA) or a gold screen printed electrode (Au SPE) operated as a working electrode. The Au SPEs were purchased from Drop Sens (DS, geometric are of 0.13 cm^2, Spain), Zensor (Zen, geometric area of 0.2 cm^2, TW) and Zimmer & Peacock (ZP, geometric area of 0.04 cm^2, Norway). All Au SPEs were used without further modifications. The surfaces of Au SPEs from ZP were cleaned with 10 mM HCl before electrochemical measurements based on a method recommended by the supplier (Zimmer & Peacock) [45]. The Au SPEs from the other two companies were used without pre-cleaning. The Au macroelectrode was polished with alumina before each measurement. All electrochemical measurements were performed in 0.1 M H_2SO_4 with various concentrations of arsenic, and were recorded with a μAutolab type III potentiostat (EcoChemie, NL) after degassing with nitrogen.

7.3. Results and Discussion

In this section, first, the electrochemical behaviour of As(V) is studied in 500 μM Na_2HAsO_4 in 0.1 M H_2SO_4 with the latter present to control the pH and act as supporting electrolyte. Cyclic voltammetry (CV) and anodic stripping voltammetry (ASV) are the electrochemical techniques used. The peaks in the CVs are assigned, and the presence of a UPD peak is noted in the ASV. Then the method of anodic stripping voltammetry with

underpotential deposition (UPD) previously reported in Chapter 6 for As(III) is then extended and, for the first time, applied to the measurement of As(V) and total As concentrations realising a low detection limit, as assessed on the basis of visually clear signals, for As(V) of 0.8 ppb well within the WHO limit of 10 ppb for safe drinking water. Finally, the determination of the total arsenic concentration and of the individual concentrations of As(III) and As(V) in mixtures of As(III) and As(V) is established using the UPD-ASV method.

7.3.1. Electrochemical response of As(V) on Au electrodes

Cyclic voltammetry of As(V)

To facilitate electrochemical analysis of As(V), cyclic voltammetry and anodic stripping voltammetry were first conducted at a gold macroelectrode. Figure 7.1 illustrates the CV response of 500 μM Na_2HAsO_4 in 0.1 M H_2SO_4 with a potential window from – 1.4 V to + 1.3 V (vs. MSE) at a gold macroelectrode. The voltammograms shown are the first scans made after polishing the electrode with alumina. The CV was started at + 0.5 V and first scanned cathodically to – 1.4 V, then scanned anodically to + 1.3 V at a scan rate of 0.1 V s^{-1}. Two features are observed on the forward. Peak 1 observed at ca + 0.37 V is assigned to the reduction of Au oxide to Au [46, 47]. Solvent decomposition onsets at potentials around - 1.3 V and comprises a mixture of the hydrogen evolution reaction (HER) [46] and the reduction of As(V) to bulk As(0) [41]. On the reverse anodic scan, four peaks were observed, denoted as peaks 2, 3, 4 and 5. Peak 2 with the potential of ca – 0.3 V represents the oxidation of bulk As(0) to As(III) [10, 47]. The peak 3 observed at ca + 0.4 V corresponds to the oxidation of As(III) to As(V) [10, 39]. Peak 4 at ca + 0.8 V was ascribed to the oxidation of Au to Au oxide [46], and peak 5 at ca + 1.3 V was considered to be the start of oxygen evolution reaction (OER) [47]. Comparing with the voltammogram that obtained in blank solution (0.1 M H_2SO_4, black

dashed line in Figure 7.1), two peaks were absent in blank solution (peaks 2 and 3) which all relate to arsenic, whilst peaks 1, 4 and 5 were ascribed to the reduction of Au oxide, oxidation of Au and OER, respectively [47].

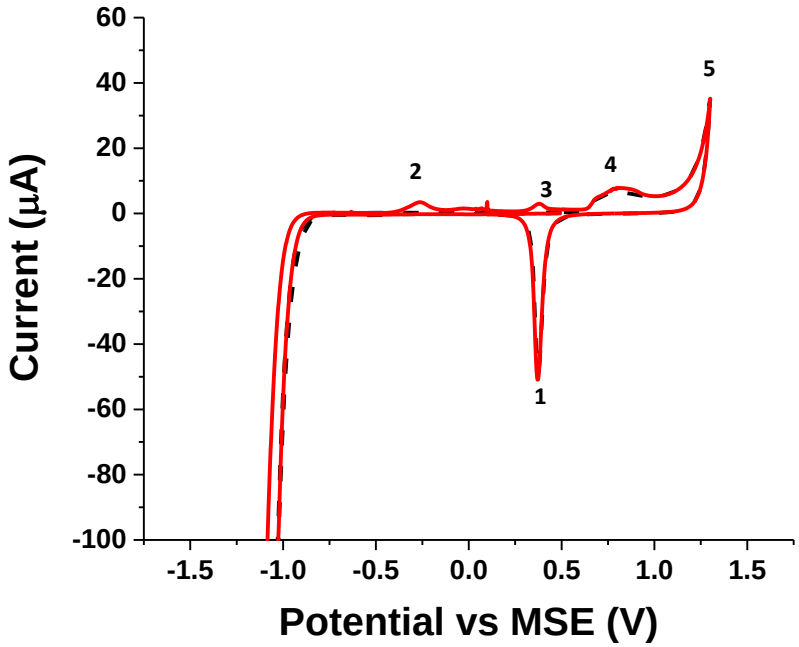

Figure 7.1 CV of 500 µM As(V) in 0.1 M H_2SO_4 (red) and blank solution (black dashed line) at Au macroelectrodes. The voltammograms were conducted from + 0.5 V vs MSE and first scanned cathodically to - 1.4 V at a scan rate of 0.1 V s^{-1} followed by an anodic scan to + 1.3 V.

Deposition and stripping of As

To further understand the electrochemistry of As(V) on the surface of gold electrodes, a 10 µM solution of Na_2HAsO_4 in 0.1 M H_2SO_4 was examined via ASV (Figure 7.2a). Pre-concentration was conducted at – 1.3 V for a period of 300 s to electro-reduce the As(V) to deposit As in the form of both bulk As and UPD As after which the potential was swept from – 1.3 V to + 0.6 V at a scan rate of 0.1 V s^{-1}. In Figure 7.2a, four peaks were observed labelled as 2, 2', 3 and 6. Peaks 2 and 3 represent the same chemistry shown above. Peak 6 observed at ca – 0.15 V is related to the deposition of H atoms and the deposition potential [8, 46]. The

peak 2' at ca + 0.04 V was assigned as the stripping peak associated with the oxidation of As(0) ad-atoms to As(III) [10, 48, 49].

To understand the relationship between the bulk As (peak 2) and UPD As (peak 2'), As(V) with much lower concentrations were next studied. A 0.1 μM solution of Na_2HAsO_4 in 0.1 M H_2SO_4 was examined via ASV (Figures 7.2b, c and d). Pre-concentration was conducted at various potentials in the range from – 1.6 V to – 1.3 V for 300 s to reduce the As(V) to deposit As(0) either in the form of bulk As or UPD As after which the potential was swept from the deposition potential to + 0.6 V at a scan rate of 0.1 V s^{-1}. Figure 7.2b illustrates as measured voltammetry of a blank solution (0.1 M H_2SO_4, black dashed line), and 0.1 μM As(V) in 0.1 M H_2SO_4 with the deposition potentials of either – 1.6 V (red) or – 1.3 V (blue). The huge reductive currents with the sweep of the potential from – 1.6 V to ca – 1.0 V is due to the large negative potential leading to the formation of hydrogen during the pre-concentration step. At less negative potentials some of the formed hydrogen is re-oxidised resulting in a peak (labelled peak 7) as seen in Figure 7.2c with a peak potential of – 0.6 V (Hydrogen oxidation reaction, HOR) [46]. The part of the voltammogram showing positive currents was magnified (framed area of Figure 7.2b) and is shown in Figure 7.2c. Peaks 2, 2' and 6 represent the chemistry discussed above. To further discuss the peaks of bulk As, peak 2 and UPD As, peak 2', the framed area of the voltammogram is further magnified and is shown in Figure 7.2d.

Figure 7.2d illustrates the ASV response of 0.1 μM Na_2HAsO_4 in 0.1 M H_2SO_4 with deposition at – 1.6 V for a period of 300 s (red) and that with deposition at – 1.3 V for 300 s (blue). Three peaks can be observed, labelled as 2, 2' and 6, where they all represent the chemistry inferred above. It is apparent that bulk As is deposited at potentials more negative than – 1.4 V, whereas UPD As is essentially exclusively deposited at the less negative potential of – 1.4 V at the concentration of As(V) and the deposition times studied (red line in Figure

2d). Deposition at more negative potentials than – 1.3 V likely causes increased evolution of H_2 gas, which may affect the reproducibility of the stripping analysis [42, 46] in addition to the formation of bulk As(0). The potential of - 1.3 V was selected as enabling the formation of As ad atoms whilst minimising the possible formation of hydrogen bubbles and avoiding the deposition of bulk As (blue line in Figure 7.2d).

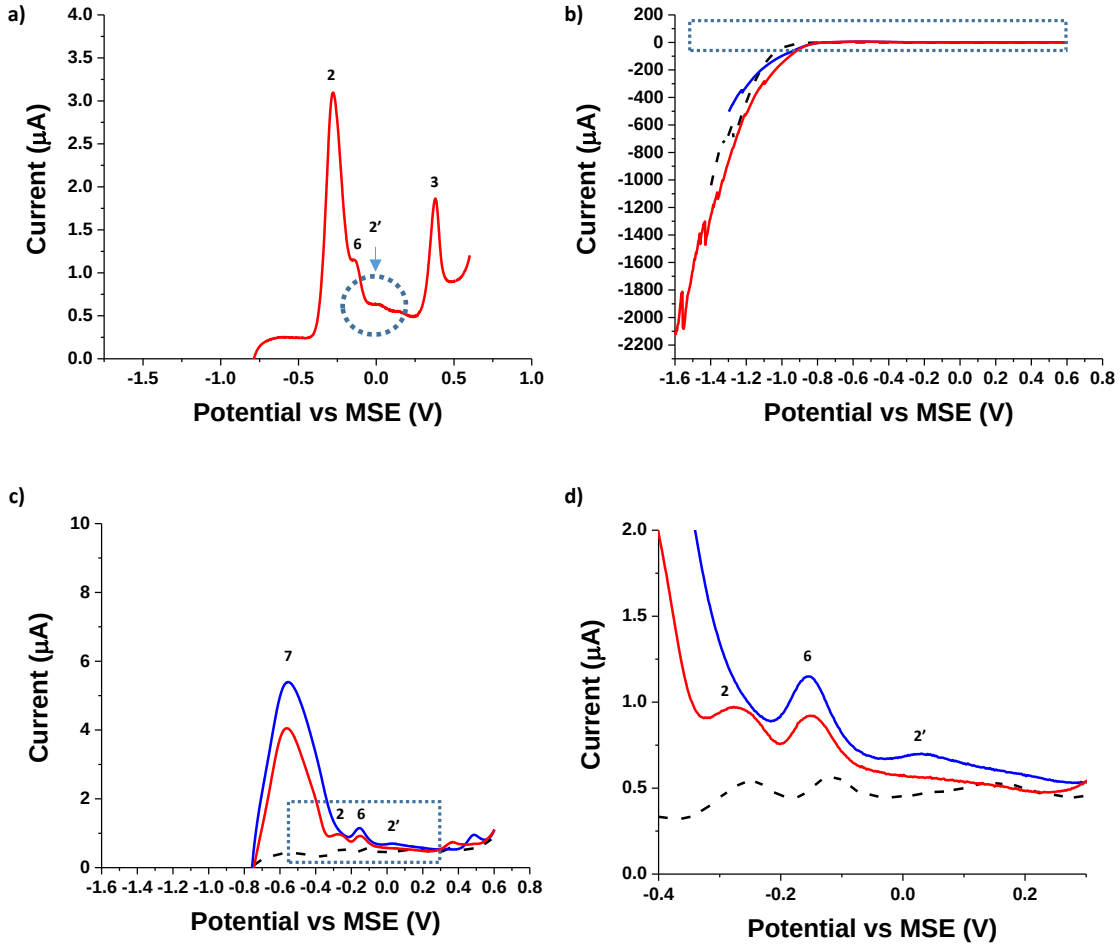

Figure 7.2 a) Anodic stripping voltammograms of 10 µM As(V) in 0.1 M H_2SO_4 at a gold macroelectrode with a pre-concentration at – 1.3 V for 300s. b) Anodic stripping voltammograms of 0.1 M H_2SO_4 (black dashed line), 0.1 µM As(V) in 0.1 M H_2SO_4 with deposition at – 1.6 V for 300 s (red) and – 1.3 V for 300 s (blue). c) is the magnification of framed part in b). d) is the magnification of framed part in c). In b), c) and d), the lines represent the voltammograms of 0.1 M H_2SO_4 (black dashed line), 0.1 µM As(V) in 0.1 M H_2SO_4 with deposition at – 1.6 V for 300 s (red) and – 1.3 V for 300 s (blue) at a scan rate of 0.1 V s^{-1}.

7.3.2. The analytical use of As UPD signals

The UPD-ASV method for the detection of low concentrations of As(III) on gold was introduced in the previous two chapters to eliminate the problems of interferences when bulk solids are deposited as the pre-concentration for ASV [10]. In this chapter, UPD-ASV is first applied for the detection of the total As content (As(V) + As(III)), then selectively detect the concentration of As(III) in mixtures with As(V) in water using gold macroelectrodes. Subtraction of the two results then allows estimates of the As(V) content. For As(V) detection in solutions containing only As(V) or for the measurement of the total As concentrations in mixtures of As(III) and As(V), the pre-concentration of As(0) was first carried out at – 1.3 V for a period of 300 s, which results in As ad-atoms being deposited at the surface of gold [39, 41, 42]. Note that at high concentrations of As(V) or for more prolonged deposition, as reported and quantified below, bulk As is deposited likely physically on the top of the layer of ad-atoms so the procedure is specific for the measurement of As at low concentrations appropriate for the detection of As in drinking water, the usual reason for detecting As. Following pre-concentration a linear sweep scan was applied from – 1.3 V to + 0.6 V at a scan rate of 0.1 V s^{-1} to strip the As ad-atoms. The charge of the stripping peak was used as the signal to quantify the concentration of As(V) in solutions of only As(V) or the total concentration for As in dilute mixtures. Figure 7.3 shows the magnified ASV of 0.1 μM As(V) with 0.05 μM As(III) in 0.1 M H_2SO_4. Two peaks can be observed, peaks 2’ and 6, which were ascribed to the chemistry discussed above. The peak of bulk As, peak at ca – 0.3 V cannot be observed, which means there is no bulk As deposited for As(III) at this concentration of mixture of arsenic. Note that in the blank solution (black dashed line in Figure 7.3), two small peaks can be observed, peaks 6 and 8, where peak 6 reflects chemistry shown above and peak 8 at ca + 0.15 V represents an oxidation of gold at the surface of electrode [48].

For As(III) detection, both in solutions containing only As(III) and in mixtures with As(V). the pre-concentration was carried out at – 0.9 V for 300 s then followed with a linear sweep voltammetry (LSV) from – 0.9 V to + 0.6 V at a scan rate of 0.1 V s^{-1}, and the charge of the stripping peak was used for the quantification of As(III). Baseline correction was applied to the voltammograms (see Appendix Section 1 for procedure), then the charge of the stripping peak was calculated from the peak area of baseline corrected voltammogram (shown in Appendix Section 2).

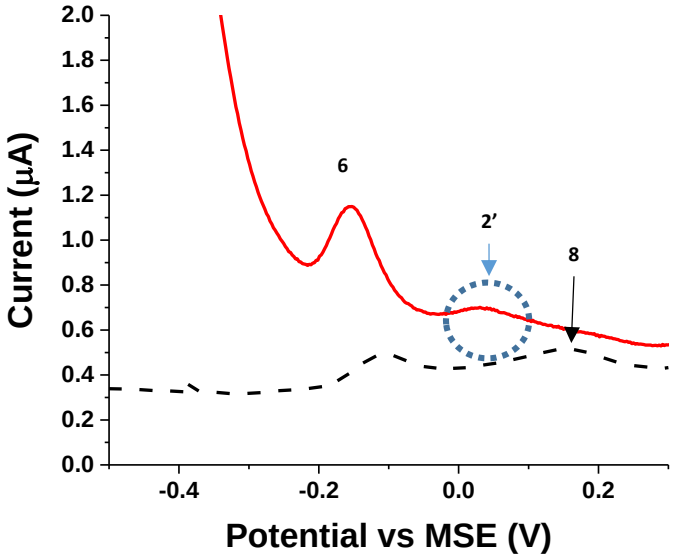

Figure 7.3 Magnified anodic stripping voltammograms of 0.1 M H_2SO_4 (black dashed line) and 0.1 µM As(V) with 0.05 µM As(III) in 0.1 M H_2SO_4 (red) at a gold macroelectrode with a pre-concentration at – 1.3 V for 300s. ASV parameters: deposition at – 1.3 V for 300 s, potential scan rate 0.1 V s^{-1}.

Observations of As(V) and As(III) UPD stripping signals

To examine the capability of the IPD-ASV method for arsenic detection in water, experiments were first conducted in various concentrations of As(V) in 0.1 M H_2SO_4 using Au macroelectrodes. The pre-concentration of As(0) was first carried out at – 1.3 V for 300 s in various concentrations of As(V) then followed with a linear potential sweep from – 1.3 V to + 0.6 V at a scan rate of 0.1 V s^{-1}. Figure 7.4a illustrates the baseline corrected linear sweep

voltammetric responses of peak 2' at gold macroelectrodes measured in As(V) solutions of concentration ranging from 0.01 μM to 1 μM in 0.1 M H_2SO_4. The stripping peak was observed at ca + 0.04 V and the charge of the peak increased with the concentration of As(V). Figure 7.4c shows the plot of charges of peak 2' against concentrations of As(V) (red). The charges first increased linearly and rapidly but then increasingly slowly until a plateau was attained at ca 1 μM consistent with the formation of 0.007 layers of As ad-atoms (See Appendix Section 3 for calculations). This is as expected for the formation of a UPD layer. The 1 μM As(V) corresponds to a surface coverage of ca (5 ± 0.2) × 10^{12} molecules cm^{-2} and ca 0.007 monolayers. It sets an upper limit (ca 1 μM, 75 ppb) for detection of As(V) via UPD-ASV method using the charge of stripping peak at Au macroelectrodes and provide a visually clear signal for concentrations as low as 0.01 μM (0.8 ppb, See Appendix Section 1 for baseline correction method). The range thus spans that likely to be encountered in drinking water with a limit of 10 ppb [31].

Analogous experiments were also made for As(III) detection as follows; the pre-concentration of As ad-atoms was carried out at – 0.9 V for 300 s in various concentrations of As(III) solution then a linear potential scan was made at a scan rate of 0.1 V s^{-1}. The baseline corrected LSVs are shown in Figure 7.4b, in which can be seen that the charge of the peak increased with the concentrations of As(III). The charges of stripping peaks plotted against the concentration of As(III) are shown in Figure 7.4c (black). A similar phenomenon can be seen as observed for As(V) with similar limiting coverages (ca 0.007 ML) in the range 0 – 1 μM (See Appendix Section 3 for calculation). In the case of concentrations above 1 μM As(III) shows slightly higher coverages than seen for As(V) which may reflect the onset of for further UPD deposition on different sites to those occupied at lower coverages. However the bespoke analytical procedure is designed for low concentrations well below 1 μM.

The analytical measurements in this study were then based on the sub-monolayer of deposited As(0) ad-atoms from As(III), As(V) or both arsenic species. Although the charge of stripping peak increased with the concentrations of arsenic in the range from 0.01 μM to 1 μM with similar sensitivities for As(III) and As(V), it is preferable to find a linear relationship so that the sensitivity can be calculated. Further attention was thus focused on the use of UPD-ASV at lower concentrations of arsenic species.

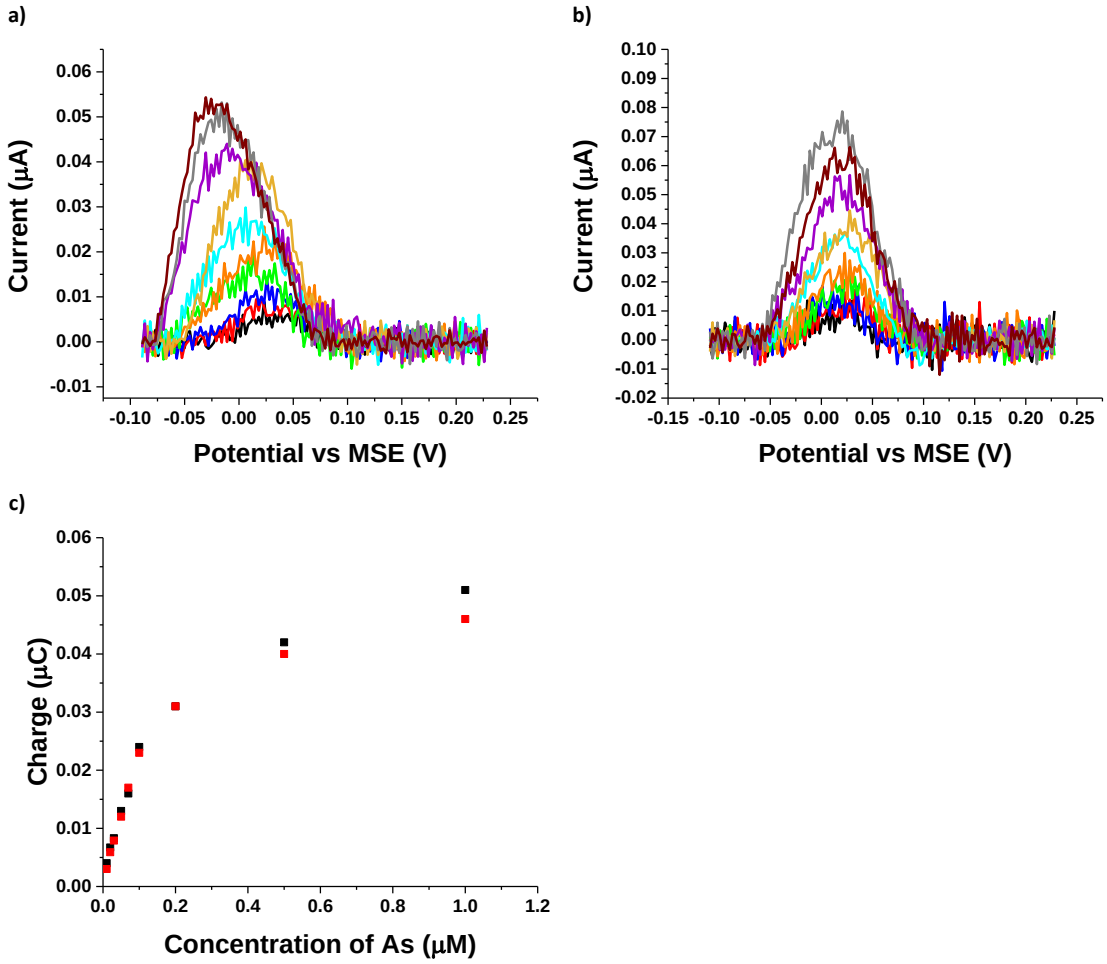

Figure 7.4 Baseline corrected stripping voltammograms of various concentrations of a) As(V) or b) As(III) in 0.1 M H_2SO_4 at Au macroelectrodes. c) Also shown are plots of the charge of peak 2' vs concentrations of As(V) (red) or As(III) (black), in 0.1 M H_2SO_4 at Au macroelectrodes. The concentrations of As(V) were 0.01 μM (black), 0.02 μM (red), 0.03 μM (blue), 0.05 μM (green), 0.07 μM (orange), 0.1 μM (cyan), 0.15 μM (yellow), 0.2 μM (purple), 0.5 μM (grey), and 1 μM (brown). ASV parameters: deposition at – 1.3 V vs. MSE for 300 s, potential scan rate 0.1 V s^{-1}, and baseline was modelled via polynomial method from - 0.1 V to + 0.22 V for peak 2'.

Calibration curves, sensitivities and limits of detection

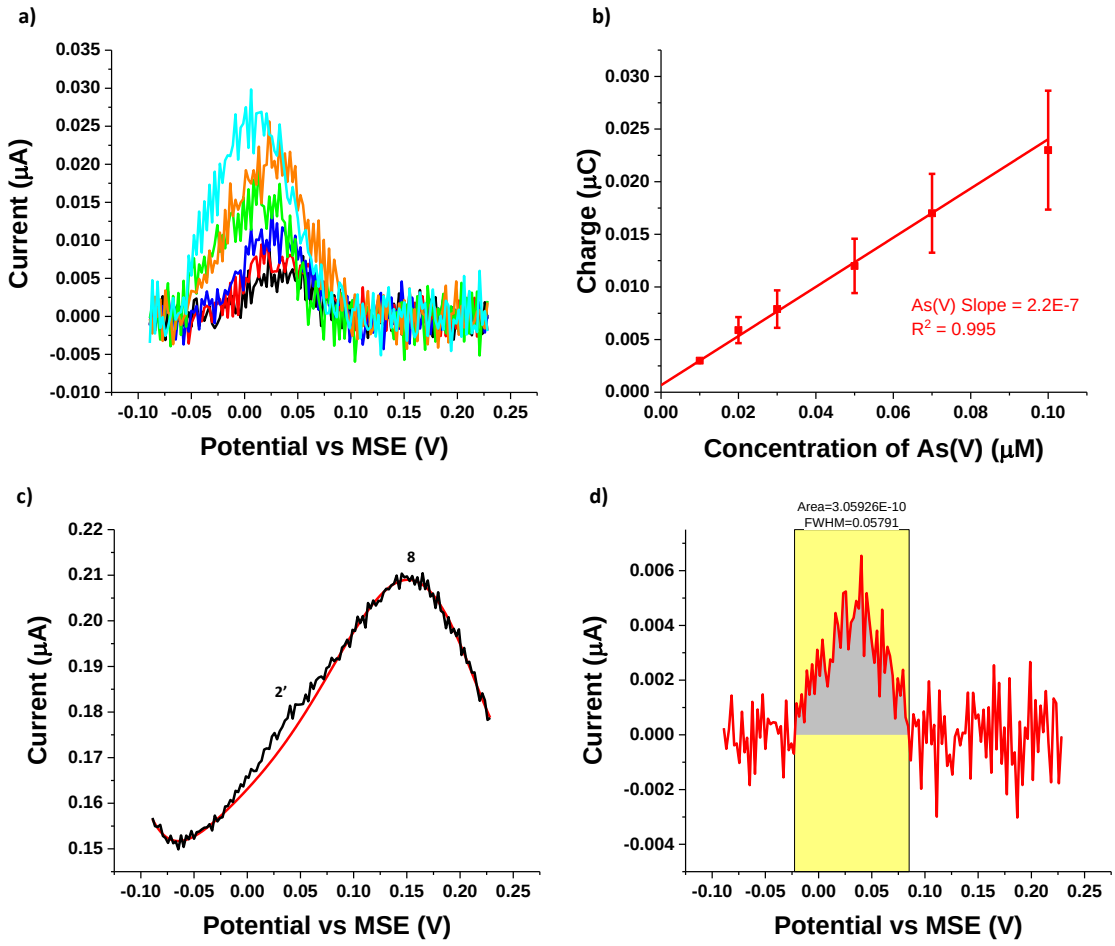

Figure 7.5 a) Baseline corrected stripping voltammograms of various concentrations of As(V) in 0.1 M H_2SO_4 at Au macroelectrodes. Also shown are plots of the charge of peak 2' vs concentrations of b) As(V) in 0.1 M H_2SO_4 at Au macroelectrodes. The concentrations of As(V) were 0.01 µM (black), 0.02 µM (red), 0.03 µM (blue), 0.05 µM (green), 0.07 µM (orange), and 0.1 µM (cyan). The charge was calculated from baseline corrected LSVs and the error bars shown are standard deviations calculated from at least three sets of data. c) The unmodified LSV curve from -0.10 V to +0.22 V (black line) and simulated baseline (red line). d) The baseline corrected LSV curve from -0.10 V to +0.22 V (red line) and the peak area (grey area). ASV parameters: deposition at – 1.3 V vs. MSE for 300 s, potential scan rate 0.1 V s^{-1}, and baseline was modelled via the polynomial method from - 0.1 V to + 0.22 V for peak 2'.

To determine the sensitivities of As(III) and As(V) under analysis via UPD-ASV, and to identify linear ranges and detection limits, concentrations of As(III) and As(V) below 0.1 µM were studied on gold macroelectrodes. The upper limit was defined by the WHO drinking water limits [31]. The linear range and sensitivity was investigated for As(V) first. To measure the concentrations of As(V) in 0.1 M H_2SO_4, pre-concentration was carried out at – 1.3 V for 300 s then followed up with a linear potential sweep from – 1.3 V to + 0.6 V at a scan rate of 0.1 V s^{-1}. Baseline corrections were applied as above. Figure 7.5a illustrates the baseline

corrected stripping voltammograms of peak 2' for analyte concentrations in the range of 0.01 μM to 0.1 μM As(V) at Au macroelectrodes. The peak 2' was observed at ca + 0.04 V and the charge of the stripping peak increased with the concentrations. To obtain the relationship between the charge of peak 2' and the concentration of As(III) at Au macroelectrodes, the charges of stripping peak were plotted against the concentrations in Figure 7.5b. A linear relationship, $Charge = 2.2 \times 10^{-7} C\ \mu M^{-1} \times [As(V)] + 7 \times 10^{-10}\ C$, was inferred over the range of concentrations studied. The error bars shown are standard deviations calculated from at least three sets of data. Rather than calculating the LOD using the 3σ method [40], which may not give a realistically low detection limit since σ can be small and result in an extremely low and artificial LOD [40], we used the 'practical detection limits' based on the concentration giving visually clear signals [7, 10], and identified the LOD to be 0.01 μM (0.8 ppb) with the sensitivity of 2.2×10^{-7} C μM^{-1} for As(V) at the Au macroelectrodes.

Figure 7.5c illustrates the raw voltammogram (black line in Figure 7.5c) in the potential range of – 0.1 V to + 0.22 V. The peak 2' at ca + 0.04 V was a shoulder of the bigger peak (peak 8) that reflects the oxidation of gold on the surface electrode as above [48] when the concentration of As(V) was as low as 0.01 μM. The peak current of peak 2' increased with the concentrations of arsenic and reached a similar height as peak 8 when the concentration was 0.1 μM. When the concentration of arsenic was higher than 0.1 μM, the peak current of peak 2' became higher than that of peak 8. Thus a baseline correction was required to eliminate the influence from the background signal. A baseline (red line in Figure 7.5c) was simulated via the polynomial method in Origin 2017 with an order of 7 from – 0.08 V to – 0.05 V and + 0.095 V to + 0.22 V. Thus, the simulated background line in the Figure 7.5c was in the range from – 0.05 V to + 0.095 V. To calculate the charge of the stripping peak of UPD As, a subtraction between the unmodified voltammogram and the simulated baseline was applied, and the baseline corrected voltammogram is shown in Figure 7.5d. The area of peak 2' (grey

area in Figure 7.5d) can be calculated via 'integrate' in Origin and the charge of the peak then can be determined (See details in Appendix Section 2). These parameters were used for the whole project for baseline corrections of peak 2'. To further explore the practical use of this method on arsenic species detection, analogous experiments were made for As(III) at Au macroelectrodes for comparison with that for As(V).

As discussed above the tiny imperfections in baseline fitting may lead to small errors in the measured signals. The LOD obtained from this method is 10 times lower than WHO limit of 10 ppb for safe drinking water. Although some careful analysis is required, it is still worthy to have it for on-site detection. If a more accurate and precise result is required, the samples could be taken to the lab for further electroanalytical quantitation.

Pre-concentration of As(0) from As(III) was carried out at – 0.9 V for 300 s in various concentrations of As(III) solution then a linear potential sweep was made from – 0.9 V to + 0.6 V at a scan rate of 0.1 V s^{-1} at Au macroelectrodes. Baseline correction followed the procedure above. Figure 7.6a presents the baseline corrected voltammograms of As(III) at Au macroelectrodes that were measured for concentrations in the range from 0.01 μM to 0.1 μM. The peak 2' was observed at ca + 0.04 V and the charge increased with the concentrations of As(III). Then the charge of peak 2' was plotted against the concentrations of As(III) in Figure 7.6b. The linear relationship, $Charge = 2.1 \times 10^{-7} C\ \mu M^{-1} \times [As(III)] + 2 \times 10^{-9}\ C$, was obtained in the range of 0.01 μM to 0.1 μM, and the error bars were again calculated from at least three sets of data. The LOD was inferred from analytical useful signals rather than the 3σ method, and was determined to be 0.01 μM (0.8 ppb), and the sensitivity was 2.1×10^{-7} C μM^{-1} for As(III). In comparison with the results of As(V), both arsenic species had the same LOD, 0.8 ppb, and a similar sensitivity, 2.1×10^{-7} C μM^{-1}. The detection limit, 0.8 ppb obtained using analytically clear signals meets, by a considerable margin the WHO guidelines for arsenic in

drinking water (10 ppb) [31]. The similar sensitivity, 2.1×10^{-7} C μM^{-1} proves that the signal of UPD As increased in a comparable manner with concentration for both As(III) and As(V). This observation allows us to use deposition at - 1.3 V to deposit As ad-atoms simultaneously from solution of As(III) or As(V) at the same rate for each species. Accordingly, we were able to apply the method to mixtures of the two species so as to permit the detection of total As concentrations. In the following section these measurements are explored and then combined with deposition at - 0.9 V to give the As(III) content, hence allowing by difference the measurement of the As(V) content.

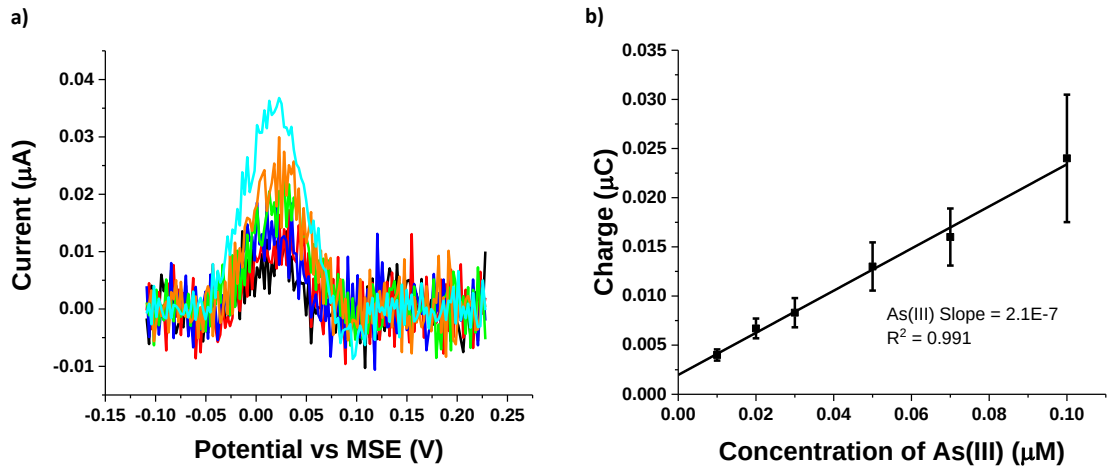

Figure 7.6 a) Baseline corrected stripping voltammograms of various concentrations of As(III) in 0.1 M H_2SO_4 at Au macroelectrodes. Also shown are plots of the charge of peak 2' vs concentrations of b) As(III) in 0.1 M H_2SO_4 at Au macroelectrodes. The concentrations of As(III) were 0.01 μM (black), 0.02 μM (red), 0.03 μM (blue), 0.05 μM (green), 0.07 μM (orange), and 0.1 μM (cyan). The charge was calculated from baseline corrected LSVs and the error bars shown are standard deviations calculated from at least three sets of data. ASV parameters: deposition at – 0.9 V vs. MSE for 300 s, potential scan rate 0.1 V s^{-1}, and baseline was modelled via the polynomial method from - 0.1 V to + 0.22 V for peak 2'.

7.3.3. Detection of the total As concentration and the As(V)/As(III) speciation

Having tested the capability of the UPD As peak for the detection of As(III) and As(V) separately at gold macroelectrodes, further experiments were conducted to explore if this method can detect both the total amount of arsenic species as well as As(III) and As(V)

individually with obvious benefits for application in the real world. Thus, in this section, first various concentrations of As(III) in the presence of different levels of As(V) were analysed for the determination of As(III) using a deposition potential of – 0.9 V. Then a range of concentrations of As(V) in the presence of different amounts of As(III) were analysed for the total concentrations of arsenic using a deposition potential of – 1.3 V. The As(V) concentrations were obtained by subtraction of the As(III) concentration from the total arsenic concentration.

Detection of As(III) in the presence of As(V) in solution

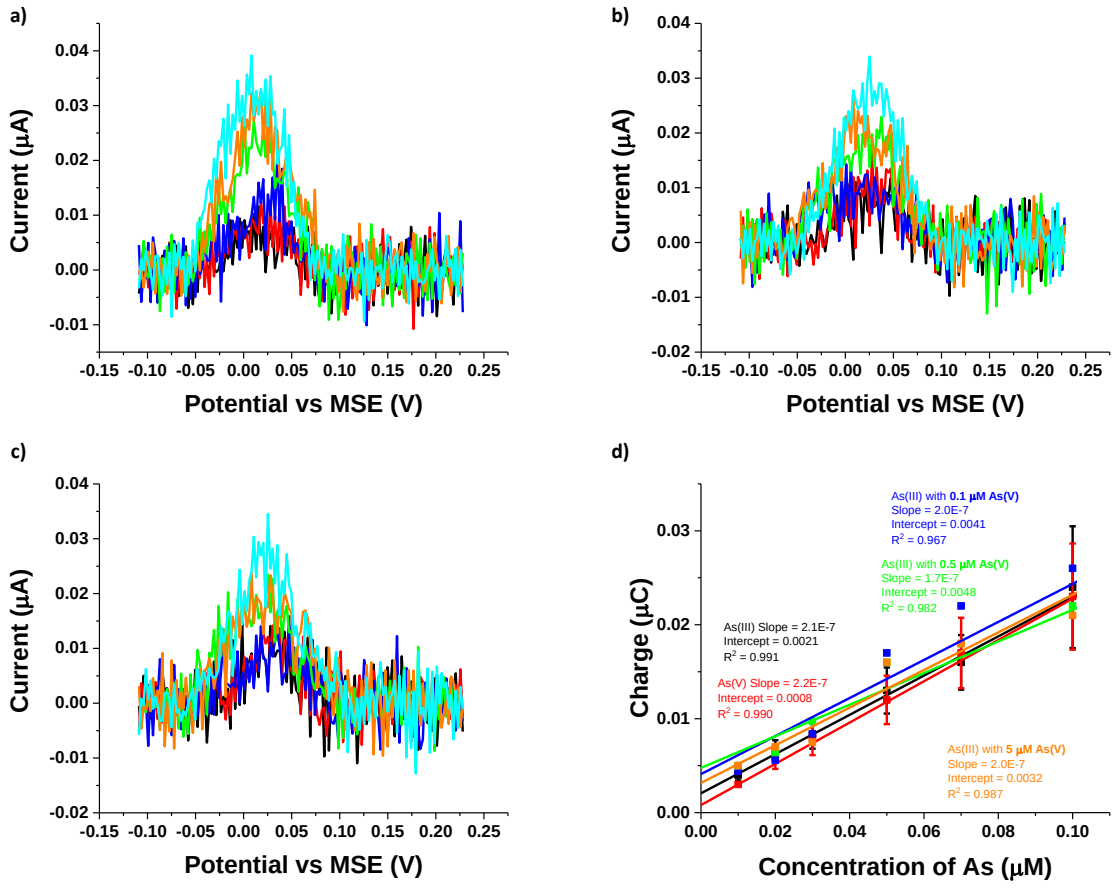

Figure 7.7 Baseline corrected stripping voltammograms of various concentrations of As(III) in 0.1 M H_2SO_4 with the presence of a) 0.1 µM, b) 0.5 µM, and c) 5 µM As(V) in solution. d) Also shown are plots of the charge of peak 2' vs concentrations of As(III) in the absence and the presence of As(V) in 0.1 M H_2SO_4 at Au macroelectrodes. The concentrations of As(III) in voltammograms were 0.01 µM (black), 0.02 µM (red), 0.03 µM (blue), 0.05 µM (green), 0.07 µM (orange), and 0.1 µM (cyan). The charge was calculated from baseline corrected LSVs and the error bars shown are standard deviations calculated from at least three sets of data. The plots of charge vs concentrations of arsenic were As(III) (black), As(V) (red), As(III) in the presence of 0.1 µM As(V) (blue), As(III) in the presence of 0.5 µM As(V) (green), and As(III) in the presence of 5 µM As(V) (orange). ASV parameters: deposition at – 0.9 V

(for As(III)) or – 1.3 V (for As(V)) vs. MSE for 300 s, potential scan rate 0.1 V s^{-1}, and baseline was modelled via the polynomial method from - 0.1 V to + 0.22 V for peak 2'.

Concentrations of As(III) in the presence of As(V) in 0.1 M H_2SO_4 were measured first, in which a pre-concentration was conducted at – 0.9 V for 300 s then followed with a linear potential sweep from – 0.9 V to + 0.6 V at a scan rate of 0.1 V s^{-1}. Figures 7.7a, b and c show the baseline corrected voltammograms of As(III) in the presence of 0.1 μM As(V), 0.5 μM As(V) and 5 μM As(V), respectively. From all these three voltammograms, the peak charges of peak 2' increased with the concentrations of As(III) and the charges were similar no matter the concentrations of As(V) were present in the solution. To further understand whether or not the As(V) interfere with the signal of As(III), the peak charges of peak 2' were plotted against the concentrations of arsenic in Figure 7.7d. It is clear to see that the sensitivities were similar. The sensitivity of As(III) in the absence of As(V) was $(2.1 \pm 0.2) \times 10^{-7}$ C μM^{-1} whilst the sensitivities in the presence of As(V) were ca $(2.0 \pm 0.3) \times 10^{-7}$ C μM^{-1}, which is similar. The presence of As(V) did not interfere with the signals of As(III). In addition, the method of using UPD As can be used for the selective detection of As(III) in the presence of As(V) using deposition at – 0.9 V. To further test the capability of detecting total arsenic concentrations by tuning deposition potentials, analogous experiments were made in various concentrations of As(V) in the presence of As(III) with a deposition potential of – 1.3 V.

Detection of As(V) in the presence of As(III) in aqueous solution and the measurement of total arsenic concentrations

Total arsenic concentrations were then measured in mixtures of As(III) and As(V) over a total As concentration range of 0.11 μM (8.25 ppb) to 0.35 μM (26.25 ppb). Pre-concentration was conducted at – 1.3 V for 300 s then a linear potential scan was made from – 1.3 V to + 0.6 V at a scan rate of 0.1 V s^{-1}. Table 7.1 (Columns 1 and 4) shows the concentrations of As(III) and As(V) in the mixture, and the concentrations determined using UPD-ASV. The latter were

based on the charges that obtained from the peak 2' (See calculations in Appendix Section4). The measured total arsenic concentrations were within the range of ca 10% of the known total arsenic concentrations, signalling that the UPD-ASV method can be used for the detection of total arsenic concentrations in drinking water using a deposition potential of – 1.3 V noting that the key deliverable of the analysis is that the total As concentration lies below the WHO threshold of 10 ppb (0.13 μM) [31].

Next, the As(III) content of the mixtures were found. Pre-concentration was applied at – 0.9 V for 300 s and then followed with a linear potential sweep from – 0.9 V to + 0.6 V at a scan rate of 0.1 V s^{-1}. Table 7.1 (Columns 2 and 5) presents the concentrations of the known As(III) in solution and the measured As(III) concentrations. It shows that the measured As(III) concentrations were within 10% of the known values confirming that the UPD-ASV method can be applied onto determination of As(III) in the mixture of both arsenic species using the deposition potential of – 0.9 V.

Finally, the concentrations of As(V) were calculated by subtraction of the measured As(III) concentrations from the measured total arsenic concentrations; the values are shown in Table 7.1 (Columns 3 and 6). The values are in reasonable agreement with the known values except at very low concentrations, below ca 3 ppb, where the accumulation of errors leads to loss of accuracy. However the method is designed for use in drinking water samples where the total arsenic concentration is the key measurement; the relative amount of As (III) and As(V) as measured using UPD-ASV nevertheless give a clear indication of the speciation of As in the water.

Table 7.1 The added concentrations of mixture of As(III)/As(V) and the measured total concentrations of arsenic and the As(V), As(III) concentrations. Measuring the total concentrations of arsenic used a deposition potential of – 1.3 V and measuring the concentration of As(III) used a deposition potential of – 0.9 V. The total concentrations of arsenic and the As(III) can be measured directly from the charge of peak 2', and the As(V) concentrations were obtained by subtraction of the As(III) concentration from the total arsenic concentration.

Added [As(III)+As(V)] (ppb)	**Added [As(III)] (ppb)**	**Added [As(V)] (ppb)**	**Measured [As(III)+As(V)] (ppb)**	**Measured [As(III)] (ppb)**	**Measured [As(V)] (ppb)**
8.25	7.5	0.75	**7**	6.75± 2.25	**0.25**± 2.25
9.75	7.5	2.25	**9.0**	6.75± 2.25	**2.25**± 2.25
15	7.5	7.5	**13.9**	7.5± 2.25	**6.4**± 2.25
18.75	7.5	11.25	**14.6**	7.5± 2.25	**7.1**± 3.75
22.5	15	7.5	**18.9**	14.25± 3.75	**4.65**± 3.75
26.25	15	11.25	**22.8**	14.25± 3.75	**8.55**± 3.75

Last gold screen printed electrodes (Au SPEs) were tested to see if they could replace gold macroelectrodes for As detection via the UPD-ASV method. However, the high capacitive currents and background signals made it impossible to transfer this method onto the Au SPEs (See details in Appendix Section 5).

7.4. Conclusions

The analytical use of underpotential deposition of As on gold surface with anodic stripping of adsorbed As ad-atoms on gold macroelectrodes has been shown to allow the detection of total As content by deposition at high potentials (- 1.3 V vs MSE) and, selectively, of As(III) by deposition at lower potential (- 0.9 V vs MSE). Limits of detections were found

to be 0.8 ppb which are well within the WHO requirements for drinking water were observed for both As(III) and As(V) with visually discernible signals.

7.5. Appendix

Section 1: Baseline correction and peak area integration for peak 2'

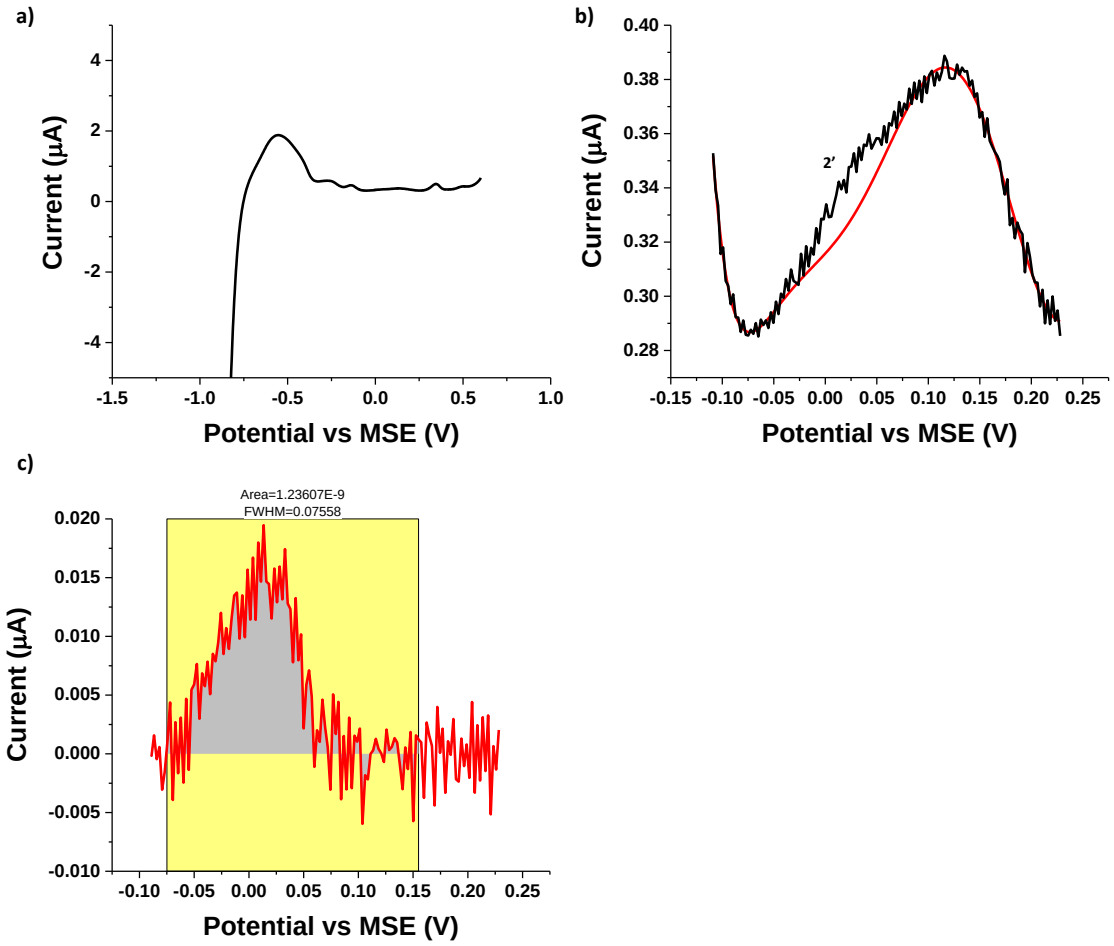

Figure A7.1 a) The original LSV curve of 0.05 µM As(III) in 0.1 M H_2SO_4 at Au macroelectrodes. b) The LSV curve from -0.10 V to +0.22 V (black line) and simulated baseline (red line). c) The baseline corrected LSV curve from -0.10 V to + 0.22 V (red line) and the peak area (grey area). LSV parameters: deposition at -1.3 V vs. MSE for 300s, potential scan rate 0.1 V s^{-1}.

The signal used for the UPD-ASV analysis is the charge of peak 2', which was calculated from the area of baseline corrected voltammogram. A sample correction is shown

in Figure A7.1. To obtain the baseline corrected peak 2', first, the voltammogram between – 0.10 V to + 0.22 V (black line in Figure A7.1b) was zoomed in from the raw LSV curve (Figure A7.1a). A baseline (red line in Figure A7.1b) was simulated via the polynomial method in Origin 2017 with an order of 7 in the range from – 0.08 V to – 0.05 V and + 0.095 V to + 0.22 V. Thus, the simulated background line in the Figure A7.1b was in the range from – 0.05 V to + 0.095 V. To calculate the charge of the stripping peak of UPD As, a subtraction between the unmodified voltammogram and the simulated baseline was applied, and the baseline corrected voltammogram is shown in Figure A7.1c. The area of peak 2' (grey area in Figure A7.1c) can be calculated via 'integrate' function in Origin 2017. The LSVs in this project were all baseline corrected voltammograms estimated using this method. The 'reduction peaks' at ca – 0.75 V and + 0.10 V were artefacts from the baseline correction, which did not relate to Faradaic reactions.

Section 2: The calculation of peak charge of peak 2'

After the area of peak 2' determined from the baseline corrected LSVs, the charge of peak 2' then can be calculated based on the equation:

$$Q = \frac{Area\ of\ peak}{Scan\ rate} \tag{7-1}$$

A sample calculation is shown for 0.05 μM As(V) in 0.1 M H_2SO_4 and the peak area was determined to be 1.2×10^{-9} C s V^{-1} in Section 1. The scan rate was 0.1 V s^{-1}. Thus, the charge of peak 2' is:

$$Q = \frac{Area\ of\ peak}{Scan\ rate} = \frac{1.2 \times 10^{-9} C s V^{-1}}{0.1\ V\ s^{-1}} = 1.2 \times 10^{-8}\ C \tag{7-2}$$

Section 3: Estimation of the surface coverage of As during pre-concentration on bulk Au

The area of peak 2' can be calculated via 'Integrate' in Origin 2017. The area of the peak 2' of 1 μM As(V) in 0.1 M H_2SO_4 at Au macroelectrodes was 9.6×10^{-9} C s V^{-1} (Figure A7.2).The charge (Q) of the peak then can be estimated as:

$$Q = \frac{Area\ of\ peak}{Scan\ rate} = 4.6\ \times\ 10^{-8}\ C \tag{7-3}$$

The corresponding number of electrons then was estimated as:

$$\frac{Charge\ of\ peak\ 2\prime}{Elementary\ charge} = \frac{4.6 \times 10^{-8}\ C}{1.6 \times 10^{-19}\ C} = 2.9\ \times\ 10^{11} \tag{7-4}$$

The number of moles of electrons was calculated as:

$$\frac{Number\ of\ electrons}{Avogadro\ constant} = \frac{2.9 \times 10^{11}}{6.02 \times 10^{23}\ mol^{-1}} =\ 4.8\ \times\ 10^{-13}\ mol \tag{7-5}$$

Each As ad-atom has three electrons transferred during the stripping sweep from As(0) to As(III). Thus, the number of moles of As can be estimated as:

$$\frac{Moles\ of\ electrons}{3} = \frac{4.8 \times 10^{-13}\ mol}{3} = 1.6\ \times\ 10^{-13}\ mol \tag{7-6}$$

The surface area of Au macroelectrode (with radius of 0.08 cm) is 0.02 cm^2 or 2×10^{12} nm^2. Hence, the estimated surface coverage of As on the surface of Au could be obtained assuming As atoms were closely packed on the surface of electrode (Figure A7.2a):

$$\frac{Number\ of\ moles\ of\ As}{Surface\ area\ of\ Au\ macroelectrode} = \frac{1.6 \times 10^{-13}\ mol}{0.02\ cm^2} = 8.0\ \times\ 10^{-12}\ mol\ cm^2 \tag{7-7}$$

Each As ad-atom has three electrons transferred during stripping sweep. Thus, the number of As ad-atoms can be estimated as $9.6\ \times\ 10^{10}$. The surface coverage of As on the surface of Au can also be obtained with the number of As atoms deposited and the surface area of the electrode:

$$\frac{Number\ of\ As\ atoms}{Surface\ area\ of\ Au\ macroelectrode} = \frac{9.6 \times 10^{10}\ molecules}{0.02\ cm^2} = 4.8\ \times\ 10^{12}\ molecules\ cm^{-2} \quad (7\text{-}8)$$

The number of monolayers of As ad-atoms were also estimated. The radius of As atom is 185 pm [50] and diameter is 370 pm. The covered area of single As atom (d^2) is calculated to be 0.14 nm^2.

The number of As deposited can be calculated from the number of moles of As and Avogadro constant, and it is:

$$Moles\ of\ As \times Avogadro\ constant = 1.6\ \times\ 10^{-13}\ mol\ \times\ 6.02\ \times\ 10^{23}\ mol^{-1}\ = 9.6\ \times\ 10^{10} \quad (7\text{-}9)$$

The number of one monolayer of As atoms on the surface of Au electrode was estimated assuming As atoms were closely packed on Au (Figure A7.2a):

$$\frac{Surface\ area\ of\ Au\ macroelectrode}{Covered\ area\ of\ single\ As\ atom} = \frac{2 \times 10^{12}\ nm^2}{0.14\ nm^2} = 1.5\ \times\ 10^{13} \quad (7\text{-}10)$$

Therefore, the number of layers of As atoms on Au is:

$$\frac{Number\ of\ As\ atoms\ deposited}{Number\ of\ one\ monolayer\ of\ closely\ packed\ As\ atoms} = \frac{9.6 \times 10^{10}}{1.5 \times 10^{13}} = 0.007 \quad (7\text{-}11)$$

This corresponds to a sub-monolayer (ca 0.007 monolayers) of As atoms on the surface of Au.

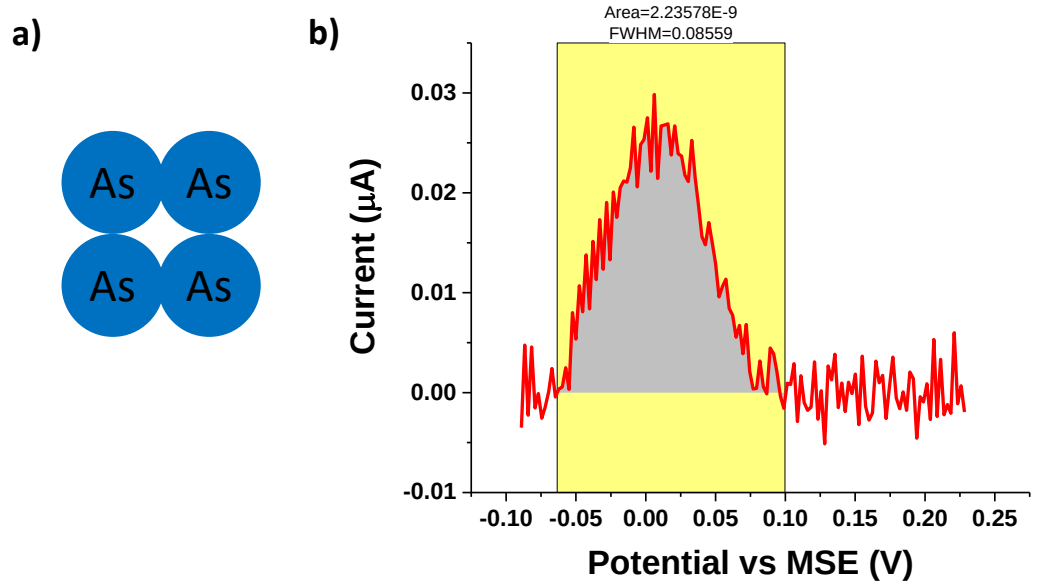

Figure A7.2 a) A scheme of As atoms closely packed at the surface of Au. b) The baseline corrected LSV curves of peak 2' of 0.1 μM As(V) in 0.1 M H_2SO_4 at Au macroelectrode. The grey areas are used for the integration. LSV parameters: deposition at -1.3 V vs. MSE for 300s, potential scan rate 0.1 V s^{-1}, and baseline was modelled via polynomial method with an order of 7 in the range from – 0.08 V to – 0.05 V and + 0.095 V to + 0.22 V.

Section 4: Calculations to determine the concentrations of total arsenic, As(III) and As(V)

The determination of the concentrations with the equations from the experimentally determined calibration line is an important method for the detection of arsenic after obtaining the signal of peak 2'. The signal of total arsenic is obtained by deposition at – 1.3 V vs MSE and of As(III) is obtained by deposition at – 0.9 V. A sample calculation for determining the concentrations of total arsenic and As(III) is shown below:

Table A7.1 The concentrations of added total arsenic, As(III) and As(V) and their measured values in ppb. To measure the concentrations of total arsenic, the deposition was conducted at – 1.3 V, and for As(III), the deposition was conducted at – 0.9 V.

Added [As(III)+As(V)] (ppb)	**Added [As(III)] (ppb)**	**Added [As(V)] (ppb)**	**Measured [As(III)+As(V)] (ppb)**	**Measured [As(III)] (ppb)**	**Measured [As(V)] (ppb)**
15	**7.5**	**7.5**	**14**	**7.5**	**6.4**

The equation obtained for the deposition at – 1.3 V was

$$Charge = 2.2 \times 10^{-7} C\ \mu M^{-1}\ \times [As] + 7 \times 10^{-10}\ C \qquad (7\text{-}12)$$

The charge of the peak 2' was determined to be 4.2 × 10^{-8} C from the baseline corrected voltammogram and the concentration of total arsenic was determined to be ca 0.19 μM, which equals to 14 ppb, which was within the range of 10% of known total arsenic concentration.

To calculate the concentration of As(III) in solution, the deposition was conducted at – 0.9 V then followed up with a linear potential sweep from – 0.9 V to + 0.6 V at a scan rate of 0.1 V s^{-1}. The equation obtained for the As(III) was

$$Charge = 2.1 \times 10^{-7} C\ \mu M^{-1}\ \times [As(III)] + 2 \times 10^{-9}\ C \qquad (7\text{-}13)$$

The charge of the concentration was determined to be 2.5 × 10^{-8} C from the baseline corrected voltammogram and the concentration of total arsenic was determined to be ca 0.1 μM (7.5 ppb).

Thus, the concentration of As(V) can be determined from the subtraction of total arsenic concentration, 14 ppb and the As(III) concentration, 7.5 ppb as 6.4 ppb, which is within 15% of the known As(V).

Section 5: Measurements on disposable, commercial gold screen printed electrodes (Au SPEs)

The gold screen printed electrodes (Au SPEs) were tested to see if they could replace gold macroelectrodes for As detection via the UPD-ASV method. Electrodes were sourced from three different companies, Zimmer & Peacock (ZP), DropSens (DS) and Zensor (Zen) and used either as received or after the manufacturer (Zimmer & Peacock) recommended method for activation [45]. In the latter case the Au SPEs from ZP were cleaned in 10 mM HCl by scanning CVs for 5 cycles in the range of – 0.9 V to - 0.2 V at a scan rate of 0.1 V s^{-1} before each electrochemical measurement. The electrodes from DS and Zen were used directly

without pre-cleaning. Pictures of the purchased electrodes are shown in Figure A7.3, where the working electrode of ZPs are rectangular (red frame in Figure A7.3a) while those from the other companies are discs (red frames in Figures A7.3 b and c). The electrodes also have printed counter and reference electrodes which were not used in the measurements reported in this thesis; only the working electrodes on the SPEs were used with the reference electrode and counter electrode added to the electrochemical cell in the form of a MSE and a graphite rod (as described in section 4.3).

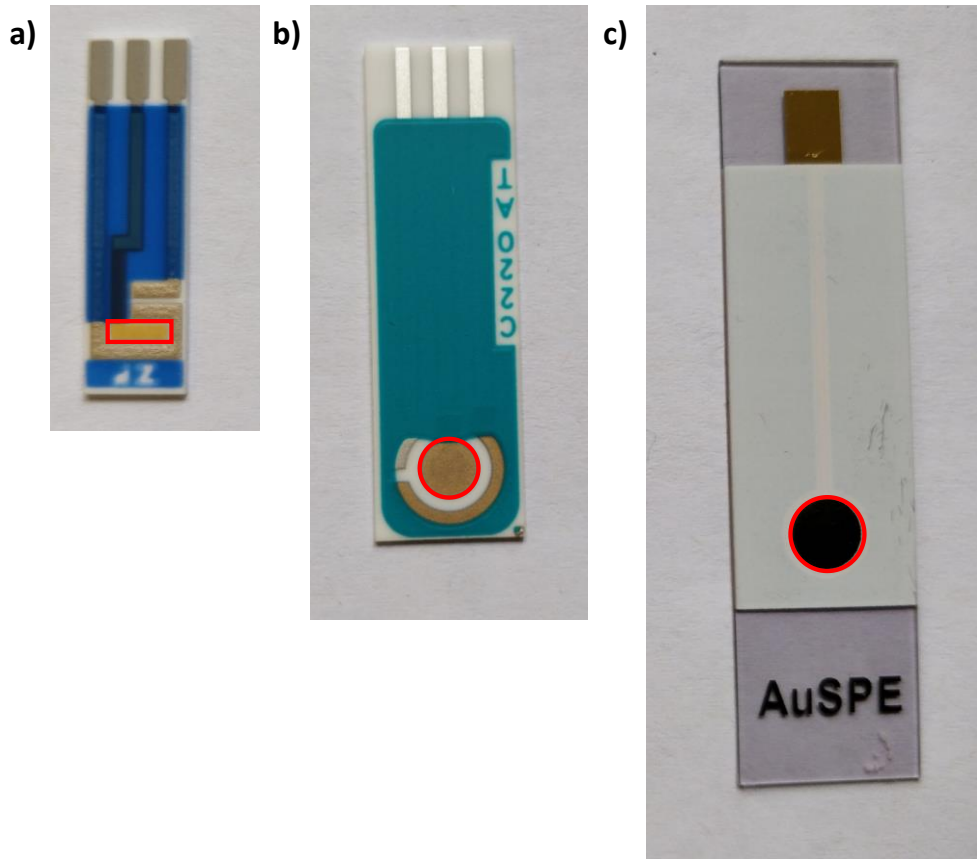

Figure A7.3 The pictures of commercial available Au SPEs from a) Zimmer & Peacock (ZP), b) DropSens (DS) and c) Zensor (Zen). The red frames show the working electrodes on the SPEs. All pictures were taken from the phone directly.

Measurements in the presence and absence of 'Ruhex' in 0.1 M KCl

First, the responses of the Au SPEs in 1 mM hexaammineruthenium(III) chloride ("Ruhex") in aqueous solution with 0.1 M KCl were recorded and compared with Au macroelectrodes to check the voltammetric response to this well studied simple, outer sphere electron transfer reaction [51].

$$[Ru(NH_3)_6]^{3+} + e^- \rightarrow [Ru(NH_3)_6]^{2+} \quad (7\text{-}14)$$

Cyclic voltammograms were started at – 0.2 V and scanned cathodically to – 0.9 V then scanned anodically back to – 0.2 V at a scan rate of 0.1 V s^{-1} on Au macroelectrodes and Au SPEs. Figure A7.4a illustrates the CVs of 1 mM Ruhex in 0.1 M KCl on Au macroelectrodes (red line in Figure A7.4a), Au SPEs from ZP (blue line in Figure A7.4a), Au SPEs from DS (green lines in Figure A7.4a) and Au SPEs from Zen (orange line in Figure A7.4a). It is clear to see that all four electrodes present a reduction peak at ca – 0.6 V ascribed to the reduction of $[Ru(NH_3)_6]^{3+}$ to $[Ru(NH_3)_6]^{2+}$, and a corresponding re-oxidation peak on the reverse scan at ca – 0.55 V [51]. The formal potential of the redox couple was ca – 0.58 ± 0.02 V (vs MSE) at all four gold electrodes (Figure A7.4). The value is similar to the literature value of – 0.55 V at 298 K [51]. The peak to peak potential was ca 60 mV at all four electrodes (Figure A7.4), which is also similar to the literature [51] and suggest that the reaction is electrochemical reversible [3]. The peak currents in Figure A7.4a were very different for all four electrodes, which was caused at least in part by the difference of the geometric area of electrodes. The geometric surface areas of SPEs were calculated from the diameters or side length of each electrode (Eqn. (7-15) and (7-16)).

$$A_{geo} = \pi r^2 \quad (7\text{-}15)$$

$$A_{geo} = a \times b \quad (7\text{-}16)$$

where A_{geo} is the geometric area, r is the radius of the circular printed electrode, a and b are the side lengths of rectangular printed electrodes. The values of geometric areas of the SPEs are shown in Table A7.2. The current densities were calculated and are shown in Table A7.2. The errors are standard deviations calculated from at least three measurements. The current densities are plotted against potential in Figure A7.4b and were within 25% for all four electrodes.

Table A7.2 Diameters/side lengths, geometric areas, peak currents and peak current densitites measured at Au SPEs in 10 mM Ruhex.

Electrode	Measured diameter or side length (cm)	Shape	Geometric areas (cm^2)	Peak current (μA)	Peak current densitites (μA cm^{-2})
Au SPE (ZP)	0.4 (± 0.01) and 0.1 (± 0.01)	Rectangle	0.04 (± 0.004)	7.5 ± 0.5	187 ± 10
Au SPE (DS)	0.4 (± 0.01)	Disc	0.13 (± 0.005)	15 ± 0.5	115 ± 5
Au SPE (Zen)	0.5 (± 0.01)	Disc	0.2 (± 0.004)	27 ± 0.5	135 ± 3

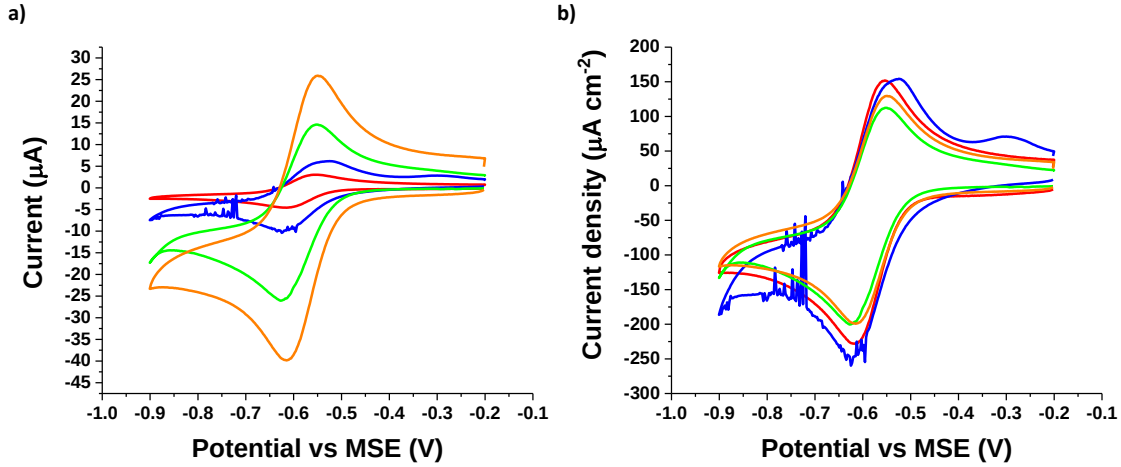

Figure A7.4 The cyclic voltammograms (CVs) of 1 mM Hexaammineruthenium(III) chloride (RuHex) in 0.1 M KCl of a) currents vs potential and b) current densities vs potential Au macroelectrodes (red), Au SPEs from ZP (blue), Au SPEs from DS (green) and Au SPEs from Zen (orange). The CV was conducted at a) -0.2 V and scanned cathodically to – 0.9 V then scanned annodically to – 0.2 V. The scan rate was 0.1 V s^{-1}. The current densities were

calculated based on currents/geometric area of electrodes. The geometric areas are 0.02, 0.04, 0.13 and 0.2 cm^2 for Au macroelectrodes, AuSPEs from ZP, AuSPEs from DS, and AuSPEs from Zen, respectively.

To measure the background currents of the four types of gold electrodes, CV was measured in 0.1 M KCl solution. The CV was started at - 0.2 V and first scanned cathodically to – 0.9 V, then scanned anodically to – 0.2 V at a scan rate of 0.1 V s^{-1}. Figure A7.5a illustrates the currents vs potential of all four electrodes. It is clear that the Au SPEs from ZP (blue), DS (green) and Zen (orange) present higher background currents, which may be caused by the difference of geometric areas of the electrodes. Thus the current densities were calculated with the geometric areas (as above) and the current densities plotted against the potential are shown in Figure A7.5b. The SPEs from DS (green) and Zen (orange) have similar background signal to the Au macroelectrodes, whilst the SPE from ZP (blue) showed a much bigger background signal, which may be partly caused by the roughness of the surface but the presence of extra peaks suggests a possible surface contamination in the supplied electrodes. Whatever the cause the ZP electrodes are unsuitable for electroanalytical measurements in the potential range of interest for As determination. To further study the commercial printed electrodes, capacitive currents were estimated in the next section.

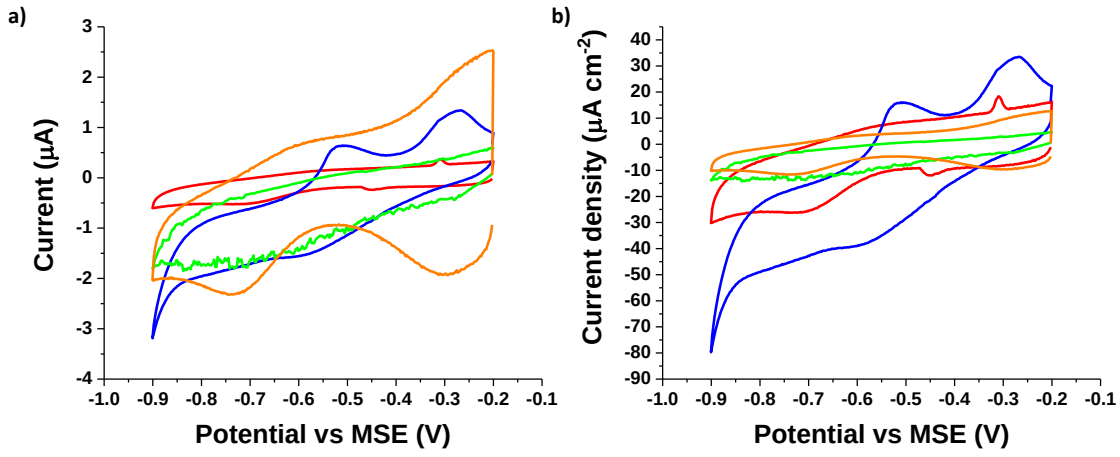

Figure A7.5 The cyclic voltammograms (CVs) of 0.1 M KCl of a) currents vs potential and b) current densities vs potential Au macroelectrodes (red), Au SPEs from ZP (blue), Au SPEs from DS (green) and Au SPEs from Zen (orange). The CV was conducted at a) -0.2 V and scanned cathodically to – 0.9 V then scanned annodically to – 0.2 V. The scan rate was 0.1 V s^{-1}. The current densities were calculated based on currents/geometric area of electrodes. The geometric areas are 0.02, 0.04, 0.13 and 0.2 cm^2 for Au macroelectrodes, AuSPEs from ZP, AuSPEs from DS, and AuSPEs from Zen, respectively.

Study on background/capacitive currents at screen printed electrodes in 0.1 M H_2SO_4

Table A7.3 Slopes, geometric areas and measured capacitance of Au macroelectrodes and Au SPEs from DS, Zen and ZP. The measurements were taken place in 0.1 M H_2SO_4.

	Au macroelectrode	Au SPE (DS)	Au SPE (Zen)	Au SPE (ZP)
CR_fA (slope)	3E-7	3E-7	2E-6	2E-5
Geometric area (cm^2)	0.02	0.13	0.2	0.04
CR_f ($\mu F\ cm^{-2}$)	**13**	**3**	**8**	**500**

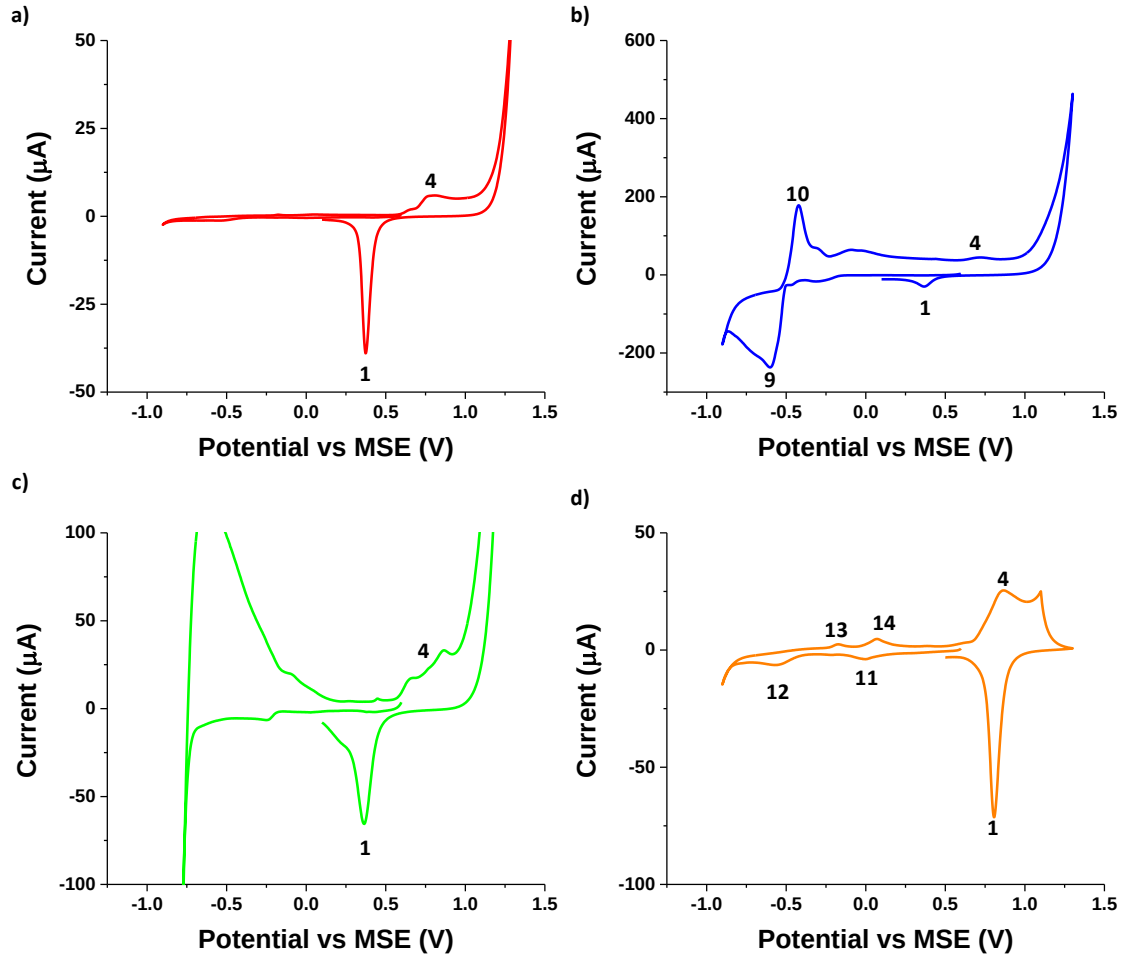

Figure A7.6 The cyclic voltammograms (CVs) of 0.1 M H_2SO_4 at a) Au macroelectrodes, b) Au SPEs from ZP, c) Au SPEs from DS and d) Au SPEs from Zen. The CV was conducted at + 0.6 V and first scanned cathodically to – 0.9 V at a scan rate of 0.1 V s^{-1} followed by an anodic scan to + 1.3 V. The scan rate was 0.1 V s^{-1}.

The CV of the gold electrodes were measured in 0.1 M H_2SO_4 with different potential windows to crudely estimate the apparent capacitive currents. The CV was started at + 0.6V and scanned cathodically to – 0.9 V then scanned anodically to + 1.3 V at a scan rate of 0.1 V s^{-1}. Figure A7.6 illustrates the CVs of all four gold electrodes in 0.1 M H_2SO_4. The CV of Au macroelectrode presented two features (Figure A7.6a), peak 1 at ca + 0.4 V and peak 4 at ca +0.8 V, which are ascribed to the Au oxide reduction and Au oxidation, respectively [47]. For ZP electrodes, four peaks can be observed as peaks 1, 4, 9 and 10 (Figure A7.6b), where peaks 1 and 4 represents the same chemistry as above. Peak 9 at ca – 0.6 V and 10 at ca – 0.4 V are possibly arise from contamination during manufacture of the surface of the electrode, and in the context of As analysis would likely overlap with the reduction peaks of As(III) to As(0) at ca – 0.6 V [43], and the oxidation peak of As(0) to As(III) at ca – 0.4 V [43]. Figure A7.6c illustrates the CV response of the DS electrode in 0.1 M H_2SO_4, which presents two peaks, peaks 1 and 4 as above. Figure A7.6d shows the CV response of SPEs from Zen, which presents six features. Apart from peaks 1 and 4, peaks 11, 12, 13 and 14 are assigned to species present on the surface of the electrode as supplied from Zen.

To make estimates of the apparent capacitance further CVs were recorded in the narrower ranges shown in the Figure A7.7. At Au macroelectrodes, the cyclic voltammograms (CV) were conducted at – 0.3 V and scanned anodically to – 0.2 V, then scanned cathodically to – 0.4 V and scanned back to – 0.3 V at the scan rates of 0.05, 0.1, 0.2, 0.4, and 0.8 V s^{-1}. As Au SPEs from DS and Zen, the CV were conducted at – 0.25 V and scaned cathodically to – 0.15 V, then scanned cathodically to – 0.35 V and stopped at – 0.25 V at the same scan rates. Au SPEs from ZP, the CVs were started from – 0.2 V with the potential window from -0.25 V to – 0.15 V at all 5 scan rates. The CV responses are shown in Figure A7.7. Significant deviation is observed from the rectangular current-voltage responses expected for an ideal

capacitive interface, especially for the ZP electrodes, so that the values for interfacial capacitance inferred below are order of magnitude estimates at best.

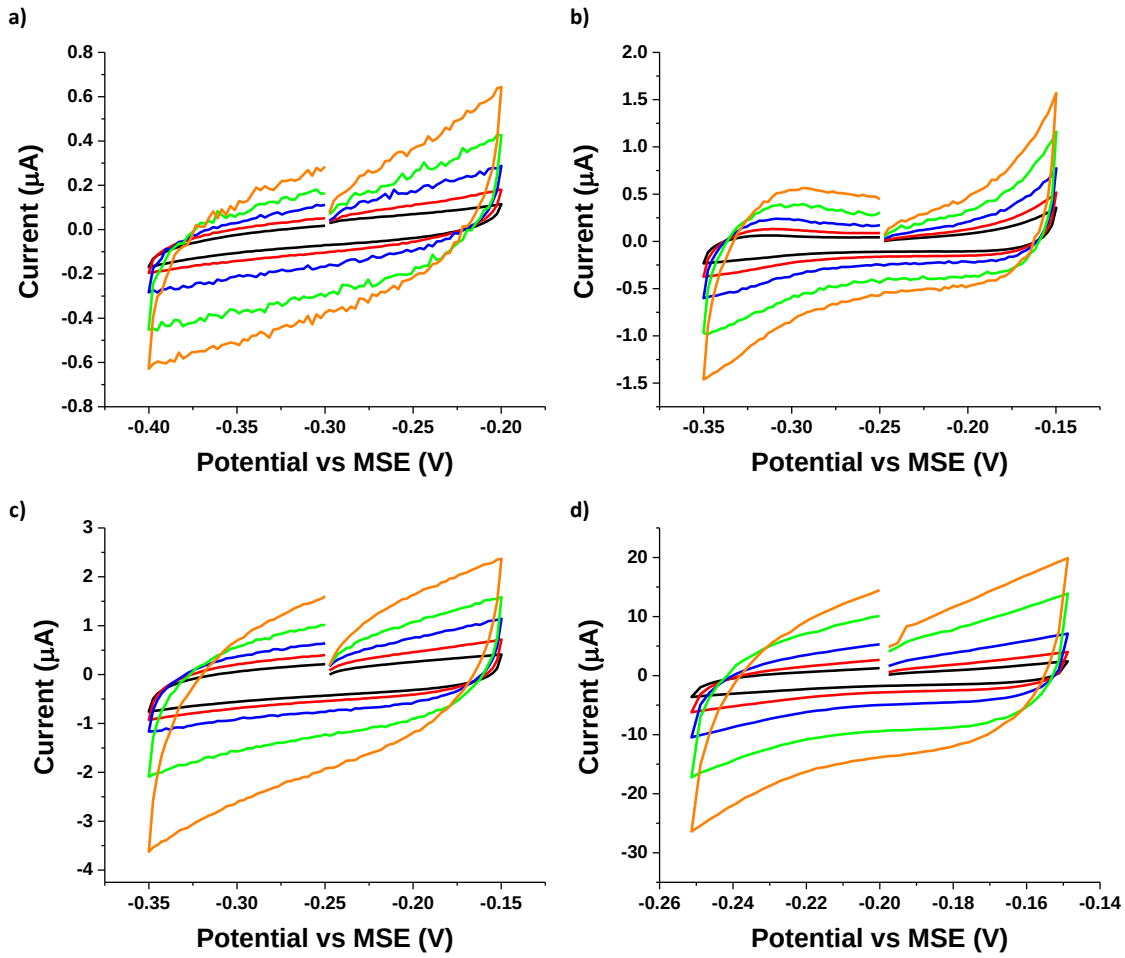

Figure A7.7 The cyclic voltammograms (CVs) of 0.1 M H_2SO_4 at a) Au macroelectrodes, b) Au SPEs from DS, c) Au SPEs from Zen and d) Au SPEs from ZP. The CV was conducted at a) -0.3 V, b) and c) – 0.25 V, and d) – 0.2 V, within the potential range of 0.2 V. The scan rates were 0.05, 0.1, 0.2, 0.4, and 0.8 V s^{-1}.

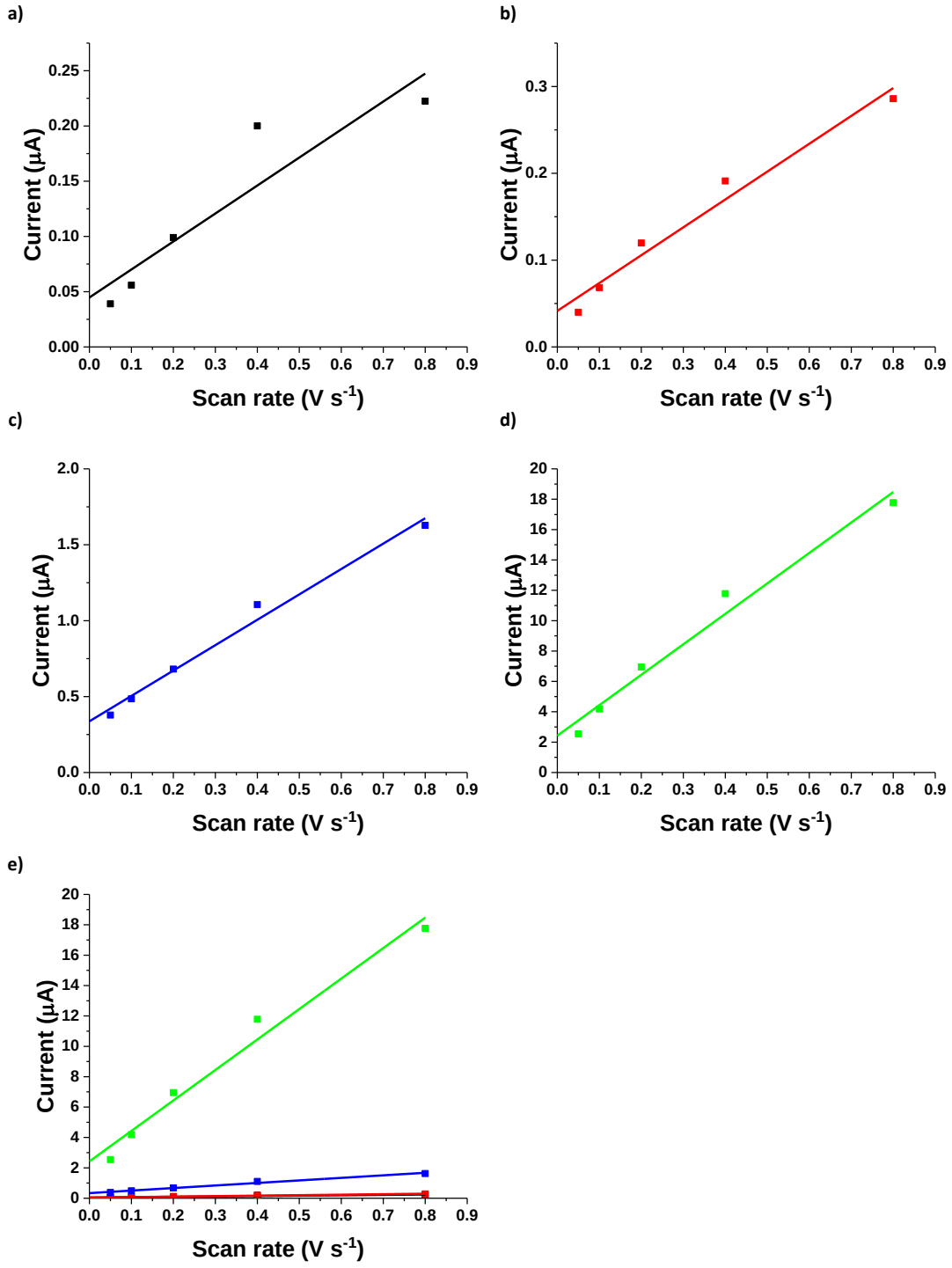

Figure A7.8 The plots of currents vs scan rate at – 0.225 V in 0.1 M H_2SO_4 at a) gold macroelectrodes, b) Au SPEs (DS), c) Au SPEs (Zen), d) Au SPEs (ZP) and e) the overlay of all four electrodes. The electrodes in e) are gold macroelectrodes (black), Au SPEs (DS) (red), Au SPEs (Zen) (blue) and Au SPEs (ZP) (green). The currents were chosen at the potential of – 0.225 V since this potential was contained in all CV measurements.

After obtaining the CVs, capacitive currents were estimated using the equation:

$$I_{ca} = C \times R_f \times A_{geo} \times v \qquad (7\text{-}17)$$

where I_{ca} is the capacitive current, C is the capacitance, R_f is the roughness factor, A_{geo} is the geometric area and v is the scan rate. A linear relationship between capacitive current and the scan rate is expected from the equation with a slope equals to $C \times R_f \times A_{geo}$. The data in Figure A7.7 were plotted as shown in Figure A7.8 in the form of current at – 0.225 V since this potential is contained in all CV measurements (Figure A7.7). An approximately linear dependence was seen and the slope calculated from the figures. In Figure A7.8, the pathologically high slope from the ZP Au SPEs suggests extreme surface roughness and/or non capacitive contributions and/or surface contamination in the as supplied electrodes.

The slopes, geometric areas and measured capacitance are shown in Table A7.3 with the calculation from the slope. The literature value for capacitance per unit area of gold in H_2SO_4 is 10 μF cm^{-2} [52]. Compared to the literature value, the DS and Zen SPEs had similar values to the literature [52], and were considered for possible use for arsenic detection current. The SPEs from ZP likely are not be suitable for arsenic. CV measurements were next made in the presence and absence of 500 μM As(III) in 0.1 M H_2SO_4.

Cyclic voltammetry of As(III) at printed electrodes

Electrochemical measurements were made in the presence and absence of 500 μM As(III) in 0.1 M H_2SO_4 with a potential window from – 1.4 V to + 1.3 V (vs. MSE) at all four electrodes. The CV was conducted at + 0.6 V and the voltammogram was first scanned cathodically to – 0.9 V at a scan rate of 0.1 V s^{-1} and then scanned anodically to + 1.3 V. Figure A7.9 illustrates the CVs in the presence (solid lines) and absence (dashed lines) of 500 μM As(III) in 0.1 M H_2SO_4 at four gold electrodes. Similar to the CVs shown in Chapter 6, all peaks appear at similar potentials except that at SPE from ZP (Figure A7.9b). The ZP electrodes have an unexpected reduction peak with anomalously high currents at ca - 0.6 V in CVs of both

presence (solid line) and absence (dashed line) of As(III), which may be caused by the electrode itself. The possible use of the UPD-ASV method with Zen and DP SPEs is explored next.

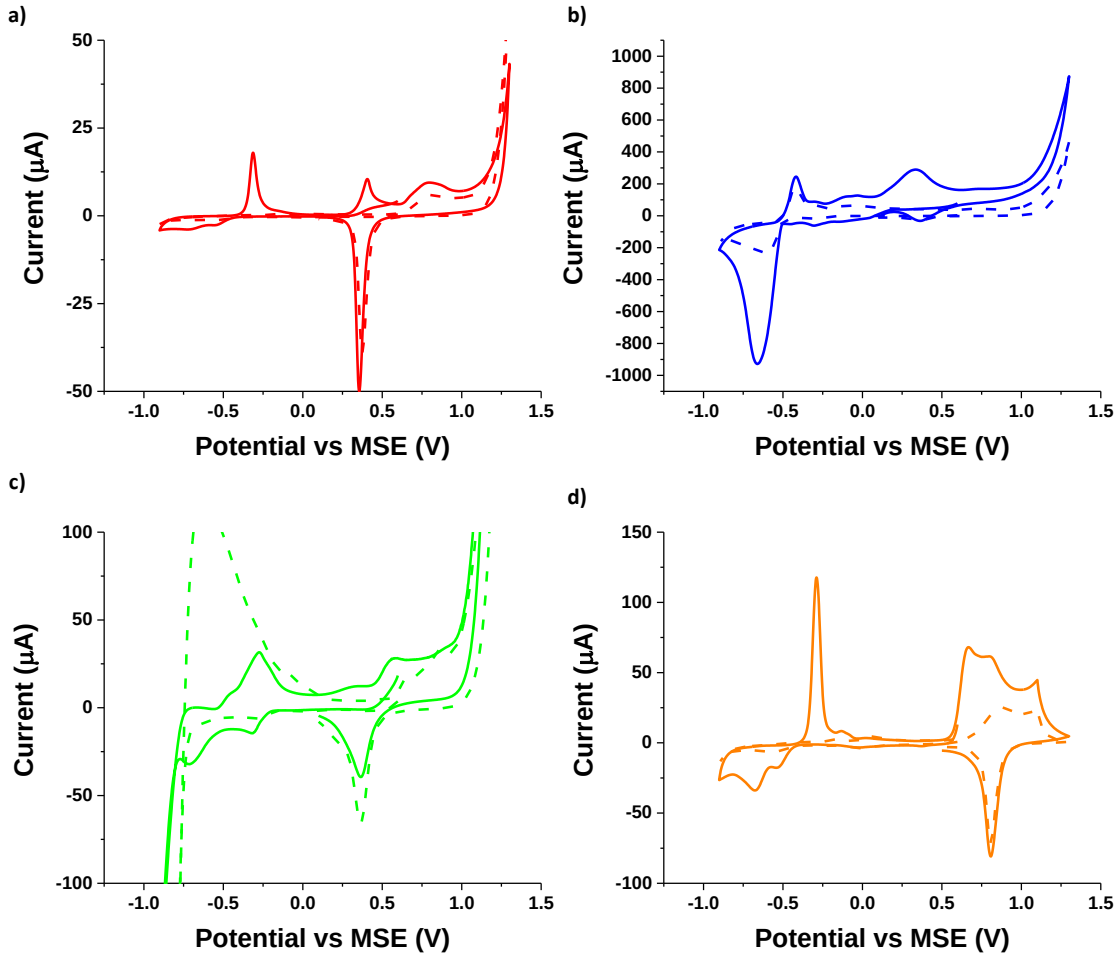

Figure A7.9 The cyclic voltammograms (CVs) of presence (solid lines) and absence (dashed lines) of 500 µM As(III) in 0.1 M H_2SO_4 at a) Au macroelectrodes, b) Au SPEs from ZP, c) Au SPEs from DS and d) Au SPEs from Zen. The CV was conducted at + 0.6 V and first scanned cathodically to – 0.9 V at a scan rate of 0.1 V s^{-1} followed by an anodic scan to + 1.3 V. The scan rate was 0.1 V s^{-1}.

Stripping voltammetry of As(III) and As(V) at printed electrodes

To study the possible use of arsenic detection via UPD-ASV method at printed electrodes, measurements were made in either As(III) or As(V) solutions for DS and Zen electrodes. The measurements were first conducted in 0.1 µM As(III) or 0.1 µM As(V) in 0.1 M H_2SO_4 at Au SPEs from DS. To detect As(III), pre-concentration was conducted at – 0.9 V for 300 s and followed with a linear sweep from – 0.9 V to + 0.6 V at a scan rate of 0.1 V s^{-1}.

Figure A7.10a illustrates the voltammograms in the presence (red) and absence (black) of 0.1 µM As(III) in 0.1 M H_2SO_4 at Au SPEs from DS. A huge peak can be seen at ca – 0.15 V for both curves, which overlaps with the potential of the expected stripping peak of UPD As at ca + 0.04 V. Meanwhile, a similar detection approach was also applied to As(V), where pre-concentration was conducted at – 1.3 V for 300 s then the potential was swept from – 1.3 V to + 0.6 V at a scan rate of 0.1 V s^{-1}. Figure A7.10b presents the voltammograms in the presence (red) and absence (black) of 0.1 µM As(V) in 0.1 M H_2SO_4 at Au SPEs from DS. Similar to the phenomenon in As(III), a tall and wide peak observed at ca – 0.15 V also overlapped with the UPD As peak at ca + 0.04 V. Thus, it is impossible to transfer this UPD-ASV method to the Au SPEs from DS due to the overlap from the huge peak at ca – 0.15 V.

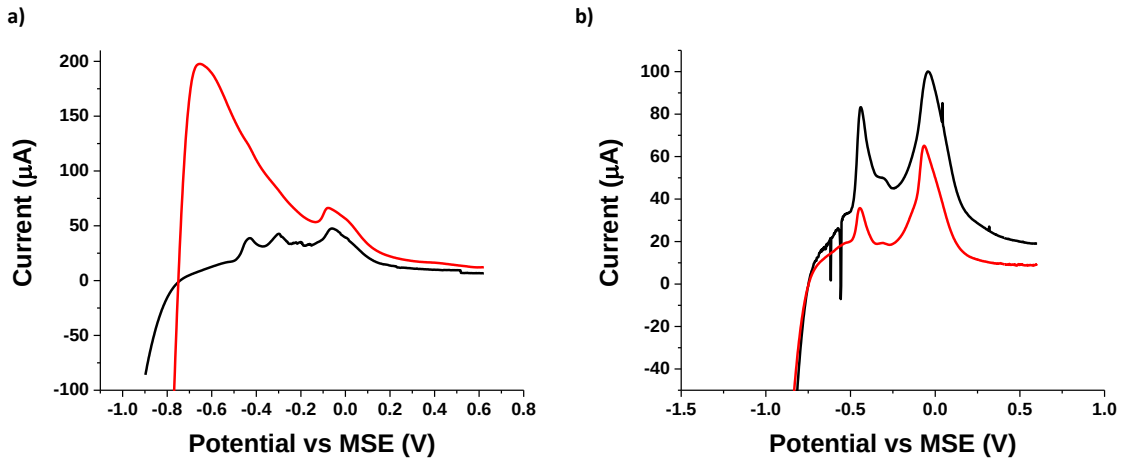

Figure A7.10 LSVs a) in the presence (red) and absence (black) of 0.1 µM As(III) in 0.1 M H_2SO_4 at Au SPEs from DS, and b) in the presence (red) and absence (black) of 0.1 µM As(V) in 0.1 M H_2SO_4 at Au SPEs from DS. ASV parameters: for As(III), deposition at – 0.9 V for 300 s then followed with a linear potential sweep from – 0.9 V to + 0.6 V at a scan rate of 0.1 V s^{-1}; for As(V), deposition at – 1.3 V for 300 s then swept a linear scan from – 1.3 V to + 0.6 V at a scan rate of 0.1 V s^{-1}.

Analogous experiments were made on Au SPEs (Zen) to find out if UPD-ASV method can be transferred onto them. To detect As(III), pre-concentration was conducted at – 0.9 V for 300 s then followed with a linear sweep from – 0.9 V to + 0.6 V at a scan rate of 0.1 V s^{-1}. Figure A7.11a illustrates the voltammograms in the presence (red) and absence (black) of 0.1 µM As(III) in 0.1 M H_2SO_4 at Au SPEs from Zen. It is clear to see a gold oxidation peak at ca

+ 0.1 V. However, the UPD As peak was at ca + 0.04 V, which was overlapped with the gold oxidation peak. Thus, the Au SPEs from Zen was not possible for the measurement of UPD As peak. On the other hand, to measure the concentration of As(V), pre-concentration was conducted at – 1.3 V for 300 s then followed with a linear sweep from – 1.3 V to + 0.6 V at a scan rate of 0.1 V s^{-1}. Figure A7.11b shows the voltammograms in the presence (red) and absence (black) of 0.1 µM As(V) in 0.1 M H_2SO_4 at Au SPEs from Zen. Similar to As(III), a gold oxidation peak is observed at ca + 0.1 V, which overlapped with the UPD As stripping peak and make it impossible for the detection of As(V) using UPD-ASV method. Thus, the UPD-ASV method is also impossible to be transferred to the Au SPEs from Zen.

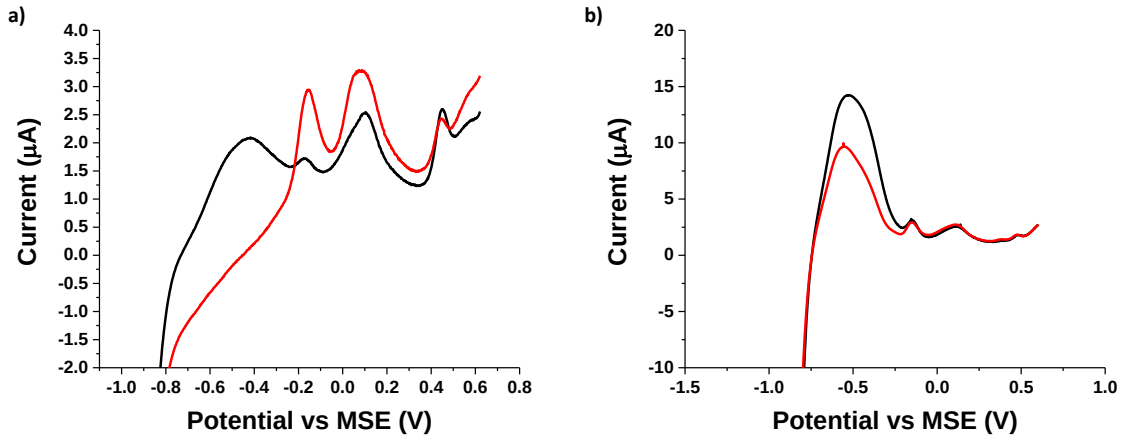

Figure A7.11 LSVs a) in the presence (red) and absence (black) of 0.1 µM As(III) in 0.1 M H_2SO_4 at Au SPEs from Zen, and b) in the presence (red) and absence (black) of 0.1 µM As(V) in 0.1 M H_2SO_4 at Au SPEs from DS. ASV parameters: for As(III), deposition at – 0.9 V for 300 s then followed with a linear potential sweep from – 0.9 V to + 0.6 V at a scan rate of 0.1 V s^{-1}; for As(V), deposition at – 1.3 V for 300 s then swept a linear scan from – 1.3 V to + 0.6 V at a scan rate of 0.1 V s^{-1}.

In conclusion, the Au SPEs cannot be used for the arsenic detection via the UPD-ASV method.

7.6. Bibliography

[1] J. Wang, Stripping analysis: principles, instrumentation, and applications, Vch Pub1985.
[2] K. Brainina, E. Neyman, Electroanalytical stripping methods, John Wiley & Sons1994.

[3] R.G. Compton, C.E. Banks, Understanding Voltammetry, 3rd Edition, World Scientific2018.
[4] M. Fleischmann, S. Pons, The behavior of microelectrodes, Anal. Chem. 59(24) (1987) 1391A-1399A.
[5] C. He, M. Tao, C. Zhang, Y. He, W. Xu, Y. Liu, W. Zhu, Microelectrode-Based Electrochemical Sensing Technology for in Vivo Detection of Dopamine: Recent Developments and Future Prospects, Crit. Rev. Anal. Chem. (2020) 1-11.
[6] R.G. Compton, G.G. Wildgoose, N.V. Rees, I. Streeter, R. Baron, Design, fabrication, characterisation and application of nanoelectrode arrays, Chem. Phys. Lett. 459(1-6) (2008) 1-17.
[7] Y. Zhang, D. Li, R.G. Compton, Arsenic (III) Detection with Underpotential Deposition and Anodic Stripping Voltammetry, ChemElectroChem (2021).
[8] L.J. Bu, J. Liu, Q.J. Xie, S.Z. Yao, Anodic stripping voltammetric analysis of trace arsenic(III) enhanced by mild hydrogen-evolution at a bimetallic Au-Pt nanoparticle modified glassy carbon electrode, Electrochem. Commun. 59 (2015) 28-31.
[9] Z. Guo, M. Yang, X.-J. Huang, Recent developments in electrochemical determination of arsenic, Curr. Opin. Electrochem. 3(1) (2017) 130-136.
[10] Y. Zhang, D. Li, R.G. Compton, Arsenic (III) Detection with Underpotential Deposition on Gold, J. Electroanal. Chem. (2022) 116154.
[11] J.H. Yoon, G. Muthuraman, J. Yang, Y.B. Shim, M.S. Won, Pt-nanoparticle incorporated carbon paste electrode for the determination of Cu (II) ion by anodic stripping voltammetry, Electroanalysis (N.Y.N.Y.) 19(11) (2007) 1160-1166.
[12] J. Pizarro, E. Flores, V. Jimenez, T. Maldonado, C. Saitz, A. Vega, F. Godoy, R. Segura, Synthesis and characterization of the first cyrhetrenyl-appended calix [4] arene macrocycle and its application as an electrochemical sensor for the determination of Cu (II) in bivalve mollusks using square wave anodic stripping voltammetry, Sens. Actuators, B 281 (2019) 115-122.
[13] Z. Zhai, N. Huang, H. Zhuang, L. Liu, B. Yang, C. Wang, Z. Gai, F. Guo, Z. Li, X. Jiang, A diamond/graphite nanoplatelets electrode for anodic stripping voltammetric trace determination of Zn (II), Cd (II), Pb (II) and Cu (II), Appl. Surf. Sci. 457 (2018) 1192-1201.
[14] A. Nsabimana, S.A. Kitte, T.H. Fereja, M.I. Halawa, W. Zhang, G. Xu, Recent developments in stripping analysis of trace metals, Curr. Opin. Electrochem. 17 (2019) 65-71.
[15] M. Dali, K. Zinoubi, A. Chrouda, S. Abderrahmane, S. Cherrad, N. Jaffrezic-Renault, A biosensor based on fungal soil biomass for electrochemical detection of lead (II) and cadmium (II) by differential pulse anodic stripping voltammetry, J. Electroanal. Chem. 813 (2018) 9-19.
[16] H. Xiao, W. Wang, S. Pi, Y. Cheng, Q. Xie, Anodic stripping voltammetry analysis of mercury (II) on a pyridine-Au/pyridine/glassy carbon electrode, Sens. Actuators, B 317 (2020) 128202.
[17] H. Abdolmohammad-Zadeh, R. Mohammad-Rezaei, A. Salimi, Preconcentration of mercury (II) using a magnetite@ carbon/dithizone nanocomposite, and its quantification by anodic stripping voltammetry, Microchim. Acta 187(1) (2020) 1-8.
[18] Y. Xia, J. Li, G. Zhu, Y. Yi, Innovative strategy based on novel Ti3C2Tx MXenes nanoribbons/carbon nanotubes hybrids for anodic stripping voltammetry sensing of mercury ion, Sens. Actuators, B 355 (2022) 131247.
[19] C.A. Paddon, R.G. Compton, Underpotential deposition of lithium on platinum single crystal electrodes in tetrahydrofuran, J. Phys. Chem. C 111(26) (2007) 9016-9018.
[20] O.A. Oviedo, L. Reinaudi, S.G. García, E.P.M. Leiva, Underpotential deposition, Monographs in Electrochemistry (2016).
[21] F.J. Sarabia, V. Climent, J.M. Feliu, Underpotential deposition of Nickel on platinum single crystal electrodes, J. Electroanal. Chem. 819 (2018) 391-400.

[22] M.K. Yadav, D. Saidulu, A.K. Gupta, P.S. Ghosal, A. Mukherjee, Status and management of arsenic pollution in groundwater: A comprehensive appraisal of recent global scenario, human health impacts, sustainable field-scale treatment technologies, J. Environ. Chem. Eng. 9(3) (2021) 105203.
[23] D. Banik, S.K. Manna, A.K. Mahapatra, Recent development of chromogenic and fluorogenic chemosensors for the detection of arsenic species: Environmental and biological applications, Spectrochim. Acta, Part A 246 (2021) 119047.
[24] M. Kobya, R.D.C. Soltani, P.I. Omwene, A. Khataee, A review on decontamination of arsenic-contained water by electrocoagulation: Reactor configurations and operating cost along with removal mechanisms, Environ. Technol. Innovation 17 (2020) 100519.
[25] D.Q. Hung, O. Nekrassova, R.G. Compton, Analytical methods for inorganic arsenic in water: a review, Talanta 64(2) (2004) 269-277.
[26] N.R. Council, Chemistry and analysis of arsenic species in water, food, urine, blood, hair, and nails, Arsenic in Drinking Water, National Academies Press (US)1999.
[27] X.P. Yu, C.L. Liu, Y.F. Guo, T.L. Deng, Speciation Analysis of Trace Arsenic, Mercury, Selenium and Antimony in Environmental and Biological Samples Based on Hyphenated Techniques, Molecules 24(5) (2019) 23.
[28] S. Li, C.C. Zhang, S.N. Wang, Q. Liu, H.H. Feng, X. Ma, J.H. Guo, Electrochemical microfluidics techniques for heavy metal ion detection, Analyst 143(18) (2018) 4230-4246.
[29] S. Sikdar, M. Kundu, A Review on Detection and Abatement of Heavy Metals, ChemBioEng Rev. 5(1) (2018) 18-29.
[30] X.C. Le, X. Lu, M. Ma, W.R. Cullen, H.V. Aposhian, B. Zheng, Speciation of key arsenic metabolic intermediates in human urine, Anal. Chem. 72(21) (2000) 5172-5177.
[31] WHO, Guidelines for drinking-water quality Fourth Edition, WHO chronicle, 2011, pp. 104-8.
[32] J.A. Cox, I.A. Rutkowska, P.J. Kulesza, Critical Review-Electrocatalytic Sensors for Arsenic Oxo Species, J. Electrochem. Soc. 167(3) (2020) 6.
[33] J. Lalmalsawmi, D. Tiwari, D.J. Kim, Role of nanocomposite materials in the development of electrochemical sensors for arsenic: Past, present and future, J. Electroanal. Chem. 877 (2020) 18.
[34] G.M. dos Santos, D. Pozebon, C. Cerveira, D.P. de Moraes, Inorganic arsenic speciation in rice products using selective hydride generation and atomic absorption spectrometry (AAS), Microchem. J. 133 (2017) 265-271.
[35] I. Komorowicz, A. Hanć, W. Lorenc, D. Barałkiewicz, J. Falandysz, Y. Wang, Arsenic speciation in mushrooms using dimensional chromatography coupled to ICP-MS detector, Chemosphere 233 (2019) 223-233.
[36] H. Cheng, W. Zhang, Y. Wang, J. Liu, Graphene oxide as a stationary phase for speciation of inorganic and organic species of mercury, arsenic and selenium using HPLC with ICP-MS detection, Microchim. Acta 185(9) (2018) 1-8.
[37] I. Švancara, K. Vytřas, A. Bobrowski, K. Kalcher, Determination of arsenic at a gold-plated carbon paste electrode using constant current stripping analysis, Talanta 58(1) (2002) 45-55.
[38] W.B. Postek, I.A. Rutkowska, J.A. Cox, P.J. Kulesza, Electrocatalytic effects during redox reactions of arsenic at platinum nanoparticles in acid medium: Possibility of preconcentration, electroactive film formation, and detection of As (III) and As (V), Electrochim. Acta 319 (2019) 499-510.
[39] E.A. Zakharova, G.N. Noskova, S.G. Antonova, A.S. Kabakaev, Speciation of arsenic (III) and arsenic (V) by manganese-mediated stripping voltammetry at gold microelectrode ensemble in neutral and basic medium, Int. J. Environ. Anal. Chem. 94(14-15) (2014) 1478-1498.

[40] C.M.A. Brett, A.M.O. Brett, Electroanalysis, Oxford Science Publications1998.
[41] H. Huang, P.K. Dasgupta, A field-deployable instrument for the measurement and speciation of arsenic in potable water, Anal. Chim. Acta 380(1) (1999) 27-37.
[42] D. Yamada, T.A. Ivandini, M. Komatsu, A. Fujishima, Y. Einaga, Anodic stripping voltammetry of inorganic species of As3+ and As5+ at gold-modified boron doped diamond electrodes, J. Electroanal. Chem. 615(2) (2008) 145-153.
[43] L. Xiao, G.G. Wildgoose, R.G. Compton, Sensitive electrochemical detection of arsenic (III) using gold nanoparticle modified carbon nanotubes via anodic stripping voltammetry, Anal. Chim. Acta 620(1-2) (2008) 44-49.
[44] A. J. Bard, L.R. Faulkner, Electrochemical Methods: Fundamentals and Applications, 2nd ed., John Wiley & Sons, Inc, New York, 2001.
[45] Zimmer&Peacock, Cleaning gold electrodes, 2017. https://www.zimmerpeacocktech.com/2017/11/21/cleaning-gold-electrodes/.
[46] L. Bu, T. Gu, Y. Ma, C. Chen, Y. Tan, Q. Xie, S. Yao, Enhanced cathodic preconcentration of As (0) at Au and Pt electrodes for anodic stripping voltammetry analysis of As (III) and As (V), J. Phys. Chem. C 119(21) (2015) 11400-11409.
[47] X. Dai, O. Nekrassova, M.E. Hyde, R.G. Compton, Anodic stripping voltammetry of arsenic (III) using gold nanoparticle-modified electrodes, Anal. Chem. 76(19) (2004) 5924-5929.
[48] A. Buffa, D. Mandler, Arsenic (III) detection in water by flow-through carbon nanotube membrane decorated by gold nanoparticles, Electrochim. Acta 318 (2019) 496-503.
[49] D. Wang, Y. Zhao, H. Jin, J. Zhuang, W. Zhang, S. Wang, J. Wang, Synthesis of Au-decorated tripod-shaped Te hybrids for applications in the ultrasensitive detection of arsenic, ACS Appl. Mater. Interfaces 5(12) (2013) 5733-5740.
[50] M. Carron, M.E. Mrose, K. Murata, Relation of ionic radius to structures of rare-earth phosphates, arsenates, and vanadates, Mineralogical Society of America, 1958.
[51] Y. Wang, J.G. Limon-Petersen, R.G. Compton, Measurement of the diffusion coefficients of [Ru (NH3) 6] 3+ and [Ru (NH3) 6] 2+ in aqueous solution using microelectrode double potential step chronoamperometry, J. Electroanal. Chem. 652(1-2) (2011) 13-17.
[52] D.R. Merrill, I.C. Stefan, D.A. Scherson, J.T. Mortimer, Electrochemistry of gold in aqueous sulfuric acid solutions under neural stimulation conditions, J. Electrochem. Soc. 152(7) (2005) E212.

Chapter 8. **Achievements and Vision**

A new electroanalytical method, based on the combination of underpotential deposition and anodic stripping voltammetry (UPD-ASV) has been developed, validated and optimised for the detection of low levels of arsenic in water. The visually clear LOD as low as 0.8 ppb of total arsenic species can be reached, which is well within the threshold value of the WHO of 10 ppb. The use of gold electrodes over platinum electrodes is preferred since the results are shown to be free from interference from copper or chloride ions which often challenge analysis via conventional ASV using the bulk deposition of As.

The UPD-ASV method can be used to detect both As(III) and As(V) concentrations individually and to measure the total arsenic concentration in water. Measurement of arsenic speciation is done by tuning the deposition potential on a gold electrode, where both ions are deposited at a similar rate at a high negative potential, - 1.3 V (vs MSE) but As(III) is selectively deposited at a less negative potential, - 0.9 V (vs MSE). The concentration of As(V) is then calculated from the subtraction of total As content and As(III) values.

As a sensitive and selective method for As analysis the approach is envisaged to be lab-based method using gold macroelectrodes. Transfer to screen printed electrodes was not realised partly due to the limitations of the commercially supplied electrodes (high background signals, unexpected peaks in the as supplied electrodes). It remains an open question as to the extent of UPD of As on the amorphous gold encountered in SPEs which may be different from that seen at polycrystalline macroelectrodes. The limitations of the SPEs may be overcome with improved methods of fabrication. Meanwhile the UPD-ASV method provides an optimised method for As detection for wet analytical laboratories with the advantages of speed and low cost instrumentation.